

**Polymer crystallization at different substrates:
flat histogram Monte Carlo simulation**

Dissertation

zur Erlangung des Doktorgrades der Naturwissenschaften
(Dr. rer. nat.)

der

Naturwissenschaftlichen Fakultät II
Chemie, Physik und Mathematik

der Martin-Luther-Universität Halle-Wittenberg

vorgelegt von

Frau M. Sc. Evgeniia Filimonova

Gutachter: PD Dr. Viktor Ivanov
Prof. Thomas Thurn-Albrecht
Prof. Jens-Uwe Sommer

Tag der öffentlichen Verteidigung: 05.09.2024

Abstract

The present work is devoted to the study of crystallization process in the melt of short semiflexible polymer chains near surfaces. In particular, systems with two unstructured hard repulsive walls, as well as systems with one repulsive and one attractive wall are considered. A comparison of the observed phenomena is made with the bulk system without confinements. The occurrence of a two-dimensional crystalline layer near the attractive wall is discussed, as well as the possibility of distinguishing between heterogeneous nucleation and prefreezing crystallization scenarios at longer computation times.

The study is carried out with the Stochastic Approximation Monte Carlo (SAMC) simulation, which is a method of the realization of the flat histogram Monte Carlo approach. We use a coarse-grained tangent hard sphere model. SAMC allows to sample configurations uniformly over the entire energy interval in the microcanonical ensemble and to analyze the transition between the isotropic melt at high energies and completely crystallized noisy structures at low energies. Inside the transition, we observe intermediate structures (configurations) consisting of crystalline and melted domains. We have also proposed new methods to analyze local crystalline ordering based on local bond order parameters (known as Steinhardt parameters) applied to properly averaged particle coordinates, which allowed us to observe the coexistence of domains with different local crystalline symmetry.

Zusammenfassung

Die vorliegende Arbeit widmet sich der Untersuchung des Kristallisationsprozesses in der Schmelze von kurzen halbflexiblen Polymerketten in der Nähe von Oberflächen. Im Speziellen werden Systeme mit zwei unstrukturierten, harten, abstoßenden Wänden sowie Systeme mit einer abstoßenden und einer anziehenden Wand betrachtet. Es wird ein Vergleich der beobachteten Phänomene mit dem Bulk-System ohne Begrenzungen durchgeführt. Das Auftreten einer zweidimensionalen kristallinen Schicht in der Nähe der anziehenden Wand wird ebenso diskutiert wie die Möglichkeit, bei längeren Berechnungszeiten zwischen heterogenen Keimbildungsszenarien und Kristallisationsszenarien durch "prefreezing" zu unterscheiden.

Die Studie wird mit Hilfe der Stochastic Approximation Monte Carlo (SAMC) Simulation durchgeführt, die eine Methode zur Umsetzung des Flat Histogram Monte Carlo Ansatzes ist. Wir verwenden ein vergrößertes tangentiales Modell harter Kugeln. Mit SAMC können wir Konfigurationen gleichmäßig über das gesamte Energieintervall im mikrokanonischen Ensemble abtasten und den Übergang zwischen der isotropischen Schmelze bei hohen Energien und vollständig kristallisierten verrauschten Strukturen bei niedrigen Energien zu analysieren. Innerhalb des Übergangs beobachten wir Zwischenstrukturen (Konfigurationen), die aus kristallinen und geschmolzenen Domänen bestehen. Wir haben auch neue Methoden zur Analyse lokaler kristalliner Ordnungen vorgeschlagen, die auf lokalen Bindungsordnungsparametern (bekannt als Steinhardt Parameter) beruhen, die auf korrekt gemittelte Teilchenkoordinaten angewandt werden, wodurch wir die Koexistenz von Domänen mit unterschiedlicher lokaler kristalliner Symmetrie beobachten konnten.

Research cannot be completed at all, it can only be stopped.

Paraphrased from M. Zhvanetsky

Contents

| | | |
|----------|--|-----------|
| 1 | Introduction | 1 |
| 1.1 | Goals, systems, methods: a short overview | 1 |
| 1.2 | Review of relevant literature | 3 |
| 1.3 | The structure of the dissertation | 8 |
| 2 | Model and simulation methods | 9 |
| 2.1 | Model | 9 |
| 2.2 | Stochastic Approximation Monte Carlo (SAMC) | 13 |
| 2.2.1 | Monte Carlo methods | 13 |
| 2.2.2 | Implementation details | 16 |
| 3 | Structural analysis: methods and results discussion | 24 |
| 3.1 | Noise evaluation in the system under study | 25 |
| 3.2 | Test structures preparation | 28 |
| 3.3 | Radial distribution function | 31 |
| 3.4 | Local bond order parameters | 33 |
| 3.4.1 | P. J. Steinhardt, R. Nelson and M. Ronchetti parameters | 33 |
| 3.4.2 | W. Lechner and C. Dellago parameters | 36 |
| 3.4.3 | H. Eslami, P. Sedaghat and F. Müller-Plathe parameters | 38 |
| 3.5 | Noise reduction procedure | 40 |
| 3.6 | Searching for translation vectors | 52 |
| 3.7 | Other methods | 62 |
| 3.7.1 | Static structure factor | 62 |
| 3.7.2 | Common neighbor analysis | 65 |
| 3.7.3 | Voronoi cell analysis | 67 |
| 3.7.4 | The local alignment of chain segments analysis | 71 |
| 4 | Phase transitions: discussion of results | 74 |
| 4.1 | Thermodynamic properties | 74 |
| 4.2 | Structural analysis of systems | 84 |
| 4.2.1 | Analysis of the transition inside the layer near the attractive wall | 85 |
| 4.2.2 | Analysis of the 3d crystallization transition | 93 |

| | | |
|----------|---|------------|
| 4.2.3 | Analysis of structural changes inside transition region | 99 |
| 4.2.4 | Possibility of prefreezing phenomenon | 106 |
| 4.3 | Transition analysis findings and predictive insights for various systems: a comprehensive summary | 109 |
| 5 | Conclusion and outlook | 113 |
| | Bibliography | 118 |
| | Appendix | 133 |

List of Abbreviations

| | |
|--------------|---|
| CG | Coarse-Grained |
| MD | Molecular Dynamics |
| CGMD | Coarse-Grained Molecular Dynamics |
| MC | Monte Carlo |
| FHMC | Flat Histogram Monte Carlo |
| SAMC | Stochastic Approximation Monte Carlo |
| WLMC | Wang - Landau Monte Carlo |
| MuMC | Multi - Canonical Monte Carlo |
| HS | Hard Spheres |
| THS | Tangent Hard Spheres |
| RDF | Radial Distribution Function |
| LBO | Local Bond Order |
| ALBO | Average Local Bond Order |
| RLBO | Relative Local Bond Order |
| NRLBO | Noise Reduced Local Bond Order |
| CNA | Common Neighbor Analysis |
| APF | Atomic Packing Factor |
| <i>bcc</i> | body-centered cubic |
| <i>fcc</i> | faced-centered cubic |
| <i>hcp</i> | hexagonal close-packed |
| <i>sc</i> | simple cubic |

Chapter 1

Introduction

1.1 Goals, systems, methods: a short overview

In this dissertation, polymer crystallization is studied by means of computer simulation of a generic coarse-grained (CG) model in the bulk and in thin films between two hard homogeneous non-structured walls which either can be purely repulsive or can have an attractive potential.

Understanding the microscopic mechanisms of crystallization in different polymer systems still remains open problem in polymer physics [1–4]. Currently, there is no doubt about the widespread use of polymer materials, in particular of semi-crystalline polymers, due to the diversity of their physical properties. The properties of semi-crystalline polymers, such as optical properties, mechanical strength, and charge conductivity, are greatly influenced by crystallization conditions, in particular, an interfacial boundary (substrate or container walls) is critical in the polymer crystallization process [5, 6]. Therefore, the study of the crystallization process in polymer systems at different substrates is not only of fundamental, but also of applied interest. Depending on polymer – substrate combination the crystallization process can occur according to one of two scenarios.

The first scenario is known as heterogeneous nucleation [7] and consists of two principal stages: the formation of crystalline nuclei exceeding a critical size and the subsequent growth of these crystalline nuclei. Since heterogeneous nucleation is an activated process, it is necessary to supercool the sample below the bulk melting temperature T_m . In this case, crystal nuclei will arise and decay on the surface of a substrate. If the nuclei size exceeds the critical size, it overcomes the energy barrier, becomes stable and the growth stage begins.

Another scenario is much less studied and is called prefreezing. Prefreezing has been observed for crystallization in low molecular weight substances, in colloids, as well as in polymers, and it has become an object of interest quite recently [8–13]. Experimental studies have demonstrated that prefreezing exhibits characteristics of a first-order transition [11, 14]. This is evidenced by the reversible and abrupt formation of the crystalline phase at a substrate, so the

melting of the prefrozen crystalline layer occurs discontinuously. In the case of prefreezing, a crystalline layer of finite thickness is formed abruptly on the surface of a substrate at a temperature T_{pref} above the bulk melting point T_m [15–18] (Fig.1.1). At the moment of appearance, this crystalline layer has the thickness about several molecular layers and a macroscopic size in directions parallel to the substrate, and then its thickness continuously grows with decreasing temperature. When T_m is reached, the system becomes completely crystallized in bulk. This process is similar to prewetting of a liquid layer from the gas phase at a solid interface [19, 20]. The understanding of wetting and prewetting transitions can be extended to prefreezing, with small distinctions arising from the different nature of vapor-liquid and crystal-melt transitions [14, 18].

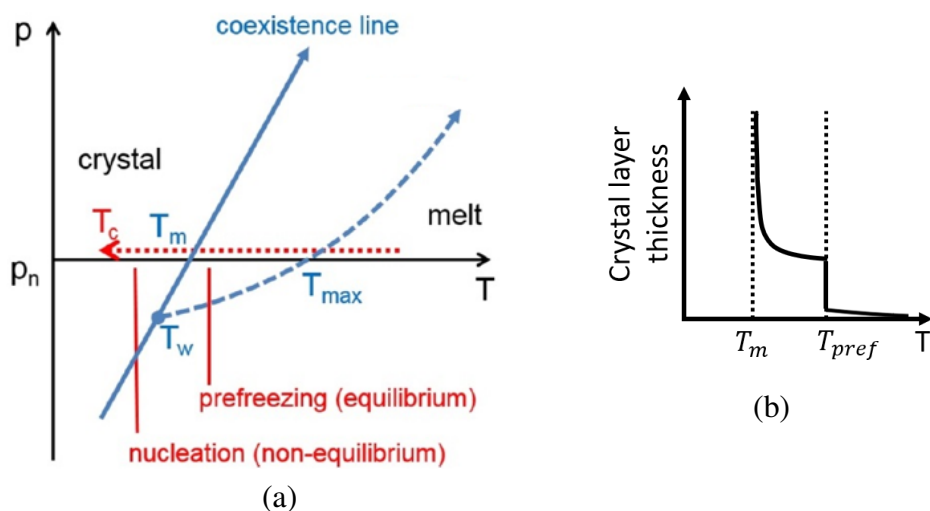


Figure 1.1: (a) Schematic phase diagram for crystallization process. Solid blue line is a coexistence line of crystal and melt, while wetting transition occurs at the wetting temperature T_w . The blue dashed line indicates a prewetting line (dashed). The dotted red horizontal line corresponds to an experiment in which crystallization occurs during cooling at ambient pressure. Crystallization can either be induced by prefreezing starting at T_{max} or by nucleation below T_m .

(b) Schematic growth of crystal layer thickness with decreasing temperature at $T < T_{pref}$ in prefreezing scenario. Both pictures are taken from Ref. [14].

Our focus in this dissertation is on the surface phenomena in polymer crystallization, in particular on the distinguishing between two scenarios – heterogeneous nucleation and prefreezing. Our main goal is to identify those distinctive features and parameter values of the model system of a polymer melt near the surface that have a decisive influence on the crystallization scenario.

Our CG model is a dense melt of semiflexible chains of tangent hard spheres (THS). Systematic computer simulation studies of crystallization in athermal dense systems of freely jointed chains of tangent hard spheres has been initiated in Refs. [21, 22], and a review of some results can be found in Ref. [23], as well as in other publications, and some of these results will be mentioned later in this dissertation. We use flat histogram Monte Carlo simulations

(FHMC) [24], in particular the Stochastic Approximation Monte Carlo (SAMC) algorithm, first suggested in Refs. [25, 26]. We have chosen this method because our goal is to study two different phase transitions – crystallization and prefreezing – that could be actually quite close to each other in temperature, and therefore we need to determine the temperature and the order of phase transitions in our simulations as exact as possible, and we should also be able to distinguish the cases when the prefreezing transition is present or absent in our model system. The main advantage of FHMC techniques is the more exact determination of the order of phase transitions and of the transition points, in comparison to the accuracy of other methods. This is due to the fact that the sampling takes place in much more broad regions of the phase space available to a system. The main shortcoming of FHMC algorithms is that only very small systems can be studied (because of the same reason of much more detailed sampling of the phase space).

Now we will present a review of literature on the bulk and surface crystallization in related systems, while the details on the model and method will be given in Chapter 2.

1.2 Review of relevant literature

A CG model with particles can shed light on the mechanisms of polymer crystallization at surfaces, in particular it is able to distinguish between scenarios of heterogeneous nucleation and prefreezing and to reveal model features responsible for each scenario, especially if it is used in combination with flat histogram Monte Carlo (FHMC) techniques. A CG model has all necessary features to take into account the essential details of polymer systems that may be responsible for phenomena under study, and at the same time, it does not include unnecessary atomistic details that most likely affect only non-essential peculiar properties of the systems behavior. To the best of our knowledge, the study of a prefreezing transition in CG polymer models by means of FHMC techniques has not yet been performed.

Simultaneously with a number of experiments to study the mechanisms of crystallization (heterogeneous nucleation and prefreezing) [12, 27], a phenomenological theory describing the phenomenon of prefreezing was developed [28, 29]. The theory based on classical nucleation theory shows that interfacial free energies determine the mechanism by which the crystallization process takes place. So, according to the Young's equation, $\gamma_{sm} = \gamma_{sc} + \gamma_{cm} \cdot \cos(\theta)$, the interfacial free energies at the interface substrate-melt (γ_{sm}), substrate-crystal (γ_{sc}), and crystal-melt (γ_{cm}) determine the contact angle θ . In the case of heterogeneous nucleation the crystal nucleus is assumed to have a shape of a spherical cap with a certain non-zero contact angle θ with the substrate. In the case of $\gamma_{sm} > \gamma_{sc} + \gamma_{cm}$ prefreezing occurs and the contact angle θ becomes equal to zero, which leads to the formation of a crystalline layer on the surface of the substrate [28] (Fig.1.2). Thus, the same polymer can follow a different crystallization mechanism depending on the substrate.

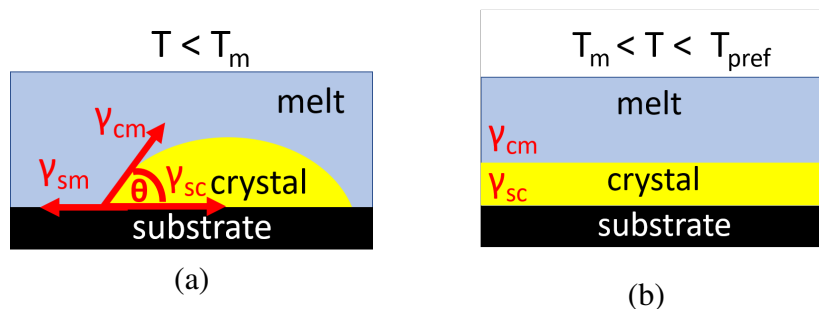


Figure 1.2: Illustration for crystallization on a flat substrate:

- (a) heterogeneous nucleation, formation of a critical crystal nucleus at $T < T_m$;
 (b) preefreezing, formation of a crystalline layer at $T_m < T < T_{pref}$. Adapted from [28].

At the same time, additional study of the phenomenon of polymer crystallization near substrates using computer simulation methods can provide a description taking into account the microscopic behavior (e.g. scenario of processes, packing and layering effects, chain conformations) of the system and complement the existing knowledge about this phenomenon. The phenomenon of preefreezing was previously discovered in computer simulations of hard spheres and Lennard-Jones particles [10, 15–18]. Since there is no connection of particles into a chain, this model describes colloidal systems. At the same time, a number of simulation studies were carried out on polymer crystallization near the walls [30–32]. It also was found out that walls contribute to orientational (nematic) ordering near them [33–35], which can also potentially exhibit a prewetting transition [18].

Computer simulations of crystallization in polymer systems have been performed by several groups using different methods [23, 36–48]. We will mention here those results that are in some aspects related to the phenomena which we observe in our study.

Different models have been studied by means of coarse-grained molecular dynamics (CGMD) simulations and the influence of different factors has been considered: intrachain stiffness [36, 37], inter- and intrachain interaction potential between particles [49], structure and interaction potential of walls (for polymer films) [50], density [51], molecular weight distribution [52, 53], chain architecture [54]. For a mesoscopic bead-spring model with an intramolecular stiffness potential, it has been demonstrated that chain stiffness alone, without an attractive inter-particle potential, is a sufficient driving force for the formation of chain-folded lamellae [36, 37]. In CGMD simulations for the same model between confining walls, a preorder is induced near the walls already in the melt at high temperature, and then it propagates into the film, while this growth can be influenced by prestructuring the wall [50]. The importance of the coupling between chain stiffness and density for polymer crystallization has been shown, e.g., in Ref. [51]. Recently, it has been shown by means of CGMD simulation using self-seeding algorithm that various chain architectures (linear vs. branched) result in different multilamella structures [54].

The CGMD simulation of hexagonal structure of crystals with long methylene sequences has been first reported in Ref. [55]. The difference between nematic and hexagonal ordering in

the melts of semiflexible chains has been first studied theoretically in Refs. [56, 57]. In these papers, a theoretical model has been developed combining density-functional theory for freezing with the Onsager theory of orientational ordering, and phase diagrams with and without intermediate nematic phase between isotropic and hexagonal phases have been obtained: for the high temperature or short persistence length, the phase diagram shows a direct isotropic-hexagonal transition as the pressure or density is increased, with no intermediate nematic phase [57]. Polymer crystallization in thin films (quasi-2d geometry) has been also studied both experimentally and theoretically [58, 59]. Some simple generic lattice model (like the diffusion limited aggregation or the percolation model) was used [58, 59], that allows to observe clusters like those seen in the experiment [58, 59], and is also suitable to study polymer crystallization on pre-patterned substrates [60]. This theoretical approach considers polymer crystallization in terms of the formation of a nonequilibrium structure, with particular focus on the morphogenesis of polymer crystals during growth and annealing processes [61, 62]. In particular, it has been demonstrated that reorganization processes precede melting, and the stability of the polymer crystal is not directly correlated with the structures that are formed at the crystallisation point [61, 62]. Several morphological phases have been identified that are observed under different growth and annealing conditions, including thickening of crystal edges, formation of hole-rim patterns, and droplet phase. The simulations reveal certain nonequilibrium properties, including internal energy and nonequilibrium heat capacity. It has been demonstrated that multi-peak melting endotherms result from morphogenetic transformations, and the concepts of melting-recrystallization phenomena have been discussed [61]. The behavior of microcrystalline domains has also been studied by molecular dynamics methods [63–65, 39].

Similar melting-recrystallization phenomena have been observed for the Asakura-Oosawa model in computer simulations of three-dimensional systems, and phase coexistence between a crystalline nucleus and surrounding fluid has been reported in Ref. [66]. These phenomena are in some sense quite similar to the droplet evaporation-condensation transition [67–69], where some intermediate structures have been observed in the course of liquid-vapor transition. The appearance of such structures also manifested itself in the form of "steps" inside the first-order transition loop in the equation of state [67–69]. Because we see similar phenomena inside our crystallization transition, although for other functions, these references were very useful for correct interpretations of our results.

In principle, the stability of particular configurations (microstates) at given values of external parameters, e.g., at a given temperature, can be studied also in our flat histogram Monte Carlo (FHMC) simulations, which deliver information on equilibrium thermodynamics of systems, because we are able to calculate probability densities for sampled microstates. However, this will be pure thermodynamic stability, while in real systems and in molecular dynamics simulations the kinetic effects influence the stability as well, because some of thermodynamically stable microstates may be inaccessible for purely kinetic reasons.

A common feature of all CG models mentioned above is that the particles (polymer

beads) in them are soft, i.e., they are in most cases either soft spheres or Lennard-Jones particles, and this is because the MD method is not very suitable for hard core potentials, although large-scale molecular dynamics simulations of hard sphere systems have been also performed [70–72].

The model of hard spheres (HS) is widely used in theory and simulations of colloidal systems and it describes rather well experimental results on crystallization in colloidal systems [73]. The model of tangent hard spheres (THS) is very popular for polymer systems. It describes flexible polymers, if tangent hard spheres are freely jointed, and semiflexible polymers, if some bending potential on the angles between rigid bonds adjacent along the chain is applied. Phase transitions in such systems, in particular crystallization and liquid crystalline transition, are entropy driven. The Monte Carlo (MC) method is very convenient for computer simulation of such models and has been widely used for more than three decades [74–76].

Due to the convenience of these models, a wide range of studies of THS systems was carried out by N. Ch. Karayiannis and M. Laso with colleagues using the MC method. As already mentioned above, systematic computer simulation studies of crystallization in athermal dense systems of freely jointed chains of tangent hard spheres has been initiated in Refs. [21–23]. The subsequent study of entropy induced crystallization in these systems was carried out using the characteristic crystallographic element (CCE) norm methodology [77–80]. In addition to fixed bond length models, those studies have highlighted the influence of bond length fluctuations on the crystallization of chains [81]. It was shown that increasing the bond gap widens the crystallization rate (nucleation and growth, measured in MC steps), and the bond tolerance affects the morphology of the structure [81]. The existence of random hexagonal close packing (rhcp), face-centered cubic (*fcc*) and hexagonal close-packed (*hcp*) morphology has been demonstrated [81]. In our semi-flexible THS model, we also observe structures similar to *fcc* and *hcp* in systems with and without confinements. An extensive research on the effect of stiffness of chains with different harmonic stiffness potentials for different densities in unconstrained systems has been performed [82].

Another research direction related to this dissertation are studies of systems with constraints in the form of parallel non-penetrating walls of flexible THS chains [83, 84]. When different average chain lengths and volume fractions were investigated, *fcc* and *hcp* structures were also observed [84]. The observed crystallization processes both in the bulk and near the walls in these systems are entropy driven. Extremely small the wall spacing equal to the bead size allows to investigate two-dimensional effects [85, 86].

Theory of the two-dimensional crystallization has been first suggested in [87]. Already there, it was shown that conventional crystalline long-range order in two dimensions for power-law potentials of the Lennard-Jones type is not possible. Appearance of long-range translational order in continuous two-dimensional models with short-range interactions is forbidden by Hohenberg-Mermin-Wagner theorem [88–90]. Theory of dislocation-mediated two-dimensional melting was proposed in [91, 92] and is known as Kosterlitz-Thouless-Halperin-

Nelson-Young (KTHNY) theory. Monte Carlo computer simulations of the two-dimensional melting transition using hard disks has been performed in Ref. [93], where all results were in good agreement with the KTHNY theory, and a first-order phase transition with small correlation length and a one-stage continuous transition was ruled out. However, in Ref. [94] the scenario of the liquid–solid transition of hard discs (first-order vs. KTHNY transition) was investigated more attentively, and the possibility of a (very weak) first-order transition from the fluid to the crystal could not be firmly ruled out. These studies are directly relevant to our work, as in our study we have also found a similar transition.

One of the advantages of MC methods is the possibility to accelerate the sampling of configurational phase space by means of using "unphysical" but very efficient trial moves [95, 96]. In our work, we have also invested a lot of time in looking for the most efficient moves, but we still have not reached desired speed of phase space sampling.

Flat histogram Monte Carlo (FHMC) simulations [24] allow to sample configurational phase space more widely and to obtain equilibrium thermodynamic behavior of a system more precisely, in order to study those effects in polymer crystallization that arise from the underlying thermodynamics, and distinguish them from purely kinetic effects [24, 97, 98]. However, FHMC is very time consuming, so that only much smaller systems can be studied by this method in comparison to CGMD. The crystallization in dense polymers melts has been studied on the model systems consisting of 720 chains, each composed of 10 beads, i.e., totally 7200 particles, by FHMC simulations in Ref.[97]. In this dissertation, we have build our research on the model and algorithm used in Ref.[97]. We perform simulations of Stochastic Approximation Monte Carlo (SAMC) method [24, 99–101], which allows to implement canonical and micro-canonical analysis. Since SAMC allows us to uniformly visit regions of phase space with different energies, this method is the most optimal for calculating (pseudo-)phase diagrams. The effectiveness of this method has been demonstrated in studies on crystallization in bulk [97]. We consider systems with a fixed chain length. The number of particles in the system and the size of the system are also fixed during the simulation process, ensuring a constant average density in the system. Our goal here is to examine the phenomenon of crystallization near walls with different wall potentials (purely repulsive and with different degree of attraction) in the hope to identify microscopic properties corresponding to different crystallization mechanisms. Also, for comparison, an additional analysis of a system without walls is carried out. To detect finite size effects, we consider systems of different sizes ($L_x = L_y = 20$ for all systems with $L_z = \{19, 20, 39, 40\}$ depending on the system (see chapter 2.1)).

Finally, in computer simulations of crystallization, the reasonable choice of parameters allowing to analyze the observed structure plays an important role. We compare existing methods (local bond order parameters [102–104], various modifications of common neighbor analysis (CNA) [105–108], Voronoi cell analysis [109, 110], local chain segments alignment parameters [48, 40]) based on the conformations of the systems under study, as well as for test structures (*sc*, *fcc*, *bcc*, *hcp*). Among mentioned methods of investigation of crystal structures

as well as radial distribution function [111], structure factor and the characteristic crystallographic element (CCE) norm [77, 80], etc., the local bond order (LBO) parameters [102] occupy a special place. The local bond order parameters or Steinhardt parameters [102] have been suggested to distinguish crystals with different symmetries. However, these parameters work well only for perfect crystals or for crystals with very weak fluctuations in the particle positions, but they need modifications for typical cases in real soft matter systems, and such modifications have been suggested [103, 104, 112, 113]. We have found that these modifications are still not entirely accurate for the systems studied in this dissertation, so that we have suggested another new modification for Steinhardt parameters and called it a noise reduction procedure. Looking ahead, we have also developed a novel methodology how to reconstruct "perfect" structure in the whole simulation box that would be most close to a real local noisy crystalline symmetry when averaged over the whole box.

Finally, I would like to mention here two my previous papers [F1,F2] which were published before I started to work on the topic of this dissertation but which are thematically related to this study. The method was different, but the studied phenomena were related – ordering transition in the bulk and at surfaces. That experience has helped me in the present study.

1.3 The structure of the dissertation

This work has the following structure.

- 2 Model and simulation methods. The chapter describes the models used and provides a detailed description of the simulation methodology used.
- 3 Structural analysis: methods and results discussion. The chapter describes a study of existing and the development of new approaches to the analysis of structures.. A comparison of methods is carried out based on the selected conformations, and the effectiveness or applicability of a particular method in our work is substantiated.
- 4 Phase transitions: discussion of results. The chapter is devoted to a discussion of the results obtained during simulation process..
- 5 Conclusion. The chapter is dedicated to summary of the findings.
- 5 Outlook. A short outlook to future projects is given.

Appendix. In the Appendix one can find information that can complement the study, but it is placed after the main text to avoid distracting the readers' attention.

Chapter 2

Model and simulation methods

2.1 Model

A semi-flexible tangent hard spheres (THS) serves as a coarse-grained model representing real polymers. The THS model used in this work is well established in works devoted to the study of crystallization in short chain melts [114, 97]. All systems that we consider are characterized by the potential of hard spheres U_b and the stiffness potential U_θ . The interactions between hard spheres can be represented as

$$U_b(r) = \begin{cases} \infty, & r \leq d, \\ 0, & r > d, \end{cases} \quad (2.1)$$

where r is the distance between the centers of the two spheres. This interaction does not give a numerical contribution to the energy, but imposes constraints on the available configuration space. Bond length l is fixed, $l = d$. As a result, possible angles between the bonds of neighboring spheres (or *beads*) θ in the chain cannot exceed 120° . Stiffness potential of the chains (Fig.2.1):

$$U_\theta(\theta) = \begin{cases} -\varepsilon, & \theta \leq \theta_s, \\ 0, & \theta_s < \theta < 120^\circ, \\ \infty, & 120^\circ \leq \theta, \end{cases} \quad (2.2)$$

The fixed value of $\cos \theta_s = 0.9$ used in this study corresponds to $\theta_s \approx 26^\circ$. The ground-state stiffness energy for systems of N_c chains of length N is defined as $E_{min}^s = -N_c(N-2)\varepsilon$, while the maximum energy equal to $E_{max}^s = 0$. During the simulation, the size of the box (L_x , L_y and L_z) and number of chains N_c do not change. The chain length $N = 10$ is fixed in all systems. We consider small systems $L_x = L_y = 20$, $L_z = 19$ and $L_x = L_y = 20$, $L_z = 20$ containing $N_c = 720$ chains, as well as large systems $L_x = L_y = 20$, $L_z = 39$ and $L_x = L_y = 20$, $L_z = 40$, containing $N_c = 1440$ chains. This ratio provides volume fractions ϕ of the polymer equal to 0.496 and

0.471, respectively (see below). Energies and temperatures are measured in units of well depth $\varepsilon = 1$, while all lengths are measured in units of solid sphere diameter $d = 1$.

Since the goal of our work was to study the phenomenon of crystallization near surfaces, we investigated the following systems: systems with repulsive (non-penetrating) walls and systems with one attractive and one repulsive walls as well as systems without walls (for comparison). Systems without walls with a volume fraction of $\phi = 0.471$ have already been studied in works Ref. [114, 97], and the results of these studies were provided to us by the author T. Shakirov for comparative analysis. This opens up the opportunity for us to study systems of the same volume fraction in the presence of walls, and also compare with the results of our study for a system of a larger volume fraction ($\phi = 0.496$) without walls. It should be noted that the predictions indicate that crystallization is possible at these densities [97].

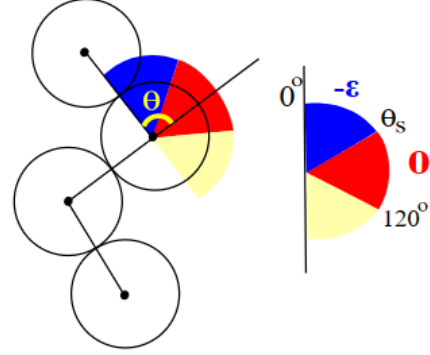


Figure 2.1: Illustration of stiffness potential.

Systems without walls

We have modeled a system that we use as a comparison system, simulating a polymer in an unconstrained bulk. Since in small size systems, the finite size effects of the system have a great impact, we use simulating boxes of two different sizes: with sizes $L_x = L_y = 20$ and $L_z = 19$ ($N_c = 720$) and $L_x = L_y = 20$ and $L_z = 39$ ($N_c = 1440$). This ratio of the number of particles and the size of the box provides the volume fraction:

$$\phi = \frac{NN_c}{L_x L_y L_z} \frac{\pi d^3}{6} \approx 0.496 \quad (2.3)$$

Since there are no constraints and the periodic boundary conditions are applied in all directions, the total energy E is composed only of the stiffness energy E^s of the chains:

$$E = E^s = \sum_{i=0}^{N_c(N-2)} U_{\theta}^i, \quad (2.4)$$

where the summation is taken over all angles between bonds in chains. In the text, we will refer to this system as *a system without walls* or *bulk*.

System with two purely repulsive walls

In the case of uniformly repulsive walls, a potential U_{rep} is applied between each bead and walls:

$$U_{rep}(z) = \begin{cases} \infty, & |z| \geq (L_z - d)/2, \\ 0, & |z| < (L_z - d)/2, \end{cases} \quad (2.5)$$

where z represents a coordinate of a bead along z axis. In fact, this potential hinders chain units from passing through the wall and does not contribute numerically to the total energy value. That is, the contribution to the energy is determined by the same summand (Eq. (2.4)) as in the case of the unconstrained system. Despite the fact that the energy contributions do not change, such a potential imposes additional confinements in the configuration space, so centres of the beads cannot come closer to the surface than their own radius of $d/2$ (Fig.2.2 (a)). The box dimensions $L_x = L_y = L_z = 20$ ($N_c = 720$) and $L_x = L_y = 20$ and $L_z = 40$ ($N_c = 1440$) provide the volume fraction $\phi = 0.471$. Thus, two parallel walls are positioned on the planes at $z = \pm 10$ and $z = \pm 20$ respectively. Along the x and y axes, the periodic boundary conditions are implemented.

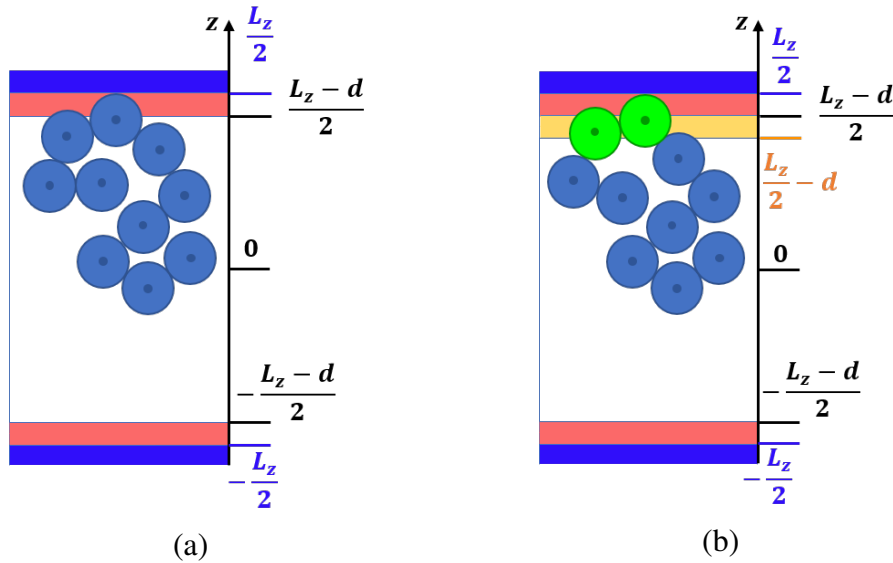


Figure 2.2: Illustration of walls potential for repulsive walls U_{rep} (a) and repulsive and attractive walls U_{at_1} , U_{at_2} (b). The walls are indicated in blue. The red region of thickness $d/2$ is unreachable for the centers of mass of the beads. The orange area represents the area of attraction. The centers of mass of the green beads are in the region of attraction, therefore, each of these beads will contribute $-\varepsilon$ (for a system with potential U_{at_1}) or -4ε (for a system with potential U_{at_2}). The ratio between L_z and d is not observed in the figure.

We will refer to these systems in the text as *systems with repulsive walls*, with potential U_{rep} , or simply as *systems with walls*.

System with repulsive and attractive walls

We also examine two small systems ($L_x = L_y = L_z = 20$, $N_c = 720$) where one wall at $z = -10$ is purely repulsive, while the second wall at $z = 10$ has an attracting potential. In the first system, we introduce a weak attraction energy $-\varepsilon$ for a bead in a wall layer of thickness $d = 0.5$ (Fig.2.2 (b)) :

$$U_{at_1}(z) = \begin{cases} -\varepsilon, & L_z/2 - d \leq z < (L_z - d)/2, \\ 0, & -(L_z - d)/2 < z < L_z/2 - d, \\ \infty, & |z| \geq (L_z - d)/2 \end{cases} \quad (2.6)$$

In the second case, the attraction is four times larger:

$$U_{at_2}(z) = \begin{cases} -4\varepsilon, & L_z/2 - d \leq z < (L_z - d)/2, \\ 0, & -(L_z - d)/2 < z < L_z/2 - d, \\ \infty, & |z| \geq (L_z - d)/2. \end{cases} \quad (2.7)$$

Thus, in these two systems, the total energy consists of two contributions, namely the attraction of beads to the wall E_w and the stiffness potential E^s :

$$E = E^s + E^w = \sum_{i=1}^{N_c(N-2)} U_{\theta}^i + \sum_{j=1}^{NNc} U_{at_k}^j, \quad (2.8)$$

where E^w is the wall energy, determined by summing over all particles j and $U_{at_k}^j$ calculated by the Eq.(2.6) or the Eq.(2.7) ($k = \{1, 2\}$). Thus, the maximum energy $E_{max} = 0$ can be realized in configurations where all angles between bonds $\theta^i > 26^\circ$ and all centers of mass of all beads are located outside the attracting layer ($z_j \leq L_z/2 - d$). Note that such a microstate is entropically unfavorable and therefore difficult to achieve. The minimum energy can also be estimated. Since the thickness of the attracting layer is $d/2$, it contains no more than one layer of particles. The surface area $S_{xy} = L_x L_y = 20 \cdot 20 = 400$ consists of the projection area $S_b = \pi(d/2)^2 = \pi/4$ of n_w beads, as well as the area of voids S_v : $S_{xy} = S_v + n_w S_b$. For a rough estimate, let us assume $S_v = 0$. Then $n_w = S_{xy}/S_b \approx 510$. Thus, let $n_w = 510$ particles be placed in the near-wall layer, and all chains are elongated ($\theta^i < 26^\circ$), then for the potential U_{at_1} the minimum energy is $E_{min}^{at_1} = -\varepsilon N_c(N-2) - \varepsilon n_w = -6270$, while for the potential U_{at_2} the minimum energy is $E_{min}^{at_2} = -\varepsilon N_c(N-2) - 4\varepsilon n_w = -7800$. We will refer to this system as a *system with weak* (or *strong*) *attraction of wall* or a system with potential U_{at_1} (or U_{at_2}).

2.2 Stochastic Approximation Monte Carlo (SAMC)

2.2.1 Monte Carlo methods

Monte Carlo (MC) [115–119] simulation in statistical physics uses the computational power of modern computers to obtain information about the collective behavior of systems consisting of numerous interacting particles. To characterize the physical properties of a system, selected observables are measured.

Let $A(\mathbf{x})$ denote an observable dependent on the degrees of freedom of N particles (formally designated as a vector \mathbf{x} giving a point in the configuration phase space of the system; in other words, \mathbf{x} is a set of coordinates - a microstate in the configuration space). According to statistical thermodynamics, in thermal equilibrium at given values of thermodynamic parameters such as temperature T , pressure p , etc., the average value of $\langle A \rangle$ should be computed as:

$$\langle A \rangle = \int d\mathbf{x} A(\mathbf{x}) \rho(\mathbf{x}), \quad (2.9)$$

where $\rho(\mathbf{x})$ is the probability that the microstate \mathbf{x} has been realized in equilibrium. For example, for a system of N particles in a volume V at a temperature T in the canonical ensemble, the probability $\rho(\mathbf{x})$ has the form:

$$\rho(\mathbf{x}) = \frac{1}{Z(T)} \exp\left(-\frac{\mathcal{H}(\mathbf{x})}{k_B T}\right), \quad (2.10)$$

where k_B is the Boltzmann constant, T is temperature, $\mathcal{H}(\mathbf{x})$ is the Hamiltonian, which describes the total energy of the system, and $Z(T)$ is the partition function:

$$Z(T) = \int d\mathbf{x} \exp\left(-\frac{\mathcal{H}(\mathbf{x})}{k_B T}\right). \quad (2.11)$$

Here and in the following we omit the arguments N, V . For ease of notation, summation can be employed, indicating that as the number of visited states \mathbf{x}_t becomes sufficiently large (as $n \rightarrow \infty$), the law of large numbers becomes applicable:

$$\lim_{n \rightarrow \infty} \sum_{t=1}^n A(\mathbf{x}_t) \rho(\mathbf{x}_t) = \langle A \rangle. \quad (2.12)$$

The MC procedure involving visiting uniformly distributed random states $\{\mathbf{x}_t\}$ is called simple sampling. However, this method can only be implemented in the simplest systems. In order for Monte Carlo methods to be applicable to more complex systems, the importance sampling approach was developed. This broad class of methods involves the non-uniform generation of microstates in configuration space based on Markov process properties. The classical example of an algorithm of this kind in the canonical ensemble is the Metropolis algorithm [120, 121]. The generation of microstates $\{\mathbf{x}_t\}$ in this case occurs with probability $\rho(\mathbf{x})$. It has

been shown that the move from the microstate \mathbf{x}_0 with energy E_0 to a microstate \mathbf{x}_1 with energy E_1 should be accepted with the probability:

$$p_{acc} = \min \left(1, \exp \left\{ -\frac{\Delta E}{k_B T} \right\} \right) \quad (2.13)$$

where $\Delta E = E_0 - E_1$. Then the Eq. (2.12) can be rewritten as

$$\langle A \rangle = \frac{1}{n} \sum_{t=1}^n A(\mathbf{x}_t). \quad (2.14)$$

Classical Metropolis MC algorithm allows to calculate the average values of physical parameters (selected observables). However, this approach does not allow a reasonable accurate calculation of thermodynamic potentials related to partition function, including entropy and free energy. For example, in canonical ensemble the free energy $F(T)$ can be calculated as:

$$F(T) = -k_B T \ln Z(T).$$

The developed family of flat-histogram MC methods allows to solve this problem [24]. In these modifications, instead of probability distribution in configuration space, the focus is on probability distribution of parameters of interest that define a macrostate. In our work, a good choice of such a parameter is the energy E . This choice is the most common, although other options are also possible. The main idea of these methods is to produce conformations uniformly distributed in E space.

Thus, we are talking about a uniform histogram of visiting microstates with the energy E , $H(E)$, which gives the name to the family of methods: flat-histogram MC. Since the probabilities $\rho(E)$ are unknown in advance, an iterative scheme is used to refine the value of $\rho(E)$ using the current value of $\rho(E)$. Ultimately, having obtained the correct estimate of $\rho(E)$, $Z(T)$ can be calculated. In general, this scheme is followed by a wide variety of methods, differing in the details of the algorithms. Among these methods are Multi-canonical Monte Carlo (MuMC or MUCA) [122–127], Wang-Landau (WLMC) [128–140] algorithms and SAMC [25, 26, 141–143, 101, 139], which can be considered as a special type of WLMC algorithms (see below). An important characteristics of the methods are their convergence and accuracy. For the SAMC method used in our study, it has been mathematically proven [25, 26] that its convergence to the true $g(E)$ (see below) occurs at a rate inversely proportional to the simulation time ($\propto 1/t$).

The main task of flat-histogram MC methods is to find the most accurate density of states function $g(E)$, which is the number of microstates $\{\mathbf{x}\}$ that implement a macrostate with a given E . With this $g(E)$ function one can calculate using Laplace transform both the partition function $Z(T)$:

$$Z(T) = \sum_E g(E) \exp \left(-\frac{E}{k_B T} \right), \quad (2.15)$$

and the average observed values:

$$\langle A \rangle(T) = \frac{1}{Z(T)} \sum_E A(E) g(E) \exp\left(-\frac{E}{k_B T}\right). \quad (2.16)$$

In the expressions above we moved from integration to summation, since in practice a finite set of energies is used for calculations.

A general scheme of the flat-histogram algorithm could be summarized as:

1. Choose an initial estimate of the density of states function $g(E) = g_0(E)$. Often $g_0(E) \equiv 1$ is used as the initial estimate. The visiting histogram is set to 0 ($H(E) \equiv 0$).
2. Make a trial change of the system configuration from the current state \mathbf{x}_0 with energy $E = E_0$ to a trial state \mathbf{x}_1 with energy $E = E_1$, accept the new state with probability:

$$p_{acc} = \min\left(1, \frac{g(E_0)}{g(E_1)}\right). \quad (2.17)$$

Thereby, configurations with larger $g(E)$ are visited less frequently than configurations with smaller $g(E)$. Given the expression Eq.(2.17) (in the case when $g(E)$ is close to the true one), visits to all macrostates should be uniformly distributed with respect to E , $H(E) \approx const$.

Let E' be the energy value after trying to make a trial step, namely $E' = E(\mathbf{x}_1)$ if the trial move is accepted or $E' = E(\mathbf{x}_0)$ if the move is rejected. The conformation is naturally updated (if a trial move is accepted) and the histogram is updated:

$$H(E') \rightarrow H(E') + 1.$$

3. If required (depending on the specific flat-histogram algorithm, see below), update the current estimate of the density of states $g(E)$.
4. Repeat steps 2 and 3 until termination criteria are satisfied.

For the MuMC algorithm the Step 3 is executed only once at the end of the simulation run. The new estimate of the density of states function $g(E)$ is calculated as

$$\ln g(E) \rightarrow \ln g(E) + \ln H(E). \quad (2.18)$$

The simulation runs are repeated until the multi-canonical histogram $H(E)$ for the run becomes "flat" ($H(E) \approx const$), which provides that the shape of $g(E)$ does not change compared to the previous run.

In Step 3 for WLMC algorithms, the density of states function is replaced at each trial step according to the expression:

$$\ln g(E) \rightarrow \ln g(E) + \gamma_t \cdot \delta(E, E'), \quad (2.19)$$

The $\delta(E, E')$ is the Kronecker symbol, which means

$$\delta(E, E') = \begin{cases} 1, & E = E' \\ 0, & E \neq E'. \end{cases}$$

The time evolution of the modification factor γ_t depends on the specific method of the WLMC algorithms. In particular, for SAMC γ_t changes with the simulation time t (trial moves counter) as

$$\gamma_t = \min\left(\gamma_0, \frac{t_0}{t}\right), \quad (2.20)$$

where γ_0 is the pre-selected maximum value of γ_t , t_0 is the parameter. With this choice of γ_t , the best functional convergence is achieved. In practice, typical values for γ_0 is less than 10^{-1} [99]. A suitable choice of γ_0 ensures visiting of a significant range of the energy space E during the initial stage of the simulation when $t < t_0$ with $\gamma_t = \gamma_0$. However, excessively small values γ_0 hinder the compensation of potential inaccuracies in the initial density of states $g_0(E)$ estimate. Hence, determining an appropriate value γ_0 necessitates balancing these opposing factors. The optimal choice of both parameters γ_0 and t_0 is an actual problem for researchers nowadays [99].

2.2.2 Implementation details

The computer program (code) for SAMC simulation in this work was written in C language and based on a program by T. Shakirov. Statistical analysis and most plotting were done in R [144]. In this part, we describe the preparation of starting conformations, describe a number of technical improvements introduced into the program, and also describe the trial movements used.

Preparation of starting conformations

Initially, for systems without walls and with repulsive walls, the conformations of elongated chains with stacking parallel to the XY planes were prepared "by hands". These ordered states correspond to the lowest possible energy E_{min} . Then, using a certain selection of parameters γ_0, t_0 , and the initial density of states function g_0 , conditions were created under which steps were taken to increase the energy. For example, $\ln g_0(E) = -3E$, $\gamma_0 \sim 0.001$; $t_0 \sim 5 \cdot 10^6$ contribute to the movement of the system from a state of low energy to a region of high energy. In this way, disordered high-energy conformations were obtained from a completely ordered system. Next, adjusting the parameters γ_0, t_0 the systems were sampled at high energies. Then, starting from these disordered high-energy states, we achieved microstates with smaller ener-

gies in order to select starting conformations for computer simulations, to accumulate the of function $\ln(g)$. To force systems to evolve toward low-energy configurations, the parameters γ_0, t_0 were changed, and restrictions on the allowed maximum energy were introduced. As the energy decreased, conformations were regularly saved to use them as starting conformations for accumulating runs. This procedure was done several times to obtain independent configurations with different energies. Note that the fundamental thing here was the initial “defreezing” of systems, and conformations for further simulation were preserved only in the reverse, “freezing”, process. Conformations from systems with repulsive walls have also been used in modeling systems with attractive walls.

Here we would like to note that chains were also elongated along the walls in the low-energy conformations obtained during “freezing” process. There is nothing unexpected in this, since conformations in which the chains are oriented perpendicular to the walls are unfavorable, since they lose a lot of entropy. However, additional runs were carried out in order to verify the fundamental possibility of such an organization. To do this, the packing of chains was set perpendicular to the walls "by hands". The goal was to ensure that the system can evolve from this state to a disordered state with high energy. Since the trial steps are reversible, in this case we can assume that returning to the state with chains extended perpendicular to the walls is fundamentally possible (although very unlikely). During these tests, such evolution turned out to be possible in a reasonable time only after introducing the additional trial move called *System reorientation* (see below). A description of this and other trial steps implemented during the simulation process is given below.

Technical improvements

The main, but not the only, goal of these technical modifications was to speed up the process of accumulation of the function $\ln(g)$. Considering the size of the systems and the potentials used, the energy range that needs to be studied for system without walls is $[-5760; 0]$ for smaller, and $[-11520; 0]$ for larger system size.

SAMC simulations involve calculations of number of parameters that require significant computational time. Thus, in order to speed up calculations at such large energy intervals, it was necessary to modify previously developed procedure [24] as follows.

- At the first stage of work, we started by defining $\ln g_0(E) = 3E$. This estimate is based on results of T. Shakirov [114] for the similar systems and is quite rough, but requires significantly less calculation time compared to $\ln g_0(E) = 0$ (derived from the commonly used $g_0(E) = 1$).
- To speed up the sampling process, a parallel computing process was implemented, using MPI modules. To do this, the entire range of energies was divided into "energy windows", that is, intervals consisting of approximately $\Delta E_w \approx 500$ energies (Fig. 2.3). The windows

are spaced at approximately $\Delta E_w^i \approx 200$ energy increments, so that each window has multiple overlaps (each energy of the entire range applies to 1-3 windows). In areas of windows overlapping, data exchanges are provided, due to which, in principle, sampling of each conformation throughout the entire energy range is possible.

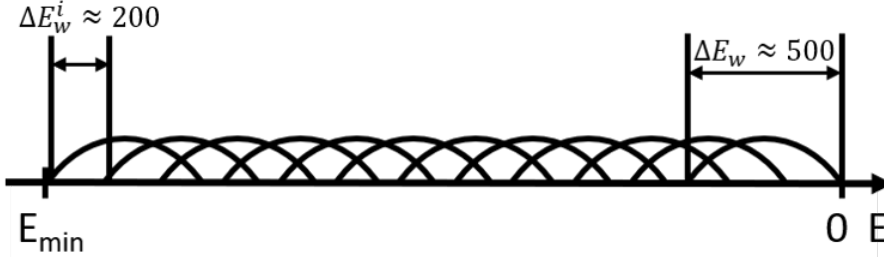


Figure 2.3: Illustration of the division of the energy range into windows

After more than one year of computation, it became evident that despite continual optimization of the code and adjustments in parameters (such as window width), convergence of the density of states function occurs at an unacceptably slow rate. Despite obtaining an estimate of the density of states function $g(E)$ that correctly reflected the anticipated trend, continuing calculations at such a slow rate left little hope of obtaining reliable results in the transition region in a reasonable time. Hence, there arose a necessity to explore additional avenues for enhancing efficiency of the algorithm.

Modification of the accumulation method 1

In the previous procedure, we updated $\ln g(E)$ exactly at the energy that we visited. In other words, we accumulated the function $\ln g(E)$ in bins with a width of $\Delta E = 1$. Now, we divide the entire energy range into $\left\lceil \left\lceil \frac{E_{max} - E_{min}}{\Delta E} \right\rceil \right\rceil + 1$ bins of width $\Delta E = 10$. Inside each bin $j = \left\lceil \left\lceil \frac{E}{\Delta E} \right\rceil \right\rceil$ the $\ln g(E)$ is approximated by a straight line with the slope

$$\tan(\beta_j) = \frac{\ln g_{j+1} - \ln g_j}{\Delta E}.$$

The square brackets in the definition of j mean taking the integer part of the number (truncate), $\ln g_j$ is the estimation of value $\ln g$ in the bin j with $\Delta E = 10$. In further calculations, the angle β_j in each bin j is fixed and does not change (Fig.2.4). Thus, if we visit the energy E_i (note that we consider $E_i < 0$), we define the bin $j = \left\lceil \left\lceil \frac{E_i}{\Delta E} \right\rceil \right\rceil$ and update $\ln g_j$ inside the bin j as

$$\ln g_j \rightarrow \ln g_j + \gamma_i.$$

Knowing the estimations of the function $\ln g_j$ and slope β_j in each bin j , the values of $\ln g(E_i)$ can be calculated for each energy E_i :

$$\ln g(E_i) = \ln g_j - \tan(\beta_j) \cdot (|E_i| - j\Delta E). \quad (2.21)$$

Hence, we can say that there is an effective accumulation of

$$\ln g(E_k) \rightarrow \ln g(E_k) + \gamma_t / \Delta E, \quad \forall k : j \cdot \Delta E < k < (j+1) \cdot \Delta E. \quad (2.22)$$

Thus, this modification allows, by visiting one specific energy E_i , to calculate updated values $\ln g$ for all energies within the bin j with width $\Delta E = 10$ (Eq. (2.22)), thereby speeding up the accumulation process.

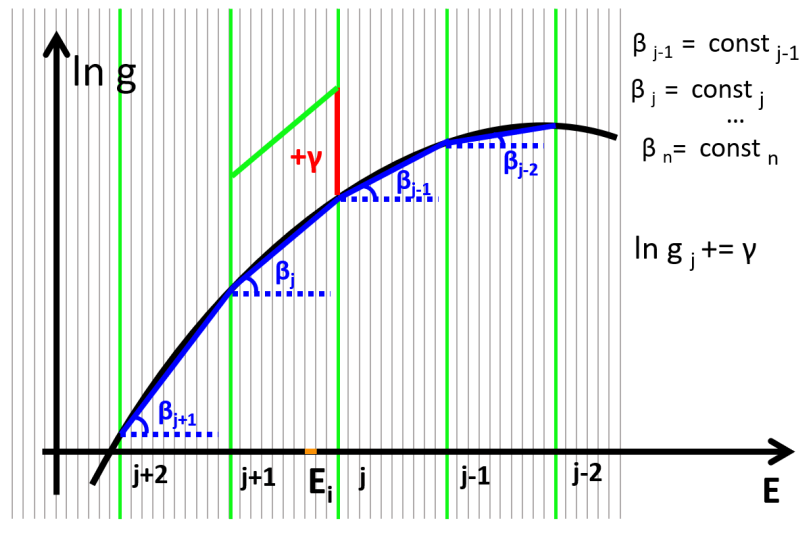


Figure 2.4: Illustration of the accumulation process (modification 1) when visiting the energy $E_i < 0$. The gray vertical lines correspond to the bin of energies with $\Delta E = 1$, while the green ones are $\Delta E = 10$; the vertical red lines are additives to the functions of $\ln g$ in the corresponding bins. The blue solid lines are a linear approximation of $\ln g$ inside the bin $\Delta E = 10$. The green inclined solid line estimates the new value of $\ln g$ inside the bin. The scale of the diagram does not reflect the actual scale.

Modification of the accumulation method 2

At the next stage of the work, the modification proposed above was refined. This involved distributing the additive at the current step, $\gamma = \gamma_t$ into two components γ_x and γ_y ($\gamma = \gamma_x + \gamma_y$), depending on the position of the visited energy E_i relative to the bin limits $\lceil \frac{E}{\Delta E} \rceil \cdot \Delta E$ and $(\lceil \frac{E}{\Delta E} \rceil + 1) \cdot \Delta E$:

$$\begin{aligned} \ln g_j &\rightarrow \ln g_j + \gamma_x, \\ \ln g_{j+1} &\rightarrow \ln g_{j+1} + \gamma_y, \end{aligned} \quad (2.23)$$

where

$$\gamma_x = \gamma \frac{\Delta E (j+1) - |E_i|}{\Delta E},$$

$$\gamma_y = \gamma \frac{|E_i| - \Delta E j}{\Delta E}, \quad (2.24)$$

$$j = \left\lceil \left\lfloor \frac{E_i}{\Delta E} \right\rfloor \right\rceil.$$

Simultaneously, to enhanced accuracy within this modification, it is assumed that the angles in the current and neighboring energy bins will be updated:

$$\begin{aligned} \tan(\beta_{j-1}) &\rightarrow \tan(\beta_{j-1}) - \frac{\gamma_x}{\Delta E}, \\ \tan(\beta_j) &\rightarrow \tan(\beta_j) + \frac{\gamma_x - \gamma_y}{\Delta E}, \\ \tan(\beta_{j+1}) &\rightarrow \tan(\beta_{j+1}) + \frac{\gamma_y}{\Delta E}. \end{aligned} \quad (2.25)$$

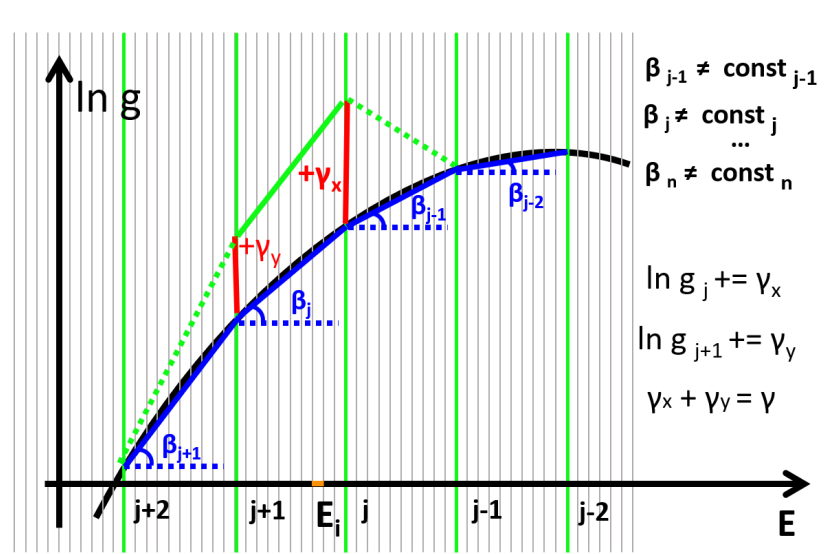


Figure 2.5: Illustration of the accumulation process (modification 2) when visiting the energy $E_i < 0$. The gray vertical lines correspond to the bin of energies with $\Delta E = 1$, while the green ones are $\Delta E = 10$; the vertical red lines are additives to the functions of $\ln g$ in the corresponding bins. The blue solid lines are a linear approximation of $\ln g$ inside the bin $\Delta E = 10$. The green inclined solid line estimates the new value of $\ln g$ inside the bin. The dotted inclined green lines illustrate the angle β changes inside the bin j and in adjacent bins $j - 1, j + 1$. The scale of the diagram does not reflect the actual scale.

Using the values $\ln g_j$ and β_j , the values of $\ln(E_i)$ can be calculated for each energy E_i (Eq.2.21).

Thus, modification 2, like modification 1, when visiting only one energy E_i , the function values $\ln g$ are updated at all energies of the bin j of width ΔE . Modification 2 does this more accurately.

In total, taking into account all the listed modifications, the calculations took about 3

years. The calculations were carried out on the computer cluster of the Institute of Physics of Martin Luther University Halle-Wittenberg. The following partitions were used for calculation:

- intel1 - 49 nodes (2 CPUs, 8 cores each, FDR Infiniband);
- intel2 - 15 nodes (2 CPUs, 8 cores each, FDR Infiniband);
- intel3 - 19 nodes (2 CPUs, 10 cores each, FDR Infiniband);
- intel4 - 24 nodes (2 CPUs, 4 cores each, DDR Infiniband);
- amd1 - 63 nodes (2 CPUs, 8 cores each, QDR Infiniband).

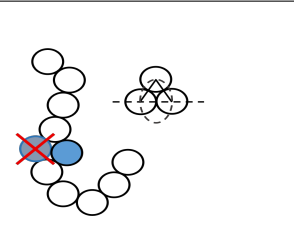
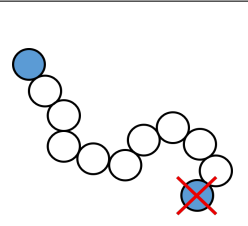
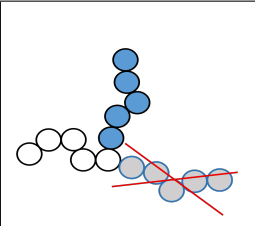
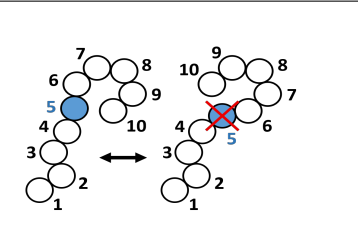
Although the computing speed on the specified partitions is different (the most efficient is intel1, and the least efficient is amd1), all resources were used as they were loaded by other users.

Trial moves

One Monte Carlo step involves trying to make $N_{MC} = (N + 8) \cdot N_c + 2$ trial steps. Trial moves are used to change the conformation, thereby contributing to the sampling in the energy space. This is part of the technical implementation of the method and does not correspond to the physical transformations in the system. The trial moves (Tab. 2.1) that are used in our work are listed below.

1. **Local displacement** or rotation. The bond length is fixed in our model, therefore the local displacement of a randomly selected particle within the chain involves rotation around the axis connecting its neighbors. The end beads of the chain possess greater freedom of movement, accounting for the fixed bond length. It is worth noting that in conformations featuring elongated chains, the displacement occurs by very small values, thereby ensuring a higher acceptance rate at lower energies.
2. **Reptation** or slithering-snake move [145–147]. This move involves the removal of one bead from the random end of a randomly selected chain, followed by the addition of a randomly oriented bead at the opposite end. Acceptance rate for reptation move is higher for high-energy conformations. This is due to the tendency, noted in our observations, for chains to align one after another at low energies in our system. This preference for alignment can lead to limited space for placing the bead at the end of the chain, and therefore the rejection of this trial move.
3. **Pivot**. This is a chain reconstruction process, wherein a non-terminal bead within a randomly selected chain is randomly chosen and is used as a rotation center. Subsequently, one of the two directions towards the chain end is randomly chosen, and the selected portion of the chain rotates around the selected center. The rotation angles are chosen randomly. Therefore, in this step, only one angle between two successive bonds is changed, while the conformation of the chain is modified significantly.

4. **Interior bridging.** The essence of this step is to reconnect closely spaced beads in a chain that are not adjacent along the chain. If the internal beads within a randomly selected chain are sufficiently close to each other in space but are not adjacent along the chain sequence, the beads are rearranged accordingly. Additionally, the beads undergo slight movements to ensure that the lengths of all bonds in the chain remain equal. The corresponding transition Jacobians are used to correct a probability bias.
5. **End bridging** [148, 149]. This is similar to the previous one, but involves the reconnection of an end bead instead of two internal beads of the chain.
6. **Double bridging** [150, 151]. This step resembles *Interior bridging*, but its execution requires the close proximity in space of the internal beads of two distinct chains. In this scenario the chains exchange their segments.
7. **Reorientation.** The *Reorientation* step entails rotating the entire chain relative to a randomly chosen axis passing through the center of the selected chain at a random angle. Therefore, this step, without altering the stiffness energy, can modify the energy of the system solely in the case of a system with an attractive wall. This step remains essential for altering the configuration of the system.
8. **System reorientation.** As mentioned previously, this step was introduced additionally to enable the system to reach and destroy the state wherein the chains are stretched perpendicular to the walls. The implementation of this step resembles the *Reorientation* step for a single chain. However, the distinction lies in the fact that the rotation angle and the axis of rotation, both randomly selected, are applied to the center of each chain in the system.

| Local displacement | Reptation | Pivot | End bridging |
|---|---|---|--|
|  |  |  |  |

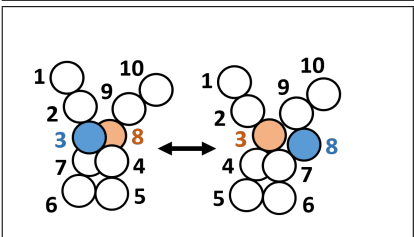
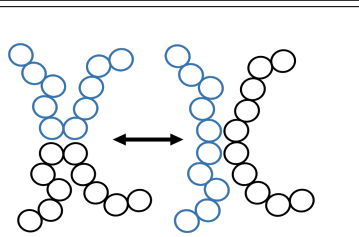
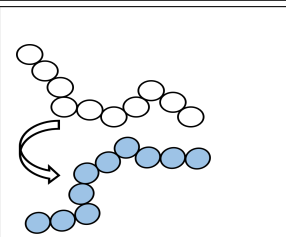
| Interior bridging | Double bridging | Reorientation |
|---|---|---|
|  |  |  |

Table 2.1: Illustrations for the trial moves.

The overall acceptance rate is $\sim 15\%$ for high energies and $\sim 30\%$ for low energies. Nevertheless, it is important to note that despite the increase in the number of trial steps taken, this does not guarantee an effective system rebuilding. For example, for low-energy conformations, local displacement are more likely to be accepted than for high-energy conformations (Tab. 2.2). This is explained by the fact that at low energies the conformations are elongated, and local rotation practically does not change the conformation. Significant efforts have been devoted to the search and development of additional effective trial steps. However, the aforementioned steps currently constitute the optimal set for addressing the task within the framework of the model employed.

| Trial move | The percentage of number of attempts to execute the trial step within one MC step | Energy trend | The ratio of the number accepted trial moves the total number of attempts of all trial moves |
|----------------------|---|--------------|--|
| Local displacement | $\frac{NN_c}{N_{MC}} \cdot 100\% \approx 56\%$ | low energy | 55% |
| | | high energy | 25% |
| Reptation | $\frac{2N_c}{N_{MC}} \cdot 100\% \approx 11\%$ | low energy | 0.003% |
| | | high energy | 0.01% |
| Pivot | $\frac{N_c}{N_{MC}} \cdot 100\% \approx 5\%$ | low energy | 0.07% |
| | | high energy | 0.03% |
| Interior bridging | $\frac{N_c}{N_{MC}} \cdot 100\% \approx 6\%$ | low energy | tends to 0% |
| | | high energy | $\sim 0.0005\%$ |
| End bridging | $\frac{2N_c}{N_{MC}} \cdot 100\% \approx 11\%$ | low energy | from 0.005% to 0.1% |
| | | high energy | 0.5% |
| Double bridging | $\frac{N_c}{N_{MC}} \cdot 100\% \approx 6\%$ | low energy | tends to 0% |
| | | high energy | $\sim 0.0005\%$ |
| Reorientation | $\frac{N_c}{N_{MC}} \cdot 100\% \approx 6\%$ | low energy | 8.5% |
| | | high energy | 9.5% |
| System reorientation | $\frac{2}{N_{MC}} \cdot 100\% \approx 0.015\%$ | low energy | 0.05% |
| | | high energy | |

Table 2.2: The proportions of attempted trial steps and trial steps accepted, expressed as percentages.

Chapter 3

Structural analysis: methods and results discussion

In general, a crystal means a solid body having a three-dimensional long-range translational order. The arrangement of atoms in a crystal is characterized by its unit cell containing one or more atoms in a certain spatial arrangement. The crystal structure of a substance is reproduced by periodic translation of the unit cell. In the study, we do not pretend to determine the exact class of a crystal in a model of polymer melt (THS), since this would represent a separate in-depth research in the field of crystallography. In addition, in polymer systems, we can only talk about local translational ordering and the formation of a set of crystallites. However, we claim to be able to detect the coexistence of various crystal symmetries. Despite the fact that a significant number of methods for analyzing crystal structures have been developed, this task is still the cornerstone of computer simulation research. In this chapter, we look at the most common methods of analysis applied to frequently considered systems such as simple cubic (*sc*), body-centered cubic (*bcc*), faced-centered cubic (*fcc*), hexagonal close-packed (*hcp*), as well as to our polymer system (THS) and propose new method of analysis that we consider the most efficient in this study.

The chapter has the following structure.

- 3.1 Noise evaluation in the system under study. The presence of noise is the fundamental reason why the application of many known methods of crystal structure analysis becomes ineffective in our task. In order to compare the effectiveness of various methods of structural analysis, it is necessary to study dependencies of studied parameters on the noise magnitude in systems. Knowing the noise magnitude, we can evaluate the suitability of a particular method.
- 3.2 Test structures preparation. We describe the procedure for preparing test structures with the imposition of a found in the section 3.1 noise. These structures are constructed in such a way that their volume fraction correlates with the polymer volume fraction in THS systems, which allows for direct comparison. The presence of such structures is necessary

for a reliable and objective study of the effectiveness of various methods depending on noise magnitude.

- 3.3 Radial distribution function. Calculation of the radial distribution function (RDF) is necessary to estimate the characteristic distances, used in various methods as preset parameters.
- 3.4 Local bond order parameters. We explore the original local bond order (LBO) parameters, also known as *Steinhardt parameters*, as well as several of the most common variations of this method.
- 3.5 Noise reduction procedure. Our results discussed in sections 3.1 - 3.4 have shown that the existing methods of structural analysis are not quite suitable for noisy systems. Therefore, we have proposed a new modification for calculation of Steinhardt parameters based on a special procedure for averaging particles coordinates (NRLBO parameters).
- 3.6 Searching for translation vectors. As an additional step to obtain more information about structures which appear in our systems, we propose a procedure to reproduce the observed crystal structure using two base particles and three translation vectors.
- 3.7 Other methods. We also discuss the application of other methods, namely structure factor calculation [152], common neighbor analysis (CNA) [105–108], Voronoi cell analysis [109, 110] and local chain segments alignment analysis [48, 40].

3.1 Noise evaluation in the system under study

Before starting to analyze the crystal structure, it is necessary to pay attention to the fact that one cannot expect to obtain a perfect crystal lattice without any noise in particles positions even at $T = 0$, because the ground state in our model, i.e. the macrostate with the smallest possible energy E_{min} , can be realized by many microstates within the framework of the model used. In the studied systems (THS), noise will be observed (even at $T = 0$) due to the width and shape of the stiffness potential. Since the condition for adding the value -1 (in ϵ units) is an angle ranging from 0° to 26° (see Eq.(2.2)), then the lowest energy of $E = -5760$ in small systems (bulk and with repulsive walls) will be realized by any microstate where all angles between chain bonds equal are between 0° and 26° . Thus, the width and the shape of the stiffness potential is the cause of noise in the resulting crystal structures. This section describes the procedure for evaluating noise in our system.

Let us choose a bulk system ($L_x = L_y = 20$, $L_z = 19$) with a sufficiently low energy, so we can consider the structure as a crystal with particles fluctuations in the lattice nodes. For example, we consider a system with energy $E = -5727$ (Fig.3.1). For other systems with sufficiently low energies and systems, estimates give a similar result.

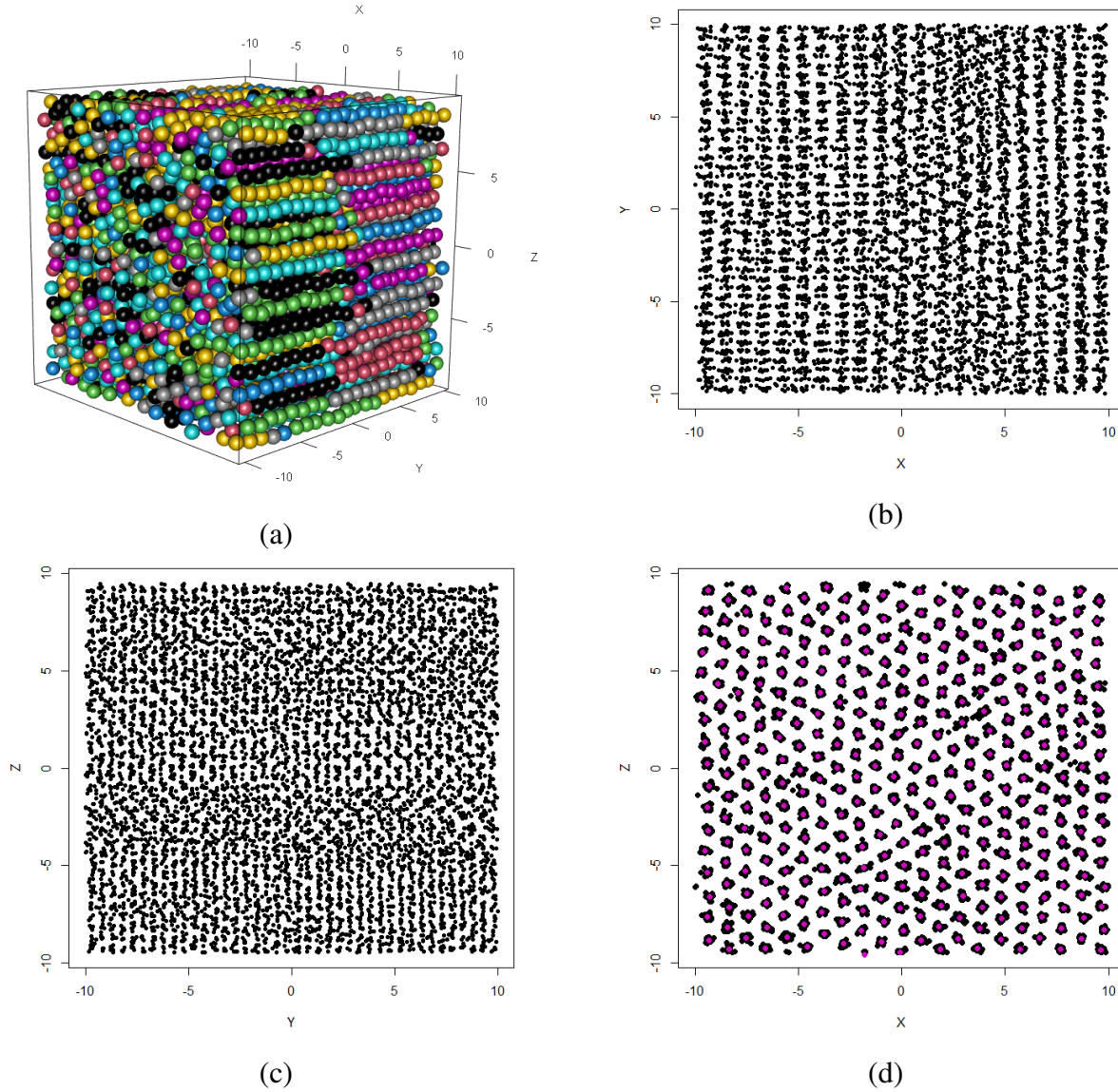


Figure 3.1: A snapshot of the system at energy $E=-5727$: (a) 3d view. The colors correspond to different chains; (b), (c), (d) the dots denote the centers of mass of each sphere in the projection onto the plane XY , YZ , XZ respectively. Purple points denote the centers of groups (d).

While in the XY and YZ planes one can notice a variety of patterned structures of particles (beads) on local scales of several bead diameters ($d = 1$), in the XZ plane one can clearly observe formation of groups. The arrangement of projections into groups in this plane is explained by the elongation of the chains along the y axis (Fig.3.1 (a)). This is a consequence of the finite size effect of the system. Thus, the centers of these groups are analogous to atoms of the crystal lattice, and the size of groups characterizes the noise magnitude in a crystal. At this stage, clustering was carried out using the k-means method [153] (with an input number of 360 groups) and a method similar to k-means, but the initial approximate size of the groups ($R = 0.8$) was specified as the input parameter, not the number of groups. Both methods give the same result for groups positions. As can be seen from the inserts in Fig.3.2, the distribution of deviations of points from the centers of groups resembles the Gaussian distribution. One

can use quantile-quantile plot (QQ plot) [154] to check the normality of distribution visually. This is a graphical method that is a probability plot and allows you to compare two probability distributions by plotting their quantiles against each other. Quantiles are cut points that divide the range of a probability distribution into continuous intervals of equal probabilities or similarly divide observations in a sample. The point (x,y) on the graph corresponds to one of the quantiles of the second distribution (y -coordinate) plotted on the same quantile of the first distribution (x -coordinate). We use the theoretical normal distribution as the first distribution (x -coordinate). The second distribution (y -coordinate) is the deviation of the projections of the centers of mass of particles from the center of the groups on the XZ plane. In a QQ plot, each observation is displayed as a single point. If the data correspond to the normal distribution, then the dots should form a straight line (Fig.3.2). Thus, in our case one can talk about the normality of the distribution. In addition to the ability to visually assess whether the distribution belongs to the normal distribution, this method allows estimating the median value of the distribution and the standard deviation. The value on the y axis at $x = 0$ corresponds to the median. We see that it is equal to zero; this correctly reflects our construction: we translated the center of each group to the origin before counting the deviation of the position of the particle of each group from its center. The tangent of the slope of the approximating lines corresponds to the standard deviation of the distribution. From the resulting plots we can extract $\sigma_o = \sqrt{\sigma_o^2} \approx 0.112$. This value characterizes the noise in our system.

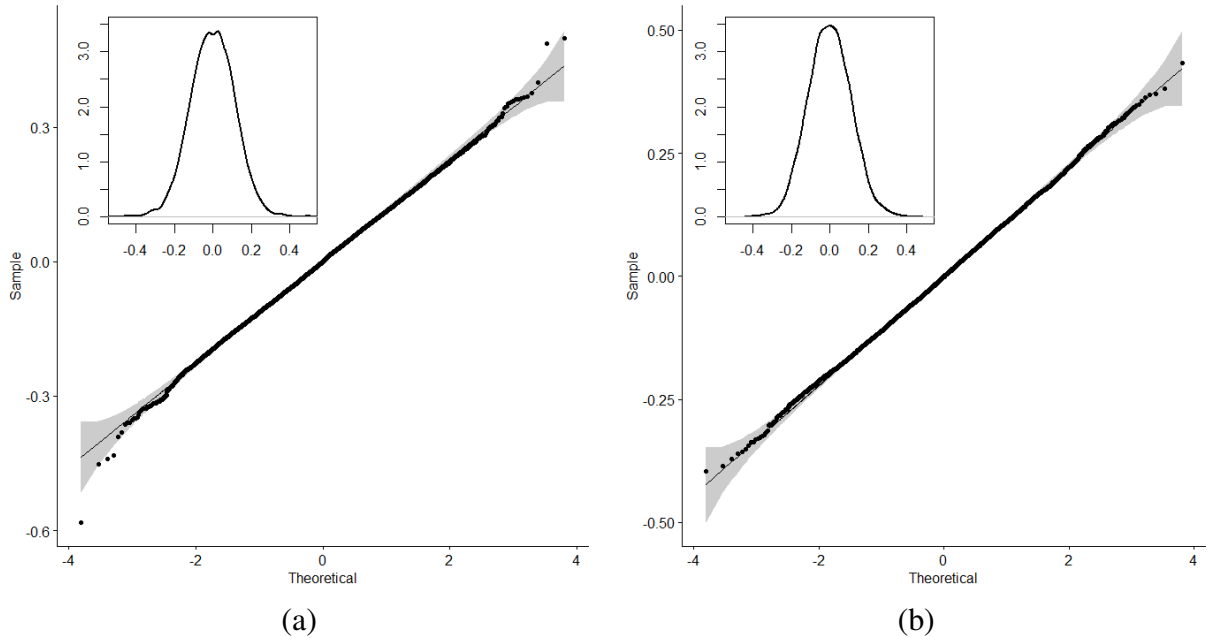


Figure 3.2: Main plots: quantile-quantile plot for deviation from the centers of the groups along x direction (a) and z direction (b); inserts: deviation from the centers of the groups along x direction (a) and z direction (b).

Another way to estimate the parameter σ_o , assuming that the distribution of deviations of particles from the centers of groups $D(x)$ is normal, is to construct a $\ln D(x)$:

$$D(x) \sim \exp \left\{ -\frac{(x-x_0)^2}{2\sigma_o^2} \right\}$$

$$\ln D(x) = \text{const}_1 - \frac{(x-x_0)^2}{2\sigma_o^2}$$

Since we assume that the centers of all groups have already been translated to the origin, then $x_0 = 0$. When taking the derivative of the distribution with respect to the coordinate, we obtain:

$$\frac{\partial \ln D(x)}{\partial x} = -\frac{x}{\sigma_o^2}$$

As can be calculated from the coefficients obtained using linear fit (Fig.3.3) σ_o is for both axes x and z equal to:

$$\sigma_o \approx 0.112, \quad (\sigma_o^2 \approx 0.0125). \quad (3.1)$$

Taking into consideration that this is an estimate for one group along one direction, for a pair of noisy groups in three-dimensional space we get $2 \cdot 3\sigma_o^2 = 6\sigma_o^2 \approx 0.075$. We will use this estimation in the following section of the work.

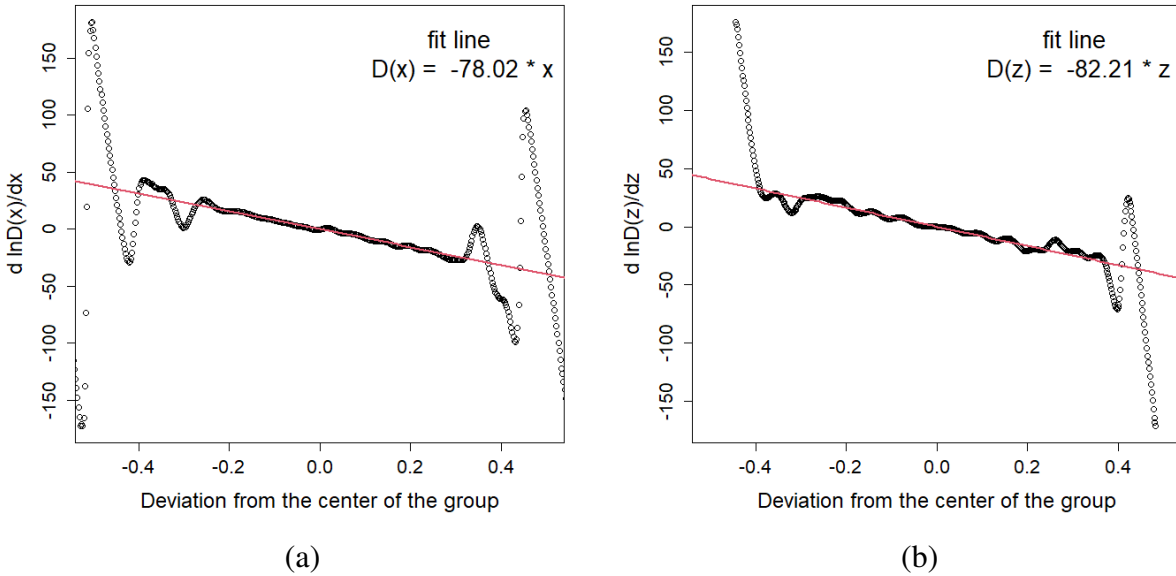


Figure 3.3: Noise estimation along x direction (a) and z direction (b).

3.2 Test structures preparation

In order to make sure that methods used are reliable, we perform tests on well-known hard spheres (HS) crystalline structures: simple cubic (*sc*), body-centered cubic (*bcc*), face-centered cubic (*fcc*), hexagonal close-packed (*hcp*). For these structures primitive lattice vectors are known, by which it is possible to reconstruct the crystal lattice. In order that the results

obtained for the test lattices could be compared with the structures of polymer system (THS) studied in this work, two conditions were taken into account: (a) the minimum distance between the lattice atoms of the perfect test structures should be equal to the length of the rigid bond in the polymer model under study, i.e. $d = 1$; (b) the atomic packing factor (APF) of the test structures should coincide with the volume fraction of the polymer in the system under study ($APF = \phi = 0.496$), since this parameter is the same for all the systems under study and does not change during simulating process.

Since the dependence of various parameters on noise σ is investigated and special attention is paid to the value estimated in the section 3.1 ($\sigma_o \approx 0.11$), here we also describe the procedure for introducing noise σ into the test structures taking into account the excluded volume.

Example

As an example, let us consider the construction of bcc structure. The construction of other test structures is carried out in full analogy.

Primitive lattice vectors for bcc :

$$\begin{aligned}\mathbf{a} &= -\frac{a}{2}\mathbf{e}_1 + \frac{a}{2}\mathbf{e}_2 + \frac{a}{2}\mathbf{e}_3, \\ \mathbf{b} &= \frac{a}{2}\mathbf{e}_1 - \frac{a}{2}\mathbf{e}_2 + \frac{a}{2}\mathbf{e}_3, \\ \mathbf{c} &= \frac{a}{2}\mathbf{e}_1 + \frac{a}{2}\mathbf{e}_2 - \frac{a}{2}\mathbf{e}_3,\end{aligned}\tag{3.2}$$

where a is the lattice parameter, or the side of the cube, related to the distance d between the nearest lattice atoms by the relation

$$a = \frac{2}{\sqrt{3}}d.\tag{3.3}$$

Usually, to calculate the APF one assumes that $d = 2r$, where r is the radius of a particle. However, to adjust the APF , we fix $d = 1$, according to assumption (a) and change the particle radius r (so, $r \neq d/2$). APF_{bcc} is expressed in terms of the volume of a single particle V_1 , the number of particles in a primitive cell N_{bcc} and the volume of a unit cell V_0 :

$$APF_{bcc} = \frac{V_1 \cdot N_{bcc}}{V_0} = \frac{\frac{4}{3}\pi r^3 \cdot 2}{a^3}.\tag{3.4}$$

After using the condition Eq.(3.3), and the requirements (a) and (b) above that $APF_{bcc} = \phi = 0.496$ from Eq. (2.3), one obtains:

$$r = \left(\frac{\phi}{\pi\sqrt{3}}\right)^{\frac{1}{3}} \approx 0.45.\tag{3.5}$$

This value is particularly important in the procedure for introducing a noise to the HS system.

Procedure for noise introduction

We assume that the noise along any direction in our system has a Gaussian distribution. Therefore, we choose orthogonal vectors $\mathbf{e}_1, \mathbf{e}_2, \mathbf{e}_3$, and we introduce a noise along each of these directions.

Step 1. In the constructed perfect lattice, each particle acquires a normally distributed Gaussian displacement

$$\Delta x = \mathcal{N}(0, \sigma^2) \quad (3.6)$$

Here we do not control overlaps of particles. In the next steps we need to eliminate overlaps of particles.

Step 2. We look for a pair of points i_0, j_0 that are at the minimum distance d_{min} in the resulting noisy system.

Step 3. Choose the particle i^0 With a probability of 1% randomly from all particles of the system. With a probability of 99%, the particle i^0 is randomly selected from i_0 and j_0 . For the particle i^0 , the displacement introduced earlier is replaced by:

$$\Delta x_1 \longrightarrow \alpha \Delta x + \mathcal{N}(0, \sigma_1^2) \quad (3.7)$$

where α is the parameter chosen "by hand" ($\alpha \in [0; 1]$). According to the properties of the normal distribution, the distribution Δx_1 will be distributed normally with a width of σ if one sets:

$$\sigma_1^2 = (1 - \alpha^2) \sigma^2. \quad (3.8)$$

An attempt to change the displacement (Eq. (3.7)) is accepted if the pair distances from any particles of the system to the particle i^0 taking into account this step are not less than d_{min} , otherwise i^0 retains its previous displacement Δx .

Step 4. If the new displacement Δx_1 is accepted, a new d_{min} and new particles i_0, j_0 are searched.

Step 5. Repeat Step 2 - Step 5 until $d_{min} < 2r$, where r was evaluated in Eq. (3.5).

Remark 1. After completing the procedure, the resulting structures were checked for the normality of the distribution of the position of the particles relative to the noiseless positions, similar to how it was done in the section 3.1. Despite the fact that at the $\sigma > 0.07$ the values of the really observed and required noise (introduced σ) no longer coincide, it is still possible to achieve observed noise with a value comparable to the estimate in the systems under study ($\sigma_o \approx 0.11$). Because of this difference, it is important to underline that later in the manuscript, using the notation σ , we will mean the actual *observed* noise in the systems.

Remark 2. Although we actually studied systems with two different polymer volume fractions ($\phi = 0.471$ and $\phi = 0.496$), all test structures will be shown only for polymer volume fraction

$\phi = 0.496$. The results of the methods described in this chapter for test structures with a volume fraction of $\phi = 0.471$ do not differ significantly.

During the study of analysis methods, tests were also carried out for accounting systems without excluded volume, which corresponds to the limit $\phi = 0.0$. In this case, the noise procedure stopped at the first step. We do not discuss of this limit, since the HS model is a more complex case and closer to the model under study (THS). However, here we note that the noise reduction procedure proposed in the subsection 3.5 works better in this case. Further in the manuscript, as test structures, we use the HS model for crystals *sc*, *bcc*, *fcc*, *hcp*, taking into account the noise described in this section.

3.3 Radial distribution function

Let us start the study of structures by calculating the radial distribution function (RDF). Let $G(r)$ be the probability density of the presence of a particle at a distance r from a given particle. Then the probability to find a particle at a distance r from this particle is defined as $G(r)dr$. Then the radial distribution function $g_2(r)$ is calculated as:

$$g_2(r) = \frac{G(r)dr}{4\pi r^2 dr} V, \quad (3.9)$$

where V is the volume of simulation box.

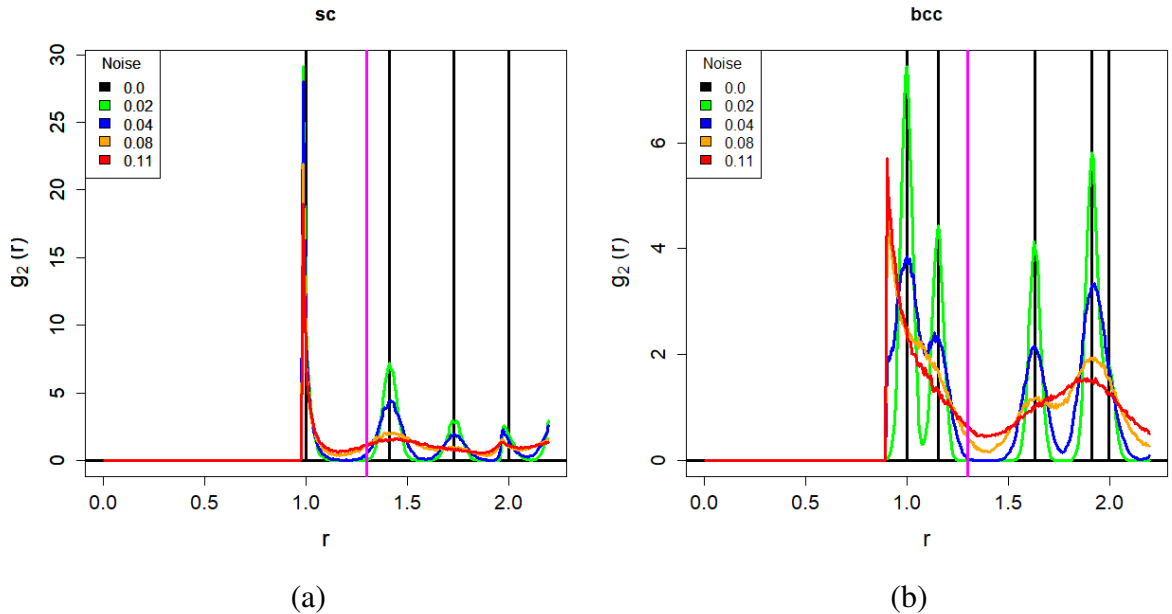


Figure 3.4: Radial distribution function for different noises for *sc* (a), *bcc* (b).

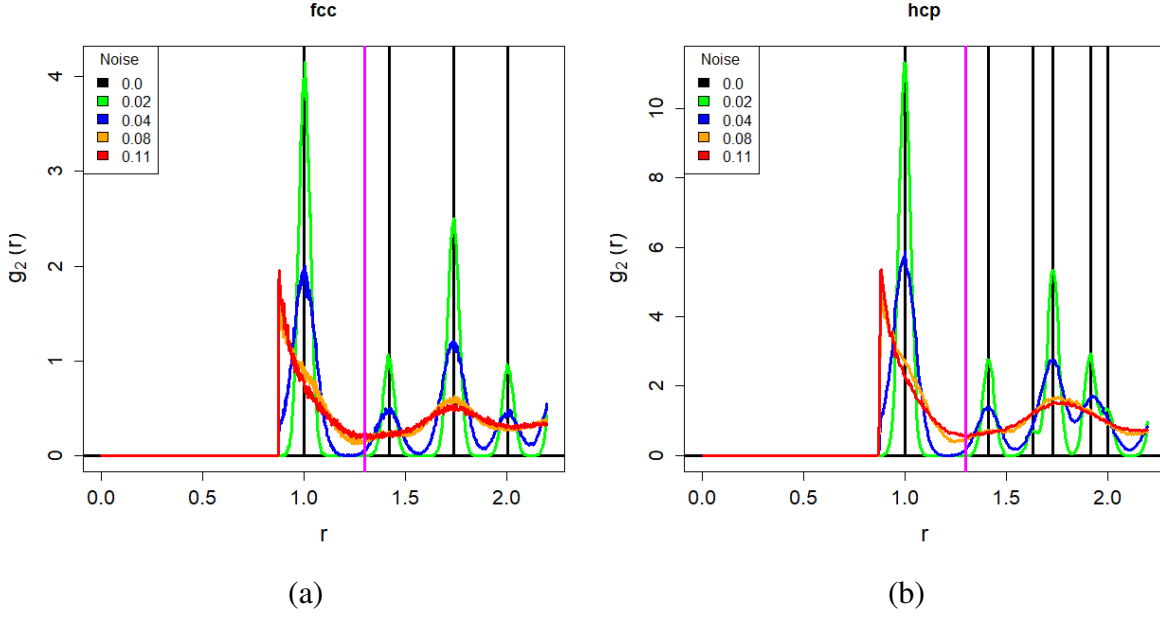


Figure 3.5: Radial distribution function for different noises for *fcc* (a), *hcp* (b).

As it was established in the section 3.1, the formation of a perfect crystal cannot be expected in our model polymer system (THS). Noise can contribute to the displacement and blurring of the radial distribution function. To study the behavior of the $g_2(r)$ depending on noise, the *sc*, *bcc*, *fcc*, *hcp* structures were selected as test structures. Gaussian noise σ is introduced into the initially perfect crystal lattice in each of the three directions, as it was described in the section 3.2. The red curves (Fig.3.4, Fig.3.5) correspond to noise magnitude estimated for THS in the section 3.1, since noise $\sigma \approx 0.11$ is introduced in this case. It can be seen from the data obtained that the number of peaks on the RDF decreases and the determination of the symmetry of the structure becomes impossible. The position of the first maxima shifts to the left on all structures with increasing noise. For small σ values, the maxima of all structures are located at the point $r = 1.0$, which corresponds to the method of constructing lattices described in section 3.2. This value corresponds to the minimum distance between the lattice nodes. With a sufficiently large σ , the peak corresponds to the minimum possible distance that the particles can approach, that is, the diameter of hard spheres.

In Fig.3.6 one can see the RDF $g_2(r)$ for the bulk system ($L_x = L_y = 20$, $L_z = 19$) at energies $E = -2040$ and $E = -5727$, which corresponds to a melt and an ordered (crystalline) structure respectively. Sharp peaks at $r = 1$, $r = 2$ and $r = 3$ are observed. These maxima correspond to adjacent beads along a chain in our THS model.

The calculation of the RDF is a necessary step for calculating the Steinhardt parameters. In general, Steinhardt and co-authors [102] recommend using particles that fall into a sphere of the cutoff radius $R_c = 1.2r_0$ as the nearest neighbors, where r_0 is the position of the first peak of the $g_2(r)$. Such a choice should ensure that all particles in the first coordination sphere are taken into account. However, since the noise estimation in our system is $6\sigma^2 = 0.075$, it was

decided to use the $R_c = 1.3r_0$. Since $r_0 = 1$ coincides with the diameter of the hard spheres in THS model below we will write $R_c = 1.3$.

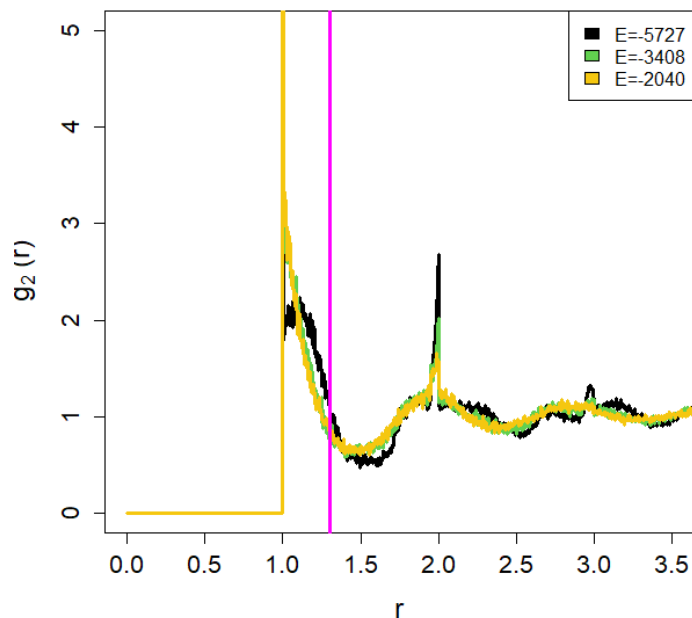


Figure 3.6: Radial distribution function for the bulk system ($L_x = L_y = 20, L_z = 19$). The magenta line corresponds to the chosen cutoff radius $R_c = 1.3$ when further calculating the order parameters.

Our experience has shown that this value is optimal for calculating parameters. If we consider the distributions for THS system (Fig.3.6), one can see that the selected value of the R_c is to the left of minima. As this value is close to the minima of both THS model (Fig.3.6) and the test noisy crystalline structures (Fig.3.4, Fig.3.5), this choice is the most optimal, since it is most likely to capture all particles from the first coordination sphere ($R_c = 1.3$ magenta in Fig.3.4, Fig.3.5).

3.4 Local bond order parameters

3.4.1 P. J. Steinhardt, R. Nelson and M. Ronchetti parameters

One of the most discussed problems of simulation of the crystallization process is how to attribute a particle to a liquid or crystal and also to determine the type of crystal symmetry. Recently, a widely used method of distinguishing the type of crystal symmetry of particles is the calculation of the local bond order (LBO) parameters, also known as Steinhardt parameters [102]. To calculate these parameters, it is not necessary to have a reference structure for comparison with the studied one, as is required in, for example, common neighbor analysis [105].

Another convenience of using this method is the absence of reference to the coordinate system, since the calculation of these parameters is based on spherical harmonics.

Local bond order (LBO) parameter of a particle i is defined as:

$$q_l(i) = \sqrt{\frac{4\pi}{2l+1} \sum_{m=-l}^l |q_{lm}(i)|^2}, \quad (3.10)$$

where l is positive integer, q_{lm} - complex vector which is defined as

$$q_{lm}(i) = \frac{1}{N_b(i)} \sum_{j=1}^{N_b(i)} Y_{lm}(\mathbf{r}_{ij}). \quad (3.11)$$

Here, $N_b(i)$ is the number of nearest neighbors of the particle i . There is no strict rule for determining the particles that are considered to be the nearest neighbors. Most studies use the concept of the cutoff radius R_c (however, different studies use different values), and some use the Voronoi cell. We prefer to use the concept of the cutoff radius with $R_c = 1.3$, as discussed in section 3.3. The functions $Y_{lm}(\mathbf{r}_{ij})$ are the spherical harmonics, \mathbf{r}_{ij} is the vector connecting the particles i and j ; m is an integer that runs from $m = -l$ to $m = l$. Along with q_l , the w_l parameters are also often used, which can be computed according to formulas:

$$w_l(i) = \frac{\sum_{m_1+m_2+m_3=0} \begin{pmatrix} l & l & l \\ m_1 & m_2 & m_3 \end{pmatrix} q_{lm_1}(i) q_{lm_2}(i) q_{lm_3}(i)}{\left(\sum_{m=-l}^l |q_{lm}(i)|^2 \right)^{3/2}}, \quad (3.12)$$

where the summation is carried out by the integers m_1, m_2, m_3 from $-l$ to l , which satisfy the condition $m_1 + m_2 + m_3 = 0$. The expression in parentheses is the Wigner 3-j symbol. Since no significant conclusions can be drawn from the calculation of the parameters w_i , the results for these parameters are presented in the Appendix (Fig.A1). To analyze the structure, the parameters q_4, q_6, q_8 are most often used, however a more complete table of values for LBO parameters of perfect crystal lattices (without noise) can be found in the Appendix (Tab.A1). In this section, we present the results for the parameters of test structures with noise, and also apply this method to analyze the structures obtained during our simulation of polymer system.

The study of Steinhardt parameters for test structures with the value $\sigma = 0.11$ showed that the structures *hcp*, *fcc*, *bcc* become absolutely indistinguishable (Fig.3.7). This fact does not allow us to apply parameters for our system.

The study of the dependence of the average parameters on σ showed that the mean values deviate strongly from the values for perfect crystal lattices (horizontal lines in Fig.3.8, Fig.3.9) with increasing noise. Starting from $\sigma \approx 0.08$, the average number of nearest neighbors also becomes indistinguishable for *bcc* and *hcp*, *fcc* and for none of these values corresponds

to the true number of neighbors.

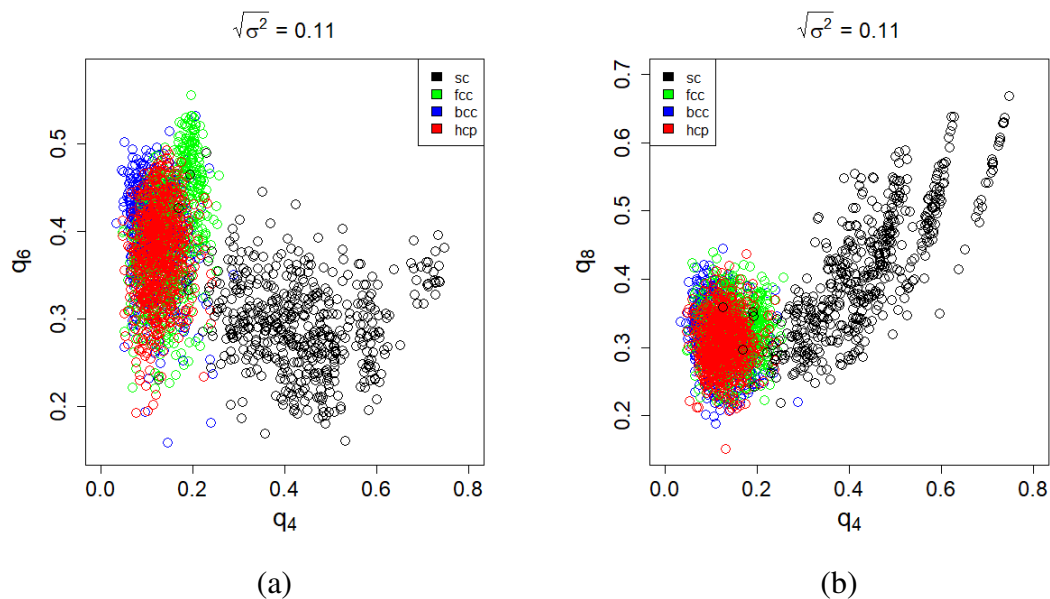


Figure 3.7: Maps of LBO parameters $q_4 - q_6$, $q_4 - q_8$ for noisy test structures (a), (b) respectively.

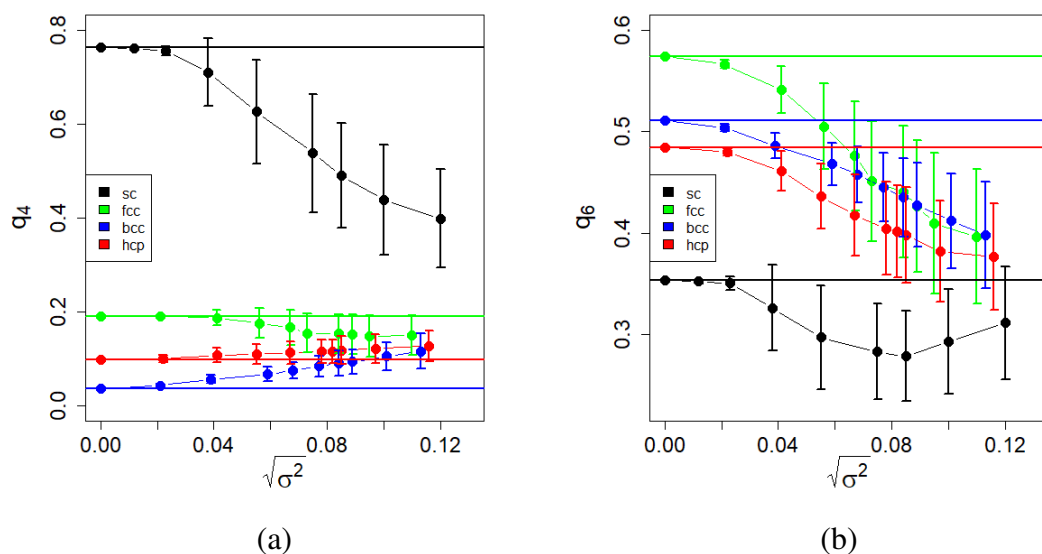


Figure 3.8: Mean values of LBO parameters q_4 (a), q_6 (b) for *bcc* (blue), *hcp* (red), *fcc* (green), *sc* (black) test structures.

Thus, for the noisy HS model, the application of classical Steinhardt bond order parameters turns out to be meaningless if one needs to distinguish between different crystalline symmetries. In all non-perfect test systems, where there is a deviation of the positions of particles (for example, due to thermal fluctuations) from perfect crystal lattice sites, difficulties arise with determining the crystal structure in simulation. Nevertheless, the potential of the

Steinhardt approach is great. Spherical invariants are reasonable functions for describing the symmetry of particle clusters. A number of works have been devoted to modifications of the LBO parameters to improve the accuracy of determining the type of structures in the presence of thermal fluctuations. In next sections, we look at several well-known modifications of this method.

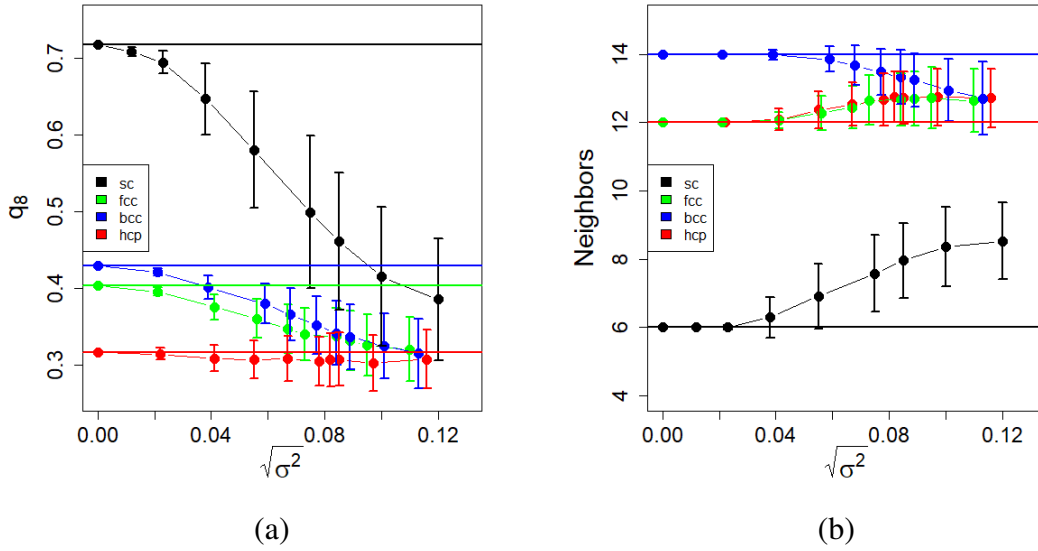


Figure 3.9: Mean values of LBO parameters q_8 (a), number of nearest neighbors (b) for *bcc* (blue), *hcp* (red), *fcc* (green), *sc* (black) test structures.

3.4.2 W. Lechner and C. Dellago parameters

In 2008, W. Lechner and C. Dellago [104] proposed a procedure for averaging Steinhardt parameters. The authors tested their results on two different systems of soft spheres. In this study, they propose to average local bond order (ALBO) parameters as follows:

$$\bar{q}_l(i) = \sqrt{\frac{4\pi}{2l+1} \sum_{m=-l}^l |\bar{q}_{lm}(i)|^2}, \quad (3.13)$$

where

$$\bar{q}_{lm}(i) = \frac{1}{\tilde{N}_b(i)} \sum_{k=1}^{\tilde{N}_b(i)} q_{lm}(k), \quad (3.14)$$

where $q_{lm}(k)$ is calculated for the neighbor k according to Eq.(3.11), $\tilde{N}_b(i)$ is the number of neighbors of the particle i including the particle i itself ($\tilde{N}_b(i) = N_b(i) + 1$).

To determine the ALBO parameters for particle i , one takes the average of q_{lm} over both the particle i itself and its nearby environment $N_b(i)$. While $q_l(i)$ reveals the structural intricacies of the first shell around particle i , its averaged counterpart $\bar{q}_l(i)$ accounts for the

influence of the second shell. The effective considering of the second particle shell is critical in this context.

In the Appendix one can also find the results for the ALBO parameters \bar{w}_l (Fig.A2) calculated using \bar{q}_{lm} :

$$\bar{w}_l(i) = \frac{\sum_{m_1+m_2+m_3=0} \begin{pmatrix} l & l & l \\ m_1 & m_2 & m_3 \end{pmatrix} \bar{q}_{lm_1}(i) \bar{q}_{lm_2}(i) \bar{q}_{lm_3}(i)}{\left(\sum_{m=-l}^l |\bar{q}_{lm}(i)|^2 \right)^{3/2}}, \quad (3.15)$$

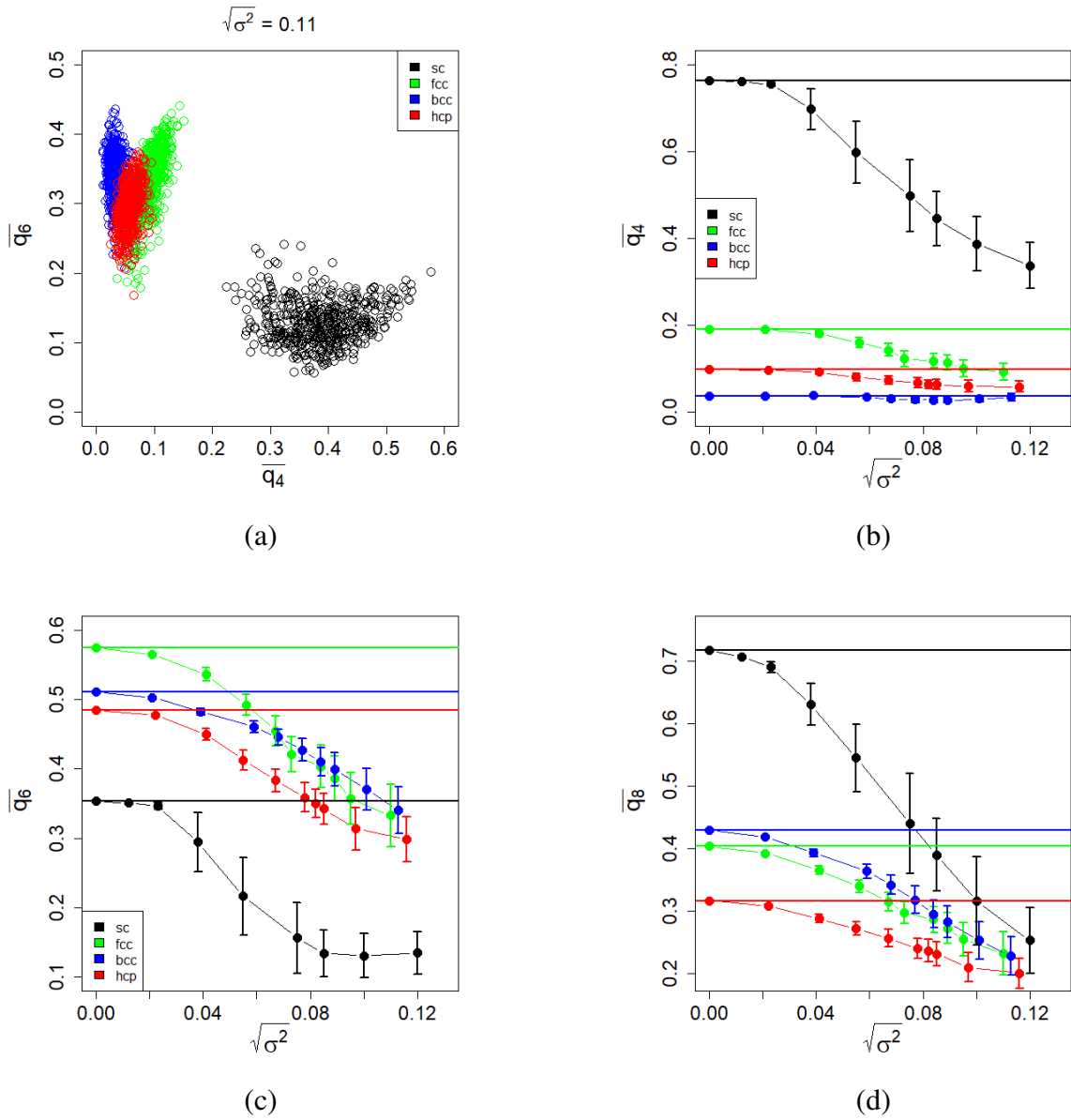


Figure 3.10: ALBO parameters $\bar{q}_4 - \bar{q}_6$ (a); mean values of ALBO parameters \bar{q}_4 (b), \bar{q}_6 (c), \bar{q}_8 (d) for *bcc* (blue), *hcp* (red), *fcc* (green), *sc* (black) test structures.

Authors [104] conducted their tests on 2 types of soft spheres: with the Lennard-Jones potential and the Gaussian core model. In contrast, we have calculated these parameters for our test structures consisting of hard spheres.

From the results obtained (Fig.3.10 and Fig.A3, Fig.A2 in the Appendix) it can be seen that the average values still vary greatly with the growth of σ , however, averaging definitely reduces the spread in values. In Fig.3.10 (b) it can be seen that the average values of the parameter q_4 are able to distinguish *bcc*, *fcc*, *hcp*, although it is still unreliable. The average value for the *bcc* structure has stabilized and slightly deviates from the undisturbed state, which was not observed with LBO parameters Fig.3.8 (a). The parameters q_6 , q_8 still do not allow us to distinguish structures with noise values comparable to those observed in the system under study ($\sigma \approx 0.11$).

3.4.3 H. Eslami, P. Sedaghat and F. Müller-Plathe parameters

A more advanced method was proposed by H. Eslami et al. [103]. In this paper, using the example of the Lennard-Jones system, a comparison was made with the parameters of W. Lechner and C. Dellago [104]. These order parameters examine the ratio of the orientational orders of the second-shell to the first-shell neighbors of a central particle, so the parameters change from 0 (disordered structure) to 1 (in all crystal symmetries). Given this essence of these parameters, we will use the term *relative local bond order* (RLBO) parameters to refer to these parameters. The authors note that despite the fact that the parameters in crystal structures are close to 1, thermal fluctuations reduce the parameters. Moreover, the deviation of RLBO from 1 is stronger in *bcc* than, for example, in *fcc*, due to the large amount of free space and lower density. At the same time, we do not know of any studies devoted to the study of the dependence of parameter changes on temperature fluctuations.

To calculate RLBO parameters one should first compute:

$$\tilde{q}_l(i) = \mathbf{q}_l(i) \cdot \mathbf{q}_l(j) = \frac{1}{N_b(i)} \sum_{j \in N_b(i)} \sum_{m=-l}^l \hat{q}_{lm}(i) \hat{q}_{lm}^*(j), \quad (3.16)$$

where

$$\hat{q}_{lm}(i) = \frac{q_{lm}(i)}{\left(\sum_{m=-l}^l |q_{lm}(i)|^2 \right)^{1/2}}. \quad (3.17)$$

After the averaging $\tilde{q}_l(i)$ over the first coordination shell of neighbors of particle i one computes the RLBO parameters as:

$$\bar{\tilde{q}}_l(i) = \frac{1}{\tilde{N}_b(i)} \sum_{j \in \tilde{N}_b(i)} \tilde{q}_l(j). \quad (3.18)$$

Despite the fact that these parameters are not intended to distinguish perfect (noiseless)

crystal structures of different symmetry, since they all equal to 1, it is interesting to investigate the dependence of these parameters on noise for systems of hard spheres. There is a possibility that using a combination of parameters q_4 , q_6 , q_8 will allow distinguishing different types of structures by the degree of deviation of these parameters from 1.

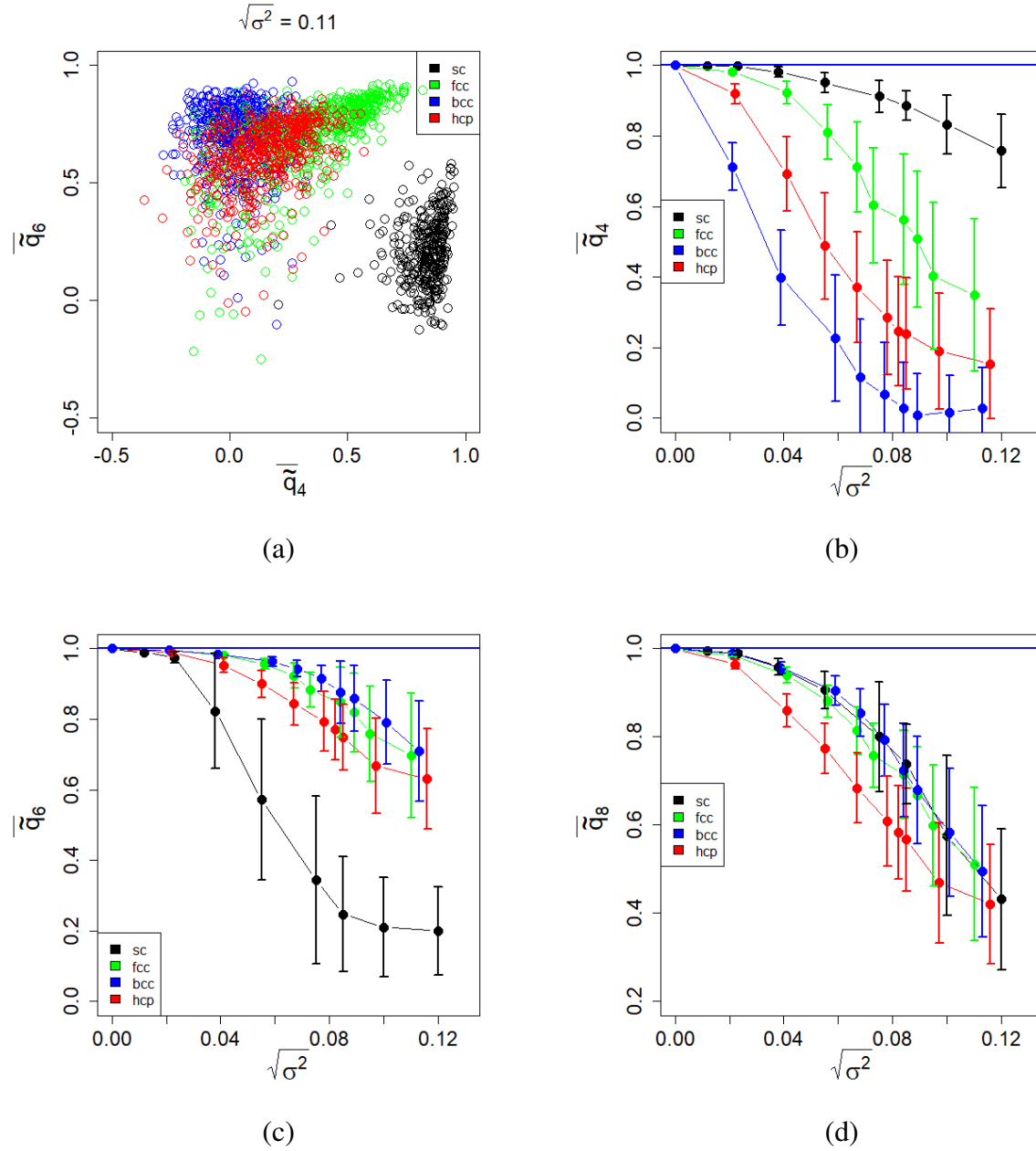


Figure 3.11: RLBO parameters $\bar{q}_4 - \bar{q}_6$ (a); mean values of RLBO parameters \bar{q}_4 (b), \bar{q}_6 (c), \bar{q}_8 (d) for bcc (blue), hcp (red), fcc (green), sc (black) test structures.

From the obtained data (Fig.3.11 and Fig.A3 in the Appendix), it can be seen that the parameter \bar{q}_4 still seems to be the most sensitive for distinguishing structures. Depending on the type of structure, noise magnitude has a different effect on the deviation of parameters from undisturbed values. Such a broad distribution of values, unfortunately, does not allow using combinations of parameters q_4 , q_6 , q_8 to distinguish between different types of structures.

Thus, since the parameters discussed in the section 3.4 do not allow us to reliably distinguish test structures with a noise value comparable to that estimated in the section 3.1, we cannot rely on them when analyzing our THS systems. In the next section, another way of using Steinhardt parameters (Eq.(3.10)) is proposed, the efficiency of the method on test structures is checked, and the use of the method on the example of the THS system is also demonstrated.

3.5 Noise reduction procedure

As we have established in the previous sections, the methods used for analyzing structures do not allow us to distinguish satisfactorily different symmetries in the presence of noise. Therefore, an attempt was made to reduce the influence of noise by averaging the position of coordinates of particles in space.

We propose the following procedure. Each point on the two-dimensional scheme (Fig.3.12) represents the projection of the center of mass of a particle on a plane. Let us choose the particle i for which one will compute Steinhardt order parameters. We draw a sphere of radius $R_s = 2$ around this particle (Fig.3.12 (a)), which contain $N_i + 1$ particles (N_i neighbors of the particles i and the particle i itself). Next, select particle j (green triangle in Fig.3.12 (b)) from the list of neighbors $\{N_i\}$. We also draw a sphere of radius $R_s = 2$ around it, into which N_j particles fall (blue particles in Fig.3.12 (b)). Then we translate particle j together with all its neighbors to the position of the particle i (Fig.3.12 (c)). We perform the same operation with all the particles from the list $\{N_i\}$ (Fig.3.12 (d)).

The next step after moving the points inside the sphere is averaging their positions. To achieve this, we set the positions of the neighbors of the particle i as the starting position of the groups \mathbf{r}'_{gr} (black dots inside the black sphere in Fig.3.12 (a)). Then we iteratively refine the present position of the centers of the groups \mathbf{r}_{gr} . To do this, we add the position of each of the moved points (blue in Fig. 3.12 (d)) to each of the existing groups as an gaussian term. To get the updated coordinates of the groups, it is necessary to weigh the amounts received.

$$\mathbf{r}_{gr} = \frac{1}{Z_{gr}} \sum_k \mathbf{r}_k \exp \left\{ -\frac{(\mathbf{r}_k - \mathbf{r}'_{gr})^2}{2 \cdot 2\sigma^2} \right\} \quad (3.19)$$

$$Z_{gr} = \sum_k \exp \left\{ -\frac{(\mathbf{r}_k - \mathbf{r}'_{gr})^2}{2 \cdot 2\sigma^2} \right\}, \quad (3.20)$$

where \mathbf{r}_k are positions of the particles relative to the particle i , \mathbf{r}'_{gr} are the group positions at previous iteration step, \mathbf{r}_{gr} are the updated group positions, $2\sigma^2 = 0.0242$, as defined in the section 3.1. We repeat this procedure several times until the positions of the groups stop changing. Thus, we obtained the averaged positions of the neighbors of the initial point i , which we use now in the following to calculate the Steinhardt parameters (Eq. (3.10)).

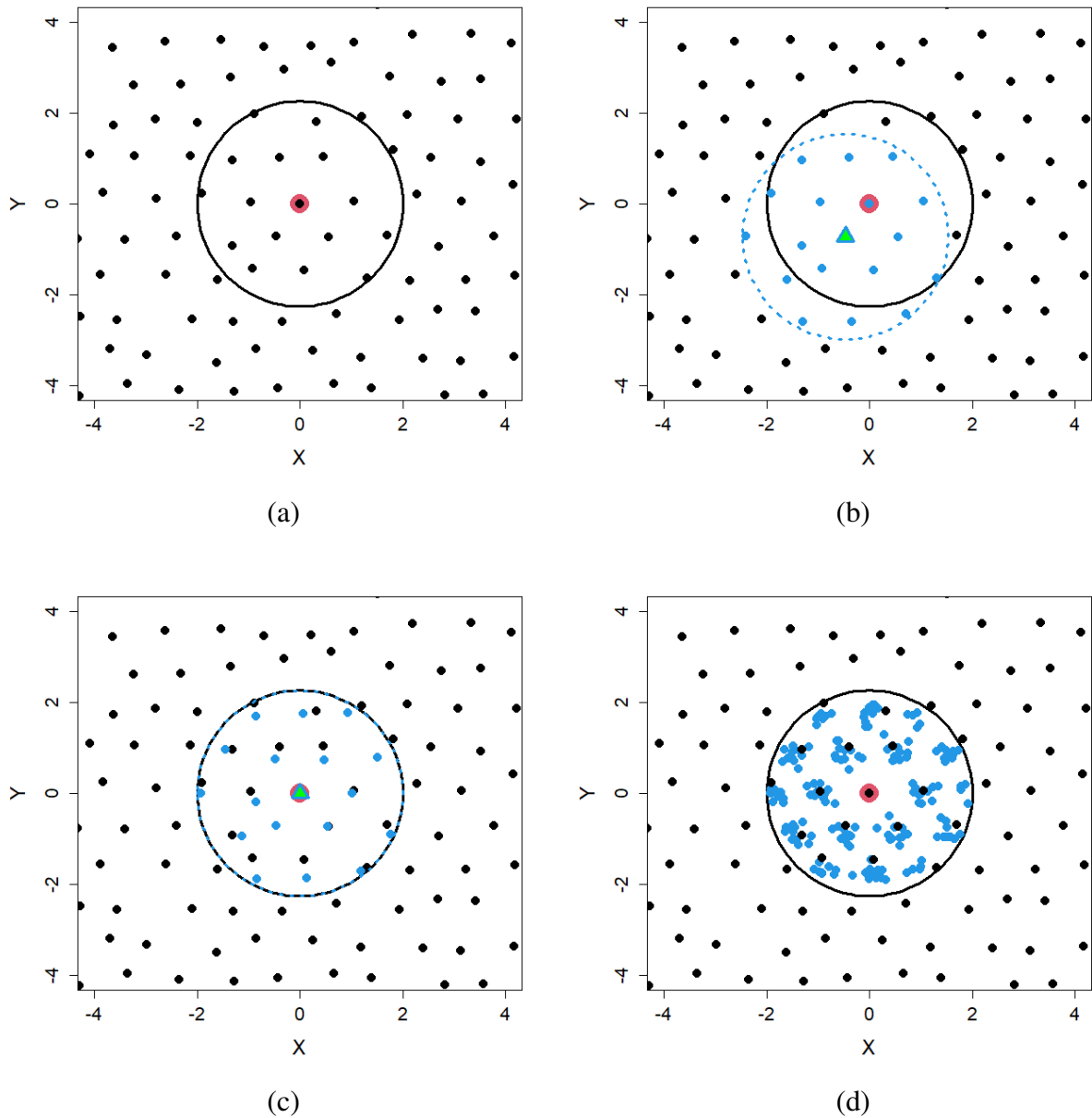


Figure 3.12: Two-dimensional coordinate averaging scheme. (a) Analyzed red particle i with its neighbors in black sphere; (b) triangle particle j from the original sphere and its blue neighbors; (c) blue sphere is completely translated into the original black one; (d) steps (b)-(c) are done for all neighbors from the black sphere.

It should be noted that for averaging coordinates, the radius of the sphere ($R_s = 2$) is set obviously larger than the cutoff radius for calculating the Steinhardt parameters, which is still equal to $R_c = 1.3$. During iterations, the coordinates of the centers of the groups \mathbf{r}_{gr} , which are used as the coordinates of neighbors at the end, may shift. Thus, if the initial point i had an insufficient or excessive number of points inside the sphere $R_c = 1.3$, then during the iteration process this number can be changed, that is, the averaged positions are less sensitive to noise magnitude around the original particle. Therefore, the choice of $R_s = 2$ provides a more reliable averaging. The local bond order parameters obtained after the noise reduction procedure will

be denoted as NRLBO.

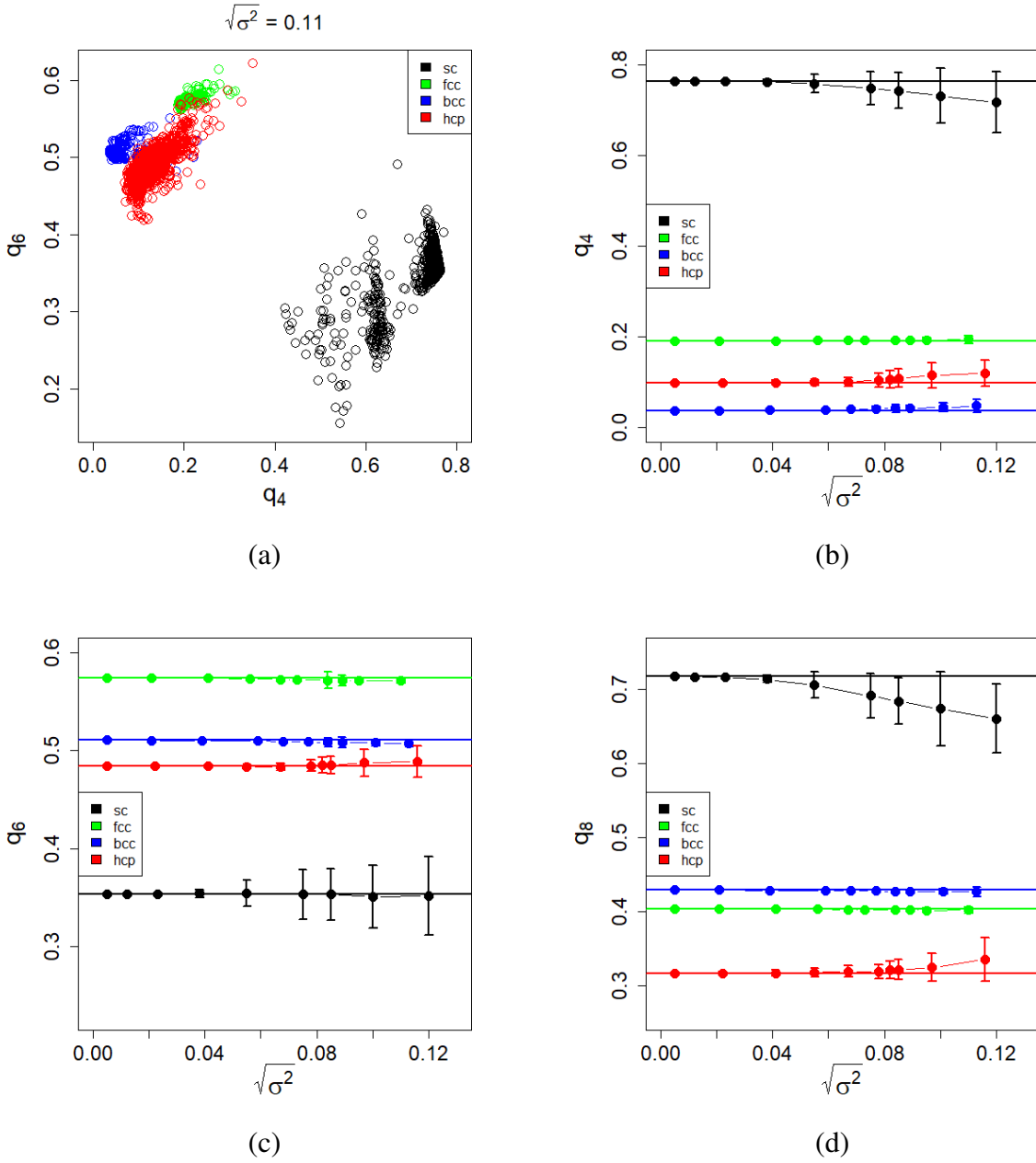


Figure 3.13: NRLBO parameters $q_4 - q_6$ (a); mean values of NRLBO parameters q_4 (b), q_6 (c), q_8 (d for *bcc* (blue), *hcp* (red), *fcc* (green), *sc* (black) test structures.

As we can see from the results obtained (Fig.3.13), the procedure of averaging coordinates in space makes it possible to make the mean values of all parameters more stable with increasing noise. At the same time, the spreading of order parameters decreases. On the plane q_4 - q_6 (Fig.3.13 (a)) it is also clearly seen that after introducing displacements in the lattice coordinates of the order $\sigma = 0.11$ the structures are clearly distinguishable. The same figure shows the division of *sc* into 3 groups. We found, that the reason for this is the different number of neighbors. Thus, one can conclude that the combination of three NRLBO parameters q_4 , q_6 , q_8 allows to distinguish different symmetries, even if there is a sufficiently large noise comparable

to that observed in our THS system.

Another modification of this method was also tested. Instead of combining the particles of the black sphere during averaging procedure by translations (Fig.3.13 (a)), the coordinates of the centers of mass for each of the spheres (black and all blue ones) were superimposed. Thus, one can say that the displacement of the central red particle is also taken into account, since its position will be also shifted after superposition of the centers of mass. However, our experience has shown that this modification does not provide significant improvements. Initially, the described method can be considered optimal, and it is used in further analysis.

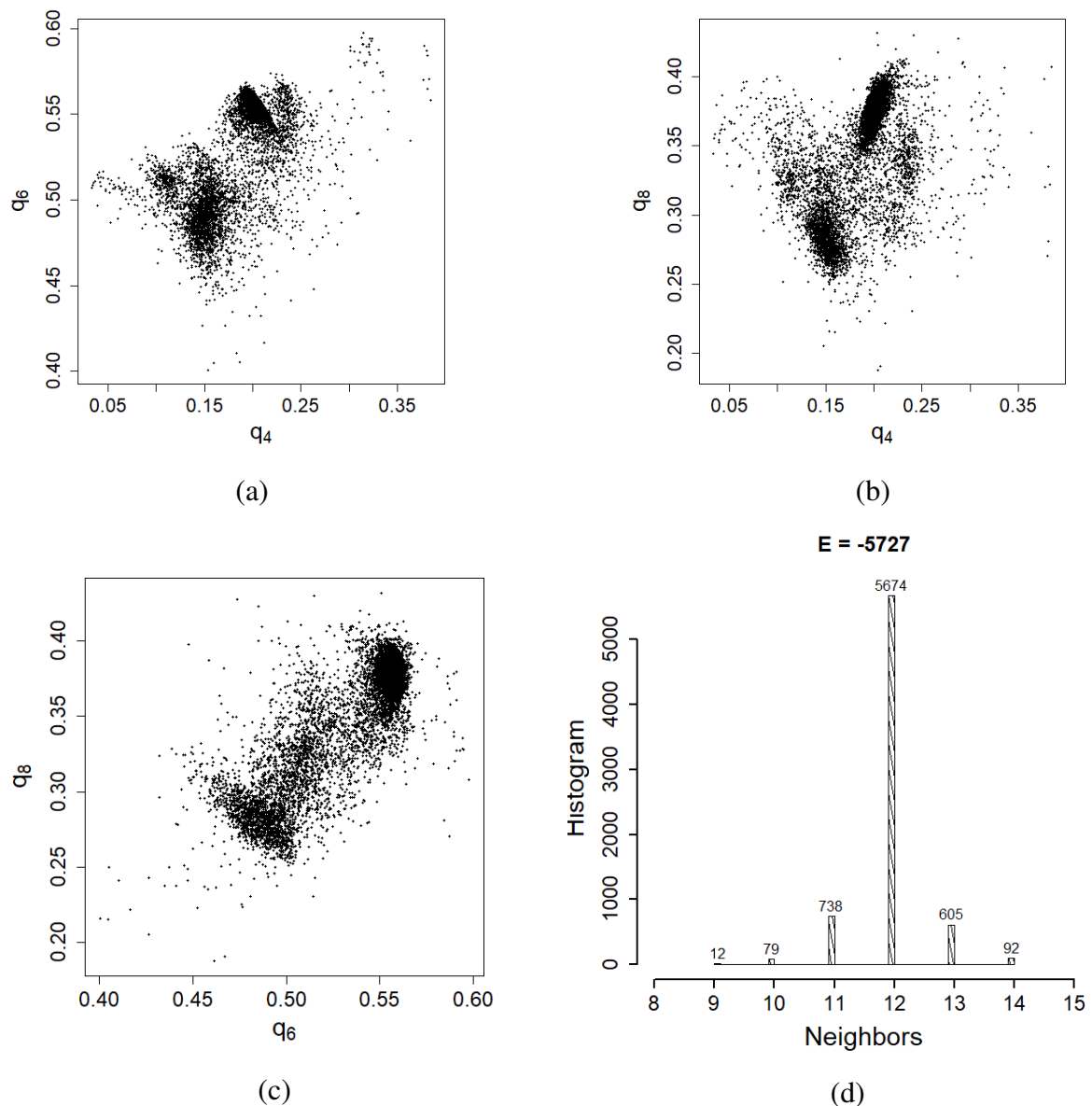


Figure 3.14: NRLBO parameters for the bulk system ($L_x = L_y = 20, L_z = 19$) $E = -5727$:
 q_4 - q_6 (a), q_4 - q_8 (b), q_6 - q_8 (c), neighbors histogram (d)

Since the proposed approach has proven itself well in relation to test structures, we can apply it to the THS system. To begin with, let us take a system without walls with low energy

$E = -5727$ (Fig. 3.1). The obtained NRLBO parameters are shown in Fig.3.14.

From the data obtained, it can be seen that the parameters q_4, q_6, q_8 are clearly divided into several groups. Two compact clusters are allocated on the plane q_6 - q_8 . On the other two planes, smaller clusters are also noticeable. However, since their size is small and they are located close to larger ones, we consider them as parts of larger clusters. It was also found that most of the particles in two biggest most compact clusters have 12 neighbors, while scattered points have a predominantly different number of neighbors than 12. Since the predominance of the correct number of neighbors can be observed on the test structures after the averaging procedure, then at this stage we can suggest that there is a coexistence of two types of symmetries with 12 neighbors in this structure, while a different number of neighbors appears because of the noise of the sample. Here we make an assumption that these two crystal structures first appear at higher energies, where they coexist with the disordered phase, which we will also call *Melt*. We present an algorithm for isolating co-existing structures at different energies.

Procedure for separating structures

Step 1. At the first stage, we calculated the parameters for the averaged coordinates of a low-energy system ($E = -5727$) and divided the particles into two clusters using the k-means method [153] built into the R environment. Parameters q_4, q_6, q_8 were used as input data for clustering. At the same time, our experience has shown that additional consideration of neighbors as input data does not significantly affect the result. The main disadvantage of this method is a strong dependence on the starting points chosen randomly. To work around this problem, in addition to the number of clusters (2), the number of program runs ($n_{start} = 500, 1000$) is also specified as an external parameter of this method. When we visually observe the results of the cluster separation on the graphs we found out that the results are well reproducible for our systems and do not change when restarted. One can also use other clustering methods (for example, various variations of the k-means method such as the c-means method [155], or expectation-maximization (EM) clustering algorithm [156]). Each of these methods has its own advantages and disadvantages, however, in our work we do not describe and compare clustering algorithms in detail. We prefer to use k-means method because of its simplicity, but testing other methods has yielded similar results. After the initial separation of the parameters of the low-energy structure into two clusters, it is necessary to clarify the positions of the clusters centers in the space $\{q_4, q_6, q_8\}$. To take into account the asymmetry of the clusters, we calculate the covariance matrix:

$$\hat{C}_k = \begin{bmatrix} \text{cov}(q_4^k, q_4^k) & \text{cov}(q_4^k, q_6^k) & \text{cov}(q_4^k, q_8^k) \\ \text{cov}(q_6^k, q_4^k) & \text{cov}(q_6^k, q_6^k) & \text{cov}(q_6^k, q_8^k) \\ \text{cov}(q_8^k, q_4^k) & \text{cov}(q_8^k, q_6^k) & \text{cov}(q_8^k, q_8^k) \end{bmatrix}, \quad (3.21)$$

here $k = \{1, 2\}$ is the number of cluster, q_j^k - the parameter of a particle related to the cluster k , $j = \{4, 6, 8\}$. Initially, the mean value of the parameter in the initial cluster is taken as the center of the cluster, then this value will be refined during the iterative process. In the iterative process the weight with which each particle i of the structure enters each cluster k is calculated:

$$\Omega_i^k = \sqrt{\det \hat{C}_k^{-1}} \exp \left\{ -\frac{1}{2} (q_{i,4} - \bar{q}_4^k, q_{i,6} - \bar{q}_6^k, q_{i,8} - \bar{q}_8^k) \hat{C}_k^{-1} \begin{pmatrix} q_{i,4} - \bar{q}_4^k \\ q_{i,6} - \bar{q}_6^k \\ q_{i,8} - \bar{q}_8^k \end{pmatrix} \right\}, \quad (3.22)$$

where \hat{C}_k^{-1} is the inverse matrix of \hat{C}_k ; \bar{q}_j^k represents the center of cluster k . Then the particles are reassigned to clusters: each particle i is attributed to the cluster k for which the weight turned out to be larger. After that, the positions of cluster centers are updated as:

$$\bar{q}_j^k = \frac{\sum_i q_{i,j}^k \Omega_i^k}{\sum_i \Omega_i^k}, \quad (3.23)$$

where $j = \{4, 6, 8\}$; i is the number of particle from the cluster k . The iterative process ends at the moment when \bar{q}_j^k stops to change.

Note: The \hat{C}_k and \hat{C}_k^{-1} do not change during the iterative process. In the case of matrix recalculation, one get nested clusters with close centers.

Thus, at the Step 1, the centers of two crystal structures (\bar{q}_j^k , $k = \{1, 2\}$, $j = \{4, 6, 8\}$) and covariance matrices (\hat{C}_k , $k = \{1, 2\}$) for them were obtained. These values are fixed and do not change in further steps.

Step 2. After two types of particles with different symmetries have been determined for this structure, we propose that these types are formed at higher energies and coexist with the polymer melt. At this step, our task is to find the values (\bar{q}_4^3 , \bar{q}_6^3 , \bar{q}_8^3 , \hat{C}_3) corresponding to the polymer melt. To do this, we choose a high-energy structure, such that only a melt

is observed. For example, let us take the energy $E = -2040$. For simplicity, assuming that there are no crystalline particles in the sample, we find $\bar{q}_4^3, \bar{q}_6^3, \bar{q}_8^3$ in the sample as the mean parameters for the entire system:

$$\bar{q}_j^3 = \frac{1}{N \cdot N_c} \sum_i q_{i,j}, \quad (3.24)$$

where $N \cdot N_c$ is the number of particles in the system ($N \cdot N_c = 7200$ in small and $N \cdot N_c = 14400$ in large systems, respectively).

Based on these data, we build the covariance matrix (Eq. (3.21)).

Thus, at the Step 2, the center of disordered structure ($\bar{q}_j^3, j = \{4, 6, 8\}$) and covariance matrix (\hat{C}_3) for it was obtained. These values are fixed and do not change in further step. One can find results for \bar{q}_j^k ($k = \{1, 2, 3\}$) in the Tab. 3.1.

| | color | \bar{q}_4 | \bar{q}_6 | \bar{q}_8 |
|-----------|-------|-------------------|-------------------|-------------------|
| Crystal 1 | black | 0.149 ± 0.030 | 0.491 ± 0.017 | 0.288 ± 0.028 |
| Crystal 2 | red | 0.201 ± 0.021 | 0.556 ± 0.011 | 0.376 ± 0.020 |
| Melt | green | 0.223 ± 0.066 | 0.401 ± 0.082 | 0.333 ± 0.053 |

Table 3.1: Centers of clusters $\bar{q}_4, \bar{q}_6, \bar{q}_8$ found in the $\{q_4, q_6, q_8\}$ space in the system without walls, $L_x = L_y = 20, L_z = 19$.

Step 3. Since we know the coordinates in the $\{q_4, q_6, q_8\}$ space for the three phases and their covariance matrices, it is now possible to separate the particles in our THS system of any energy into three types. First of all, we can return to the low-energy structure and redistribute the particles over the three sets of $\{\bar{q}_4, \bar{q}_6, \bar{q}_8\}$ found so far, using weights (Eq.(3.22)) (Fig.3.15). Since the system we have chosen does not have the lowest of all possible energies ($E = -5760$), the presence of several isotropic phase particles is possible.

Remark. To make sure that the sets obtained in the Tab.3.1 for these three clusters do not depend significantly on the choice of specific structures, additional tests were performed. The procedure of searching \bar{q}_j^k and \hat{C}_k ($j = \{4, 6, 8\}, k = \{1, 2, 3\}$) was repeated for several sets of low and high energy conformations. The set of conformations obtained during SAMC can be considered to be statistical independent, since they were taken with a large time difference (on the order of several months of computer calculations). The values \bar{q}_j^k and \hat{C}_k do not depend significantly on the choice of conformations. The assignment of a particles to different clusters (Step 3) also does not change significantly.

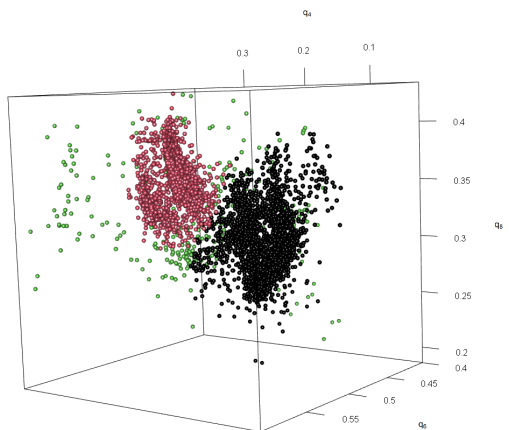


Figure 3.15: 3d view of NRLBO parameters for the bulk system at $E = -5727$, $L_x = L_y = 20, L_z = 19$.

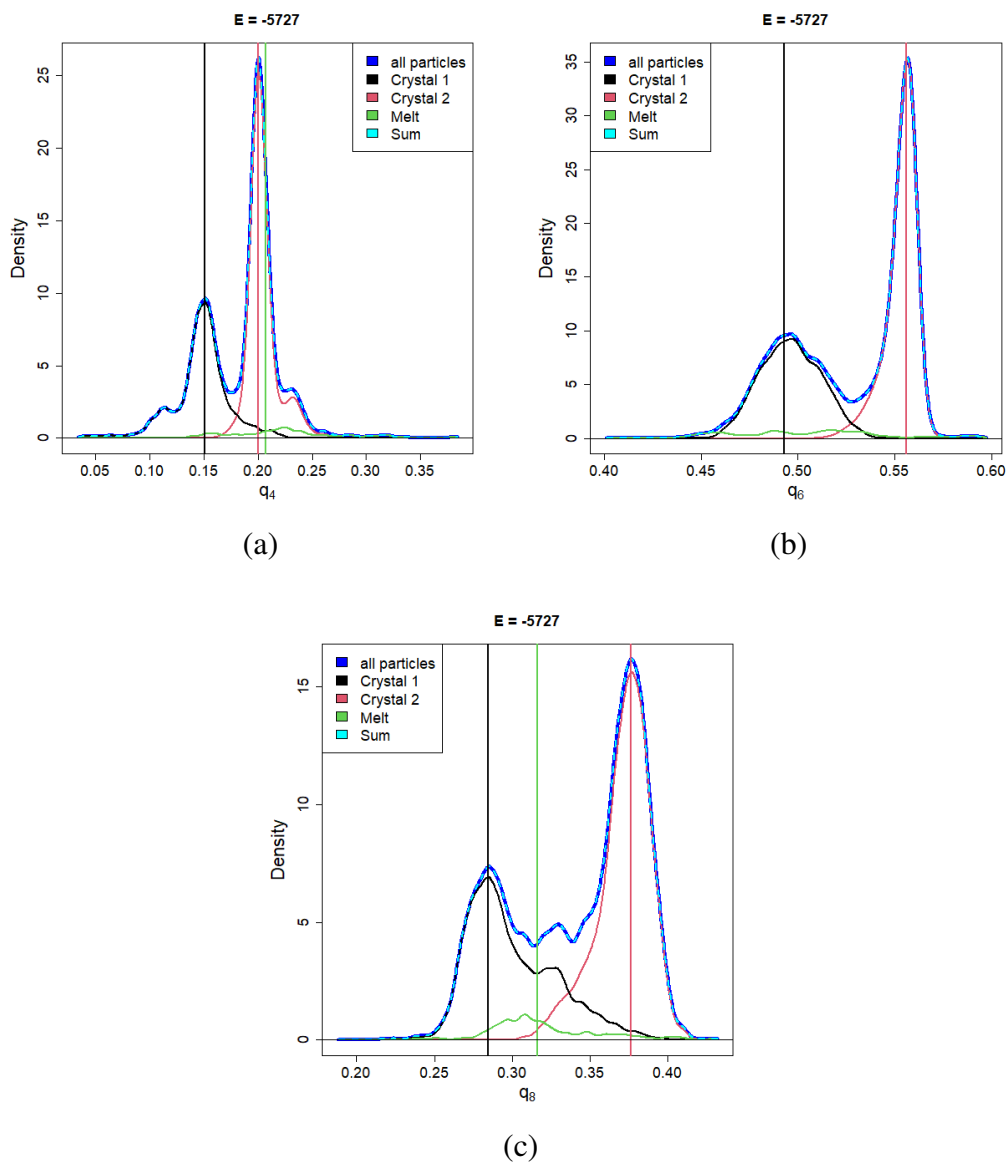


Figure 3.16: NRLBO parameters distribution for the bulk system at $E = -5727$, $L_x = L_y = 20, L_z = 19$.

In Fig.3.16, the distributions of the parameters q_4 , q_6 , q_8 for the system under study are shown in blue. Black, red and green colors represent the distributions of particles parameters of the corresponding clusters. The dashed line of the cyan color represents the sum of these individual contributions. It is obvious that the distribution of parameters for all particles is actually a set of distributions of particles belonging to individual clusters, since the blue curve exactly coincides with the cyan dashed line. The shoulder in the black curve at q_8 distribution around $q_8 \approx 0.33$ for *Crystal 1* (Fig.3.16 c) corresponds to the number of neighbors other than 12 (detailed distributions can be seen in the Appendix Fig.A6).

| | color | \bar{q}_4 | \bar{q}_6 | \bar{q}_8 |
|-----------|-------|-------------------|-------------------|-------------------|
| Crystal 1 | black | 0.151 ± 0.036 | 0.504 ± 0.018 | 0.300 ± 0.038 |
| Crystal 2 | red | 0.211 ± 0.047 | 0.552 ± 0.019 | 0.360 ± 0.031 |
| Melt | green | 0.225 ± 0.073 | 0.385 ± 0.071 | 0.330 ± 0.058 |

Table 3.2: Centers of clusters \bar{q}_4 , \bar{q}_6 , \bar{q}_8 found in the $\{q_4, q_6, q_8\}$ space in the system with repulsive walls, $L_x = L_y = L_z = 20$

The method was also tested on a system with repulsive walls (Tab.3.2). In these two studied systems, structures with identical sets of \bar{q}_j^k are formed. If we compare the spatial arrangement of the structures (Tab.3.3 and Tab.3.4), the dominant crystalline phase in both systems is the *Crystal 2* (red). In the system with repulsive walls, the alternation of crystal phases is observed parallel to the walls, while in a system without walls, alternation occurs in the planes located at an angle to the planes of the simulation box. The conformations are dominated by layered crystal phases, with the *Crystal 2* dominating near the walls. The observed structures (*Melt*, *Crystal 1*, *Crystal 2*) found do not exactly define any of the test structures (*sc*, *bcc*, *fcc*, *hcp*) (see Tab.3.1 and Tab.A1 in the Appendix). However, taking into account the estimated spread of the values obtained, it can be seen that the parameters of the *Crystal 2* (red structure) are quiet close to *fcc*, while the *Crystal 1* (black structure) is close in parameters to *hcp*. The only significant difference is observed for the parameter q_4 of the *Crystal 1* and *hcp*. The deviation of this parameter from the reference value can indicate the deformation of the *hcp* structure. Indeed, when considering the projections of the centers of the particles of the system on different planes, irregular, deformed hexagons were observed (Fig.3.1(d)). The reason for the deformation is the connectivity in the chain and the dimensions of the box. So, for example, if in low energy conformations chains are stretched along the y axis one after the other, then in the perpendicular plane XZ we see sections of only 360 chains. There are no transformations which allow to fill rectangle of size $L_x \cdot L_z = 20 \cdot 19$ by regular polygon. Note that although in reality the y direction is not highlighted, the final, small size of the system has a strong influence on the packing in our case. Nevertheless, the organization of short chains into layers was tested on a similar system in the work of T. Shakirov [97].

For other studied THS systems (bulk $L_x = L_y = 20$, $L_z = 39$, system with repulsive walls $L_x = L_y = 20$, $L_z = 40$, with attractive wall U_{at_1} and U_{at_2} , $L_x = L_y = L_z = 20$), we found a separation into similar clusters (see the Appendix, Tab.A2, Tab.A3, Tab.A4, Tab.A5).

Thus, it can be argued that the approaches developed in this work are valid within the framework of this model.

3.5. Noise reduction procedure

| E | Crystal 1 (black) | Crystal 2 (red) | Melt (green) | View |
|-------|----------------------|--------------------|-----------------|------|
| -5727 | 2803 (39%) | 4070 (56%) | 327 (5%) | |
| -5104 | 2449 (34%) | 3329 (46%) | 1422 (20%) | |
| -4715 | 1601 (22%) | 3194 (44%) | 2405 (34%) | |
| -3408 | 1034 (14%) | 1266 (18%) | 4900 (68%) | |
| -2040 | 394 (5%) | 113 (2%) | 6693 (93%) | |

Table 3.3: The number of particles (and percentage) related to a clusters for different energies in the system without walls, $L_x = L_y = 20$, $L_z = 19$. The colors in the snapshots correspond to the colors used to indicate clusters in the space $\{q_4, q_6, q_8\}$.

| E | Crystal 1 (black) | Crystal 2 (red) | Melt (green) | View |
|-------|----------------------|--------------------|-----------------|------|
| -5754 | 2316 (32%) | 4587 (64%) | 297 (4%) | |
| -5205 | 1262 (17%) | 4289 (60%) | 1649 (23%) | |
| -4740 | 1626 (23%) | 2548 (35%) | 3026 (42%) | |
| -3600 | 282 (4%) | 1728 (24%) | 5190 (72%) | |
| -2050 | 237 (3%) | 475 (7%) | 6488 (90%) | |

Table 3.4: The number of particles (and percentage) related to a clusters for different energies in the system with repulsive walls, $L_x = L_y = L_z = 20$. The colors in the snapshots correspond to the colors used to indicate clusters in the space $\{q_4, q_6, q_8\}$.

3.6 Searching for translation vectors

After we have learned to distinguish structures, it is interesting to find an answer to the question: "what do the detected structures look like?". In other words, we asked ourselves the question of finding translation vectors with which a reconstruction of the crystalline lattice would be possible. Knowledge of test structures says that for *sc*, *bcc*, *fcc* it is enough to know three translation vectors to reconstruct the lattice. For *hcp*, in addition to three translation vectors, it is necessary to set not a single base point, but two. Since the first base point can always be placed at the origin, we can say that knowledge of four vectors is required: one vector (let us call it **h**) determines the position of the second base particle, and three more vectors, {**a**, **b**, **c**}, define translation vectors. Note that you can also reconstruct *sc*, *bcc*, *fcc* by specifying four vectors {**a**, **b**, **c**, **h**}. The cells formed by these vectors will no longer be elementary cells of minimal volume. However, searching for the elementary cell is not our goal.

So, we formulate the following problem: find the vectors {**a**, **b**, **c**, **h**}, with which we can construct a crystal lattice that we observe in our system. Thus, we expect that all lattice nodes can be described by the expression:

$$\mathbf{r}_i^{lat} = \mathbf{a} \cdot n_i + \mathbf{b} \cdot m_i + \mathbf{c} \cdot l_i + \mathbf{h} \cdot \alpha_i, \quad (3.25)$$

where $n_i, m_i, l_i \in \mathbb{Z}$, $\alpha_i \in \{0, 1\}$.

The search for vectors is performed for each particle of the system. For the neighbors of the selected particle inside a sphere of radius $R_s = 2.0$ the coordinates are averaged, as described in 3.5. *Further in this part we work with the averaged coordinates of the neighbors and set the origin of coordinates in the selected particle position.*

Let the selected particle has N_b neighbors with position \mathbf{r}_i . The key assumption in the procedure is that the vectors of the desired structure can be chosen close to the positions of the neighbors of the considered particle. Thus, during the procedure we consistently direct the vectors **a**, **b**, **c**, **h** from the central, selected particle to its neighbors.

Translation vectors search procedure

Step 1. Select a set of vectors {**a**, **b**, **c**, **h**} directed from a particle under study to its neighbors.

Step 2. The following conditions must be applied:

1. The vector **h** must be inside a parallelepiped constructed on the vectors **a**, **b**, **c**. Mathematically this condition is expressed as follows:

$$\begin{aligned} 0 &\leq (\mathbf{h} \cdot \mathbf{a}) \leq \mathbf{a}^2, \\ 0 &\leq (\mathbf{h} \cdot \mathbf{b}) \leq \mathbf{b}^2, \end{aligned} \quad (3.26)$$

$$0 \leq (\mathbf{h} \cdot \mathbf{c}) \leq \mathbf{c}^2.$$

2. We cannot allow the case when $\mathbf{a}, \mathbf{b}, \mathbf{c}$ form one plane. Therefore, the angles between these vectors should not be too small, since in this case the search may lead to degeneration. To fulfill this condition, the following expressions must be fulfilled:

$$\begin{aligned} \frac{(\mathbf{a} \cdot \mathbf{c})}{|\mathbf{a}| \cdot |\mathbf{c}|} &\leq 0.9, \\ \frac{(\mathbf{a} \cdot \mathbf{b})}{|\mathbf{a}| \cdot |\mathbf{b}|} &\leq 0.9, \\ \frac{(\mathbf{b} \cdot \mathbf{c})}{|\mathbf{b}| \cdot |\mathbf{c}|} &\leq 0.9. \end{aligned} \quad (3.27)$$

3. Note also that the cell should not be too small: an extremely small cell can form a lattice in which the nodes will actually fall into the desired positions, however, in addition to these atoms, there will obviously be extra atoms in the lattice. To avoid this, we impose a condition on the volume of the cell built on the vectors $\mathbf{a}, \mathbf{b}, \mathbf{c}$. Let us estimate the minimum possible cell volume. The distances between real beads in our system cannot be less than 1, however, taking into account the noise magnitude and influence of the noise reducing procedure, we assume that the minimum length of each vector is 0.9. To estimate, let us assume that the cell is elongated so that the angles between all vectors are 30° . Then

$$|V_{abc}| = |(\mathbf{a}, \mathbf{b}, \mathbf{c})| = |0.9^3 \sin(30^\circ) \cos(60^\circ)| \geq 0.18225 > 0.18. \quad (3.28)$$

4. Finally, consider that the vector \mathbf{h} must not be a linear combination of the vectors $\mathbf{a}, \mathbf{b}, \mathbf{c}$.

Step 3. If all conditions are met for the selected set of vectors, then we proceed to the next stage: we match the coordinates \mathbf{r}_i for each of the $N_b + 1$ particles with an individual set of integers $\{n_i, m_i, l_i, \alpha_i\}$ such that the distance $|\mathbf{r}_i - \mathbf{r}_i^{lat}|$ will be minimal.

To find this correspondence, two systems of equations (for $\alpha_i = 0$ and $\alpha_i = 1$) are solved for each particle i taking into account Eq. (3.25):

$$\begin{cases} \frac{\partial}{\partial n_i} (\mathbf{a}n_i + \mathbf{b}m_i + \mathbf{c}l_i + \mathbf{h}\alpha_i - \mathbf{r}_i)^2 = 0 \\ \frac{\partial}{\partial m_i} (\mathbf{a}n_i + \mathbf{b}m_i + \mathbf{c}l_i + \mathbf{h}\alpha_i - \mathbf{r}_i)^2 = 0 \\ \frac{\partial}{\partial l_i} (\mathbf{a}n_i + \mathbf{b}m_i + \mathbf{c}l_i + \mathbf{h}\alpha_i - \mathbf{r}_i)^2 = 0. \end{cases} \quad (3.29)$$

Then the integers closest to the found real numbers $\{n_i, m_i, l_i\}$ are selected. Of the two found sets integers $\{n_i, m_i, l_i, \alpha_i\}$ with $\alpha = \{0, 1\}$ defining \mathbf{r}_i^{lat} , the particle \mathbf{r}_i corresponds to that one for which the distance $|\mathbf{r}_i^{lat} - \mathbf{r}_i|$ is minimal.

Step 4. Now we have a comparison of particles \mathbf{r}_i with nodes \mathbf{r}_i^{lat} built on the vectors $\{\mathbf{a}, \mathbf{b}, \mathbf{c}, \mathbf{h}\}$ of the lattice and, since there is noise in the systems, we need to refine these vectors. To do this, we solve 3 systems (for x, y, z components of vectors $\{\mathbf{a}, \mathbf{b}, \mathbf{c}, \mathbf{h}\}$) of 4 equations, implying that n_i, m_i, l_i, α_i are found:

$$\begin{cases} \frac{\partial}{\partial a_x} \sum_i (\mathbf{a}n_i + \mathbf{b}m_i + \mathbf{c}l_i + \mathbf{h}\alpha_i - \mathbf{r}_i)^2 = 0 \\ \frac{\partial}{\partial b_x} \sum_i (\mathbf{a}n_i + \mathbf{b}m_i + \mathbf{c}l_i + \mathbf{h}\alpha_i - \mathbf{r}_i)^2 = 0 \\ \frac{\partial}{\partial c_x} \sum_i (\mathbf{a}n_i + \mathbf{b}m_i + \mathbf{c}l_i + \mathbf{h}\alpha_i - \mathbf{r}_i)^2 = 0 \\ \frac{\partial}{\partial h_x} \sum_i (\mathbf{a}n_i + \mathbf{b}m_i + \mathbf{c}l_i + \mathbf{h}\alpha_i - \mathbf{r}_i)^2 = 0. \end{cases} \quad (3.30)$$

After the vectors are found, we perform a final check of their linear independence.

Step 5. At the next stage, we calculate a function that allows us to estimate how well the lattice \mathbf{r}^{lat} constructed from the selected vectors matches the positions of neighbors \mathbf{r}_i of the chosen particle. To do this, a lattice \mathbf{r}^{lat} is constructed on the obtained vectors $\{\mathbf{a}, \mathbf{b}, \mathbf{c}, \mathbf{h}\}$ and $N_b + 1$ nodes of the lattices are selected that are closest to the origin.

Then we consider the function:

$$F_1 = \sum_{i,j=1}^{N_b+1} \exp \left(-\frac{(\mathbf{r}_j^{lat} - \mathbf{r}_i)^2}{2 \cdot (6 \cdot \sigma^2)} \right), \quad (3.31)$$

where coefficient 6 refers to the noise magnitude evaluation in the section 3.1: a multiplier of 3 should be added to account for three-dimensional space, since the noise magnitude evaluation was performed in one-dimensional space; an additional multiplier of 2 corresponds to the mutual noise of two groups. The function F_1 is constructed in such a way that, on the one hand, it describes the similarity of the constructed lattice with the existing one ($(\mathbf{r}_j^{lat} - \mathbf{r}_i)^2$), and on the other hand, it takes into account the noise magnitude in the system (parameter σ^2).

Alternative ways to construct a function by which we determine the best set of vectors are based on constructing a correspondence between the environment of the particle under study \mathbf{r}_i with lattice nodes, similar to how we do it in Step 3.. After the corresponding lattice points $\mathbf{r}_i^{lat'}$ are found, we use them to construct the following functions:

$$F_2 = \sum_{i=1}^{N_b+1} \exp \left(-\frac{(\mathbf{r}_i^{lat'} - \mathbf{r}_i)^2}{2 \cdot (6 \cdot \sigma^2)} \right), \quad (3.32)$$

$$F_3 = \sum_{i,j=1}^{N_b+1} \exp \left(-\frac{(\mathbf{r}_j^{lat'} - \mathbf{r}_i)^2}{2 \cdot (6 \cdot \sigma^2)} \right). \quad (3.33)$$

Thus, we consider $N_b + 1$ points of the found lattice: \mathbf{r}_i^{lat} are closest to the origin, while $\mathbf{r}_i^{lat'}$ are closest to the neighbors of the selected particle inside the radius $R_s = 2.0$. Note that the maximum possible value of all functions F_1, F_2, F_3 is equal to $(N_b + 1)$.

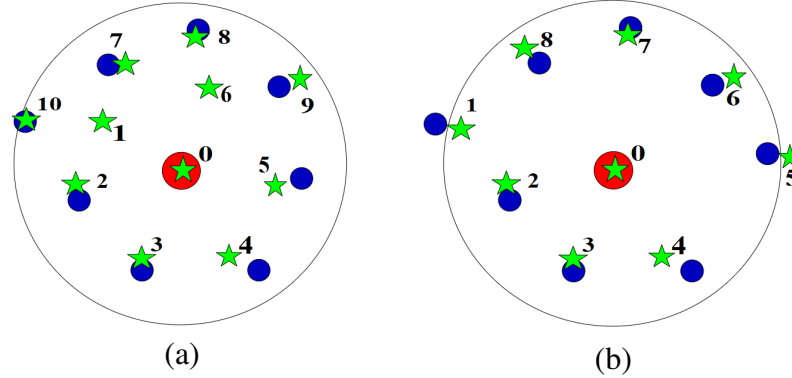


Figure 3.17: illustration of the action F_1, F_2, F_3

Each of these functions has its own advantages and disadvantages. We prefer to use of the F_1 function because it seems to be more reliable. Indeed, consider the following two-dimensional illustration (Fig.3.17) as an example. Let the circles in the diagram be the beads of our system (red - the original particle, blue - its neighbors, $N_b = 8$), and the green stars are the nodes of the found lattice constructed by the current set of vectors $\{\mathbf{a}, \mathbf{b}, \mathbf{c}, \mathbf{h}\}$. If we use the F_1 function, we select the closest $N_b + 1$ stars $\{0 - 8\}$ to the red particle (Fig. 3.17 (a)). The $\{1, 6\}$ stars are far away from the particles of the system, so the summands containing \mathbf{r}_1^{lat} and \mathbf{r}_6^{lat} will give a small contribution to F_1 . As a result, F_1 for this set $\{\mathbf{a}, \mathbf{b}, \mathbf{c}, \mathbf{h}\}$ is small. That is, this lattice is considered to be not quiet similar to our system. This correctly reflects the fact that the nodes found in the lattice $\{1, 6\}$ are redundant. For the same example, F_2, F_3 would be quite large because the stars $\{0, 2 - 5, 7 - 10\}$ are used in the calculation of these parameters, while the points $\{1, 6\}$ will be ignored. That is, these functions are not sensitive to the presence of extra points.

At the same time, the functions F_2, F_3 are more sensitive to noise at the sphere boundary. Let us consider another illustration in Fig.3.17 (b). The calculation of function F_1 involves stars $\{0 - 4, 6 - 8\}$. Although this set visually describes the points of the system quite well, F_1 is small for them, due to the loss of summands associated with the $\{1, 5\}$ stars. F_2, F_3 would give a more accurate account of the boundary points: the star 5 will be taken into account, and 1 will be ignored.

Our experience has shown that F_1 qualitatively better selects vectors similar to the observed structure, so we will present results for this function. However, we find it necessary to describe the functions F_2, F_3 , since they can give an additional information, or the calculation of these functions together with additional conditions can give satisfactory results for other problems.

At this stage, we save the value of the function F_1 (or F_2, F_3) and the corresponding set of vectors $\{\mathbf{a}, \mathbf{b}, \mathbf{c}, \mathbf{h}\}$.

Step 6. Next, we go back to Step 1 and repeat the procedure for a new set. Note that if at any stage the check reveals violations (for example, some of conditions in the Step 2 are not fulfilled, or the system of equations has no solution), we automatically proceed to Step 1, choosing a new set of four vectors $\{\mathbf{a}, \mathbf{b}, \mathbf{c}, \mathbf{h}\}$. Let us also pay attention to the fact that it is expected that for a highly noisy structure (or, for example, a melt), there will not be a single set of vectors satisfying all the requirements described above.

Step 7. After all possible vectors have been checked for the particle under study and F_1 has been calculated for each set, the set of vectors $\{\mathbf{a}, \mathbf{b}, \mathbf{c}, \mathbf{h}\}$ with the maximum F_1 is selected from the data obtained. After that, one can start exploring the next particle.

Remark. Note that this approach does not use additional constraints that guarantee the uniqueness of the set. For example, for test systems without noise, one value of F_1 corresponds to several sets of vectors. Since our goal was to find a set of vectors that allows us to reconstruct a structure similar to the observed one, we are satisfied with any of the found sets. However, of course, this task can be further developed if one set the goal of finding a unique set. In this case, it is necessary to define additional rules that filter out equivalent sets among the found ones. One of such rules could be, for example, the requirement to search only for the right triples of vectors $\mathbf{a}, \mathbf{b}, \mathbf{c}$. This rule does not specify uniqueness yet, but it may reduce the number of equivalent vectors.

Knowing the fact that the maximum value of F_1 is $F_1^{max} = N_b + 1$, it is possible to assess how well the found set describes the structure under study. Depending on the conditions of the problem, one can use some fixed value or a percentage of the maximum possible value of F_1 as a critical value of F_1^{cr} . Further, one can assume that if the obtained value is $F_1 < F_1^{cr}$, then the environment of this particle cannot be reconstructed by a crystal lattice. In this case, it can be attributed to an unordered structure (isotropic state).

Test structures

To make sure that this method works, we have checked it for test structures. To reduce the number of equivalent sets of vectors in noiseless structures, we chose sets with the smallest vector lengths. Here we again give as an example the table (Tab.3.5) of the obtained vectors for *bcc*, since the vectors for this structure were mentioned in section 3.2.

| Vectors | a | b | c | h |
|-----------|---|---|---|--|
| Reference | $(-\frac{\sqrt{3}}{3}, \frac{\sqrt{3}}{3}, \frac{\sqrt{3}}{3})$ | $(\frac{\sqrt{3}}{3}, -\frac{\sqrt{3}}{3}, \frac{\sqrt{3}}{3})$ | $(\frac{\sqrt{3}}{3}, \frac{\sqrt{3}}{3}, -\frac{\sqrt{3}}{3})$ | |
| Set 1 | $(-\frac{2\sqrt{3}}{3}, 0, 0)$ | $(0, -\frac{2\sqrt{3}}{3}, 0)$ | $(0, 0, \frac{2\sqrt{3}}{3})$ | $(-\frac{\sqrt{3}}{3}, -\frac{\sqrt{3}}{3}, \frac{\sqrt{3}}{3})$ |
| Set 2 | $(0, 0, -\frac{2\sqrt{3}}{3})$ | $(-\frac{2\sqrt{3}}{3}, 0, 0)$ | $(0, \frac{2\sqrt{3}}{3}, 0)$ | $(-\frac{\sqrt{3}}{3}, \frac{\sqrt{3}}{3}, -\frac{\sqrt{3}}{3})$ |
| Set 3 | $(0, 0, -\frac{2\sqrt{3}}{3})$ | $(0, \frac{2\sqrt{3}}{3}, 0)$ | $(\frac{2\sqrt{3}}{3}, 0, 0)$ | $(\frac{\sqrt{3}}{3}, \frac{\sqrt{3}}{3}, -\frac{\sqrt{3}}{3})$ |
| Set 4 | $(0, -\frac{2\sqrt{3}}{3}, 0)$ | $(\frac{2\sqrt{3}}{3}, 0, 0)$ | $(0, 0, \frac{2\sqrt{3}}{3})$ | $(\frac{\sqrt{3}}{3}, -\frac{\sqrt{3}}{3}, \frac{\sqrt{3}}{3})$ |

 Table 3.5: Found vectors for *bcc* without noise.

It is not difficult to see that linear combinations of the values given in the table can really give reference values. For example, using the Set 1 of vectors $\{\mathbf{a}^1, \mathbf{b}^1, \mathbf{c}^1, \mathbf{h}^1\}$, we can verify:

$$\begin{aligned}
 \mathbf{a}^{ref} &= \mathbf{h}^1 - \mathbf{b}^1; \\
 \mathbf{b}^{ref} &= \mathbf{h}^1 - \mathbf{a}^1; \\
 \mathbf{c}^{ref} &= \mathbf{c}^1 - \mathbf{a}^1 - \mathbf{b}^1;
 \end{aligned} \tag{3.34}$$

For the other sets, as well as for other structures, tests can be done in a similar way. Note that we can use the vector \mathbf{h} only with a coefficient of 0 or 1. Thus, we have verified the suitability of the method for perfect (noiseless) test structures.

We also considered noisy *sc*, *bcc*, *fcc*, *hcp* structures as a test. Let us illustrate the result of this method with Fig.3.18 for *bcc* (the results for *sc*, *fcc*, *hcp* one can find in the Appendix, Fig.A7, Fig.A8).

In this structure a noise magnitude equal to the noise observed in our THS system is introduced ($\sigma = 0.11$). A point i of the system is considered. The set of vectors $\{\mathbf{a}, \mathbf{b}, \mathbf{c}, \mathbf{h}\}$ is found for it. The crystal structure is reconstructed from this set using Eq.(3.25).

The initial point i with its nearest neighbors in the cutoff radius $R_c = 1.3$, is translated to the origin and depicted by green points (Fig.3.18). The points of the reconstructed structure at the same radius, are depicted in black in Fig.3.18. The same is done for all points of the noisy structure. Red crosses indicate the positions of the particles of the perfect structure. It can be seen from the results that the displacement of the reconstructed structures from the positions of the perfect structure is smaller than for the original green particles. This is explained by the fact that the average positions of neighbors are used in the translation vectors search procedure.

To provide the validity of this approach an additional test was performed. For lattices constructed on $\{\mathbf{a}, \mathbf{b}, \mathbf{c}, \mathbf{h}\}$, the values of Steinhardt parameters (LBO) were calculated. Fig.3.19 shows that the distributions of the LBO parameters for the reconstructed structures are much compact compared to the Steinhardt parameters obtained after the noise reduction procedure. In addition, the obtained values become closer to the parameters for the perfect structures (horizontal and vertical straight lines). The exception is the simple cubic lattice. Points that deviate

3.6. Searching for translation vectors

strongly from the perfect lattice values vary greatly in the number of neighbors (>10 instead of 6). We do not apply additional filters on the number of neighbors, since the initial number of neighbors in our structure is not uniquely defined, however we use these values for analysis, so the preferred number of neighbors in each structure is clearly visible. Thus, this test also proved the validity of the approach used.

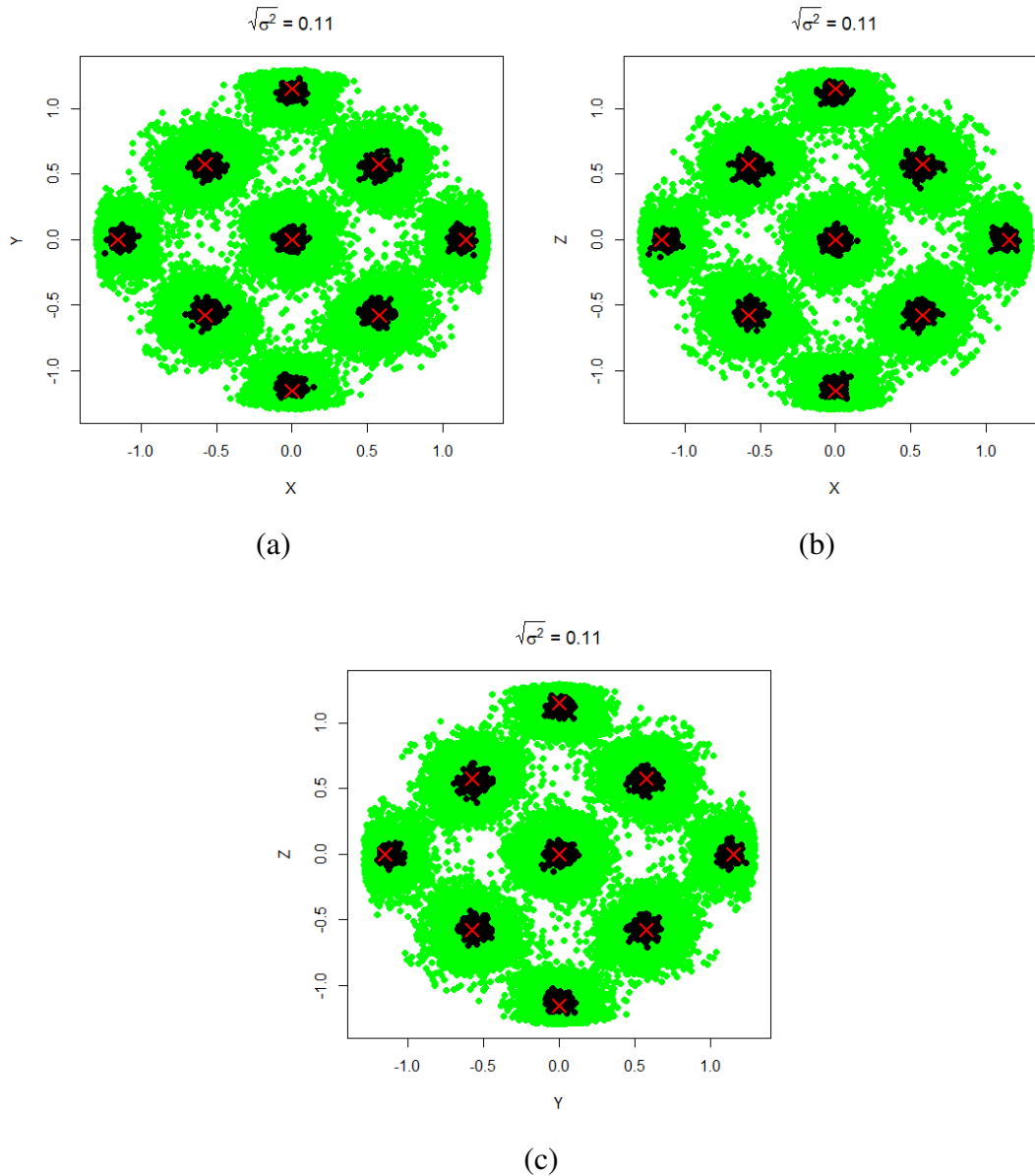


Figure 3.18: Illustration of reconstructing noisy crystal lattice *bcc*. Green points indicate the particles of the noisy structure *bcc* with their nearest neighbors in the cutoff radius $R_c = 1.3$, translated to the origin. Black denotes the points of the crystalline structure constructed by found vectors. Red crosses indicate the positions of the particles of the perfect structure (without noise).

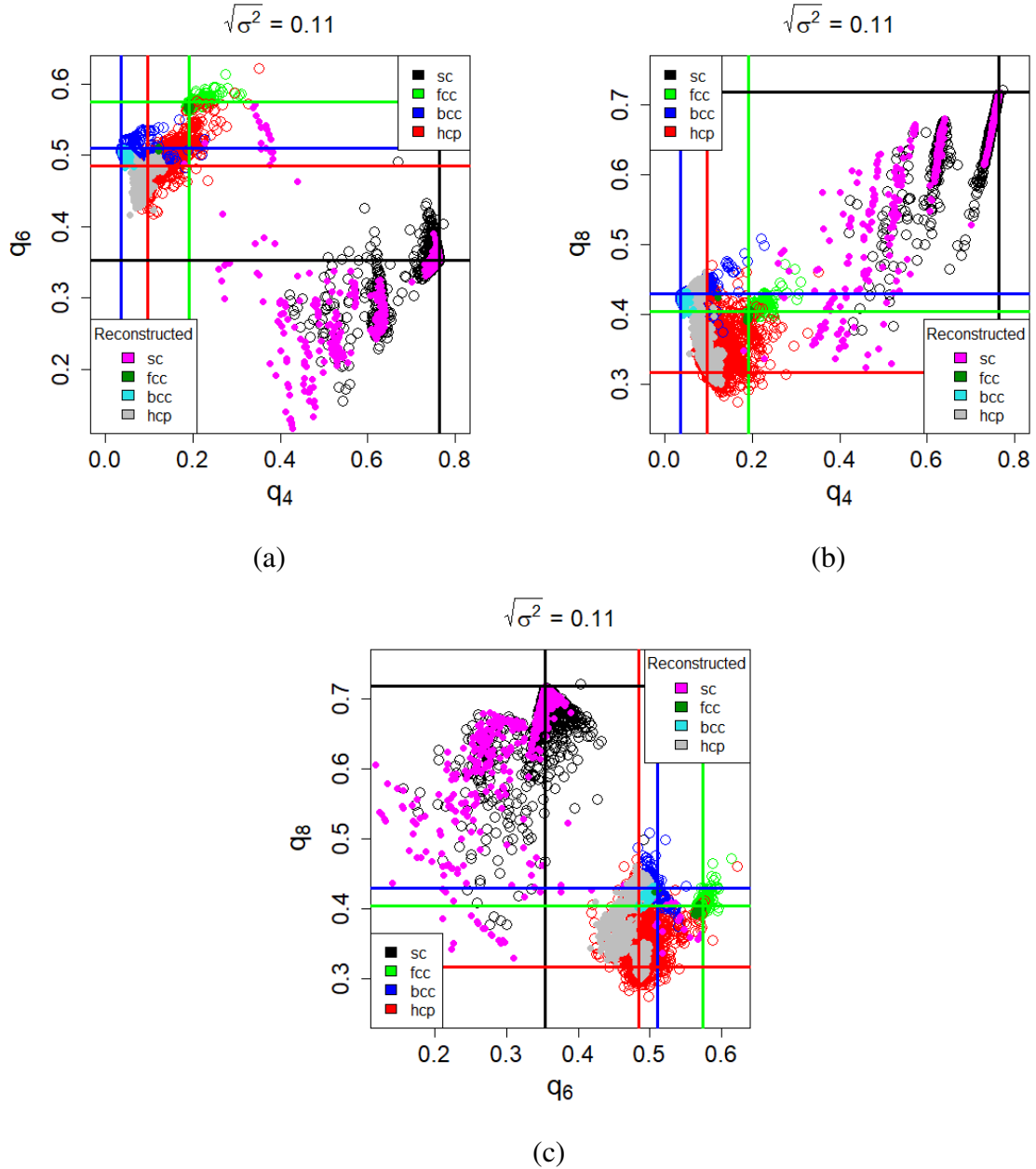


Figure 3.19: LBO parameters for reconstructed test systems.

System analysis

Finally, tests of the studied structures were performed for our THS system without walls $L_x = L_y = 20$, $L_z = 19$. A set of vectors was found for each particle of the system under study, the corresponding function F_1 was determined, after which the lattice was reconstructed to the found set and the Steinhardt parameters were calculated. Since we assume the presence of not only crystal structures in our system, but also an isotropic phase, we will pay attention to the method of selection of isotropic particles. Firstly, it is possible that there is not a single set of vectors for a particle that satisfies the conditions described in the vector search procedure (Step 2). If there is no such set for a particle, then it can be considered non-crystalline. The second

important criterion for particles for which a set of vectors is found is the need to set the critical value of F_1^{cr} , as mentioned above. To determine F_1^{cr} for our system, density distributions of F_1 for different energies were constructed. From the resulting dependency (Fig. 3.20) it can be seen that the minimum of distributions where there are both crystalline and molten components coincides with the intersection point of the high-energy structure ($E = -2040$), where there is lack of crystallites, and the low-energy phase ($E = -5727$) which is almost totally crystalline. We take this point as critical $F_1^{cr} = 22.6$. Thus, the particles of our system for which $F_1 < F_1^{cr}$ are considered as a melt.

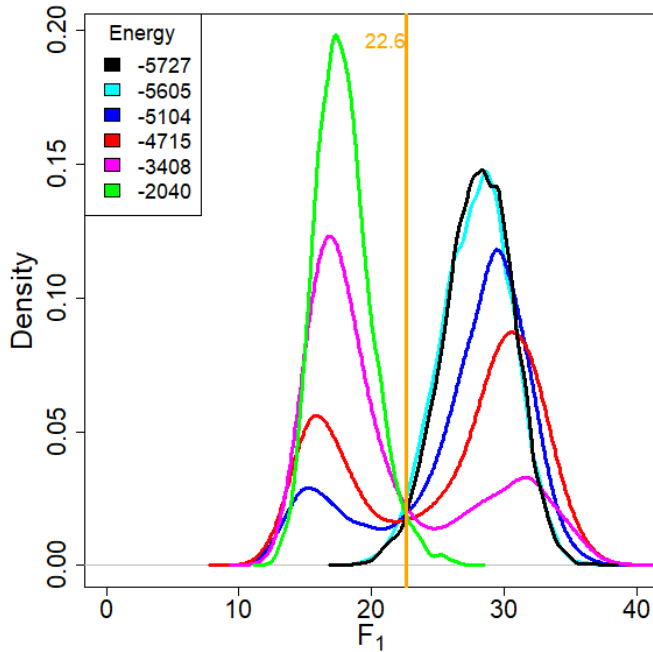


Figure 3.20: Density of F_1 for reconstructed system without walls with $L_x = L_y = 20$, $L_z = 19$. $F_q^{cr} = 22.6$ (orange line) is chosen.

Consider a low-energy box ($E = -5727$). After we have eliminated the melt particles according to the criterion $F_1 < F_1^{cr}$, for the remaining particles we can perform the procedure of separating the particles into two crystal clusters in the space $\{q_4, q_6, q_8\}$, as described in the section 3.5.

In Fig.3.21 the points q_4, q_6, q_8 (LBO) for the reconstructed structures (blue, cyan) are plotted on top of the NRLBO parameters for the original structure (black, red). Vertical and horizontal lines indicate the centers \bar{q}_i of the corresponding clusters (numerical values are defined in Tab.3.6). It is clearly seen that the centers of the new clusters are close to the centers of the "clouds" of the original particles. In addition, it is obvious that clusters of LBO parameters for the reconstructed structures are more compact than clusters of NRLBO parameters for the original system (Fig.3.21). In other words, the spread between the points becomes smaller, and they tend to group more compact. Small and large clusters of the same color differ from each

other mostly in the number of neighbors. In the process of reconstructing structures, the number of particles with 12 neighbors has slightly increased (see the Appendix Fig.A9). The fact that the number of neighbors for the reconstructed structures becomes closer to the expected (perfect) state was also observed in the test structures.

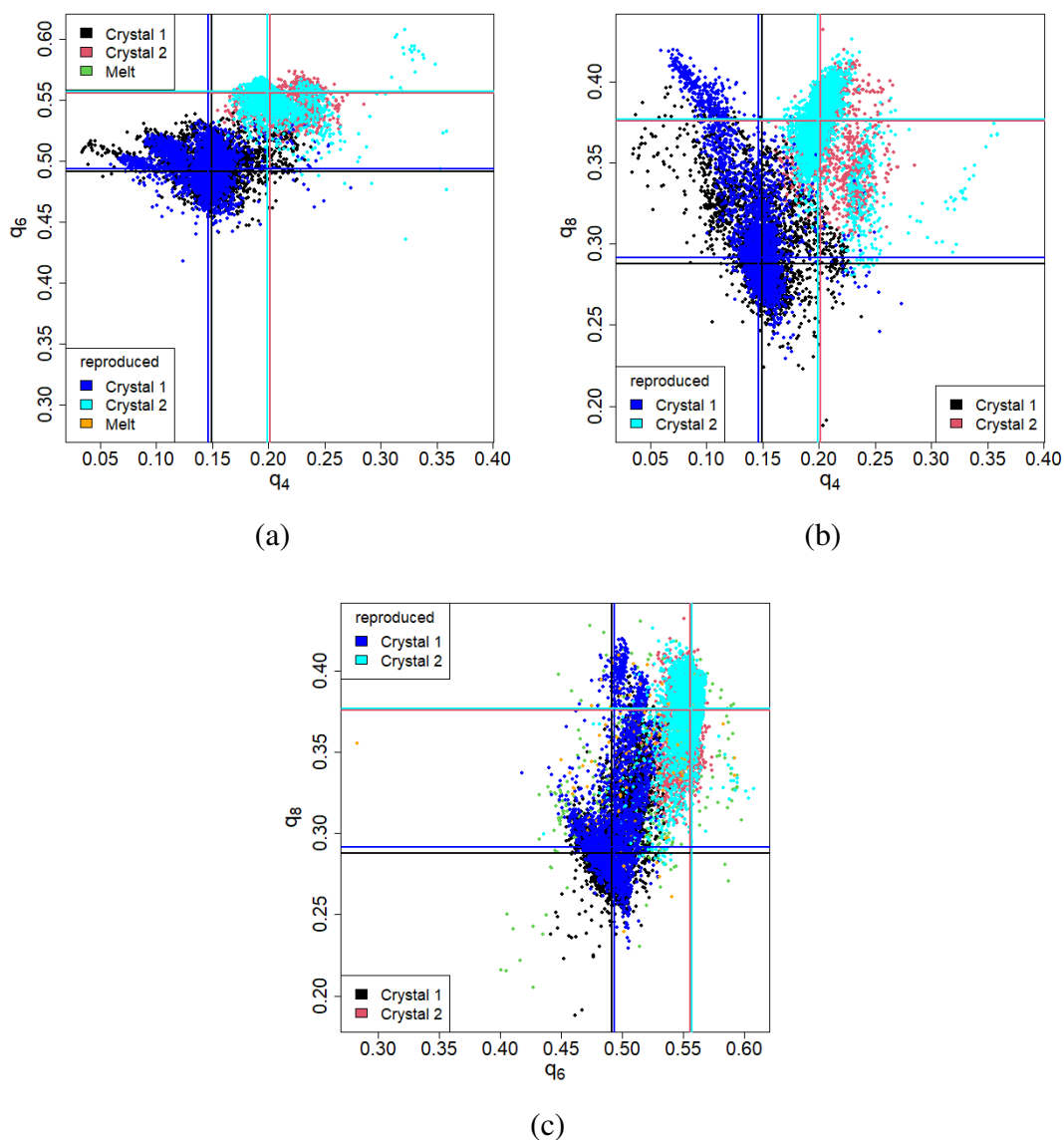


Figure 3.21: LBO parameters for reconstructed system without walls (blue and cyan) cover NRLBO parameters for the system (black and red). $E = -5727$, $L_x = L_y = 20$, $L_z = 19$.

We also discuss the issue of the stability of the assignment of particles to a particular cluster. The number of particles which were initially assigned to *Crystal 1* and then have changed their structural type to *Crystal 2* in the process of restoring structures is equal to 396, and 70 particles have changed their type to *Melt*. From the *Crystal 2*, 242 particles have changed their structural type to *Crystal 1* and 39 to *Melt*. The number of particles that were first defined as a *Melt*, and then were redefined as *Crystal 1* is equal to 135, and 273 particles have changed to *Crystal 2*. Additional analysis showed that in the initial structure, the particles

that have changed their cluster in all cases are located mainly on the periphery of the "clouds" in the space $\{q_4, q_6, q_8\}$ (see the Appendix, Fig.A9, Fig.A10, Fig.A11). This reflects the fact that the separation into clusters in our systems occurs along rather sharp boundaries. Due to the large noise magnitude, points near the border are ambiguously related to one or another cluster and may be redistributed to other clusters as a result of the reconstructing procedure. The results of the reconstructing procedure seem to be slightly more reliable, since the points for these particles are grouped into more compact "clouds" compared to the NRLBO parameter for original points. However, given that the particles on the periphery of the clusters are subject to cluster changes, in order to reconstruct crystals in the most reliable way, the value should be taken as close as possible to the centers of the clusters (Tab.3.6).

| | color | \bar{q}_4 | \bar{q}_6 | \bar{q}_8 |
|-------------------------|-------|-------------------|-------------------|-------------------|
| Crystal 1 original | black | 0.151 ± 0.036 | 0.504 ± 0.018 | 0.300 ± 0.038 |
| Crystal 1 reconstructed | blue | 0.146 ± 0.024 | 0.493 ± 0.015 | 0.292 ± 0.040 |
| Crystal 2 original | red | 0.211 ± 0.047 | 0.552 ± 0.019 | 0.360 ± 0.031 |
| Crystal 2 reconstructed | cyan | 0.199 ± 0.018 | 0.557 ± 0.012 | 0.377 ± 0.019 |

Table 3.6: Centers of clusters $\bar{q}_4, \bar{q}_6, \bar{q}_8$ found in the $\{q_4, q_6, q_8\}$ space in the system without walls, $L_x = L_y = 20, L_z = 19$. We use NRLBO for original system and LBO for reconstructed system.

The analysis of particles in coordination space also showed that "unstable" particles (particles that have somehow changed their cluster) are located in areas with ambiguous phase definitions (see the Appendix, Table A6). For example, if in the original system a green particle was surrounded by black ones, it will most likely become black itself. Similarly, in systems where a crystal and a melt coexist, points at the boundary will more likely change their structure type compared to particles in the middle of a particular structure (crystal or melt). The results of this chapter will be published in [F3].

3.7 Other methods

3.7.1 Static structure factor

Another way to verify the developed method is to calculate the static structure factor (or structure factor for short). The main advantage of this parameter is that in addition to the theoretical calculation given in this chapter, it can be obtained from experimental data by scattering techniques [157]. Determination of the static structure factor is achieved without determining the energy associated with scattered photons, electrons, or neutrons. Conversely, energy-resolved measurements offer insights into the dynamic structure factor. Since for the

conformation considered in the previous chapters (the system without walls $L_x = L_y = 20$, $L_z = 19$) the chains are stretched parallel to the plane XY , we calculate the two-dimensional structural factor as

$$S(\mathbf{q}) = \frac{1}{N} \sum_{\mathbf{r}} \exp\{i 2\pi (\mathbf{q} \cdot \mathbf{r})\}, \quad (3.35)$$

where $\mathbf{q} = q_y \mathbf{e}_2 + q_z \mathbf{e}_3$ is a wave vector in which the components q_y and q_z change from 0 to 2.6 in increments of 0.04. A two-dimensional structural factor is computed for each plane parallel to the z axis, covering a complete range of 2π with increments of 0.01 radians (ϕ). Thus, \mathbf{r} is the position of particles in the system, where their simulation coordinates $\{x, y, z\}$ are recalculated as $\mathbf{r} = y' \mathbf{e}_2 + z' \mathbf{e}_3$, where $z' = z$, $y' = x \sin \phi + y \cos \phi$, $x' = -x \cos \phi + y \sin \phi$, \mathbf{e}_3 is the unit vector directed along the z axis, and \mathbf{e}_1 is the unit vector of the normal to the plane for which the structural factor is calculated, $\mathbf{e}_2 = [\mathbf{e}_3 \times \mathbf{e}_1]$. Following the calculation of the structural factor for each of the 629 planes, an averaging process is undertaken over all rotation.

The observed image (Fig.3.22 (a)) reveals distinct peaks alongside numerous indistinct spots, posing challenges in accurate localization. Interpretation becomes difficult due to the significant influence of noise, as discussed in previous sections. In addition, the system demonstrates the coexistence of two types of crystals, which complicates the analysis. Consequently, signals undergo increased blurring.

To assess how well the reconstructed structures describe the original system, two particles were chosen from those designated to *Crystal 1* and *Crystal 2*, based on minimal squares of deviations of q_4, q_6, q_8 from the centers of their respective clusters following the noise reducing procedure. Subsequently, the vectors $\{\mathbf{a}, \mathbf{b}, \mathbf{c}, \mathbf{h}\}$ determined for these two particles were found in accordance with the methodology outlined in section 3.6. Then, the structures were reconstructed these vector within boxes of the size $L_x = L_y = 20$, $L_z = 19$, and two-dimensional structural factors were computed and averaged over all rotation. The images depicting these reconstructed "perfect" structures are presented in the Appendix (Fig.A12).

The structural factor for these particles exhibits enhanced clarity compared to the images of the system under investigation. However, it does not manifest as delta functions, akin to the scenario observed in ideal crystals. This phenomenon arises due to the finite size of the system. The finite size of the system additionally contributes to the blurring of system's peaks. Given that signal intensity diminishes with distance from the picture's center, a detailed localization of peaks in the acquired images of reconstructed structures necessitated an analysis of the structural factor's magnitude through concentric rings. To implement this procedure, a ring with a radius of r_q and a thickness of dq is considered. The maximum value of $S(\mathbf{q})$ within the ring is identified, and subsequently, at points where $S(\mathbf{q}) < w_1 \cdot \max S(\mathbf{q})$, the value of $S(\mathbf{q})$ is set to zero. Here, w_1 is a predetermined parameter within the range (0, 1). Consequently, we can say that an additional enhancement in image contrast is achieved through this process. Following this procedure, peak identification becomes more straightforward.

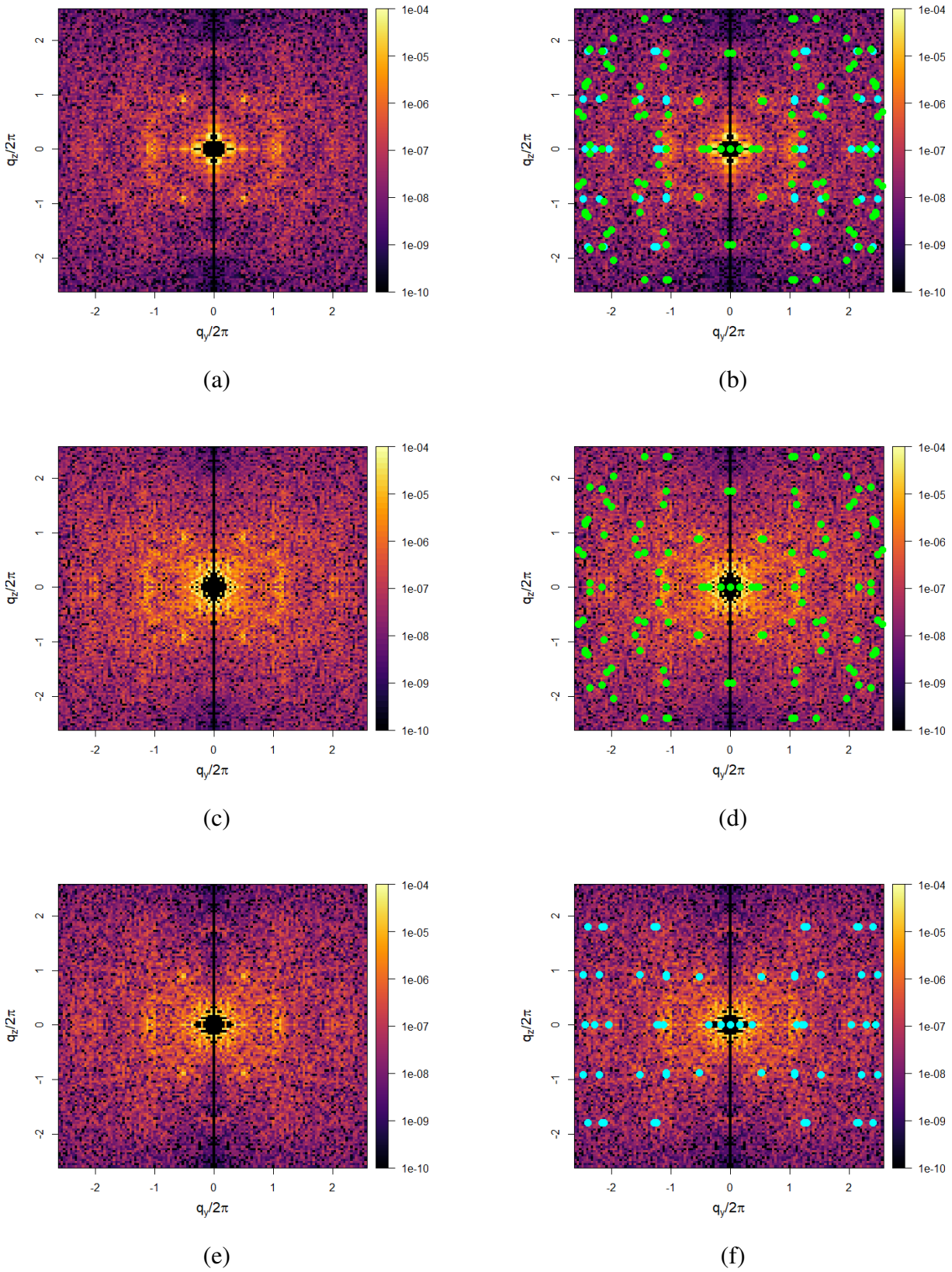


Figure 3.22: Two-dimensional structure factor for system without walls, $E = -5727$, $L_x = L_y = 20$, $L_z = 19$: for the whole system (a); for the particles from *Crystal 1* (c); for the particles from *Crystal 2* (e); the same structures as (a), (c), (e) with peaks from reconstructed *Crystal 1* (green) and *Crystal 2* (cyan) (b), (d), (f).

As a verification step, two-dimensional structure factors are separately calculated by considering particles from only *Crystal 1* and only *Crystal 2* (Fig. 3.22 (c),(e)). To validate the method, the peaks defined for the reconstructed structures were applied to these images (Fig. 3.22(b), (d), (f)). Despite the fact that only a few peaks are clearly visible in the original paintings of the two-dimensional structural factor, the points based on reconstructed structures are close to matching with the prominent features in the images of the two-dimensional structural factor for the investigated systems.

Remark. It is crucial to highlight that the aforementioned method encounters several challenges, preventing its reliable utilization as a tool for validating the accuracy of the vector search method.

1. A pronounced noise structure is still present. Despite careful selection of particles to reconstruct the structure, including checking the NRLBO and LBO parameters and taking into account the numbers of neighbors for both the original particles (with and without noise reduction) and for the reconstructed structures, the two-dimensional structure factor is calculated for the original system in which the structures remain undetected without resorting to additional noise reduction methods.
2. The finite (and exceedingly small) size of the system.
3. The presence of a crystal mixture.
4. Potentially different domain orientations within the structure are not adequately taken into account.
5. Despite the partially analytical approach employed for structural factor analysis (peak search), the task involves numerous parameters that necessitate subjective adjustment, such as the ring consideration step, ring thickness dq , and the parameter w_1 .

In general, the structural factor, despite its limitations, retains utility as an analysis tool. The challenges outlined argue for caution in relying solely on this method, however it still serves as a valuable tool for visualizing structures and establishing connections between theory and experiment. Through this parameter, it becomes possible, in principle, to collect information about the suggested structures in the sample (as reconstructed *Crystal 1* and *Crystal 2*) and facilitate comparisons with experimental observations.

3.7.2 Common neighbor analysis

One of the most common methods of studying structures is the *Common Neighbor Analysis (CNA)* [105, 106]. This method of structural analysis, utilizing more complex high-dimensional signatures to characterize the arrangement of atoms, typically better distinguishes multiple structures. In contrast to *Centrosymmetry Parameter (CSP)* [108, 158] and local bond

order parameters [102], *CNA* does not directly account for spatial vectors pointing from the central atom to its neighbors. Instead, the characteristic signature is computed based on the topology of bonds connecting adjacent atoms. Typically, in this context two atoms are referred to as neighbors or bonded atoms if they are within a specified cutoff distance from each other.

The original method analyzes pairs of atoms (the so-called *root pairs*) [105]. Their nearest neighbors and the connections between them are also considered in the *set*. The nomenclature for describing root pair is introduced as follows. Each *set* is characterized by a sequence of four integers. The first integer, either 1 or 2, designates the "type" of the root pair, indicating whether the atoms comprising the root pair are nearest neighbors or not. The second integer denotes the count of nearest neighbors shared by the root pair. The third integer signifies the number of connections between common neighbors. While these three numbers are insufficient for a unique characterization of the *set*, a fourth integer is introduced. Its value is arbitrary, provided it is used sequentially to ensure a distinct correlation between the numbers and the *sets*. Then the ratios with which the resulting combinations are included in the cluster are considered.

A slightly more simplified scheme of this analysis is given in the work of A. Stukowski [107]. In the same article, a variation of this method is proposed, the so-called *Adaptive Common Neighbor Analysis* (*a-CNA*). Another variation of the *CNA* method was proposed by P. M. Larsen in 2020 [108]. This modification is known as *Interval Common Neighbor Analysis* (*i-CNA*). Both modifications of *a-CNA* and *i-CNA*, unlike the conventional *CNA*, do not require a predetermined cutoff distance to choose neighboring particles.

To implement all these methods, we used the OVITO package. At the first stage, we tested the methods on test structures (perfect and with a noise of 0.11 *fcc*, *bcc*, *hcp*, *sc*). In perfect, noiseless structures, all particles were identified, far from the boundaries of the cube (exactly those that are used for tests in subsequent sections). All modifications of the *CNA* method for perfect structures give the same result, which indicates the validity of these methods for systems without deformations and imperfections, and also opens up opportunities for analyzing systems with small distortions. The cutoff distance in the classic *CNA* in a fairly wide range does not change the results. At the same time, for highly noisy systems, changing this distance by 0.01 significantly changes the result. The Tab.3.7 shows the results of the *CNA* method for the cutoff distance with the best particle recognition (when the number of particles not assigned to any structure is minimal). Changing the cutoff distance shown in the table in the case of noisy structures by 0.05 may make all particles in the system unrecognizable.

It can be seen from these results that in the presence of such noise in the system, the use of any of the variations of the *CNA* method does not seem reliable in the framework of our task.

| Technics | Found type | Structure under study | | | | | | | |
|----------------|------------------|-----------------------|-------|------------|-------|------------|------|-------------|-------|
| | | <i>fcc</i> | | <i>hcp</i> | | <i>bcc</i> | | <i>bulk</i> | |
| | | noise | | noise | | noise | | Energy | |
| | | 0 | 0.11 | 0 | 0.11 | 0 | 0.11 | -2040 | -5727 |
| <i>CNA</i> | Cutoff distance | 1.1-1.4 | 1.24 | 1.1-1.4 | 1.23 | 1.2-1.59 | 1.39 | 1.1-1.59 | 1.38 |
| | <i>fcc</i> | 9838 | 333 | 0 | 0 | 0 | 0 | 0 | 161 |
| | <i>hcp</i> | 0 | 0 | 8892 | 445 | 0 | 0 | 0 | 141 |
| | <i>bcc</i> | 0 | 0 | 0 | 0 | 7471 | 801 | 0 | 1 |
| | <i>undefined</i> | 2351 | 11856 | 2862 | 11309 | 3268 | 9938 | 7200 | 6897 |
| <i>a – CNA</i> | <i>fcc</i> | 9803 | 512 | 0 | 0 | 0 | 3 | 0 | 273 |
| | <i>hcp</i> | 0 | 0 | 8892 | 595 | 0 | 17 | 0 | 243 |
| | <i>bcc</i> | 0 | 5 | 0 | 16 | 7471 | 1124 | 0 | 88 |
| | <i>undefined</i> | 2351 | 11667 | 2862 | 11143 | 3268 | 9595 | 7200 | 6595 |
| <i>i – CNA</i> | <i>fcc</i> | 9838 | 1131 | 0 | 0 | 0 | 3 | 0 | 530 |
| | <i>hcp</i> | 0 | 0 | 8892 | 1248 | 0 | 36 | 0 | 487 |
| | <i>bcc</i> | 0 | 14 | 0 | 35 | 7471 | 3043 | 0 | 221 |
| | <i>undefined</i> | 2351 | 11045 | 2862 | 10471 | 3268 | 8657 | 7200 | 5862 |

Table 3.7: Number of particles detected with *CNA*, *a – CNA*, *i – CNA* in the perfect systems *fcc*, *hcp*, *bcc*, in the *fcc*, *hcp*, *bcc* with introduced noise 0.11, and for the small systems without walls ($L_x = L_y = 20$, $L_z = 19$) with energies $E = -2040$ and $E = -5727$

3.7.3 Voronoi cell analysis

The problem of choosing neighbors has several solutions. In our work, we prefer the use of a sphere with a fixed cut-off radius due to the simplicity of the implementation of this method, as well as versatility. However, it is impossible to ignore another popular method - the construction of Voronoi cells.

All research related to Voronoi cell calculations was carried out using the open source Voronoi++ package [109]. The Voronoi cell analysis of test structures (*fcc*, *hcp*, *bcc*, *sc*), as the analysis of all modifications of Steinhardt parameters, involved only particles located far enough from the boundaries of the cube to avoid a shortage of neighbors at the edges. A simple check of the number of neighbors for Voronoi cells for test noiseless structures, unambiguously gave the expected result: *sc* has 6 neighbors, *bcc* - 14, *fcc* and *hcp* - 12 neighbors.

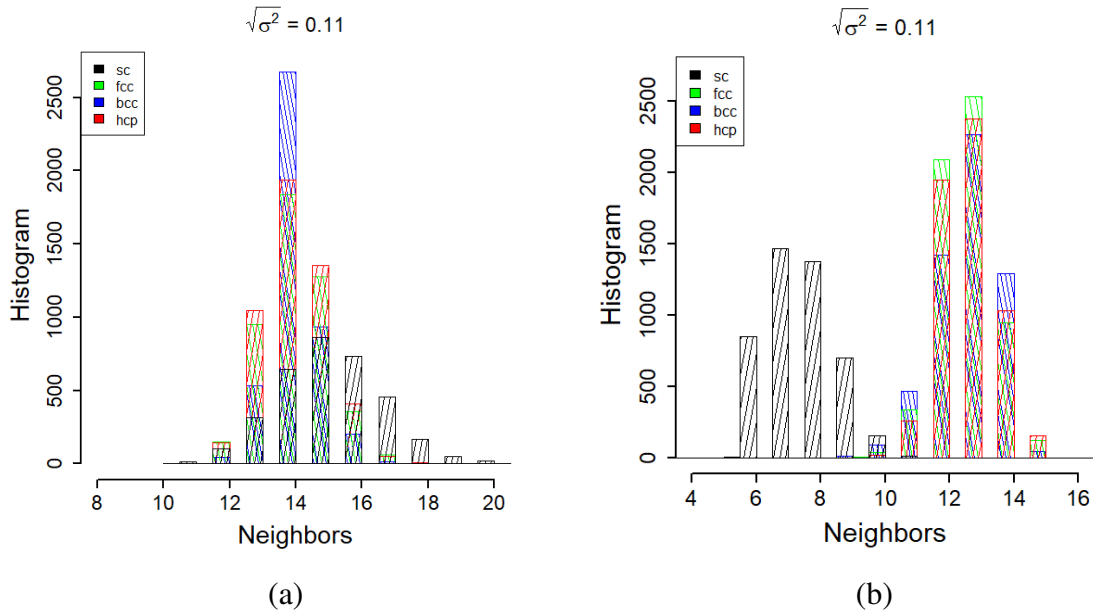


Figure 3.23: Histograms of the number of neighbors for noisy test structures (*fcc*, *bcc*, *hcp*, *sc*), calculated using Voronoi cells (a), and the number of neighbors in a sphere with a cut-off radius $R_c = 1.3$ (b).

However, when analyzing test structures with noise $\sigma = 0.11$ (Fig.3.23 (a)) it turned out that the maximum distribution of the numbers of neighbors for *fcc*, *hcp* is shifted relative to the unperturbed state towards more neighbors (from 12 to 14 neighbors). The distribution of the structure's neighbors becomes very wide and the structures become completely indistinguishable even for *sc*. The distribution for *sc* became very wide with a distribution maximum at 15 neighbors, while particles with the correct number of neighbors for this structure (6 neighbors) were not detected at all. Thus, the distributions of systems with high noise by the number of neighbors of Voronoi cells in their original form become completely indistinguishable. Using a fixed cut-off radius, even without an additional averaging procedure, leads to a smaller deviation from the undisturbed values (although such a deviation also does not allow for a reliable analysis) (Fig.3.23(b)).

Therefore, using the number of neighbors obtained directly from Voronoi cells does not seem to be the optimal method for our problem. One way to optimize could be to ignore too small edges and, accordingly, faces. This way of calculations leads to a decrease in the number of neighbors (our results especially for *sc* confirm that the number of neighbors calculated by this method is indeed an overestimate). At the same time, only the correct number of neighbors does not guarantee a reducing in the effective noise in the system, facilitating further analysis. Although this method opens up wide scope for improvement and application to scientific purposes, we do not contribute into modifications that improve the method of constructing Voronoi cells, since the methodology we proposed in section 3.5 is more simple and solves the problems.

Another practically important quantity that Voronoi cell analysis allows us to extract is the volume of this cell. The inverse volume of a Voronoi cell can be interpreted as the local

density (Fig. 3.24).

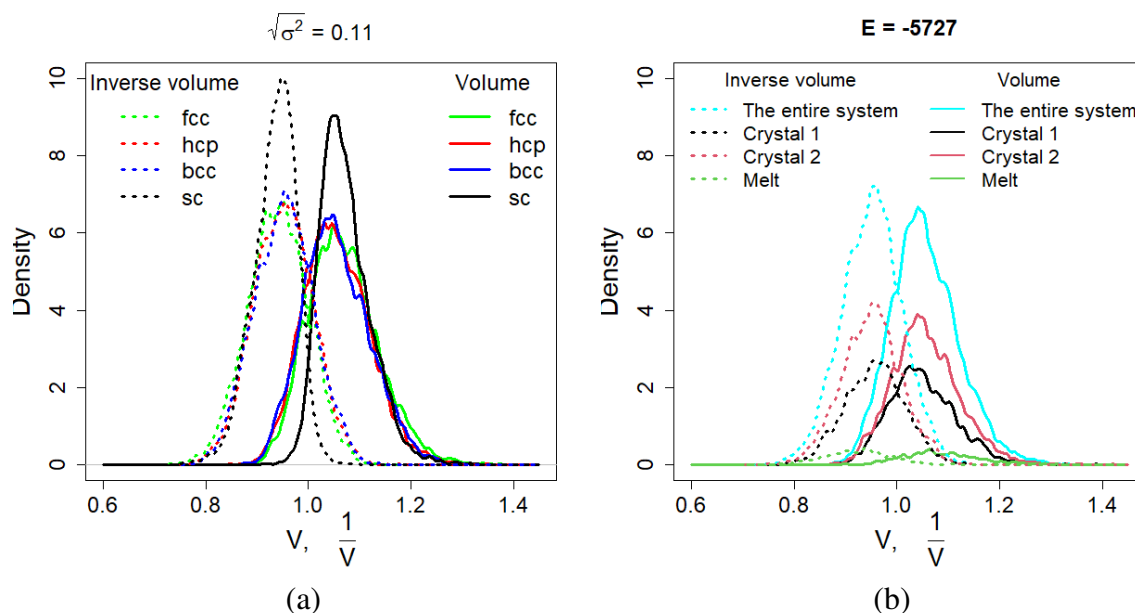


Figure 3.24: Distributions of volumes of Voronoi cells (solid lines) and inverse volumes of Voronoi cells (dashed lines) for test structures (*fcc*, *bcc*, *hcp*, *sc*) (a) and for the system without walls ($L_x = L_y = 20$, $L_z = 19$) with energy $E = -5727$ (b). Voronoi cell volume is normalized to the third power of the smallest possible distance between particles.

It should be noted here that when constructing test structures, we required the same volume fraction as in the observed system. This is manifested in the fact that the maximum of the local density distribution (the inverse volume of Voronoi cells) is approximately the same for all structures (~ 0.95). Naturally, the Voronoi cells volumes themselves are similarly equal (~ 1.05).

At the same time, the local densities can be used to study the local densities profiles of systems. Fig.3.25(a) shows local density profiles for a system without walls for selected energies. Note that although the density profiles in these systems are calculated along the z direction, there is no physical reason for highlighting this direction in systems without walls. The choice of axis is determined by the choice of specific conformations. The resulting profiles were calculated for particles in layers of thickness 1 with a step of 0.2. Comparison of these profiles with a visual representation of conformations from the Tab.3.3 allows us to say that local densities correctly describe features of the systems. In high energy system where mostly melt is observed ($E = -2040$), and low energy system with mainly crystallized polymer ($E = -5727$), we see that the local density fluctuates around one average value (~ 0.95). At the same time, in systems with intermediate energies ($E = \{-5104, -4715, -3804\}$), conformations where both melt and crystal are observed. It is clearly seen that the crystalline region has a more dense structure, while the isotropic part of the system has lower density. However, the average density in the system, of course, remains constant.

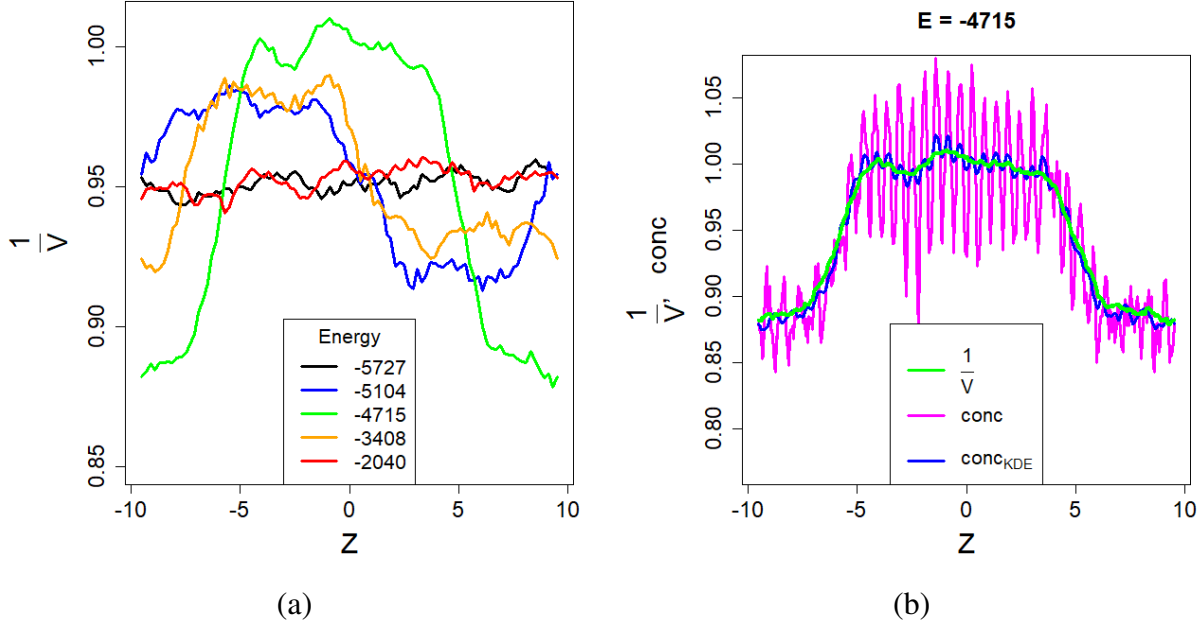


Figure 3.25: Local density profile in z direction for the system without walls ($L_x = L_y = 20$, $L_z = 19$) (a); local density profile in z direction for the system without walls ($L_x = L_y = 20$, $L_z = 19$) with energy $E = -4715$ (green line), the concentration profile in z direction (magenta line), and the concentration profile in z direction calculated using averaging using the Epanechnikov kernel (blue line) (b). Voronoi cell volume is normalized to the third power of the smallest possible distance between particles, the increment along z axis equals 0.2 for all profiles.

As an alternative way to estimate the local density of structure, one can calculate the particle concentration $conc$ in the layer: the number of particles in a layer of thickness 1 per unit area Fig.3.25(b). As an example, consider the configuration of a system without walls, where both crystalline and molten regions are observed ($L_x = L_y = 20$, $L_z = 19$, $E = -4715$). Since the calculation of inverse Voronoi cell volume profiles actually averages the density value in the layer, the curve is quite smooth (the green line in Fig.3.25 (b)). For comparison, concentrations, calculated with steps of 0.2 (the magenta line) is presented. Despite strong fluctuations, the concentration profile behaves similarly to the inverse volume profile of Voronoi cells. Therefore, there is no fundamental difference in the use of these parameters. It is often convenient for analysis to use smoothed data that does not have strong fluctuations. Fluctuations can be reduced, for example, by averaging the function values at neighboring points, increasing the layer thickness or the calculation step. As a more advanced smoothing method, a *kernel density estimation* (*KDE*) [159, 160] can be used. As an example, a *KDE* with the Epanechnikov kernel [161] is used:

$$conc_{KDE}(z) = \frac{1}{NNc \cdot h} \sum_i^{NNc} K\left(\frac{z - z_i}{h}\right); \quad (3.36)$$

$$K(u) = K^{Ep}(u) = \frac{3}{4} \max(1 - u^2, 0), \quad (3.37)$$

where $h = 1$, and z changes with the increment 0.2.

As we can see, this method makes it possible to smooth out the concentration curve, preserving information about the structure. In the analysis of various parameters (orientation order parameter, Steinhardt parameters, concentrations), we give preference to kernel density estimation of profiles with the Epanechnikov kernel, since tuning the parameters of this method allows us to obtain results with the desired degree of detailing.

Despite the efficiency of using the inverse volume of the Voronoi cell, preference in the work is given to the concentration of particles. This choice was made for several reasons:

1. Simplicity and speed of calculation.
2. For a system with walls, the volume of Voronoi cells has a non-obvious interpretation near the walls.
3. Avoidance of excessive smoothing. Tuning the *KDE* parameters allows for controlled smoothing.

Remark. Let us recall that here we are discussing the structure of specifically selected conformations. Here we are not talking about the stability of the structures found. Since here we are discussing the bulk system, due to the absence of a dedicated direction for averaging density profiles over all conformations with a given energy, averaged density profiles do not provide information about the system. Physical analysis of systems can be found in the chapter 4.

3.7.4 The local alignment of chain segments analysis

To distinguish particles in a crystal-melt system, a method that actually describes the local alignment of chain segments is often used. Despite the fact that this parameter describes a local nematic ordering, in a number of works this method is used to determine crystallites in a system [40, 48]. In our work, this method also showed good correlation with the results of the NRLBO method which we have proposed.

The procedure described below is part of the two-step approach used in the work of P.Kos et al. [48]

Let us consider the bond \mathbf{v}_i connecting successive beads i and $i + 1$ of a chain. We take the coordinates of the bond center as the position of the bond. We examine whether the bond is "aligned" or not. If the bond is "aligned", then we consider both monomers belonging to this bond to be crystalline. To analyze bonds we use the following algorithm.

1. We draw a sphere of radius $R_{al} = 2.4$ around the center of the bond \mathbf{v}_i and determine the bonds that fall inside this sphere. Let us consider such bonds as neighboring ones. The reasonable choice of radius R_{al} is determined by the position of the second minimum on the radial distribution function (Fig.3.6). The radius chosen in the work [48] also

approximately falls on the second minimum of the distribution given in the supplementary materials to the article [48].

2. Among all these neighboring bonds, we define those that are collinear with the original bond \mathbf{v}_i : if the angle θ_{ij} between the bond \mathbf{v}_i and its neighboring bond \mathbf{v}_j is less than $\theta_{cr} = 15^\circ$, then we consider the bond \mathbf{v}_j as collinear one.
3. We calculate the ratio of the number of collinear vectors to the total number of neighboring bonds. If this ratio is greater than 0.4, then the bond \mathbf{v}_i is considered to be "aligned".

To test the effectiveness of this method, we compared this analysis with the results obtained for a system without walls by NRLBO parameters (Tab.3.8). From the resulting table it is clear that these two fundamentally different methods not only select approximately the same number of particles, but the choice of these particles is also highly correlated.

| E | N_{al} | N_{cr} | N_{both} |
|-------|----------|----------|------------|
| -5727 | 6810 | 6873 | 6509 |
| -5605 | 6752 | 6778 | 6362 |
| -5104 | 5664 | 5732 | 5368 |
| -4715 | 4555 | 4747 | 4315 |
| -3408 | 1936 | 2232 | 1731 |
| -2040 | 48 | 440 | 3 |

Table 3.8: Number of particles defined as "aligned" N_{al} ; number of particles defined as crystal (*Crystal 1* or *Crystal 2*) using Steinhardt parameters after averaging procedure N_{cr} ; number of particles defined as both "aligned" and crystalline N_{both} in the systems without walls ($L_x = L_y = 20, L_z = 19$).

For clarity, Fig.3.26 illustrates several systems described in the Tab.3.3. However, here the need for an integrated approach should be noted, since this parameter selects particles that not only can claim to be classified as crystalline, but also have *only* nematic ordering. The chosen critical angle is of great importance in this matter. Since in our model the stiffness potential is determined by the characteristic angle $\theta_s = 26^\circ$, the condition for the critical angle of this method $\theta_{cr} = 15^\circ$ is quite strict. This fact, combined with a good correlation of the results with the analysis of Steinhardt parameters (Tab.3.8), allows us to use local alignment of segments of chains as a base for cluster analysis of systems.

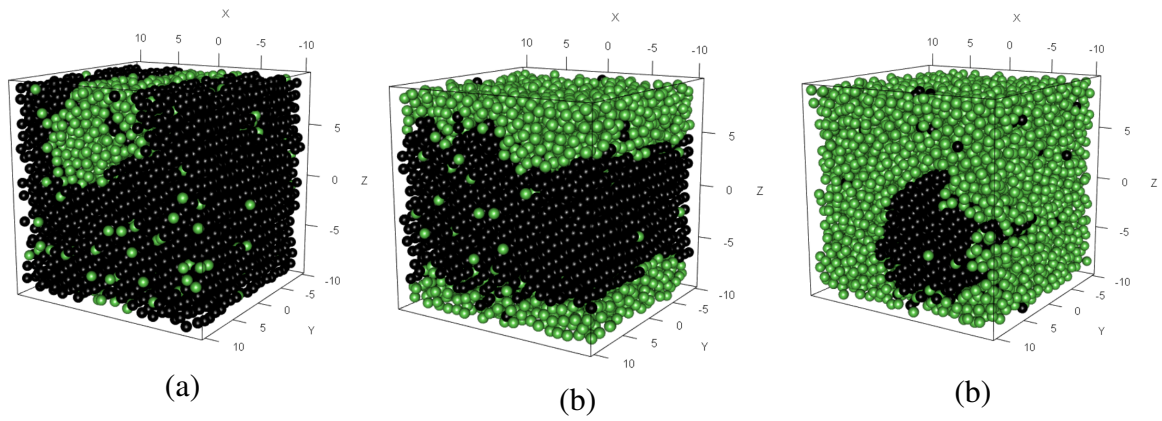


Figure 3.26: 3d view of the systems without walls $L_x = L_y = 20$, $L_z = 19$ with $E = -5104$ (a), $E = -4715$ (b), $E = -3408$ (c); black particles are defined as "aligned", and green particles are not "aligned". Green particles can be considered as molten ones.

Chapter 4

Phase transitions: discussion of results

The chapter has the following structure.

- 4.1 Thermodynamic properties. The section describes the results obtained from the accumulation stage of the density of states function $g(E)$, followed by a discussion of the reliability of these results. Here, the thermodynamic properties of all systems are discussed.
- 4.2 Structural analysis of systems. We consistently study structural (morphological) features of systems discovered during thermodynamic analysis, relying on parameters describing the geometric characteristics of the structures. We begin by considering the peculiarities of the behavior of systems near the attractive wall (systems U_{at_1}, U_{at_2} , section 4.2.1). Then we analyze the phase transition region for the bulk system and for system with repulsive walls, arguing that the observed first order phase transition is an isotropic melt-crystal transition (section 4.2.2). A more detailed analysis in the first-order transition region is given, identifying intermediate unstable structures (section 4.2.3). The section ends with a discussion of the possibility of the phenomenon of prefreezing in systems with walls (section 4.2.4). For this purpose, an example of repulsive walls and a system with weak attraction (U_{at_1}) is used.
- 4.3 Transition analysis findings and predictive insights for various systems: a comprehensive summary. Here we summarize the results of the analysis and make assumptions about systems that have not yet achieved sufficient convergence of the density of state function $g(E)$.

4.1 Thermodynamic properties

First of all, it is necessary to pay attention to the following important points.

- The analysis performed in this study is based on the configuration (potential) energy U . As demonstrated in the work of T. Shakirov et al. [143] the inclusion of kinetic

components is potentially feasible using the equation:

$$g(E) \propto \sum_U (E - U)^{f/2-1} g(U) \Theta(E - U), \quad (4.1)$$

where $E = U + K$ is the full energy with kinetic energy K , f is the number of degrees of freedom of the system, and Θ designates the Heaviside step function. However, accounting for kinetic energy K within our model is a challenge due to the fixed bond length imposing significant constraints on particle velocities. Such calculations are nontrivial and require taking into account massive transition matrices, and remain beyond the scope of this study. Thus, everywhere below the symbol E stands for potential energy. Therefore, all calculated values in this study actually reflect configuration properties. Although this approach may seem insufficient, it has value because it clarifies the complex relationship between system configuration and its parameters.

- Since our work examines systems of finite, small size, we can only talk about *pseudo-phase transitions*. However, for brevity, we will use *phase transition* terminology.
- The phase transitions observed in our systems are mainly energetically driven (that is, determined by the potentials used), however entropy effects also affect the observed process.
- The manuscript describes the regions into which the function $\ln g$ has (or has *not*) achieved sufficient convergence. We consider a region to be sufficiently converged if the values of the energy derivative of the function $\ln g$ stop changing with time. The control time periods are 14 days of calculations.

The main result of the SAMC simulation is the accumulated state density function $g(E)$ as accurately as possible. In microcanonical thermodynamics, the logarithm of this quantity is directly related to the entropy $S(E)$ through the following relation:

$$S(E) = k_B \ln g(E). \quad (4.2)$$

The Boltzmann constant, conventionally denoted as k_B , is assumed to be unity ($k_B = 1$) throughout this study.

The obtained dependencies are illustrated in Fig.4.1, as well as an additional density of state function $g(E)$ for a system without walls ($L_x = L_y = L_z = 20$, black curve in Fig.4.1 (a)), provided by T. Shakirov for comparative analysis. The analysis of this system was documented in the research conducted by T. Shakirov and W. Paul [97].

Note that Fig.4.1 shows the logarithm of density of states function. The maximum of the function $\ln g$ is shifted to zero. For small systems (size of $L_x = L_y = L_z = 20$ and $L_x = L_y = 20, L_z = 19$, Fig. 4.1 (a), (c)) the range of the function $\ln g$ changes is about 12000

4.1. Thermodynamic properties

($\Delta \ln g \sim 12000$). Let us recall that density of states function $g(E)$ itself represents the number of microstates that realize a macrostate with a given energy E . Consequently, a macrostate with high energies (at maximum $\ln g$) can be realized in e^{12000} by more number of microstates than macrostates with low energy (at minimum $\ln g$). For systems twice the size, this difference is approximately 2 times larger (Fig. 4.1 (b)).

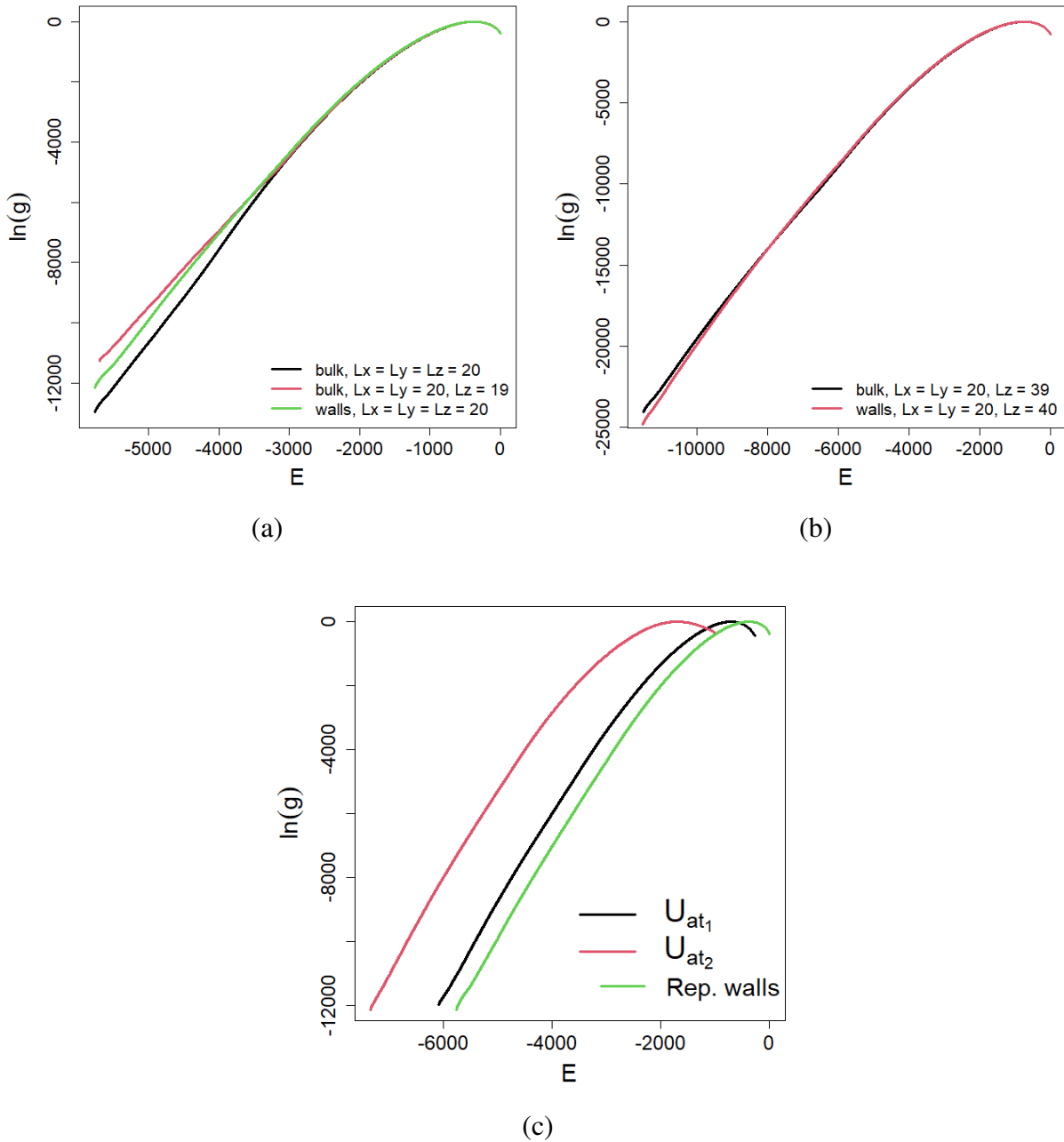


Figure 4.1: Configurational entropy given by Eq.(4.2): (a) bulk (black) and system with repulsive walls (green) with $L_x = L_y = L_z = 20$, and bulk (red) with $L_x = L_y = 20, L_z = 19$; (b) system with repulsive walls (red) with $L_x = L_y = 20, L_z = 40$, and bulk (black) with $L_x = L_y = 20, L_z = 39$; (c) systems with attractive wall U_{at1} (black), U_{at2} (red) and with repulsive walls (green) with $L_x = L_y = L_z = 20$

Fig.4.1 (c) shows dependencies for systems with the size $L_x = L_y = L_z = 20$ with dif-

ferent walls (U_{at_1} (black), U_{at_2} (red), repulsive walls (green)). From these dependencies it is clearly seen that the range of energies visited by the system in systems with an attractive wall is shifted to the left relative to a system with two repulsive walls. This is due to the fact that there are always about 400 particles in the layer near the attractive wall. Therefore, the function $\ln g$ for a system with a weak wall attraction potential (U_{at_1}) is shifted by about 400 energy units to the left, and a system with a strong attraction potential (U_{at_2}) is shifted by about 1600 energy units to the left relative to a system with repulsive walls.

Thus, despite the fact that the density (volume fraction, ϕ) of these systems theoretically allows us to achieve states with energy $E = 0$ (disordered states where there is not a single particle near the attractive wall), in practice we have not achieved such states, since they are entropically unfavorable. For all systems without an attractive wall (Fig.4.1 (a), (b)), the entire range of available energies is visited.

Although it is possible to renormalize functions for large systems (Fig.4.1 (b)) to match the energy range of small systems (Fig.4.1 (a)), and the logarithm of the density of states function holds a clear physical interpretation (Eq.(4.2)), analyzing and comparing the behavior of systems using the dependencies depicted in Fig.4.1 proves challenging. Much more information can be gained from the first derivative of entropy with respect to energy, which gives the inverse temperature:

$$T(E) = \left(\frac{\partial S}{\partial E} \right)^{-1}. \quad (4.3)$$

Fig.4.2 shows the dependence of the inverse temperature on energy. Despite the extensive calculation time (about 3 years), satisfactory convergence is only achieved in small systems without walls (black and red curves in Fig.4.2 (a)). In the study [97], the authors demonstrate that the observed first-order transition is an isotropic melt – crystal transition. The paper also predicts that an increase in density contributes to crystallization within this model. In the following parts of this chapter, we will provide a justification for the fact that the phase transition observed in our work (bulk system, red curve in Fig.4.2 (a)) is also an isotropic melt – crystal transition, which correlates with the prediction [97].

The inset in Fig.4.2 (a) shows a schematic view of a single first-order phase transition. The shape of the inverse temperature curves for studied systems shown in main part of Fig.4.2 (a) currently suggests the presence of a single isotropic melt – crystal transition loop (see insert Fig.4.2 (a)). In these systems in transition regions (Tab.4.1) it is possible to draw horizontal lines, similarly to Maxwell rule, so that the areas between the curve and the horizontal line above and below the line are equal (see insert in Fig.4.2 (a)). The horizontal straight line corresponds to the inverse temperature ($1/T_t$), from which the transition temperature T_t is calculated. Fig.4.2 (a) shows, that the black curve exceeds the red curve, it is concluded that the transition temperature T_t for the more dense system (red curve) will exceed the transition temperature T_t for the less dense system (black curve). Additionally, the inclusion of repulsive walls (green curve) increases the transition temperature T_t compared to a system without walls of equivalent

4.1. Thermodynamic properties

density (black curve). Despite the lack of convergence of a system with repulsive walls, which precludes definitive conclusions regarding the nature and number of transitions, at the moment, this graph rather indicates a single first order phase transition (isotropic melt – crystal). Although further refinement of the $\ln(g)$ is required for this system, this system will be used for comparative analysis, taking into account that the statements made are preliminary.

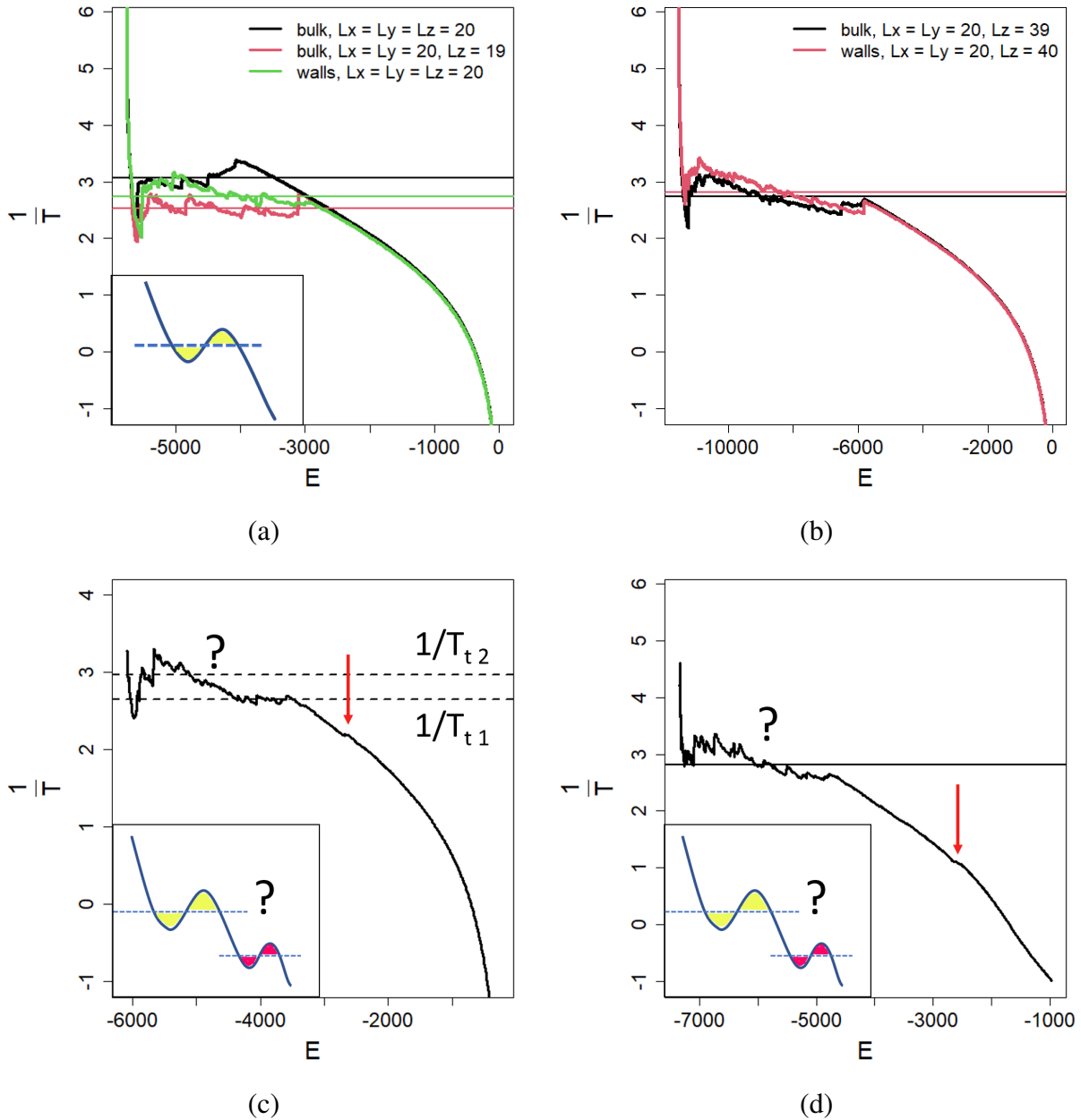


Figure 4.2: The inverse temperature given by Eq. (4.3): (a) for the bulk and system with repulsive walls with $L_x = L_y = L_z = 20$, and bulk with $L_x = L_y = 20$, $L_z = 19$; (b) for the system with repulsive walls with $L_x = L_y = 20$, $L_z = 40$, and bulk with $L_x = L_y = 20$, $L_z = 39$; (c) for the system with U_{at1} potential ($L_x = L_y = L_z = 20$); (d) for the system with U_{at2} potential ($L_x = L_y = L_z = 20$). Inserts: possible shape of the curve in the presence of one (a) or two (c), (d) first-order phase transitions. The horizontal lines correspond to the assumed inverse phase transition temperatures calculated from $C_v(T)$.

Note that the obtained transition loops has the shape of "steps" (the main part of Fig.4.2 (a)). These "steps", observed in systems with different volume fractions ($\phi = 0.471$, $\phi = 0.496$), presumably indicate the presence of structural transitions not considered in the study Ref.[97]. A comprehensive study of this area will be discussed in detail in the section 4.2.3.

Estimation of the transition temperatures T_t are derived from dependencies of the canonical heat capacity $C_v(T)$, as determined by the function maxima, instead of Maxwell area rule (see below). In a system where convergence has been achieved, these two methods would yield coinciding temperatures.

| Structure | Volume fraction, ϕ | System size, L_z | Energy transition region, E_t |
|-----------------|-------------------------|--------------------|---------------------------------|
| Bulk | 0.471 | 20 | $[-5700; -4000]$ |
| Bulk | 0.496 | 19 | $[-5700; -3100]$ |
| Bulk | 0.496 | 39 | $[-11400; -5700]$ |
| Repulsive walls | 0.471 | 20 | $[-5700; -2900]$ |
| Repulsive walls | 0.471 | 40 | $[-11400; -5700]$ |
| U_{at_1} | 0.471 | 20 | $[-6000; -3200]$ |
| U_{at_2} | 0.471 | 20 | $[-7200; -4500]$ |

Table 4.1: Estimation of the energy range for the phase transition region with $L_x = L_y = 20$ for all systems.

Differences between large and small systems of the same density are expected due to finite size effects that were originally intended to be studied (Fig.4.2 (a), (b)). For large systems (bulk with $L_x = L_y = 20$, $L_z = 39$, and system with repulsive walls with $L_x = L_y = 20$, $L_z = 40$ Fig.4.2 (b)), the transition temperature currently appears to be smaller than for similar small systems (Fig.4.2 (a), red and green curves). The fact that the transition temperature can depend on the size of the system was shown in the Ref.[97]. However, additional observations of the change in the inverse temperature versus energy dependence over time showed that these data still vary greatly in the transition region (Tab.4.1). This indicates that the results are highly inaccurate. Therefore, we will not focus on big systems (Fig.4.2 (b)).

As for systems with different magnitudes of wall attraction, the results within the transition region ($E \in [-6000; -3200]$ for U_{at_1} in Fig.4.2 (c) and $E \in [-7200; -4500]$ for U_{at_2} in Fig.4.2 (d), see Tab.4.1) are not considered trustworthy due to still bad convergence up to now. Note that despite the fact that for now we tend to identify only one phase transition of the first order (single horizontal line in Fig.4.2 (d)), we cannot reliably exclude the presence of two phase transitions with temperatures T_{t1} and T_{t2} located close to each other (the scheme in the insets of Fig.4.2 (c), (d), see discussions below). We assume that the convergence of the function $\ln g$ outside the transition region for these and all other systems has been achieved. It is noteworthy

that for systems with attractive wall, special points (red arrows) outside the transition region in the inverse temperature-energy dependency require further study (see section 4.2.1). For U_{at_1} this point is located at $E \approx -2700$, $T^{-1} \approx 2.2$, $T \approx 0.45$, while for U_{at_2} a noticeable change in the behavior of the inverse temperature occurs at $E \approx -2600$, $T^{-1} \approx 0.087$, $T \approx 0.92$. Special points can be inflection points (a continuous transition) or a small loop (a weak first-order transition). One should take a derivative of the inverse temperature with respect to energy to accurately characterize these points. If a positive local maximum in the derivative of the inverse temperature is observed at the indicated location, then the observed transition is the first order. On the contrary, a negative local maximum indicates a continuous transition. Our experience has shown that due to noise, these data are not reliable, and in order to describe the system at these points, the relevant system parameters should be further considered (see section 4.2.1).

Remark. Avoiding confusion when we talk about this phase transition (at $E \approx -2700$ for U_{at_1} , and at $E \approx -2600$ for U_{at_2} system), we will use *special point* terminology, if there are no additional clarifications. While to describe the broad transition region described in Tab.4.1, we will talk about *phase transition*, *transition region*, *first-order phase transition*.

In canonical thermodynamics, the primary functions of interest include the average energy $\langle E \rangle(T)$ and the heat capacity given by:

$$C_v(T) = \frac{\langle E^2 \rangle - \langle E \rangle^2}{k_B T^2}. \quad (4.4)$$

It is important to note that although in the definition we refer to the total energy of the system, in this context we refer to heat capacity as a similar quantity derived solely from the configurational aspect of energy. This applies similarly to other system parameters.

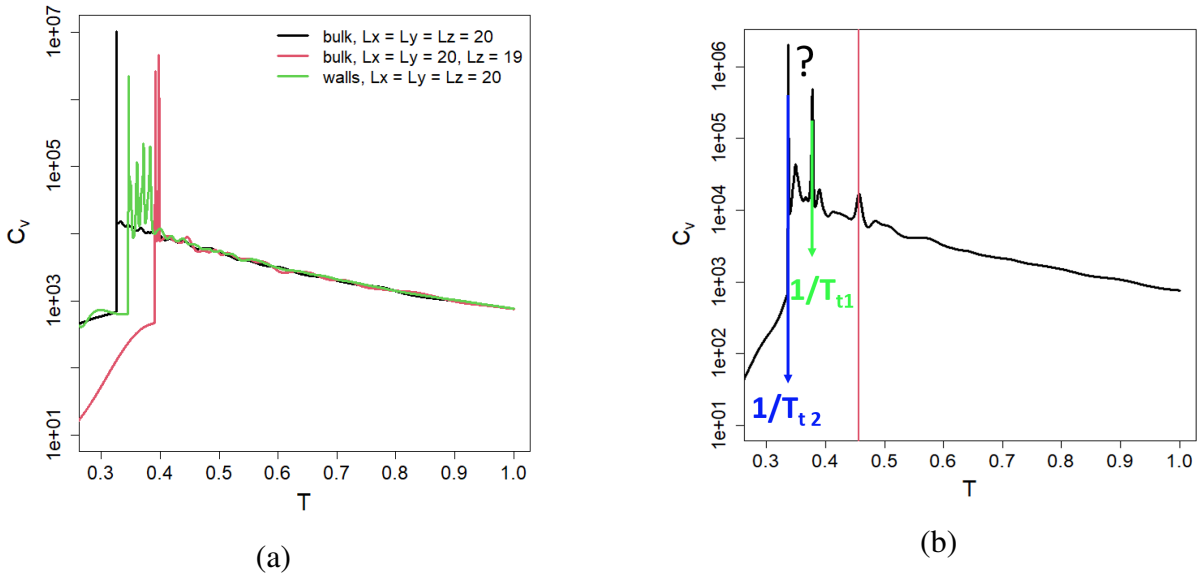


Figure 4.3: Canonical heat capacity $C_v(T)$: (a) for the bulk and system with repulsive walls with $L_x = L_y = L_z = 20$, and bulk with $L_x = L_y = 20, L_z = 19$; (b) for the system with U_{at_1} potential

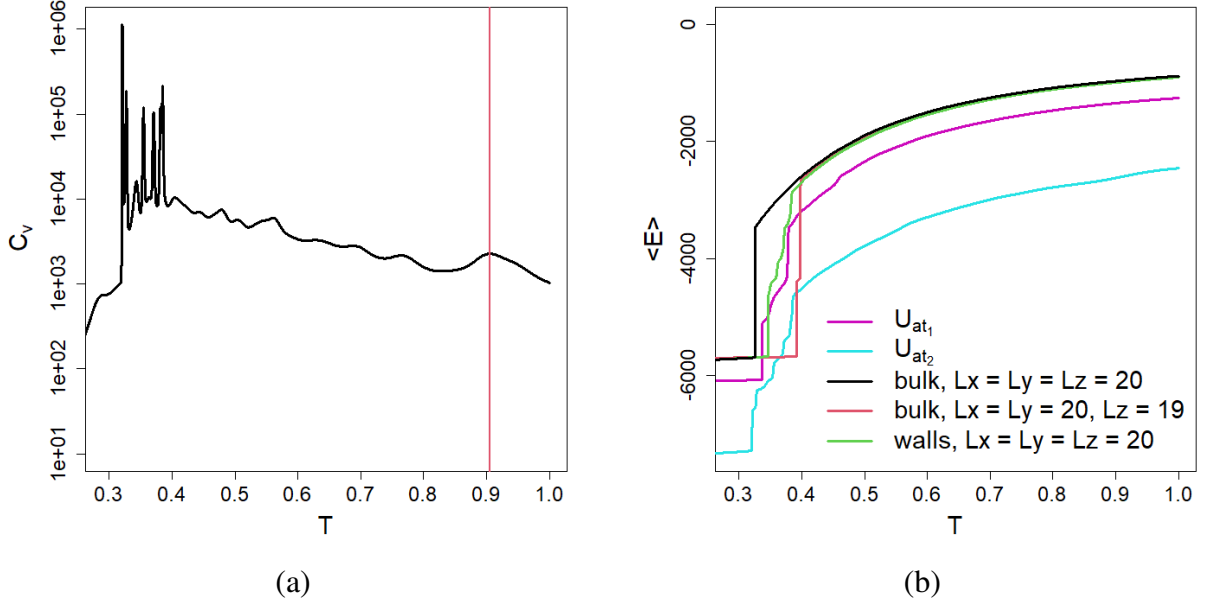


Figure 4.4: (a) canonical heat capacity $C_v(T)$ for the system with U_{at_2} potential; red vertical line corresponds to red arrow in Fig.4.2. (d) $\langle E \rangle(T)$ for all small systems

The results obtained for the heat capacities $C_v(T)$ make it possible to quite accurately determine the transition temperatures for small systems without walls (black and red curves in Fig.4.3 (a)). For these systems, pronounced peaks are observed in the heat capacity graphs, which indicate a first-order phase transition (in the thermodynamic limit, they would become delta peak). For a system with a lower volume fraction ($\phi = 0.471$, black curve), the first-order transition temperature is $T_t = 0.326 \pm 0.001$, while an increase in the volume fraction ($\phi = 0.496$, red curve) leads to an increase in the transition temperature $T_t = 0.395 \pm 0.003$. The red curve shows two closely spaced peaks in $C_v(T)$, which we attribute to imperfect convergence of the system. For the transition temperature T_t , we choose a point located in the middle between these peaks (Tab.4.2).

| Structure | Volume fraction, ϕ | System size, L_z | Expected T_t |
|-----------------|-------------------------|--------------------|--|
| Bulk | 0.471 | 20 | 0.326 |
| Bulk | 0.496 | 19 | $T_t \in [0.392; 0.398] \approx 0.395$ |
| Bulk | 0.496 | 39 | $T_t \in [0.340; 0.391]$ |
| Repulsive walls | 0.471 | 20 | $T_t \in [0.346; 0.383]$ |
| Repulsive walls | 0.471 | 40 | $T_t \in [0.316; 0.396]$ |
| U_{at_1} | 0.471 | 20 | $T_t \in [0.332; 0.381]$ |
| U_{at_2} | 0.471 | 20 | $T_t \in [0.316; 0.398]$ |

Table 4.2: Expected transition temperatures T_t with $L_x = L_y = 20$ for all systems.

In a system with weak wall attraction (U_{at_1}), the temperature dependence of the heat capacity (Fig.4.3 (b)) currently shows two sharp peaks at $T_{t1} = 0.378 \pm 0.025$ and $T_{t2} = 0.337 \pm 0.025$ in the region $T_t \in [0.332; 0.381]$. At the moment, we cannot give a reliable analysis of this region because of insufficient convergence of the density of states function in the transition region, and because in addition to these large sharp peaks smaller fluctuations in heat capacity are observed. However, if we assume that on a sufficiently accurate density of states these observed peaks will become more pronounced, then they should be interpreted as two successive phase transitions of the first order. The transition temperatures T_{t1} , T_{t2} may slightly change their values compared to those currently observed. In this case, two scenarios are possible.

- Transitions in the whole system: isotropic melt \rightarrow nematic \rightarrow crystal. In this case, one can expect that when the temperature decreases to the temperature T_{t1} , orientational order parameters will change abruptly from the small values to a value close to one ($T_{t1} = T_{n-i}$ Fig.4.5 (a), (b)). In this point, the number of particles classified as crystalline will not demonstrate a sharp jump (Fig.4.5 (b)). At temperature T_{t2} the number of crystalline particles will experience a jump ($T_{t2} = T_{cr-n}$ Fig.4.5 (a), (b)). Thus, T_{t2} is expected to coincide with the melting point T_m , for a system of the same size without walls.
- Transitions: isotropic melt \rightarrow formation of a crystalline layer of finite thickness near attractive wall \rightarrow crystallization in the entire system. In this case, we can talk about the phenomenon of prefreezing (Fig.4.5 (c)). When the temperature decreases to T_{t1} (which have a sense of T_{pref} in the chapter 1, Fig.1.2), the orientational order parameters, as well as the number of crystalline particles in the system, will experience a jump to a certain (not maximum) value. This will characterize the formation of a crystal layer of a finite thickness. Then these parameters will gradually increase with decreasing temperature, which will indicate the growth of the crystalline layer. At temperature T_{t2} , all order parameters (including orientational order parameters, see in section 4.2) in the system, as well as the number of crystalline particles, will experience a sharp jump to a maximum value or logarithmic growth, as predicted by phenomenological theory [29]. This will indicate crystallization within the entire system. At the moment we do not dare to predict the behavior of this dependence in the vicinity of the point T_{t2} in this scenario. So, T_{t2} has a meaning of T_m for this system with considered size. Note that it was shown [97] that the small size of the system contributes to an increase in T_m , which is a consequence of the ordering of the system through periodic boundary conditions.

The given scenarios and methods of analysis are simplified here. Since at the moment the density of states function has not been accumulated accurately enough, we cannot carry out a detailed analysis of this system in the transition region, nor can we guarantee that the final data will indicate two transitions, and not one (isotropic melt – crystal transition by the heterogeneous nucleation mechanism).

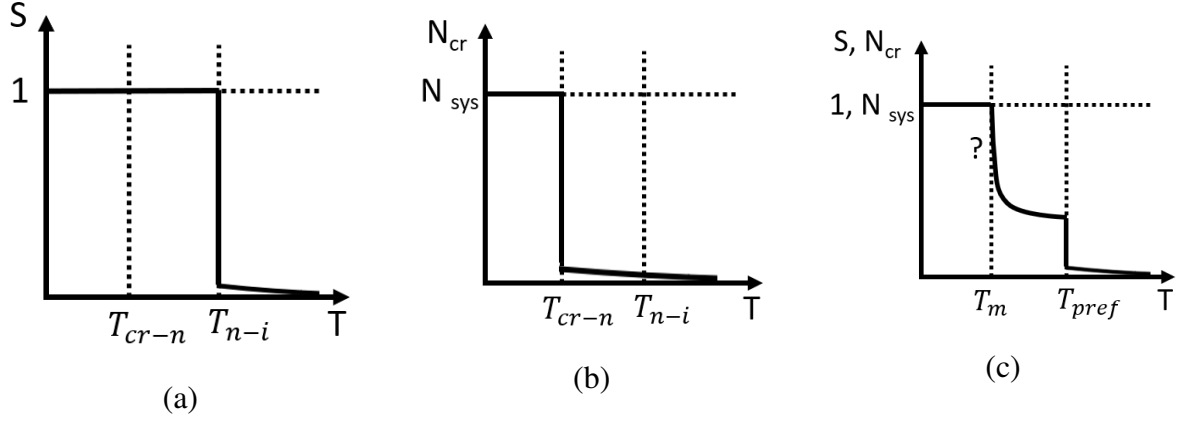


Figure 4.5: Schemes of two possible scenarios of phase transitions in the case of the presence of two loops on the graph of the dependence of the inverse temperature on energy (Fig.4.2).

Temperature dependence of the orientational order parameter (a) and the number of crystallized particles (b) in the scenario of the transition between an isotropic melt - nematic (T_{n-i}) and a nematic - crystal (T_{cr-n}). Temperature dependence of the orientational order parameter and the number of crystallized particles (c) in the prefreezing scenario: melt - crystalline layer of finite thickness (T_{pref}) and melting point (T_m). As the temperature decreases $T \in [T_m; T_{pref}]$, the thickness of the crystalline layer increases.

Although it cannot be ruled out that continued accumulation of the $\ln g(E)$ function may reveal two phase transitions for systems with attractive wall, we currently expect only single isotropic melt – crystal phase transition. Refining the regions that exhibit pronounced variations in the $C_v(T)$ dependencies is expected to eventually lead to a single noticeable peak. It is worth noting that although we analyze the available data and provide an estimate of the current transition region, there is no guarantee that the final peak will necessarily be within the specified region. For the remaining systems under study (bulk $L_x = L_y = 20$, $L_z = 39$, repulsive walls $L_x = L_y = 20$, $L_z = 20$ and $L_x = L_y = 20$, $L_z = 40$ and for U_{at_2}), accurate determining the transition temperature is also currently hardly possible.

Outside the transition region indicated in Tab.4.2 for systems with attractive walls, the red vertical lines (Fig.4.3 (b), Fig.4.4 (a)) indicate heat capacity peaks corresponding to special points on the inverse temperature graphs (Fig.4.2 (c), (d)). The positions of these peaks facilitate the most accurate determination of the corresponding temperatures ($T^* = 0.457 \pm 0.002$, $E^* = -2650 \pm 10$ for U_{at_1} and $T^* = 0.905 \pm 0.007$, $E^* = -2610 \pm 15$ for system U_{at_2}). Note that the corresponding peaks are quite broad rather than sharp. A more detailed discussion of these points will be given in the section 4.2.1.

The dependence of the average energy on temperature (Eq.(2.16)) illustrates the characteristic downward shift of the curves for systems with an attractive wall. This phenomenon arises from the predominance of conformations in which approximately 400 particles are located in the wall layer (near the attractive wall) in these systems. Consequently, in the system with potential U_{at_1} , the dependence $\langle E \rangle(T)$ (Fig. 4.4 (b)) shows a downward shift of approxi-

mately 400, while in the system with potential U_{at_2} , the shift is about 1600 relative to systems without an attractive wall. This also explains why, for all energy dependencies, the maximum energy for systems with an attractive wall does not reach $E = 0$.

For the bulk system ($L_x = L_y = 20$, $L_z = 19$, Fig.4.4 (b), the red curve) at energy $E \approx -4500$, a small area with a small slope is observed. We attribute this jump to insufficient convergence, which also results in a doubling of the peak in the heat capacity dependence (Fig.4.3 (a), the red curve). We expect that as accumulation continues, two closely spaced jumps will merge into one. Note that for bulk system ($L_x = L_y = L_z = 20$, Fig.4.4 (b), the black curve), the transition region represents a sharp jump, while similar regions for all other systems with walls are more blurred. We expect that with better convergence $\ln g$ for these systems, there will be a sharp jump in the case of one transition. If for any system there are two closely located phase transitions of the first order of transition (see discussion of the insets in Fig.4.2 (c),(d)), then we will see two jumps, clearly separated by a slowly growing part.

We estimate the magnitude of the energy jump $\Delta\langle E \rangle$ as the difference between the average energy value $\langle E \rangle$ reaching a plateau at low temperatures and the average energy $\langle E \rangle$ when the curve reaches smooth saturation at high temperatures. The smallest jump is observed in the system without walls with $L_x = L_y = L_z = 20$, $\phi = 0.471$ (Fig.4.4 (b), black curve), where $\Delta\langle E \rangle \approx |-5760 - (-3560)| = 2200$. Conversely, in a system without walls with a larger volume fraction ($L_x = L_y = 20$, $L_z = 19$, $\phi = 0.496$, Fig.4.4 (b), red curve), the jump height is the highest, with $\Delta\langle E \rangle \approx |-5760 - (-2760)| = 3000$. While jump heights may vary for other systems, the current values are closer to those of a denser system (for a system with repulsive walls: $\Delta\langle E \rangle \approx |-5760 - (-2940)| = 2820$; U_{at_1} : $\Delta\langle E \rangle \approx |-6150 - (-3550)| = 2600$; U_{at_2} : $\langle E \rangle \approx |-7340 - (-4440)| = 2670$). This suggests that the presence of walls, as well as an increase in the density of the system, promotes the phase transition.

In our study, we refrain from using the microcanonical heat capacity as its computation involves the second derivative of entropy:

$$c(E) = \left(\frac{\partial T}{\partial E} \right)^{-1} = -\frac{1}{T^2} \left(\frac{\partial^2 S}{\partial E^2} \right)^{-1}.$$

Given the significant noise observed in the graphs of the first derivative of entropy, the second derivative amplifies this effect, making the microcanonical heat capacity unsuitable for analysis.

Additional quantities commonly encountered in statistical physics such as the partition function $Z(T)$, the free energy $F(T) = -k_B T \ln Z(T)$, the Boltzmann probabilities $p(E, T)$ are not relevant in this context.

4.2 Structural analysis of systems

In this section, we perform a structural analysis to clarify the observed phenomena described in the previous section. To describe features near special points, we consider systems

with attractive potentials U_{at_1} and U_{at_2} (section 4.2.1). To analyze the transition region (first-order transition) for the energy range indicated in the Tab.4.1, we use a system without walls (bulk) with density ($L_x = L_y = 20$, $L_z = 19$, $\phi = 0.496$) and a system with repulsive walls ($L_x = L_y = L_z = 20$, $\phi = 0.471$) (section 4.2.2). We assume that in the bulk with the volume fraction $\phi = 0.496$ and with the volume fraction $\phi = 0.471$, structural features remain unchanged. This statement is confirmed by similar diagrams of the dependence of inverse temperature on energy (Fig.4.2 (a)). Therefore, for the structural analysis we will use the data obtained from our simulation for the system without walls ($L_x = L_y = 20$, $L_z = 19$, $\phi = 0.496$). In addition, comparisons will be made with the small system with repulsive walls ($L_x = L_y = L_z = 20$, $\phi = 0.471$). Finally, there is a discussion of the possibility of the phenomenon of prefreezing in systems with repulsive walls and with weak attractive wall U_{at_1} (section 4.2.4).

4.2.1 Analysis of the transition inside the layer near the attractive wall

Since in this part we intend to explore only special points, here we will consider the energy regions $E \in [-3000; -2000]$ for the systems U_{at_1} and U_{at_2} . This range selection facilitates full exploration of points of interest ($E^* = -2650 \pm 10$ for U_{at_1} and $E^* = -2610 \pm 15$ for system U_{at_2}) and avoids capturing redundant areas where additional effects may contribute. Since this effect is observed in our work only in systems with an attractive wall far from the phase transition region (Tab.4.1), we assumed the formation of a crystalline layer near the attractive wall. In this case, the use of Steinhardt parameters or local alignment of chain segments analysis is inappropriate, since in the near-wall layer we inevitably encounter a deficit in the number of neighboring particles.

The assumption that the transition occurs in a layer near the attractive wall is confirmed by visualizing the particles in the layer, and then by calculating the corresponding parameters. Fig.4.6 shows projections of the centers of mass of the beads on the planes XZ , XY for two randomly selected conformations: on the left ($E = -2785$, $E < E^*$), and on the right ($E = -2379$, $E > E^*$) from the special point.

From the projections onto the XZ plane it is clear that near both walls for both selected conformations the wall layers can be clearly distinguished (black dots between the blue and red lines in Fig.4.6 (a), (d)). If we consider the projections of particles from these layers onto the XY plane, we see that near the attractive wall at energies above E^* (Fig.4.6 (b)) the particles in the layer are disordered, while for energies below E^* (Fig.4.6 (e)) ordering appears. Near the repulsive wall for both conformations, the particles are disordered (Fig.4.6 (c), (f)). Thus, preliminary observation of conformations indicates that there is a transition occurs in the attractive wall layer at point E^* .

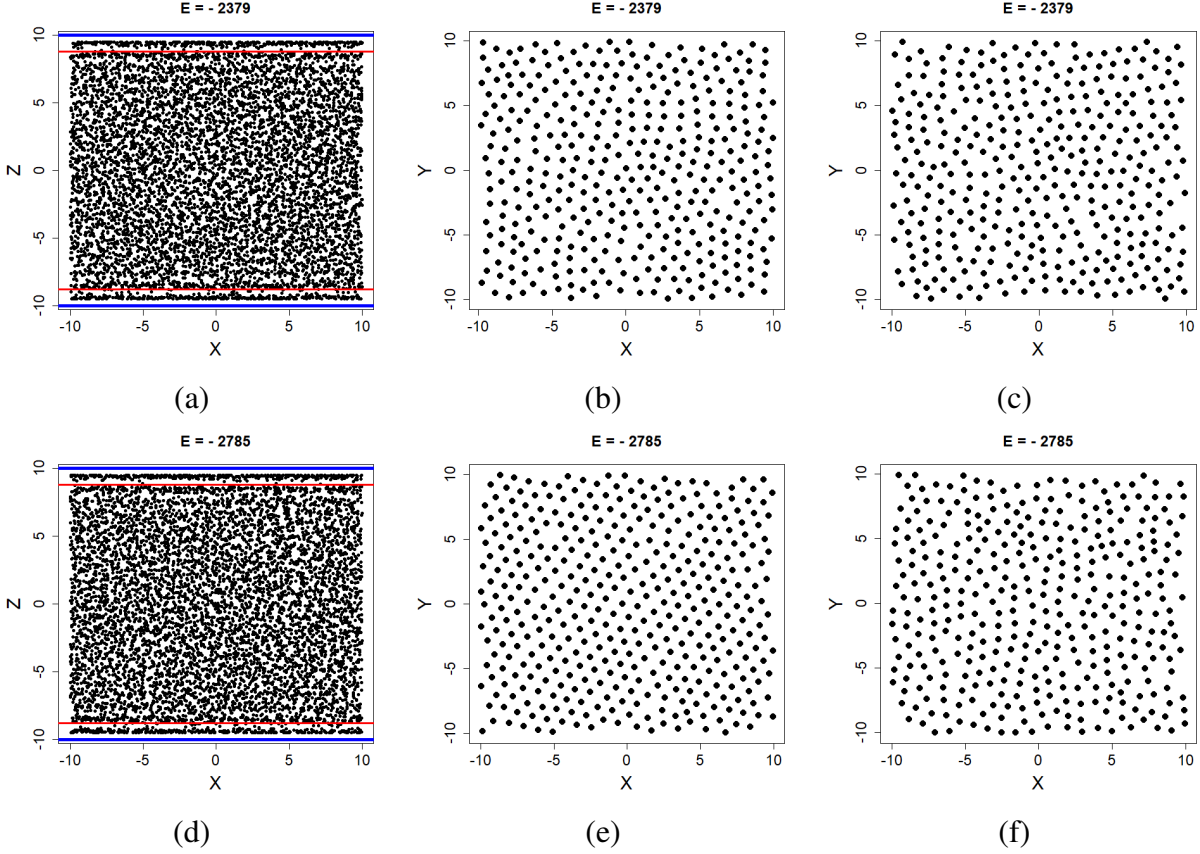


Figure 4.6: Projections of center of mass of beads for conformations with energy $E = -2379$ (a-c) and $E = -2785$ (d-f) for the U_{at_1} system. (a), (d) projection of all particles onto the plane XZ . Blue lines indicate walls at $Z = \pm 10$, red lines at $Z = \pm 8.8$ indicate the edge of the first layers near walls. (b), (e) projections of particles from the layer near attractive wall $8.8 < z < 10$ onto the plane XY . (c), (f) projections of particles from the layer near repulsive wall $-10 < z < -8.8$ onto the plane XY .

To assess the orientational order within a layer, we examine several layers with a thickness of one, which are parallel to the walls at $Z = \{\pm 9.5, \pm 8.5, \pm 7.5\}$. Centers of particles from layer l are projected onto the plane Z , after which the following hexagonal parameters are calculated:

$$|\langle \psi_6 \rangle| = \left| \frac{1}{N_l} \sum_{k=1}^{N_l} \frac{1}{n_k} \sum_{j=1}^{n_k} \exp(i6\alpha_{kj}) \right|, \quad (4.5)$$

where the α_{kj} are angles between the vectors connecting bead k to its neighbors j and a fixed axis in this plane, N_l is a number of particles in the layer l , and n_k is a number of neighbors of the particle k . Averaging, indicated by angle brackets, means averaging over particles in the layer l . In the case of this parameter, we consider particles falling into a cylinder with a height 0.5 and a radius 1.6, outlined around the particle k , as its neighbors. This choice of radius ensures the selection of particles within the first coordination sphere in the plane under study (Fig.4.10). The axis of the cylinder is directed perpendicular to the plane under consideration.

We also consider the average of the absolute value of ψ_6 , which can be calculated as follows:

$$\langle |\psi_6| \rangle = \frac{1}{N_l} \sum_{k=1}^{N_l} \left| \frac{1}{n_k} \sum_{j=1}^{n_k} \exp(i6\alpha_{kj}) \right|. \quad (4.6)$$

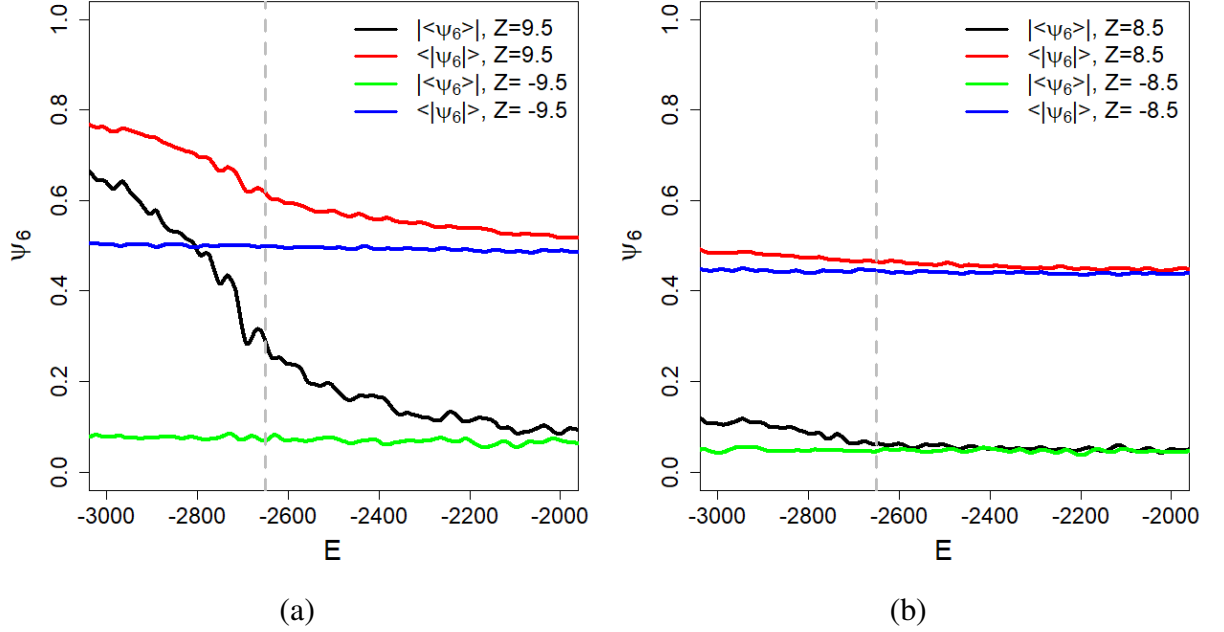


Figure 4.7: The hexagonal parameters ψ_6 in the systems with potential U_{at_1} in planes $Z = \pm 9.5$ (a) and $Z = \pm 8.5$ (b). The gray dotted line indicates the temperature $E^* = -2650$.

From the data obtained (Fig.4.7) it is clear that near the attractive wall in the first layer ($Z = 9.5$, black and red curve in Fig.4.7 (a)) there is a strong increase in both parameters (Eq.(4.5), Eq.(4.6)), with decreasing energy and when the energy reaches E^* (gray line $E^* = -2650$). Parameters in the second layer ($Z = 8.5$, black and red curves in Fig.4.7 (b)) are much less sensitive to this change in energy. In the third layer ($Z = 7.5$, see the Appendix, Fig.A14) parameters do not change when the energy reaches $E^* = -2650$. At the same time, analysis of the parameters near the repulsive wall (blue and green curves) shows that no changes indicating ordering occur in this energy range.

We do not go into a detailed analysis of these parameters near the walls of the transition region (for energies less than $E = -3000$), since we do not have enough data for an accurate analysis at the moment in this region. However, from the currently available data it can be concluded that these parameters increase to a value close to 0.8 for both repulsive and attractive walls in the transition region (see the Appendix, Fig.A14).

For the system with stronger attraction (U_{at_2} , Fig.4.8), the observed effects are more pronounced. Higher attractive potential promotes the formation of an ordered layer at the attractive wall at higher temperature ($T^* = 0.905$ for U_{at_2} instead $T^* = 0.457$ for U_{at_1} , which corresponds to $E^* = -2610$ and $E^* = -2650$, respectively), long before the phase transition in the whole

system (see Fig.4.2). The second layer ($Z = 8.5$), as in the case of weak attraction U_{at_1} , also gives a weak response in the parameters.

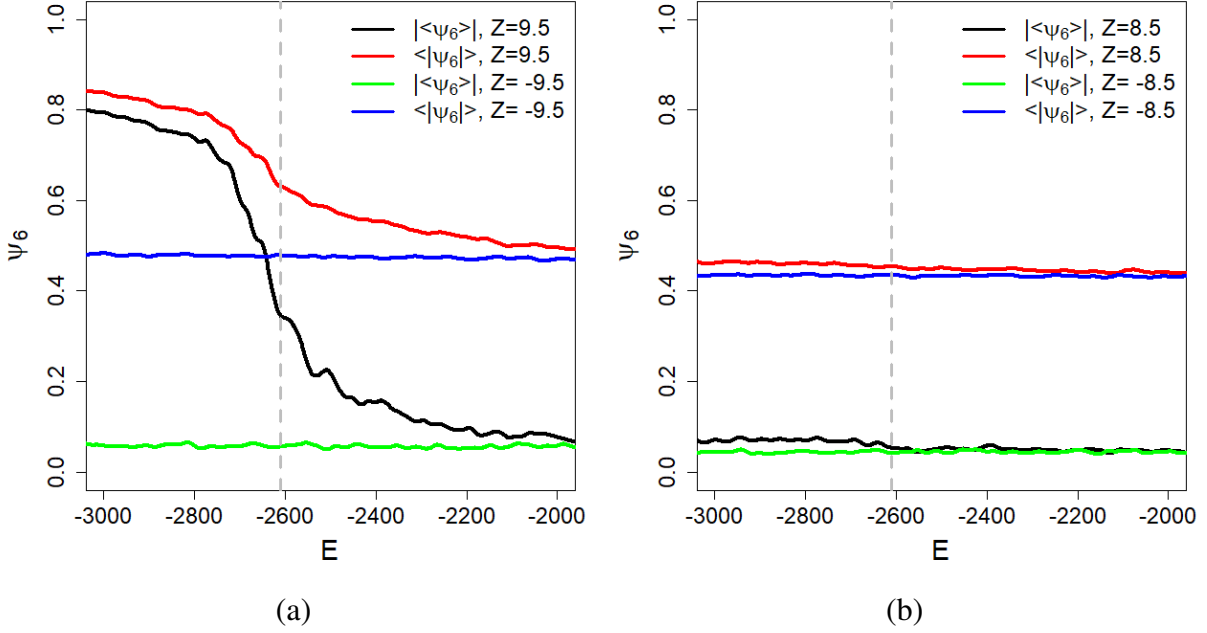


Figure 4.8: The hexagonal parameters ψ_6 in the systems with potential U_{at_2} in planes $Z = \pm 9.5$ (a) and $Z = \pm 8.5$ (b). The gray dotted line indicates the temperature of $E^* = -2610$.

Since the parameters described above characterize *local* orientational order, it is impossible to say from these data whether an increase in ψ_6 indicates the formation of a two-dimensional crystal layer or a hexatic (anisotropic fluid) layer. In order to clarify the type of two-dimensional structure obtained, we considered the orientational correlation function between particles i, k in the layer near attractive wall [162]:

$$g_6(|\mathbf{r}|) = \langle \psi_6(\mathbf{r}_i) \psi_6^*(\mathbf{r}_k) \rangle, \quad (4.7)$$

where $|\mathbf{r}| = |\mathbf{r}_i - \mathbf{r}_k|$ is the distance between projection of particles i, k onto the plane Z (i. e. $\mathbf{r} = \mathbf{r}(x, y)$). Angle brackets here denote the statistical average for all pairs of particles with distance $|\mathbf{r}|$ and orientation order parameter ψ_6 , defined as:

$$\psi_6(\mathbf{r}_k) = \frac{1}{n_k} \sum_{j=1}^{n_k} \exp(i6\alpha_{kj}). \quad (4.8)$$

All designations in Eq.(4.8) correspond to those described in Eq.(4.5).

The orientational correlation function $g_6(|\mathbf{r}|)$ is used to distinguish between a two-dimensional crystal, a hexatic (anisotropic liquid), and an isotropic liquid. In the case of a two-dimensional crystal, the orientational correlation function does not depend on the distance ($g_6(|\mathbf{r}|) \propto \text{const}$), demonstrating long-range order. In the case of an anisotropic liquid, quasi-long range order is observed, described by a power law ($g_6(|\mathbf{r}|) \propto r^{-\eta_6}$, where η_6 is an exponent). An isotropic liquid have a short range order that decreases exponentially with distance

($g_6(|\mathbf{r}|) \propto e^{-r/\mu_6}$, where μ_6 is a constant). To analyze systems with attractive walls, we examine four energy intervals: (a) $E > E^*$; (b) $E^* > E > E_t$ (see E_t in Tab.4.1); (c) $E \in E_t$; (d) $E_t > E$.

In the region (a) we expect to observe an isotropic melt near both repulsive and attractive walls, in the region (b) an isotropic melt is expected in the repulsive wall layer, and an ordered structure in the attractive wall layer (hexatic or two-dimensional crystal), the region (c) corresponds to a transition in the entire simulation box, and in the region (d) a crystal phase is expected throughout cell volume.

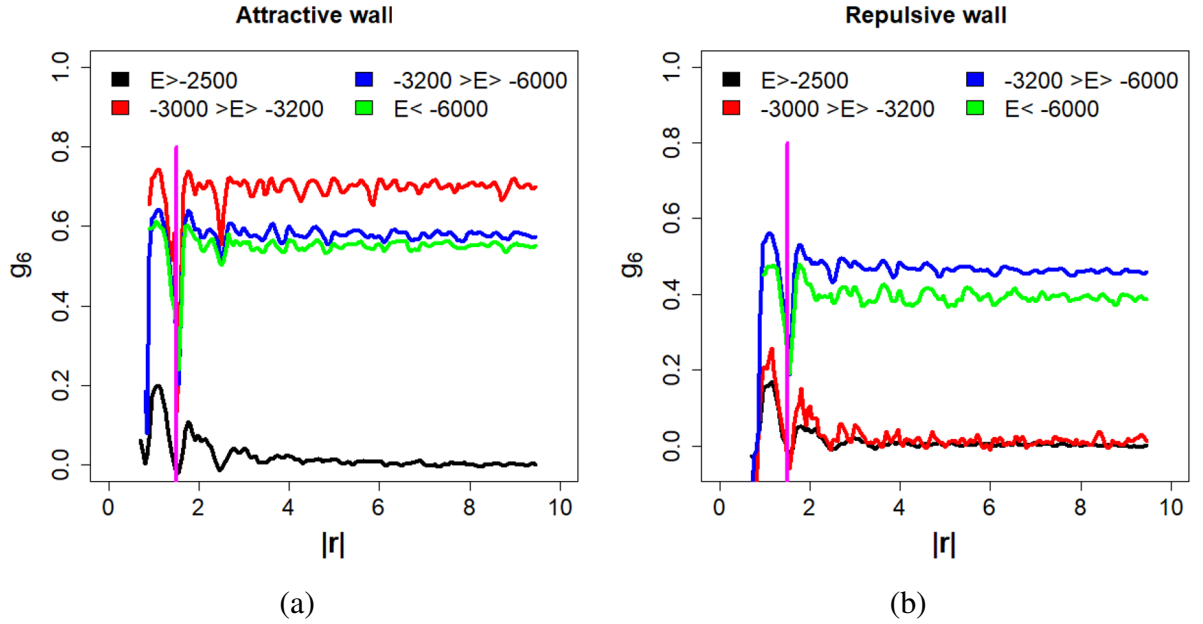


Figure 4.9: The orientational correlation function $g_6(|\mathbf{r}|)$ in the systems with potential U_{at_1} in planes $Z = 9.5$ (attractive wall) (a) and $Z = -9.5$ (repulsive wall) (b). The magenta line indicates the first minima of the 2d rdf at $|\mathbf{r}| = 1.5$.

From the data obtained for the system U_{at_1} it is clear that in the high-energy region (black curves in Fig.4.9), the maximum values of the orientational correlation function $g_6(|\mathbf{r}|)$ are small (~ 0.2), both near the attractive wall (Fig.4.9 (a)) and near the repulsive wall (Fig.4.9 (b)). Also according to expectations, there is a fast decay for the correlation function $g_6(|\mathbf{r}|)$ in this region, as expected for an isotropic fluid. At the same time, the assumption that an isotropic melt is observed in this region is confirmed by the dependence of the two-dimensional radial distribution function (2d-RDF) g_2^{2d} , calculated for the wall layer by analogy with the three-dimensional case (Eq.(3.9)). At high energies, the 2d-RDF decays rapidly, so that only the first three peaks are clearly visible (black curves in Fig.4.10). This behavior is typical for an isotropic melt. Combination of these factors indicate the absence of long-range orientational order.

The region (b), $E^* > E > E_t$, is characterized by the highest values of the correlation function near the attractive wall (the red curve in Fig.4.9 (a)). Such high values indicate the presence of a two-dimensional crystal. In addition, 2d-RDF shows persistent peaks (the red

curve in Fig.4.10 (a)). The height of the peaks does not decrease with the distance. Based on the totality of these data, we can conclude that the observed structure is a two-dimensional crystal. Thus, the found special point $E^* = -2650 \pm 10$, $T^* = 0.457 \pm 0.004$ should be considered as a phase transition from isotropic state to a two-dimensional crystal. One should take a derivative of the inverse temperature with respect to energy to accurately characterize these points. As mentioned in section 4.1, the second derivative of the density of states function over energy should be used to determine the transition order. However, our experience shows that the resolving power of our method is not sufficient to determine the transition order. Therefore, we cannot rule out that the indicated point E^* (Fig.4.2) is actually a small loop indicating a weak first order phase transition or inflection point indicating a continuous transition. The dependencies of the ψ_6 parameters on temperature, given in the Appendix (Fig.A15), demonstrate a continuous increase in the parameters at the transition point T^* . This may indicate a continuous transition. Thus, we can say that at this scale, our method does not have enough resolution to reliably determine the type of transition. It is worth noting that studying of crystallization in 2d systems is a non-trivial problem that has not been solved for all two-dimensional systems [94]. In addition, here we want to make a remark. We recall that in our consideration we take into account only potential energy. Additional consideration of kinetic energy in conjunction with number of factors (such as the connectivity in the chain, the relatively high density of the system, the stiffness of the chains, as well as the small size of the system) can also determine more complex behavior. For example, we cannot exclude sequence of transitions (isotropic - hexatic - two-dimensional crystal).

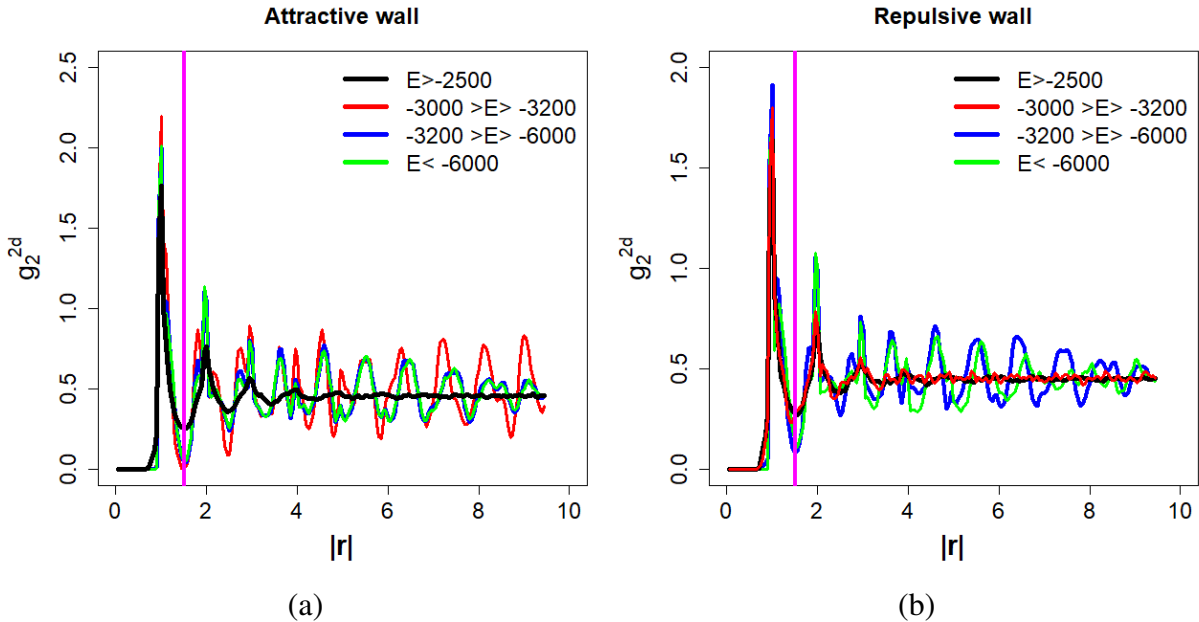


Figure 4.10: 2d RDF function g_2^{2d} in the systems with potential U_{at1} in planes $Z = 9.5$ (attractive wall) (a) and $Z = -9.5$ (repulsive wall) (b). The magenta line indicates the first minima of the 2d rdf at $|r| = 1.5$.

In the same energy range near the repulsive wall, only a small increase in the correlation function (the red curve in Fig.4.9 (b)), compared with high energies (the black curve in Fig.4.9 (b)), combined with a rapidly decaying g_2^{2d} (the red curve in Fig.4.10 (b)) indicates an isotropic melt.

Although convergence in the transition region has not yet been achieved, several important points can be noted from the available data for the region (c) $E \in E_t$. The dependencies of the orientational correlation function have a similar shape for the layer near the attractive and repulsive walls (blue curves in Fig.4.9). The values of these functions are lower for this region than for higher energies near attractive wall (the red curve in Fig.4.9 (a)). In addition, g_2^{2d} has a clearly a damping trend (the blue curves in Fig.4.10). This suggests that the formation of a crystal in the entire system slightly destroys the crystalline order near the attractive wall. Similar observations are true for the energy region below the transition ((d) $E_t > E$, green curves in Fig.4.9, Fig.4.10). However, the results in this area are the least reliable due to the complexity of sampling process in this region.

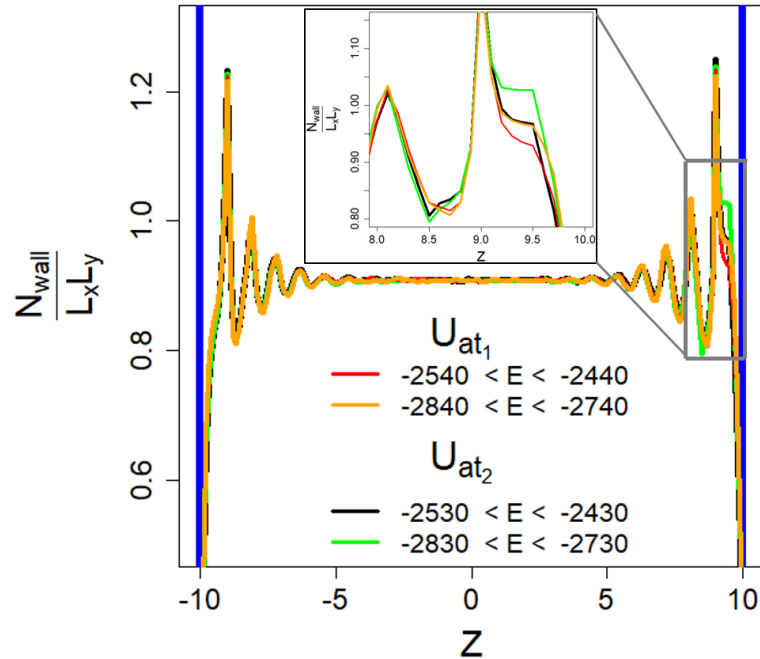


Figure 4.11: Profile of the number of particles in a layer with a thickness of one per unit area for systems U_{at_1} , U_{at_2} . Blue lines indicate walls positions.

We also examined the profiles of the ratio of the number of particles in a layer of unit thickness to the area of the layer under consideration. In fact, the dependence under consideration is a density profile. We averaged the resulting profiles in energy intervals $\Delta E = 100$ to the left and right of the transition points E^* in the layer for both systems U_{at_1} , U_{at_2} (Fig.4.11). From the obtained dependencies it is clear that for $E > E^*$ the density profiles are symmetrical

for both systems. The decrease in densities near the walls compared to the values in the center of the cell is explained by the fact that centers of beads cannot approach the wall at a distance closer than half the diameter of the bead. However, for $E < E^*$, the density of the ordered layer near the attractive wall is noticeably higher compared to the values in the cell center. Thus, in conformations where an isotropic melt and a crystalline layer coexist, the density of the crystalline part is higher. For a system with greater attraction (U_{at_2}), this effect is more pronounced. A similar effect will be demonstrated for the bulk transition in the section 4.2.3.

In addition, we asked whether the ordering of the wall layer is accompanied by the adsorption of chains. In order to answer this question, we calculated the number of monomer units (beads) in the wall layer M_l , and the number of chains C_l , whose units included into the wall layer. The ratio of these quantities $K_a = M_l/C_l$ can serve as a characteristic value of chain adsorption. Let us consider limiting cases for this value, assuming that there are approximately 400 beads ($M_l = 400$) in a layer with area $L_x * L_y = 400$. In the case of a perpendicular arrangement of the chains to the wall, in the near-wall layer each monomer unit belongs to a separate chain and $C_l = 400$, therefore $K_a = 1$. In the case of complete adsorption of all chains, $C_l = 40$, which leads to $K_a = 10$. The parameter K_a experiences significant changes only in the transition region in the whole system ($E < -3000$). At low energies ($E \approx -6000$ for U_{at_1}) $K_a \sim 10$, while for high energies near both the repulsive and attractive walls $K_a \sim 5$. Similar observations are made for the system U_{at_2} .

Thus, we can conclude that the points E^* , which were previously interpreted as special points on the dependence of the inverse temperature on energy (Fig.4.2), in fact, represents isotropic melt – two-dimensional crystal transition, rather than an isotropic melt – hexatic phase transition near the attractive wall. The argument in favor of this conclusion is the two-dimensional radial distribution function g_2^{2d} (Fig.4.10) in combination with the orientational correlation function g_6 (Fig.4.9) which indicate the presence of long-range orientational order. It was found that this process is not accompanied by chain adsorption. In addition, the density of the ordered wall layer ($Z = 9.5$) is higher than the density in the middle of the cell. Similarly, the density of crystalline domains is higher than the average density in the sample in the region of the crystallization transition in the bulk (will be shown in the section 4.2.3). However, the order of transition cannot be unambiguously defined in our system. Moreover, we cannot exclude the presence of two transitions (isotropic melt – hexatic phase – two-dimensional crystal), instead of one transition (isotropic melt – two-dimensional crystal). Since we are considering only the configuration part of the energy, which is very noisy, calculating the second derivative of entropy with respect to energy does not allow us to verify this conclusion. In addition, it is important to note that accounting for kinetic energy can affect the transition temperature [143]. The connectivity in the chain, the relatively high density of the systems, as well as the small size of the system also can significantly affect the analysis and the observed results.

4.2.2 Analysis of the 3d crystallization transition

Introducing the stiffness potential into our model systems results in chain elongation and increasing of anisotropic steric repulsion between neighboring chains, potentially leading to Onsager-type orientational ordering. This phenomenon depends on the density and rigidity of chains, as discussed in the Ref.[163]. To describe an ordering transition, the order parameter is computed using the Mayer-Saupe tensor:

$$S_{\alpha\beta} = \sum_{n=1}^{N_c} \sum_{i=1}^{N-1} \frac{1}{2} (3\hat{b}_{ni\alpha} \hat{b}_{ni\beta} - \delta_{\alpha\beta}), \quad (4.9)$$

where the $\hat{b}_{ni\alpha}$ represents α component of the unit vector along bond i in chain n . The largest eigenvalue of this tensor, denoted $S_1(E)$, serves as an orientational bond order parameter in the system. The direction associated with the corresponding eigenvector denotes the director of that order. In addition to this parameter, it is also useful to study the ordering of the vectors connecting the ends of the chains. To achieve this, we consider a tensor of the following form:

$$S_{\alpha\beta}^{\mathbf{r}_e} = \sum_{n=1}^{N_c} \frac{1}{2} (3\hat{r}_{n\alpha} \hat{r}_{n\beta} - \delta_{\alpha\beta}), \quad (4.10)$$

where the $\hat{r}_{n\alpha}$ represents α component of the unit vector along the vector \mathbf{r}_e connecting the ends of the chain n . The largest eigenvalue of the tensor Eq.(4.10) $S_{\mathbf{r}_e,1}$ defines the orientational order parameter for the end-to-end vectors \mathbf{r}_e .

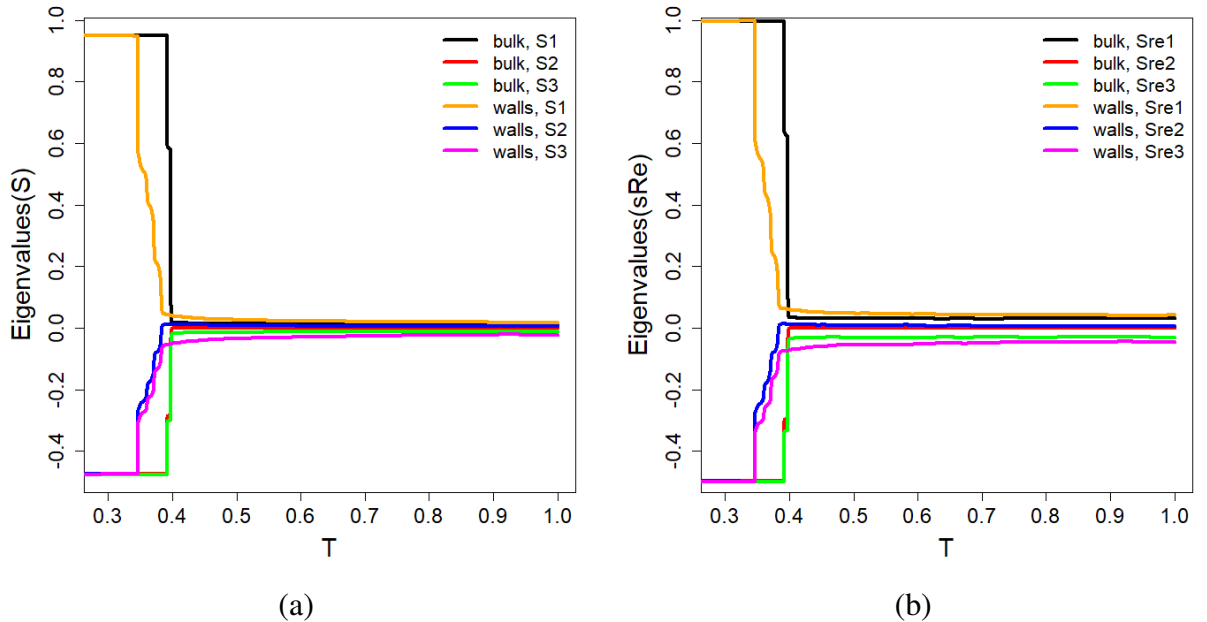


Figure 4.12: The temperature dependencies of eigenvalues of the orientation ordering tensor for the bond vectors (a) and for the end-to-end vectors (b).

From the obtained temperature dependencies (Fig.4.12) it is clear that the temperature,

at which sharp jumps in eigenvalues of $S_{\alpha\beta}$ and $S_{\alpha\beta}^{\mathbf{r}_e}$ are observed for a system without walls (black, red, green curves in Fig.4.12), coincides with the temperature T_t obtained from the dependence $C_v(T)$ (red curve in Fig.4.3 (a), $T_t = 0.395$). Consequently, the first-order transition in this system is accompanied by an abrupt change in the orientational order parameter. Small deviation of eigenvalues S_1 and $S_{\mathbf{r}_e1}$ near the value of 0.6 (black curves in Fig.4.12), as well as $S_{2,3}$ and $S_{\mathbf{r}_e2,3}$ about -0.3 (red and green curves in Fig.4.12) at $T_t \in [0.392; 0.398]$ can be explained in the same way as the doubling of heat capacity peaks: imperfect convergence of the function $\ln(g)$ at the moment. The value S_1 at low temperatures ($T < T_t$) is slightly smaller than the value $S_{\mathbf{r}_e1}$. This discrepancy arises due to slightly larger fluctuations in the orientation of the bond vectors, while the orientation of the vectors \mathbf{r}_e predominantly reflects the tendency of chains to elongate.

It is also interesting to compare these graphs with the graphs of a system with repulsive walls (orange, blue, magenta curves in Fig.4.12). In such a system, when we approach the transition region from above ($T > T_t$), there is a slight increase in the parameter S_1 , $S_{\mathbf{r}_e1}$ and a more pronounced decrease in the parameters S_3 , $S_{\mathbf{r}_e3}$, indicating a corresponding change in S_2 , $S_{\mathbf{r}_e2}$. Conversely, for a bulk system, as T_t approaches from above, all these parameters close to zero and when the temperature T_t is reached, a sharp jump in all parameters occurs. This observation suggests that the presence of repulsive walls promotes ordering. This effect becomes more noticeable on the energy dependencies (Fig.4.13).

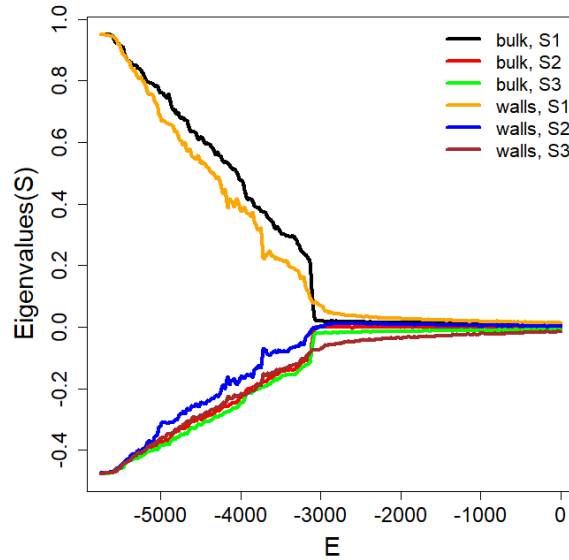


Figure 4.13: The energy dependencies of eigenvalues of the orientation ordering tensor for the bond vectors.

We attribute the presence of "humps" ($E \in [-4200; -3800]$ and $E \in [-3800; -3000]$) in the orange and blue curves to poor sampling of statistics in the transition region. Therefore, for a system with repulsive walls, we expect a clearer picture with continued data accumulation: a slight increase in S_1 , $S_{\mathbf{r}_e1}$ and a decrease in S_3 , $S_{\mathbf{r}_e3}$ along with the corresponding change in

S_2 , S_{r_e2} as the temperature decreases to T_l . When the transition temperature T_l is reached, we expect a prominent single jump in the orientation parameters. Although the walls contribute to increasing the transition temperature, the actual transition temperature is expected to be lower compared to the bulk system. This phenomenon is explained by the decrease in system density, as discussed earlier in section 4.1. It is expected that with a further decrease in temperature, the orientation parameters of both systems will coincide and approach 0.95.

Further validation of chain elongation at low temperatures based on eigenvalues $\lambda_1^j, \lambda_2^j, \lambda_3^j$ of the gyration tensor $G_{\alpha\beta}^j$ for the chain j , determined as follows:

$$G_{\alpha\beta}^j = \sum_{i=1}^N (r_{i\alpha}^j - r_{CM\alpha}^j) (r_{i\beta}^j - r_{CM\beta}^j), \quad (4.11)$$

where $r_{i\alpha}^j$ represents α component of the particle i within chain j , and $r_{CM\alpha}^j$ is α component of the center of mass of the chain j . Considering that the eigenvalues of the tensor are arranged in descending order $\lambda_1^j > \lambda_2^j > \lambda_3^j$, in order to analyze the system as a whole, we compute the mean of the corresponding eigenvalues across all chains within the system and use the following notation:

$$R_{g1,2,3}^2 = \frac{1}{N_c} \sum_{j=1}^{N_c} \lambda_{1,2,3}^j. \quad (4.12)$$

Drawing an analogy with the definition of the square of the gyration radius for a single chain, and relative shape anisotropy κ^2 , we apply the following definition:

$$R_g^2 = R_{g1}^2 + R_{g2}^2 + R_{g3}^2, \quad (4.13)$$

$$\kappa^2 = 1 - 3 \frac{R_{g1}^2 R_{g2}^2 + R_{g1}^2 R_{g3}^2 + R_{g2}^2 R_{g3}^2}{(R_{g1}^2 + R_{g2}^2 + R_{g3}^2)^2} \quad (4.14)$$

The parameter κ^2 reflects both the symmetry and dimensionality inherent in the polymer conformation. Its range is limited from 0 to 1, reaching a value of one for an fully elongated linear chain and decreasing to zero for spherical conformations. In the case of flat symmetrical objects, the relative anisotropy of the shape approaches the value of 0.25 [164].

In Fig. 4.14, the temperature dependencies of the parameters determined by the equations (4.12), (4.14) are presented. At low temperatures the parameter R_{g1} is approximately equal to 8. Drawing a rough analogy with the moment of inertia of the rod relative to the axis passing through its center $I_r = ml^2/12$, where $l = Nd = 10$ with $d = 1$ (diameter of beads) and $N = 10$ (number of beads in the chain), we get an estimate $I_r = 8.3$ in our case. Consequently, at low temperatures the square of the gyration radius R_g^2 is very close to the moment of inertia of the rod I_r . This observation provides evidence for chain elongation at low temperatures. We emphasize that this is only a rough estimate for this simple case, while for more complex configurations such a comparison is not appropriate. In addition, the chain elongation is evidenced by

the relative anisotropy of the shape (Fig.4.14(b)), which approaches unity. It is noteworthy that at high temperatures, the relative shape anisotropy κ^2 , as well as the values of R_{gi} ($i = 1, 2, 3$), indicate the absence of spherical symmetry, as expected for short chains with stiffness potential in our model. The transition between these two temperature regimes occurs abruptly at the same temperature $T_t = 0.395$ in the bulk system (black curves in Fig.4.14). Furthermore, the anisotropy coefficient κ^2 in the system with repulsive walls is slightly larger for $T > T_t$ (red curve in Fig.4.14 (b)).

This analysis suggests that the phase transition is accompanied by chain ordering and stretching, without implying additional internal changes, like, for example, coil-globule transition, as expected due to the potential and length characteristics of the chains.

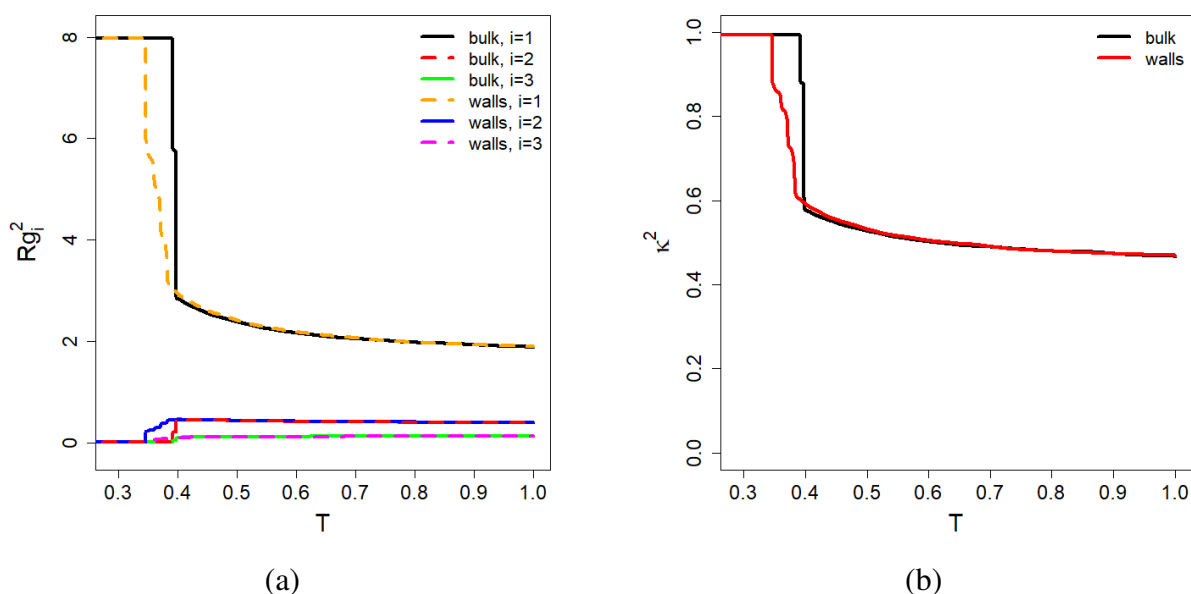


Figure 4.14: Temperature dependencies of the mean values of the eigenvalues of the gyration tensor across chains (a), and the relative shape anisotropy κ^2 (b)

To ascertain that the observed transition is an isotropic-crystal transition rather than, for instance, an isotropic-nematic transition, we will employ the method outlined in the section 3.5 for computing the modified Steinhardt local bond order parameters (NRLBO). Throughout the simulation, parameters q_4 , q_6 and q_8 were computed for each particle as described in section 3.5. Subsequently, the particles within the system were classified into two types of crystals and melt based on Tab.3.1. After this classification, the positions of the maxima in the distribution of parameters q_4 , q_6 , q_8 (e.g. Fig.3.16) for each type of particle were estimated.

The temperature dependencies of the fractions of particles belonging to different types are presented in Fig.4.15 (a). These dependencies reveal that at the transition temperature T_t , the ratio of crystalline and amorphous phases undergoes abrupt changes. Since in the temperature dependencies of both the number of crystalline and orientational order parameters (as well as local alignment parameters of segments, see the Appendix Fig.A17) we observe a jump from

the minimum value to the maximum, we can talk about the nucleation scenario (in the case of a system without walls, homogeneous nucleation).

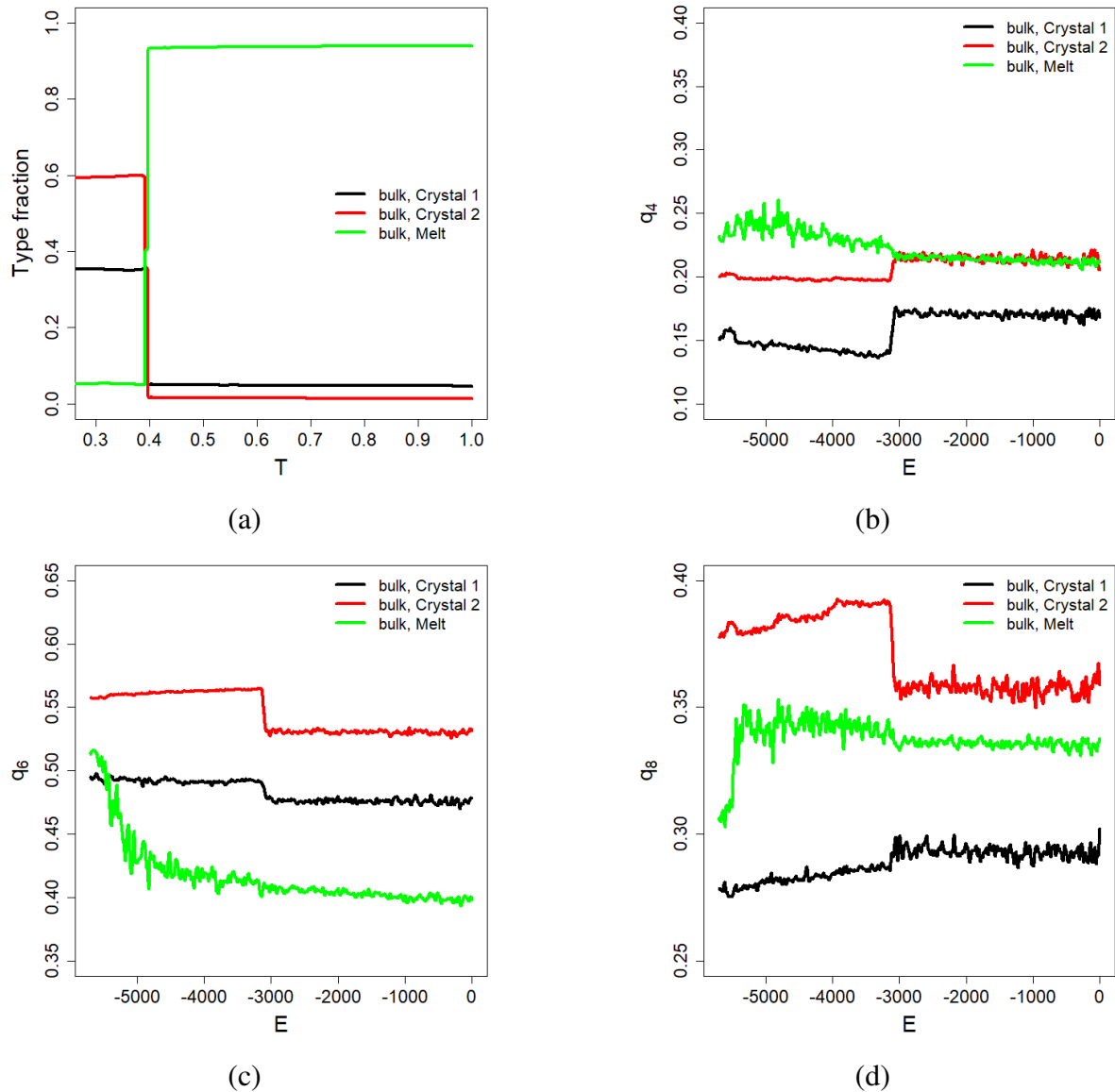


Figure 4.15: The temperature dependency of the proportion of particles assigned to different structure types based on the NRLBO parameters (a); the energy dependencies of q_4 (b), q_6 (c), q_8 (d) for the bulk system $L_x = L_y = 20$, $L_z = 19$.

Notably, the jumps on the energy dependencies of the parameters q_4 , q_6 , and q_8 (Fig.4.15 (b), (c), (d)) are somewhat speculative, as these values provide only a rough estimation of the maxima positions of their distributions. Consequently, in regions where only few particles belong to a particular phase (e.g., for the melt fraction at $T < T_i$ and for both crystal fractions at $T > T_i$), the parameter values are estimated less accurately. However, in regions with a substantial number of particles, the parameter values correspond to those listed in the Tab.3.1. We chose the estimate of the maximum position of the distribution as a representative parameter because of the asymmetry and width of the distributions of parameters q_4 , q_6 and q_8 , which can

distort the mean value of these distributions. Alternatively, median values could also be used, as they are less sensitive to outliers than mean values.

Analysis of the dependence of NRLBO parameters on energy (Fig.4.15) indicates that a sufficient number of particles of each structure type also helps to decrease fluctuations in these parameters. However, in regions of high energy ($T > T_t$) where the number of crystalline particles is extremely small, the estimation of distribution maxima is subject to significant fluctuations. So, for large number of particles parameters fluctuations are reasonably small.

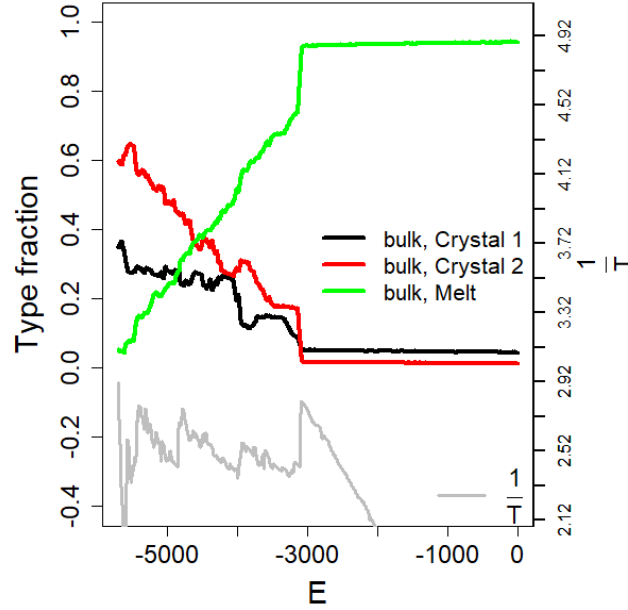


Figure 4.16: The energy dependency of the proportion of particles assigned to different structure types based on the Steinhardt parameters for the bulk system $L_x = L_y = 20$, $L_z = 19$.

Studying the dependence of particle fractions on energy reveals interesting patterns (Fig.4.16). While the fraction of the amorphous phase in the transition region ($E \in [-5700; -3100]$) changes monotonically (leading to a corresponding monotonic decrease in the total fraction of crystalline particles with increasing E), individual crystal types exhibit fluctuations corresponding to "steps" on dependence of the inverse temperature on energy ($E \in [-4000; -3100]$).

In addition, two important observations are noteworthy.

- Firstly, for *Crystal 2*, parameters q_6 and q_8 exhibit slight increases in the transition region with increasing energy (Fig.4.15 (c), (d)), making them somewhat more similar to the *fcc* crystal (see Tab.A1 in the Appendix).
- The proportion of particles attributed to *Crystal 2* predominates over those of *Crystal 1*.

We intend to delve deeper into these observations and offer our interpretation of this phenomenon in subsequent analyses in section 4.3.

Thus, the consistency between the NRLBO parameters and the classification of particles into classes by the proposed method supports the conclusion that the observed first-order phase transition, as depicted in the dependencies $1/T(E)$ and $C_v(T)$, represents an isotropic melt - crystal type transition. This finding aligns with the hypotheses proposed by T. Shakirov and W. Paul in similar systems [97]. Similarly, conclusions can be drawn from the dependencies of alignment of segments analysis (see the Appendix Fig.A17). At the transition temperature T_t , a sharp change in the ratio of the number of particles with aligned segments (bonds) is observed. Taken together, these findings confirm the phenomenon of crystallization. It is worth noting that due to the complexity of studying long-range translational order in polymers (where chain connectivity can complicate the process of "uniform" crystallization and lead to the formation of crystalline domains with different orientations), we focused on *local* parameters. However, we are convinced that such consideration in this model is justified.

Additional tests were conducted on this model for systems with different densities. Specifically, we examined small systems with low energy, comprised of $N_c = 90$ chains of length $N = 10$ in cubic boxes with sides $L = \{10.0, 10.5, 10.7\}$, corresponding to volume fractions $\phi = \{0.471, 0.407, 0.385\}$. Instead of providing an exhaustive analysis of these tests, we highlight the key finding that in all mentioned systems at low energies (temperatures), the orientational order parameters are notably high, even in the dilute system ($L = 10.7$, $\phi = 0.385$), exceeding $S_1 = 0.75$ for bond vectors and $S_{r_{e1}} = 0.85$ for end-to-end vectors. At the same time, the NRLBO parameters identify 65%, 2.5%, 1.5% of crystalline particles, while the alignment parameters determine 92%, 40%, 35% for densities $\phi = \{0.471, 0.407, 0.385\}$, respectively. This suggests that at low temperatures for low densities, a nematic phase is established, and an increase in density promotes crystallization, consistent with the predictions of T. Shakirov and W. Paul [97]. It is important to note that in their work and conclusions, the authors relied on the calculation of the parameter $|\psi_6|$ computed across the entire system, which to some extent characterizes long-range order. It is also notable that our tests applied noise reduction methodology (see section 3.5) to these test systems using the same parameters as in this study, without adapting to new volume fractions and noise levels in the systems. Despite this simplification, the proposed method using Steinhardt parameters reliably distinguishes between crystallization and nematic ordering.

All observations so far have related exclusively to the phase transition evident in the heat capacity. To clarify the rearrangements occurring in the transition region ($E \in [-5700; -3100]$), in particular the "steps" observed in the inverse temperature dependence (Fig.4.2 (a)), we performed a cluster analysis based on the alignment parameters.

4.2.3 Analysis of structural changes inside transition region

To study the structural changes that occur during the transition, we use clustering algorithm based on bond alignment parameters. These parameters provide partitions between

crystal and melt types very close to those obtained from Steinhardt parameters but are less computationally intensive. This approach proves to be an optimal solution for cluster analysis. This section demonstrates how this approach explains structural changes within the transition region ("steps" in Fig.4.2).

To implement this approach, the particles were initially classified into crystalline and amorphous phases, as described in section 3.7.4. Subsequently, clusterization was performed as follows:

- A particle i_1 assigned to the desired type (crystal or melt) was selected, and a cluster number was assigned to it.
- The nearest neighbors of the particle i_1 (particles within a radius of ($R_c = 1.3$)) were examined sequentially.
- Upon encountering a particle of the same type among these neighbors, which has not yet been assigned to any cluster, it was assigned to the current cluster, and the process extended to its neighbors.
- This procedure continued until all branches of the neighbors of i_1 were explored.
- Subsequently, a transition to the next particle of the same type (crystal or melt), i_2 , which is not assigned to any cluster, was executed, and the search for the next cluster ensued.

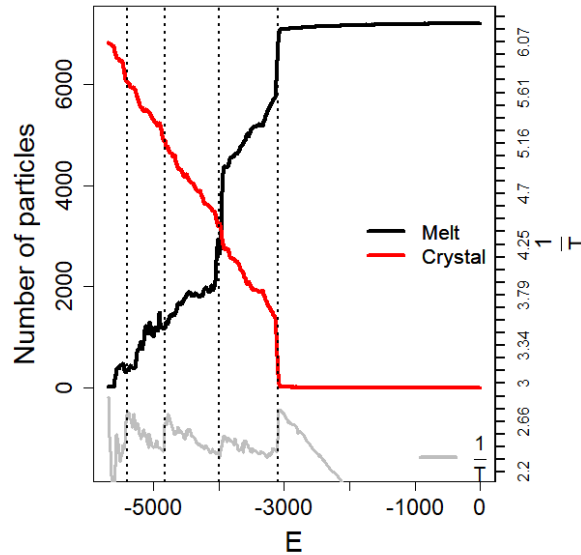


Figure 4.17: The number of particles assigned to the largest clusters of of crystal and melt based on the bond alignment parameters for the bulk system $L_x = L_y = 20$, $L_z = 19$. The inverse temperature dependency on energy is supplemented with a gray curve. The vertical dotted lines correspond to the boundaries of the "steps" on $T^{-1}(E)$.

After assigning each particle to a specific type and cluster, we select the largest cluster for each type based on the number of particles. Subsequently, we examine these largest clusters for both crystal and melt phases. While it is possible to conduct a more detailed cluster analysis for each specific configuration, our primary focus here is to identify common characteristics across certain energy ranges.

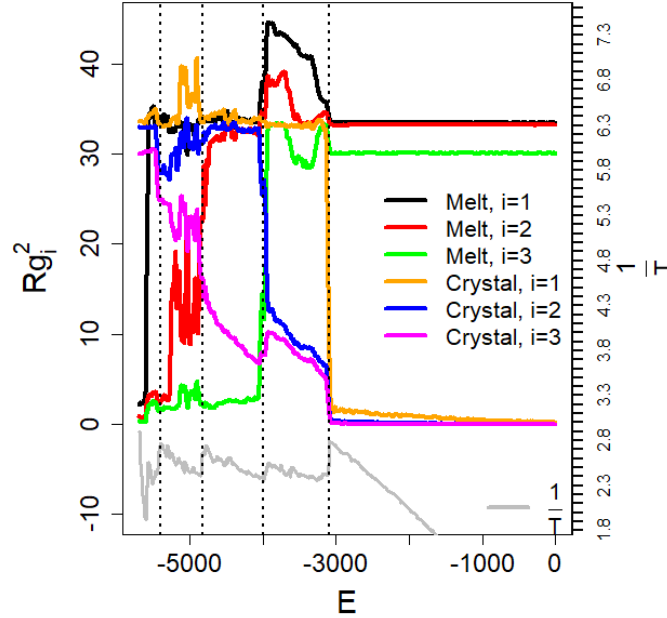


Figure 4.18: The eigenvalues of the gyration tensor of the largest clusters for crystal and melt based on the bond alignment parameters for the bulk system $L_x = L_y = 20$, $L_z = 19$. The inverse temperature dependency on energy is supplemented with a gray curve. The vertical dotted lines correspond to the boundaries of the "steps" on $T^{-1}(E)$.

Based on the inverse temperature dependence on energy, the entire energy range can be divided into 5 regions.

A The energy range $E = [-5760; -5400]$. The crystalline phase with a rare inclusion of molten particles is observed here. The largest molten cluster encountered during the simulation in this region comprises less than 500 particles, which accounts for less than 7% of the total number of particles. Conversely, the largest crystal cluster in this region encompasses 6835 particles, constituting almost 95% of the total. However, it is technically challenging to execute effective particles rearrangements in this energy regime. Introducing additional trial steps may potentially contribute to better rearrangements and the growth of the crystal cluster.

The eigenvalues of the gyration tensor for the crystal cluster in this region are extremely high, indicating that the cluster occupies the entire volume provided in the box. It is noteworthy that R_{g3}^2 is not equal to $R_{g1}^2 = R_{g2}^2$, which can be attributed to the asymmetry

of the box ($L_x = L_y = 20$, $L_z = 19$). Conversely, all eigenvalues for the molten cluster in this region are small.

- B The energy range $E = [-5400; -4820]$. In this region, an increase in energy triggers the formation of a molten cylinder. Consequently, R_{g1}^2 for the melt (the black curve in Fig.4.18) becomes large, while the other two values, R_{g2}^2 and R_{g3}^2 , are still small around the energy $E = -5400$. Subsequently, with further energy increasing, one of the dimensions of the gyration ellipsoid expands significantly, eventually leading to closure into a layer (increase in R_{g2}^2 of the melt, the red curve in Fig.4.18, at the right boundary of the considered region). Concurrently, the number of particles in the molten cluster continues to increase steadily. At the same time, a change in $R_{g1,2,3}$ in a crystal indicates a change in the shape of the crystalline part. Since the crystalline part itself is now the whole box containing a cylindrical pore of the melt, the principal axes of the of this object are no longer aligned with the axes of the simulation box. This leads to an increase in eigenvalue R_{g1} compared to the previous region.
- C The energy range $E = [-4820; -4000]$. The observation of two clusters (crystal and melt) forming layers in this region is substantiated by the increasing of parameters R_{g1}^2 , R_{g2}^2 (black, red, orange, blue curves in Fig.4.18), along with the small R_{g3}^2 (green and magenta curves). Additionally, R_{g3}^2 decreases for the crystal (magenta curve) with increasing energy, while it remains small for the melt (green curve). This observation suggests that the crystalline particles contribute to a smaller molten cluster as they undergo melting.
- D The energy range $E = [-4000; -3100]$. In the last region inside the transition region, the presence of a crystal cylinder is indicated by the large R_{g1}^2 and small R_{g2}^2 and R_{g3}^2 . The high eigenvalues of the gyration tensor for the melt cluster suggest its large size in all directions. The complex shapes of the curves within this region, as well as in a similar region with an amorphous cylinder (the region B), are associated with the orientation of the axes of the gyration ellipsoid of this cluster does not coincide with the axes of the simulating box. In such cases, the eigenvalues of the gyration tensor may exceed the values typical for the sides of the box.
- F The energy range $E = [-3100; 0]$. The prevailing phase here is the isotropic melt phase, with occasional inclusions of crystalline particles. Here, once again, we observe that the eigenvalue R_{g3}^2 of the cluster filling the sample (melt, green curve in Fig.4.18) is less than the other two (R_{g1}^2 , R_{g2}^2) due to the asymmetry of the box ($L_x = L_y = 20$, $L_z = 19$). Crystal clusters in this region consist of only a few particles, typically ranging from 1 to 5. It is noteworthy that in this area, the ratio of cluster sizes undergoes a jump at $E = -3100$ (Fig.4.17), indicating the exit from the phase transition region (Tab.4.1).

It would be interesting to perform a similar analysis for the system with repulsive walls ($L_x = L_y = L_z = 20$). Although the inverse temperature dependence on energy is not precise yet

due to not accurate convergence $\ln g$, rough estimates can still be made to predict changes in structure in the transition region.

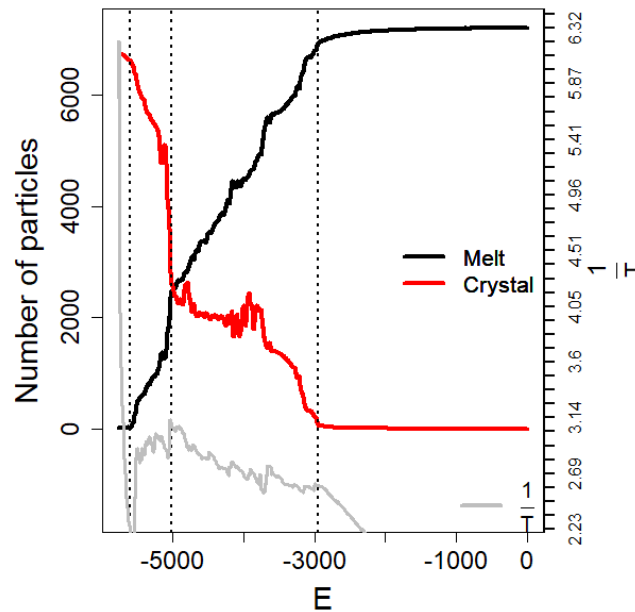


Figure 4.19: The number of particles assigned to the largest clusters of of crystal and melt based on the bond alignment parameters for the system with repulsive walls $L_x = L_y = L_z = 20$. The inverse temperature dependency on energy is supplemented with a gray curve. The vertical dotted lines correspond to the boundaries of the "steps" on $T^{-1}(E)$.

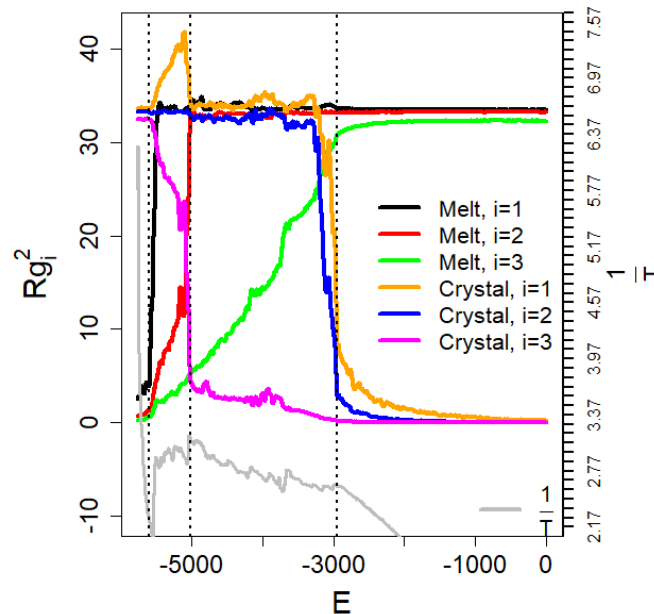


Figure 4.20: The eigenvalues of the gyration tensor of the largest clusters for crystal and melt based on the bond alignment parameters for the system with repulsive walls $L_x = L_y = L_z = 20$. The inverse temperature dependency on energy is supplemented with a gray curve. The vertical dotted lines correspond to the boundaries of the "steps" on $T^{-1}(E)$.

At present, four characteristic regions can be identified for this system.

- A The energy range $E = [-5760; -5600]$. In this narrow low-energy region, the predominance of a crystal filling the entire simulation box with single inclusions of molten particles is observed. All eigenvalues of the gyration tensor for the crystal cluster are large, while for the molten cluster, they are small (Fig.4.20). It is important to note that within our model, particles are termed "molten" if their bonds are insufficiently ordered. Indeed, within the framework of our model, the bond angles up to 26° contribute to the lowest energy, and the alignment criterion is set to an angle of 15° . As a result, the criterion for particle melting is quite strict.
- B The energy range $E = [-5600; -5020]$. In this region, eigenvalues $R_{g1,2}^2$ of the gyration tensor for the crystal cluster are large, while R_{g3}^2 for this cluster is small. It is anticipated that a molten cylinder with an oval cross-section may occur in this region, as R_{g1}^2 (the black curve in Fig.4.20) is significantly larger than the other two values, but R_{g2}^2 (the red curve) increases more rapidly than R_{g3}^2 with increasing energy.
- C The energy range $E = [-5020; -2950]$. In this area, the coexistence of crystalline and molten flat domains is observed. Upon transitioning to layers, the number of particles in a crystalline cluster drops by almost half (Fig.4.19). This decreasing is due to the fact that with the existence of the cylinder in the region B, the wall crystallites remain connected and belong to the same cluster. However, when a molten layer is formed, the crystal cluster is divided in two approximately equal-sized parts. As we analyze only the largest cluster, the size of such a cluster is halved. The eigenvalues for the molten and crystalline layers confirm the presence of flat domains (with large values of R_{g1}^2 and R_{g2}^2 , and small values of R_{g3}^2 (Fig.4.20). Additionally, the increase in R_{g3}^2 for the melt indicates an increase in the thickness of the layer.
- D The energy range $E = [-2950; 0]$. This region lies outside the phase transition (Tab.4.1). Here, the entire box is occupied by a melt with a small number of crystalline particles. Notably, in the extreme cases of low and high energies, all three eigenvalues R_{g1}^2 , R_{g2}^2 , R_{g3}^2 of the dominant structure are approximately equal, reflecting the symmetry of the box ($L_x = L_y = L_z = 20$).

Thus, when comparing a system without walls and with repulsive walls, a notable difference lies in the absence of a crystal cylinder in the latter. This disparity arises because the presence of walls promotes ordering and crystallization near the walls. Consequently, in systems with walls, as the energy decreases, crystals tend to form specifically in the wall layers. These structural changes in these two systems resemble the phenomena discussed in studies on evaporation/condensation transition in finite systems [67–69].

Concluding the discussion on structural changes, we will now consider density (volume fraction) profiles for specific configurations. As energy averaging is not feasible in a system

without walls, particularly due to the lack of dedicated directions in the system, we will focus solely on certain configurations of the system. Specifically, we will examine system configurations that were utilized to demonstrate the analysis methods outlined in the chapter "3 Methods of structural analysis".

Snapshots of these systems can be found in Tab. 3.3. Fig.4.21 shows the particle densities depending on the z coordinate for different energies ($E = \{-2040, -4715, -5104, -5727\}$). The blue color represents the particle density for the entire system, calculated in increments of 0.22 along the z axis using smoothing by the Epanechnikov kernel [161], as discussed in the section 3.7.3. The black and green curves correspond to the density profiles of crystalline particles (*Crystal 1* or *Crystal 2*) and melted particles determined by the Steinhardt method.

From the obtained dependencies, it is evident that at the lowest energies ($E = -5727$, Fig.4.21(a)), where the crystal is uniformly distributed throughout the volume, the density profile fluctuates around the average density $\phi = 0.496$ (horizontal magenta line). A similar pattern is observed for high energies outside the transition region ($E = -2040$, Fig.4.21(d)), where the sample is a melt with uniform inclusions of crystalline particles. Thus, outside the transition region, the densities of melt and crystal are equal to the average density of the system ($\phi = 0.496$ in this case). However, a change in the crystal-melt ratios in local regions alters the density profile. This effect is most pronounced for the energy $E = -4715$ (Fig.4.21(c)). In this configuration, a crystalline layer is observed in the center of the cell ($-5 \leq z \leq 5$), parallel to the z axis. This crystalline domain coexists with polymer melt domain ($-10 \leq z \leq -5$, $(5 \leq z \leq 10)$). From these dependencies (Fig.4.21(c)), it is evident that in the transition region the local density of the crystal phase is higher than the average density (the blue line in the center of the cell is above the magenta line), while the local density of the melt is smaller than the average density (the blue line at the edges of the cell is below the magenta line). In configurations with energy $E = -5104$, at $z = 5$, the number of crystalline particles is approximately equal to the number of melt particles, and these densities are almost compensated on average in the layer resulting in proximity of the blue and magenta lines.

Thus, it can be argued that in the transition region, the crystal has a slightly more dense structure, while the melt is more dilute compared to equilibrium homogeneous states in which the densities of the crystal and the melt are equal ($\phi = 0.496$). It is worth noting that this analysis fully correlates with the results presented in the Voronoi cell analysis for these systems (Fig.3.25).

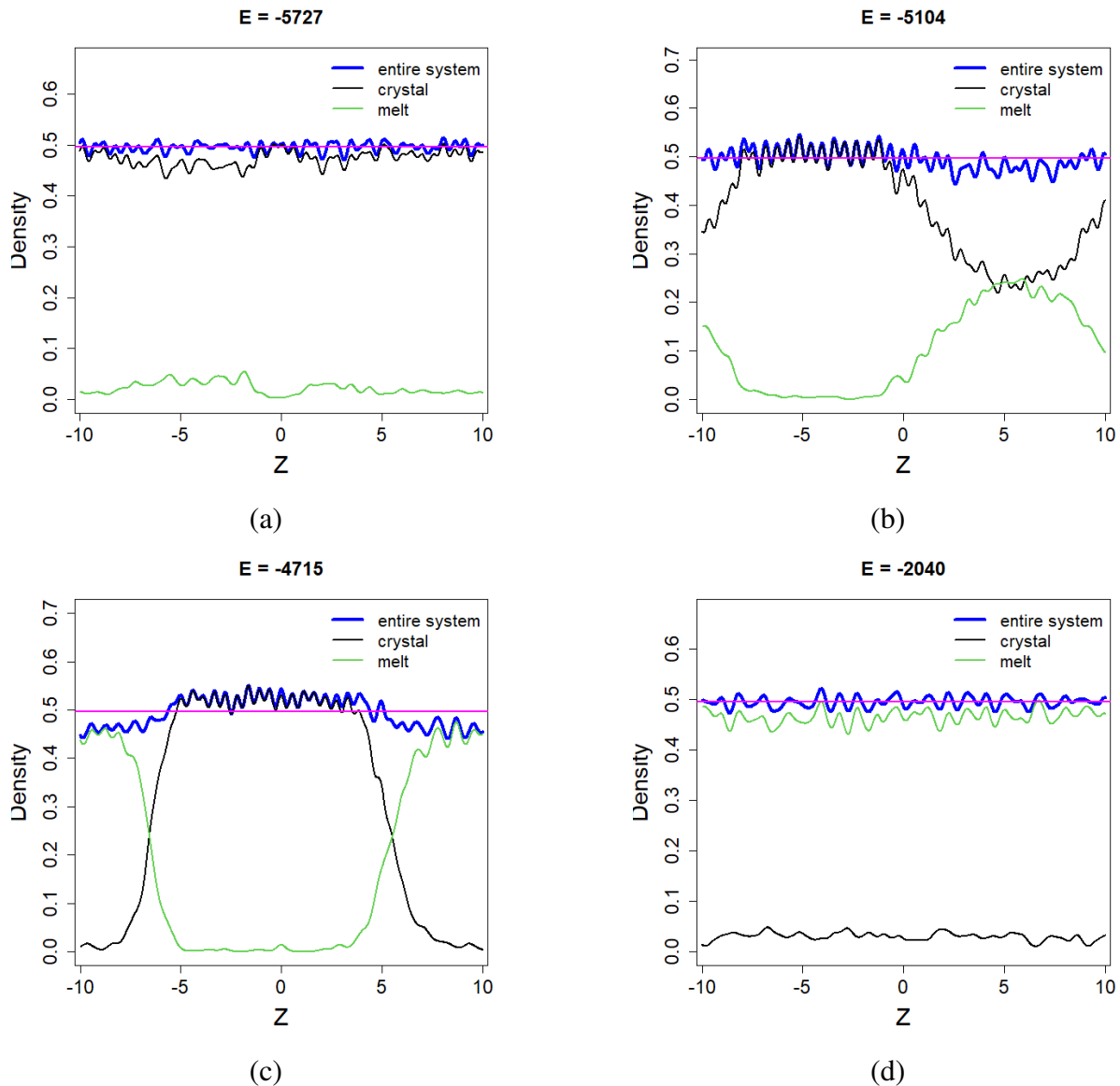


Figure 4.21: The density profiles for the bulk system ($L_x = L_y = 20$, $L_z = 19$). Magenta line shows the average density (volume fraction) in the system ($\phi = 0.496$).

4.2.4 Possibility of prefreezing phenomenon

As already mentioned, at the moment we do not have sufficient data to reliably determine not only the type, but also the number of transitions in systems with walls (we observe changes in the inverse temperature-energy dependence with time). However, in this section we will provide additional considerations about what transitions can occur in systems with walls when convergence is achieved.

Let us consider a zoomed representation of the dependence of heat capacity on temperature for a system with repulsive walls (the green curve at Fig.4.3 (a), Fig.4.22).

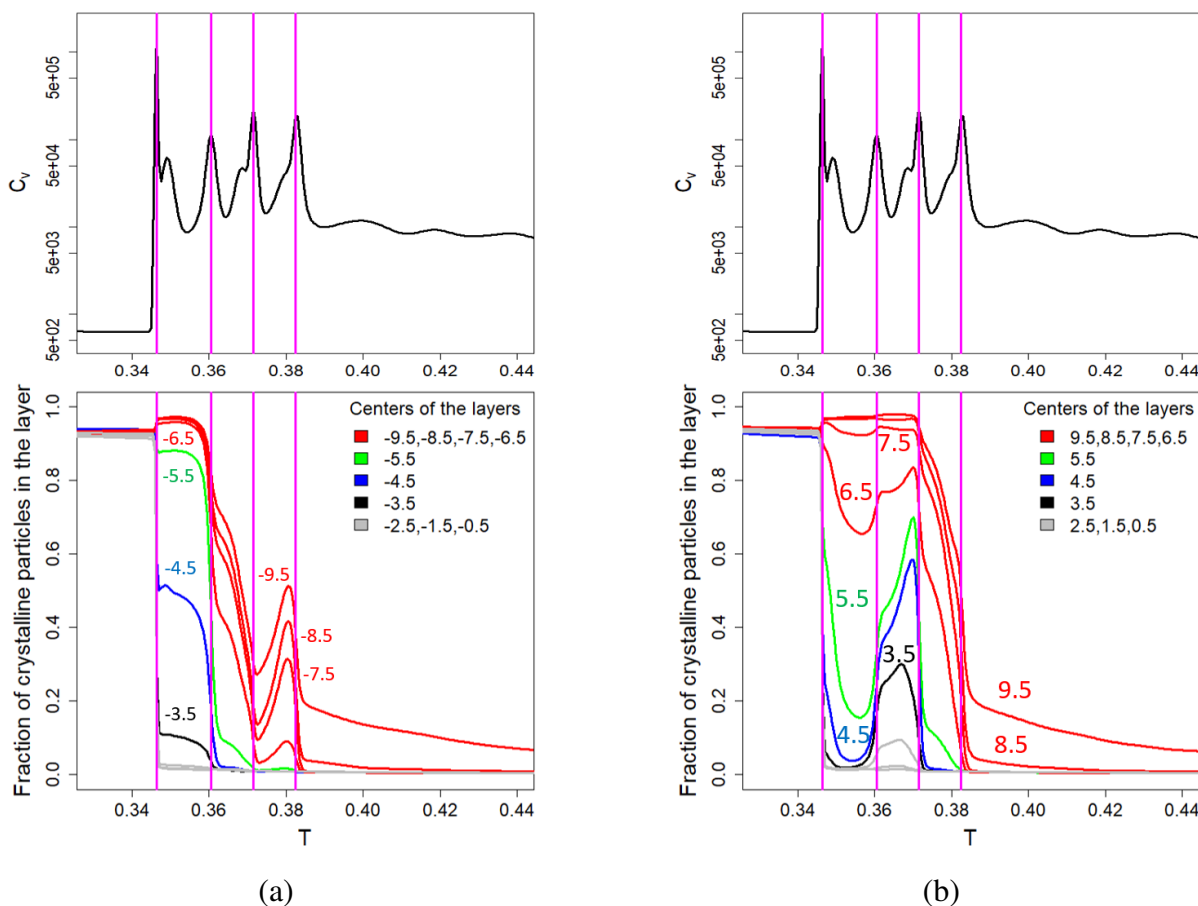


Figure 4.22: Layer-by-layer dependence of the fraction of crystalline particles on temperature for the system with repulsive walls with $L_x = L_y = L_z = 20$ for $z < 0$ (a), and for $z > 0$ (b). The magenta vertical lines correspond to the most prominent heat capacity peaks.

Along with this dependence, let us consider the layer-by-layer dependence of the fraction of crystalline particles on temperature. The crystalline particles here are determined according to the criterion of chain segment alignment analysis (see section 3.7.4). The thickness of all layers is equal to 1, the centers of the layers are shifted in increments of 1 (see legend in Fig.4.22). The magenta vertical lines correspond to the most pronounced heat capacity peaks. Fig.4.22 (a) and Fig.4.22 (b) correspond to halves of the box with negative and positive z coordinates. Note that since both walls in this case have the same repulsive potential, there is no reason for the absence of symmetry between these two pictures. However, we clearly different dependencies for both halves of the box (red curves jump at different temperatures in Fig.4.22 (a) and Fig.4.22 (b)). This fact once again points to the lack of statistical data. However, here we would like to emphasize the similarities on these figures: the first four layers near each wall (red curves) are clearly grouped and a jump in the fraction of crystalline particles occurs in all red curves simultaneously. This may indicate the phenomenon of prefreezing. The finite size effects have a significant impact on the ability to observe layer-by-layer crystal growth. Apparently, the size of our cell is not enough to observe this phenomenon. Instead, at the melting temperature T_m , several central layers will crystallize simultaneously (at the moment we are ob-

serving this effect, see the gray curves in Fig.4.22). Due to insufficient convergence, we cannot determine the prefreezing temperature T_{pref} as well as melting temperature T_m . We assume that if the prefreezing phenomenon occurs in this system, then with the subsequent accumulation of statistics only two peaks in the heat capacity remain, however, we cannot predict the temperatures at which these transitions will be observed (they will not necessarily coincide with the peaks that are visible at the moment).

At the same time, it cannot be ruled out that the size of the box along the x,y directions is too small to reliably distinguish the formation of a large crystalline droplet (as in the case of heterogeneous nucleation) from the formation of truly crystalline layers (prefreezing phenomenon). In other words, in a system with repulsive walls, two difficult to distinguish scenarios are possible:

- Structural transitions within a single phase transition at T_m (with the observation of a single loop in dependence of inverse temperature on energy). This scenario is similar to that observed in a system without walls and is discussed in section 4.2.3. That is, these four observed layers could be part of a crystalline droplet on the surface (in this case, the size of the system does not allow us to see the entire droplet). In this case all peaks on heat capacity will collapse at T_m .
- A prefreezing phenomenon. In this case two transition temperatures and a sequence of two loops will be observed.

A similar consideration was carried out for the system with an attractive wall U_{at_1} (Fig.4.23). The main difference between an attractive and a repulsive wall is the formation of a two-dimensional crystalline layer, as discussed in section 4.2.1 ($T^* \approx 0.457$). In contrast, the dependencies for negative and positive z give a more symmetric picture in the transition region than for the system with repulsive walls (Fig.4.22). Near walls, both attractive and repulsive, four layers crystallize simultaneously (red curves in Fig.4.23). Together with the current shape of the inverse temperature for this system and the heat capacity, we tend to assume that the phenomenon observed in this system is the prefreezing.

Note that we cannot rule out more complex behavior of the systems, which will require additional research. Reliable conclusions for all systems with walls require more computational time and consideration of larger systems.

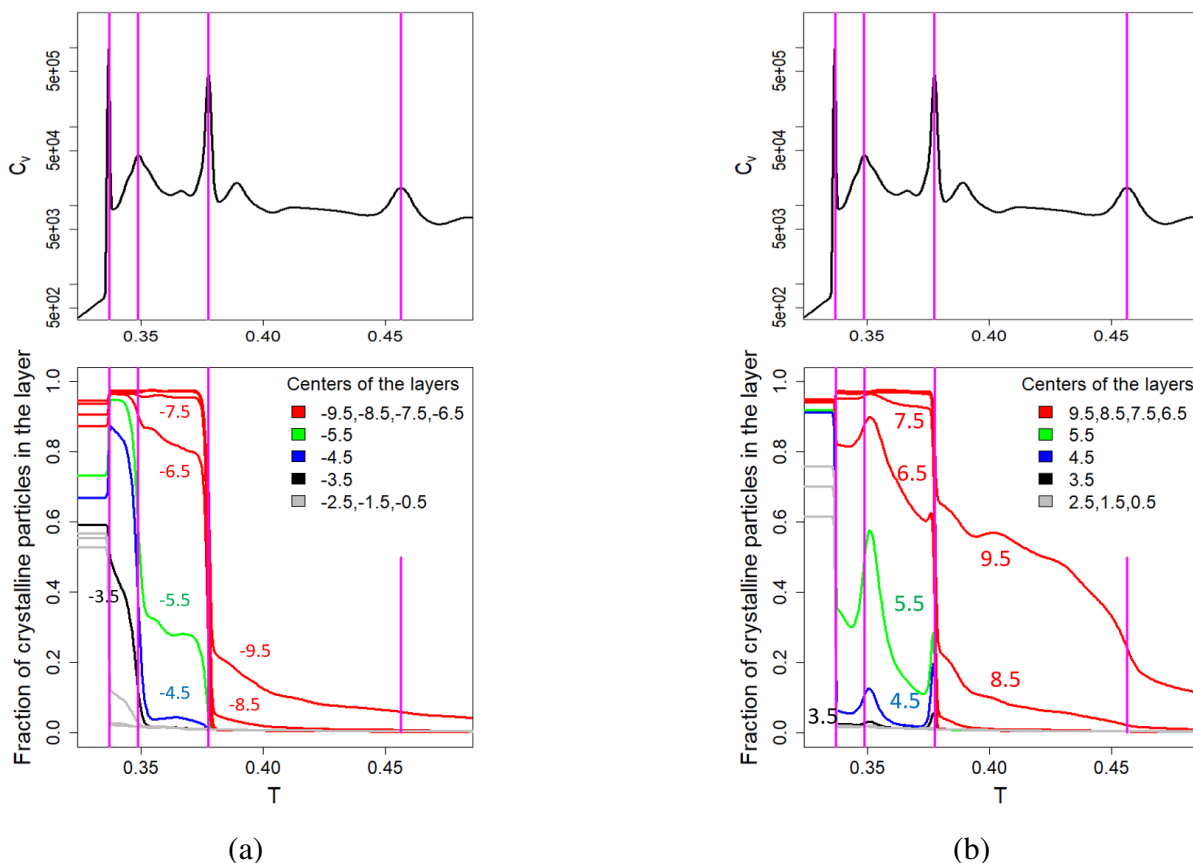


Figure 4.23: Layer-by-layer dependence of the fraction of crystalline particles on temperature for the system U_{at1} $L_x = L_y = L_z = 20$ for $z < 0$ (a), and for $z > 0$ (b). The magenta vertical lines correspond to the most prominent heat capacity peaks.

4.3 Transition analysis findings and predictive insights for various systems: a comprehensive summary

The previous sections have provided considerable insight into the behavior of small systems, both with repulsive walls ($L_x = L_y = L_z = 20$, $\phi = 0.471$) and without walls ($L_x = L_y = 20$, $L_z = 19$, $\phi = 0.496$), during phase transitions (Tab.4.1, Tab.4.2). Notably, accurate convergence allowed for reasonable precise determination of the first-order transition temperature $T_t = 0.395 \pm 0.003$ for the system size of $L_x = L_y = 20$, $L_z = 19$ without walls ($\phi = 0.496$). Comparison with other studies [97] has shown that an increase in density contributes to an increase in the transition temperature ($T_t = 0.326 \pm 0.001$, $\phi = 0.471$). Analysis of orientational parameters, gyration tensor eigenvalues, NRLBO parameters and chain segments alignment parameters elucidated the transition characteristics, revealing a concomitant orientation ordering and chain stretching alongside translational ordering — a hallmark of an isotropic-crystal transition.

Further study of the transition region revealed several distinct transitions in systems without walls: from a stable crystalline state (outside the transition region) throughout the sam-

ple to the appearance of an isotropic melt cylinder inside the crystal, followed by the coexistence of crystalline and isotropic melt layers, further formation of a crystalline cylinder inside the isotropic melt leads, eventually to a stable fully molten state (outside the transition region). In contrast, systems with repulsive walls exhibit similar transitions, excluding the formation of a crystalline cylinder within the melt due to the ordering effects induced by the walls favoring crystallization at the walls. These structural changes resemble the phenomena discussed in papers on evaporation/condensation transition in finite systems [67–69]. Indeed, the observed transitions can be attributed to a multitude of factors inherent to the system under study. Several key factors include:

- **System size:** The final size of the system plays a crucial role in determining the observed transitions. Small systems exhibit distinct behavior compared to larger ones due to finite-size effects.
- **Potentials:** The choice of interaction potentials within the system significantly influences its behavior. Factors such as the strength, range, and functional form of potentials, including the chain stiffness potential, dictate the system behavior and stability.
- **Chain length and system size correlation:** The correlation between chain length and system size is another crucial factor. The interplay between the length of polymer chains and the size of the system can lead to unique structural arrangements and phase behaviors.

By considering these factors, we can better understand the underlying mechanisms driving the observed transitions and elucidate the complex interplay between system parameters in confined systems.

Inside the transition region, the number of particles of the *Crystal 2* increased with increasing energy and approached the *fcc* crystal in terms of parameters q_4 , q_6 , q_8 . This phenomenon can be ascribed to the influence of the system size and shape on crystal structure. In low-energy regions, where crystallization predominates, the simulation box size significantly affect crystal formation, prompting crystals to adapt to the box constraints and optimize interactions with the employed potentials. Consequently, inside the transition region, the melt phase exhibits decreasing density, allowing for the creation of favorable crystal structures within the available space. This suggests a decreasing impact of the simulation box size on crystal formation process in this phase transition. Moreover, given previous results [30, 72, 165, 166] demonstrating the coexistence of *fcc* and *hcp* structures in hard spheres, coupled with evidence indicating a slight gain in free energy for *fcc* structures, it is plausible to assume that the chain connectivity and stiffness potential in our model further favors *fcc* crystal structures.

In systems without walls ($L_x = L_y = L_z = 20$), characterized by lower densities ($\phi = 0.471$) as explored in previous studies [97], we anticipate observing similar structural transitions accompanied by corresponding changes in eigenvalues of gyration tensor of the largest clusters. In regions outside the transition, for systems with symmetrical boxes ($L_x = L_y = L_z = 20$),

the eigenvalues are expected to exhibit uniformity $R_{g1} = R_{g2} = R_{g3}$ (as in the small system ($L_x = L_y = L_z = 20$) with repulsive walls Fig.4.20 A, D). At the same time for asymmetric box ($L_x = L_y = 20, L_z = 39$) the interpretation of $R_{g1,2,3}$ can be complicated. However, the finite size effect in such case (bulk, $L_x = L_y = 20, L_z = 39$) is likely to influence the arrangement of the cylinders, whether crystalline or molten. We assume that the cylinder axes are directed along the short axes of the box, which greatly simplifies data analysis. For systems with both repulsive and attractive walls, we expect a continuation of the tendency for crystallization at the walls, especially evident in small systems with repulsive walls ($L_x = L_y = L_z = 20$).

In larger systems with repulsive walls ($L_x = L_y = 20, L_z = 40$) and bulk ($L_x = L_y = 20, L_z = 39$), we expect a singular first-order phase transition from an isotropic melt to a crystal. Nevertheless, we cannot definitely exclude the phenomenon of prefreezing in a system with repulsive walls. At the same time, for systems with attractive walls, the preliminary observations of the dependence of inverse temperature on energy (Fig.4.2) and temperature dependencies of heat capacity (Fig.4.3, Fig.4.4) do not rule out the possibility of the second phase transition (close to crystallization in bulk), i.e. prefreezing, which would require additional study. It cannot be excluded that a more accurate convergence of the function $\ln g$ will show two phase transition temperatures in the intervals $T_{t1,2} \in [0.337; 0.378]$ for U_{at1} , and $T_{t1,2} \in [0.316; 0.396]$ for U_{at2} . One of these transitions may turn out to be prefreezing ($T_{pref} > T_m$), and the other is complete crystallization in the entire sample at melting point T_m . Another possible scenario for the implementation of two consecutive transitions is the following: isotropic melt – nematic – crystal. However, despite the fact that we do not exclude such a scenario, at the moment, from the available data, we tend to assume that prefreezing scenario will be observed in these systems. Obtaining more precise insights into these systems would necessitate a significant increase in computational time, estimated optimistically at approximately 1-2 years. Despite ongoing efforts to optimize the data accumulation process, progress has been limited, although progress in technology may expedite these tasks in the future.

In systems with an attractive wall ($U_{at1}, U_{at2}, L_x = L_y = L_z = 20$), additional ordering of the only near-wall layer was revealed at temperatures ($T^* = 0.457 \pm 0.002$ for U_{at1} , and $T^* = 0.905 \pm 0.007$ for U_{at2}) above the crystallization temperature in the bulk ($T_t = 0.326 \pm 0.001$) of the same density $\phi = 0.471$. The formation of a two-dimensional crystal near the attractive wall is confirmed by the characteristic dependence of the two-dimensional radial distribution function g_2^{2d} , as well as the orientation correction function g_6 . An unambiguous determination of the type (order) of the transition is hardly possible due to the small size of the system and the resolution of the method. Also we do not rule out a sequence of two very close transitions (isotropic melt – hexatic – two-dimensional crystal).

Note that we also cannot interpret this phenomenon (transition at T^*) as prefreezing. In the case of prefreezing, usually several crystalline layers are formed abruptly (while we observe only one), and then, with a decreasing temperature, the thickness of the crystallized layer gradually increases. On contrary, in our case, the second crystalline layer is formed together

4.3. Transition analysis findings and predictive insights for various systems: a comprehensive summary

with the third and fourth ones in the region of the phase transition T_t of crystallization in the bulk (see Fig.4.23 and Appendix Fig.A15). A more strong argument is that the layer of a two-dimensional crystal formed near the attractive wall changes its structure with decreasing energy and approaching the transition region in the entire system (Fig.4.9 (a), Fig.4.10 (a)).

Finally, for all systems with walls we cannot exclude the phenomenon of prefreezing in the transition region indicated in the Tab.4.2. We observe the simultaneous formation of four crystalline layers near the walls, both in the U_{at_1} system (Fig.4.23) and in the system with repulsive walls Fig.4.22). However, this change may be associated with both the phenomenon of prefreezing and the formation of a nucleus of a critical size in the case of heterogeneous nucleation. In the first case, we expect a sequence of two first-order transitions. In the second case, one transition temperature and the presence of structural transitions depending on energy are expected, as observed in a system without walls and as described in section 4.2.3. Note that the size of the system plays the crucial role and may not be sufficient to observe the nucleus (crystalline droplet) near the wall. In this sense, it is easy to confuse then nucleus (crystalline droplet) with the layer. At the moment, we cannot accurately determine the number and type of transitions due to the lack of accumulated data. The results of this chapter will be published in [F4].

Chapter 5

Conclusion and outlook

The previous two chapters presented the results of the study and development of methods for analyzing crystal structures in computer simulation (Chapter 3), and the results of computer simulation (Chapter 4) for melts of semiflexible chain of tangent hard spheres in the bulk and in thin films between different walls (purely repulsive and with two magnitudes of attraction).

Studying different crystallization scenarios (heterogeneous nucleation or prefreezing) near a substrate requires the ability to reliably distinguish crystal structures (characterized by both orientational and translational ordering) from nematic states (characterized only by orientational ordering) and isotropic melt. Since polymer systems are characterized by polycrystallinity, it is not always possible to detect long-range translational ordering, so we focused on local structural parameters. Our computer simulation studies have shown that the presence of significant fluctuations in particle positions (for example, due to thermal fluctuations), which we call *noise* in the system, makes it ineffective to use a number of modern methods for analyzing crystal structure. These methods include well-known variations of common neighbor analysis [105–108], the classical method of calculating Steinhardt parameters [102], as well as modifications of this method [103, 104]. We examined how strongly the average characteristics of the methods (such as parameter values, the number of neighbors of the particles under study) deviate from the known values of unnoisy test structures (*sc*, *fcc*, *bcc*, *hcp*) depending on the magnitude of Gaussian noise, and also estimated the dispersion of these values. Thus, we have shown the effectiveness of each of these methods depending on the noise magnitude, which allows to talk about the scope of application of a particular method.

Among the studied methods, good resolution for our systems was demonstrated by the local chain segments (bonds) alignment analysis [40, 48]. However, this method is focused on distinguishing bond alignment (which is essentially close to orientational ordering, but not to translational one). Thus, this method does not guarantee the distinction of crystalline domains (combining orientational and translational ordering) from nematics with a high degree of orientational ordering of bond vectors, but lacking translational ordering. Additional studies on test small model systems ($N_c = 90$ chains) of different densities have proven that in low-density systems, where nematic ordering is expected [97], this method also identifies particles with lo-

cal bond alignment analysis. Thus, this method can only be used to determine crystal structures in combination with other methods. As a consequence, this method is also unable to distinguish between different classes of symmetries. The lack of suitable tools for analyzing crystal structures in the presence of noise prompted us to develop a method to reduce the effective noise in the system. This method is based on the Steinhardt parameters, as applied to the averaged coordinates of particles within the second coordination sphere (NRLBO parameters). We demonstrated on test structures (*sc*, *fcc*, *bcc*, *hcp*) that this method allows to determine the type of noisy structure with high accuracy. The results of using this method are in good agreement with the results of the bond alignment analysis in the studied polymer model systems (THS).

Additionally, a method that makes it possible to reconstruct crystal lattices from the average positions of particles of a noisy structure was proposed. The structures were constructed using the three translation vectors and two base points, and they correlate well in Steinhardt parameters with the original noisy structure under study. This technique is of significant importance, as it enables to establish a relationship between the structures observed in computer simulations and those observed in real experiments. This can be achieved, for example, by calculating the structure factor and comparing it with the results of a scattering experiment.

Therefore, the Chapter 3 contains an extensive methodological research. The original scientific results presented in this part are also of great value and can be widely used in the analysis of structures in computer simulation of crystallization in different systems.

In the Chapter 4, the results on computer simulations of semiflexible polymers in bulk and in films conducted using the SAMC method were presented. The analysis demonstrated that reliable results for systems with walls in the transition region require a greater computational investment. Concurrently, the simulation of the system without walls ($L_x = L_y = 20, L_z = 19$) yielded satisfactory results, enabling the reliable drawing of conclusions about the transition region.

In a system without walls ($L_x = L_y = 20, L_z = 19, \phi = 0.496$), a single first-order isotropic melt – crystal phase transition is observed at $T_m = 0.395 \pm 0.003$, and the scenario of nucleation and growth occurs. An increase in density contributes to an increase in the phase transition temperature (from $T_m = 0.326 \pm 0.001$ at $\phi = 0.471$ to $T_m = 0.395 \pm 0.003$ at $\phi = 0.496$). Inside the transition region, as energy increases, a structural reorganization is observed. Namely, in the region of low energies (energies below the energies of the transition region), a completely crystallized state is observed. As the energy increases, a molten cylinder is formed, which then develops into a molten layer. The last region inside the transition region is characterized by the presence of a crystalline cylinder inside an isotropic melt. Finally, when the energy is higher than the energy of the transition region, the entire sample is completely melted. It can be considered that such a structural transformation is analogous to the growth of a nucleus during nucleation. The complex shape of crystalline domains is mainly related to the finite size of the system and the length and stiffness of the chains. These structural changes in these two systems resemble the phenomena discussed in studies on evaporation/condensation

transition in finite systems [67–69].

An analysis of the NRLBO parameters for the system without walls ($L_x = L_y = 20$, $L_z = 19$, $\phi = 0.496$), calculated according to the method developed in Chapter 3, showed that the two types of crystals formed in the system at low energies are close to *fcc*, *hcp* crystals, with the dominance of an *fcc*-like crystal. However, due to the finite size effect of the system, these structures are distorted. At the same time, with increasing energy and the formation of molten domains, the dominant crystal structure (*fcc*-like crystal) becomes more similar to *fcc* in terms of Steinhardt parameters. This becomes possible due to the redistribution of local density in the system: the isotropic melt domain has a lower density compared to the average density in the system. Due to this, the influence of the simulation box size on the crystal is reduced, which acquires the ability to organize the most advantageous structure (*fcc* crystal) with a higher local density. Thus, our results are in agreement with a number of studies that reveal the dominance of the *fcc* structure in hard sphere models [30, 32, 72, 165, 166].

Similar structural transformations inside the transition region are also typical for a system with repulsive walls ($L_x = L_y = L_z = 20$, $\phi = 0.471$). The significant difference in structural transformations is only in the absence of a region of coexistence of a crystalline cylinder inside the melt. This feature is caused by the fact that the presence of walls promotes the orientation of chains near the walls. It can be argued that the presence of walls promotes also crystallization, since the melting point ($T_m = 0.365 \pm 0.025$) in this system tends to be higher compared to the transition temperature ($T_m = 0.326 \pm 0.001$) for a system without walls of the same density ($\phi = 0.471$). Despite the fact that the data in the transition region for a system with repulsive walls cannot be considered reliable at the moment, we tend to assume that the observed transition is a single first-order isotropic melt – crystal phase transition according to the heterogeneous nucleation scenario, since the structural transformations inside the transition are similar to those in the system without walls. However, it cannot be completely ruled out that continued accumulation of data in the transition region will not reveal the prefreezing phenomenon. That is, our observations do reveal the abrupt formation of four near-wall crystalline layers. Nevertheless, since the temperature of this transition cannot be established at this time, we do not dare to draw a clear conclusion about the presence or absence of prefreezing.

Similarly, larger systems ($L_x = L_y = 20$, $L_z = 39$, $\phi = 0.496$ without walls and $L_x = L_y = 20$, $L_z = 40$, $\phi = 0.471$ with repulsive walls) have not achieved sufficient accuracy of the density of states function $\ln g$. This is confirmed by large fluctuations in the dependence of heat capacity on temperature (see the Appendix Fig.A13). Currently, estimates for the transition temperature for a bulk system ($T_m = 0.366 \pm 0.026$, $L_x = L_y = 20$, $L_z = 39$, $\phi = 0.496$) are slightly lower than for a similar smaller system ($T_m = 0.395 \pm 0.003$, $L_x = L_y = 20$, $L_z = 19$, $\phi = 0.496$). Most likely, this observation reflects the correct trend, since the small size of the system can promote ordering (and consequently crystallization in this case) through periodic boundary conditions. This conclusion correlates with the results of the work [97]. At the same time, for a large system with repulsive walls ($L_x = L_y = 20$, $L_z = 40$, $\phi = 0.471$), the estimate

($T_m = 0.356 \pm 0.04$) is less accurate and cannot be reliably interpreted.

In a system with a weak wall attractive potential ($U_{at_1}, L_x = L_y = L_z = 20, \phi = 0.471$) there is a hint of two closely lying first-order phase transitions ($T_{t1} = 0.378 \pm 0.025$ and $T_{t2} = 0.337 \pm 0.025$). We revealed the abrupt formation of four near-wall crystalline layers, which could indicate the prefreezing phenomena. To confirm this assumption, a more precise estimation of the density of states function is necessary. In case of prefreezing, it will be possible to determine the temperatures T_{pref} (which will be equal to T_{t1} in the case of pre-freezing) and T_m (which will be equal to T_{t2}) for the given size and density of the system. However, at the moment, discussions about the transition scenario are speculative. In a system with a strong attractive potential ($U_{at_2}, L_x = L_y = L_z = 20, \phi = 0.471$), we can only give a rough estimate of the temperature range over which the first order transition(s) is (are) expected ($T_t \in [0.316; 0.396]$).

However, despite the inaccuracy of data inside the transition region for both attractive systems, an additional transition was discovered, indicating two-dimensional crystallization of the near-wall layer ($T^* = 0.457 \pm 0.002$ for U_{at_1} , $T^* = 0.905 \pm 0.007$ for U_{at_2}). We have found that the structure of this layer has local ordering, as well as long-range six-fold orientational ordering. It should be noted that the obtained temperatures may vary slightly due to the refinement of the transition region, as the entire energy range is of significance when calculating the heat capacity. The resolution of the our approach does not allow draw conclusion about the order of transition in our system. We also cannot rule out the presence of two very close transitions (isotropic melt - hexatic phase - two-dimensional crystal), instead of one transition (isotropic melt - two-dimensional crystal).

Thus, despite the rather simplified model used, the technical features of the SAMC method require more computational time to obtain a detailed picture of all systems under study. In the dissertation, an analysis of the results obtained so far has been performed. However, it should be noted that the accumulation of further data may reveal more complex effects.

Based on the results of our work, we can formulate the following outlook for future studies.

Outlook

Since the scenario of prefreezing in polymer systems has not been sufficiently studied by computer simulation methods, this area represents a wide field for possible research. As was shown in this work, the SAMC method is time-consuming and requires significant computational costs, but it provides accurate information about the equilibrium state of systems. The use of more modern technologies in combination with additional simulation techniques, such as new sampling techniques [99], or dividing the energy interval into a larger number of segments computed in parallel, can help reduce computation time. A logical continuation of this work would be to study systems of larger size (for example, $L_x = L_y = 20, L_z = 40$) with attractive walls, since increasing the size of the system contributes to a better understanding

of processes in the thermodynamic limit. Since studies show that the prefreezing scenario can also occur in systems with a structured substrate [12, 10], it is interesting to consider how the (in)commensurability of the substrate pattern and the characteristic size of the polymer chain monomers (beads) influence the crystallization process.

Finally, to compare the results of simulation and experiment, it is interesting to consider a slightly more detailed model of a polymer, for example, polyethylene [12], near different walls (purely repulsive, purely attractive with different attractive potentials, as well as substrates with different patterns, including those simulating the geometry of graphite).

All such studies can contribute to the understanding of the crystallization process and complement the existing understanding with the relationship to the microscopic parameters of the system.

Bibliography

- [1] G. Reiter and J.-U. Sommer (Eds.). *Polymer Crystallization: Observations, Concepts and Interpretations. Lecture Notes in Physics*. Springer Verlag, 2003. doi: <https://link.springer.com/book/10.1007/3-540-45851-4>.
- [2] G. Reiter and G. R. Strobl (Eds.). *Progress in Understanding of Polymer Crystallization*. Springer Verlag, 2007. doi: <https://doi.org/10.1007/3-540-47307-6>.
- [3] M. Muthukumar. Nucleation in polymer crystallization. *Advances in chemical physics*, 128:1–64, 2003. doi: 10.1002/0471484237.ch1.
- [4] M.C. Zhang, B.-H. Guo, and J. Xu. A review on polymer crystallization theories. *Crystals*, 7(1):1–37, 2017. doi: 10.3390/cryst7010004.
- [5] H. Li and S. Yan. Surface-induced polymer crystallization and the resultant structures and morphologies. *Macromolecules*, 44(3):417–428, 2011. doi: 10.1021/ma1023457.
- [6] J. C. Wittmann and P. Smith. Highly oriented thin films of poly(tetrafluoroethylene) as a substrate for oriented growth of materials. *Nature*, 352:414–417, 1991. doi: 10.1038/352414a0.
- [7] R. P. Sear. Nucleation: theory and applications to protein solutions and colloidal suspensions. *Journal of Physics: Condensed Matter*, 19(3):033101, 2007. doi: 10.1088/0953-8984/19/3/033101.
- [8] R. P. Sear. The non-classical nucleation of crystals: microscopic mechanisms and applications to molecular crystals, ice and calcium carbonate. *International Materials Reviews*, 57(6):328–356, 2012. doi: 10.1179/1743280411Y.0000000015.
- [9] M. Iwamatsu. Heterogeneous critical nucleation on a completely wettable substrate. *The Journal of Chemical Physics*, 134(23):234709, 2011. doi: 10.1063/1.3599710.
- [10] M. Heni and H. Löwen. Surface freezing on patterned substrates. *Physical Review Letters*, 85(17):3668, 2000. doi: 10.1103/PhysRevLett.85.3668.

- [11] A. K. Löhmann, T. Henze, and T. Thurn-Albrecht. Direct observation of prefreezing at the interface melt–solid in polymer crystallization. *Proceedings of the National Academy of Sciences*, 111(49):17368–17372, 2014. doi: 10.1073/pnas.1408492111.
- [12] M. Tariq, O. Dolynchuk, and T. Thurn-Albrecht. Effect of substrate interaction on thermodynamics of prefreezing. *Macromolecules*, 52(23):9140–9148, 2019. doi: 10.1021/acs.macromol.9b01499.
- [13] M. Eshraghi and J. Horbach. Molecular dynamics simulation of charged colloids confined between hard walls: Pre-melting and pre-freezing across the bcc–fluid coexistence. *Soft Matter*, 14:4141–4149, 2018. doi: 10.1039/C8SM00398J.
- [14] A. K. Flieger, M. Schulz, and T. Thurn-Albrecht. Interface-induced crystallization of polycaprolactone on graphite via first-order prewetting of the crystalline phase. *Macromolecules*, 51(1):189—194, 2017. doi: 10.1021/acs.macromol.7b02113.
- [15] D. J. Courtemanche, T. A. Pasmore, and F. Van Swol. A molecular dynamics study of pre-freezing. *Molecular Physics*, 80(4):861–875, 1993. doi: 10.1080/00268979300102721.
- [16] A. J. Page and R. P. Sear. Freezing in the bulk controlled by prefreezing at a surface. *Physical Review E*, 80(3):031605, 2009. doi: 10.1103/PhysRevE.80.031605.
- [17] M. Dijkstra. Capillary freezing or complete wetting of hard spheres in a planar hard slit? *Physical Review Letters*, 93(10):108303, 2004. doi: 10.1103/PhysRevLett.93.108303.
- [18] A. J. Archer and A. Malijevský. Crystallization of soft matter under confinement at interfaces and in wedges. *Journal of Physics: Condensed Matter*, 28(24):244017, 2016. doi: 10.1088/0953-8984/28/24/244017.
- [19] J. W. Cahn. Critical point wetting. *The Journal of Chemical Physics*, 66(8):3667–3672, 1977. doi: 10.1063/1.434402.
- [20] D. Bonn. Wetting transitions. *The Journal of Chemical Physics*, 6(1):22–27, 2001. doi: 10.1016/S1359-0294(00)00083-2.
- [21] N. Ch. Karayiannis and M. Laso. Dense and nearly jammed random packings of freely jointed chains of tangent hard spheres. *Physical Review Letters*, 100(5):050602, 2008. doi: 10.1103/PhysRevLett.100.050602.
- [22] N. Ch. Karayiannis, K. Foteinopoulou, and M. Laso. The structure of random packings of freely jointed chains of tangent hard spheres. *The Journal of Chemical Physics*, 130(16):164908, 2009. doi: 10.1063/1.3117903.

- [23] N. Ch. Karayiannis, K. Foteinopoulou, and M. Laso. Spontaneous crystallization in athermal polymer packings. *International journal of molecular sciences*, 14(1):332–358, 2012. doi: 10.3390/ijms14010332.
- [24] W. Janke and W. Paul. Thermodynamics and structure of macromolecules from flat-histogram Monte Carlo simulations. *Soft Matter*, 12:642–657, 2016. doi: 10.1039/C5SM01919B.
- [25] F. Liang. A theory on flat histogram Monte Carlo algorithms. *Journal of Statistical Physics*, 122:511–529, 2006. doi: 10.1007/s10955-005-8016-8.
- [26] F. Liang, C. Liu, and R. J. Carroll. Stochastic approximation in Monte Carlo computation. *Journal of the American Statistical Association*, 102(477):305–320, 2007. doi: 10.1198/016214506000001202.
- [27] M. Tariq, T. Thurn-Albrecht, and O. Dolynchuk. Heterogeneous crystal nucleation from the melt in polyethylene oxide droplets on graphite: kinetics and microscopic structure. *Crystals*, 11(8):924, 2021. doi: 10.3390/cryst11080924.
- [28] O. Dolynchuk and T. Thurn-Albrecht. On thermodynamics and kinetics of interface-induced crystallization in polymers. *Macromolecular Chemistry and Physics*, 224(8):2200455, 2023. doi: 10.1002/macp.202200455.
- [29] O. Dolynchuk, M. Tariq, and T. Thurn-Albrecht. Phenomenological theory of first-order prefreezing. *The journal of physical chemistry letters*, 10(8):1942–1946, 2019. doi: 10.1021/acs.jpcelett.9b00608.
- [30] M. Herranz, J. Benito, K. Foteinopoulou, N. Ch. Karayiannis, and M. Laso. Polymorph stability and free energy of crystallization of freely-jointed polymers of hard spheres. *Polymers*, 15(8):1335, 2023. doi: 10.3390/polym15061335.
- [31] P. M. Ramos, M. Herranz, D. Martínez-Fernández, K. Foteinopoulou, M. Laso, and N. Ch. Karayiannis. Crystallization of flexible chains of tangent hard spheres under full confinement. *The Journal of Physical Chemistry B*, 126(31):5931–5947, 2022. doi: 10.1021/acs.jpcc.2c03424.
- [32] M. Herranz, K. Foteinopoulou, N. Ch. Karayiannis, and M. Laso. Polymorphism and perfection in crystallization of hard sphere polymers. *Polymers*, 40(20):4435, 2022. doi: 10.3390/polym14204435.
- [33] V. A. Ivanov, A. S. Rodionova, E. A. An, J. A. Martemyanova, M. R. Stukan, M. Müller, W. Paul, and K. Binder. Orientational ordering transitions of semiflexible polymers in thin films: A Monte Carlo simulation. *Physical Review E*, 84(4):041810, 2011. doi: 10.1103/PhysRevE.84.041810.

- [34] V. A. Ivanov, A. S. Rodionova, J. A. Martemyanova, M. R. Stukan, M. Müller, W. Paul, and K. Binder. Wall-induced orientational order in athermal semidilute solutions of semiflexible polymers: Monte Carlo simulations of a lattice model. *The Journal of Chemical Physics*, 138(23):234903, 2013. doi: 10.1063/1.4810745.
- [35] V. A. Ivanov, A. S. Rodionova, J. A. Martemyanova, M. R. Stukan, M. Muller, W. Paul, and K. Binder. Conformational properties of semiflexible chains at nematic ordering transitions in thin films: A Monte Carlo simulation. *Macromolecules*, 47(3):1206—1220, 2014. doi: 10.1021/ma402138c.
- [36] H. Meyer and F. Müller-Plathe. Formation of chain-folded structures in supercooled polymer melts. *The Journal of Chemical Physics*, 115(17):7807–7810, 2001. doi: 10.1063/1.1415456.
- [37] H. Meyer and F. Müller-Plathe. Formation of chain-folded structures in supercooled polymer melts examined by MD simulations. *Macromolecules*, 35(4):1241–1252, 2002. doi: 10.1021/ma011309l.
- [38] C. Luo and J.-U. Sommer. Frozen topology: Entanglements control nucleation and crystallization in polymers. *Physical Review Letters*, 112(19):195702, 2014. doi: 10.1103/PhysRevLett.112.195702.
- [39] C. Luo and J.-U. Sommer. Role of thermal history and entanglement related thickness selection in polymer crystallization. *ACS Macro Letters*, 5(1):30–34, 2016. doi: 10.1021/acsmacrolett.5b00668.
- [40] M. Anwar, F. Turci, and T. Schilling. Crystallization mechanism in melts of short n-alkane chains. *The Journal of Chemical Physics*, 139(21):214904, 2013. doi: 10.1063/1.4835015.
- [41] M. Anwar and T. Schilling. Crystallization of polyethylene: A molecular dynamics simulation study of the nucleation and growth mechanisms. *Polymer*, 76:307–312, 2015. doi: 10.1016/j.polymer.2015.08.041.
- [42] P. Yi, C. R. Locker, and G. C. Rutledge. Molecular dynamics simulation of homogeneous crystal nucleation in polyethylene. *Macromolecules*, 46(11):4723—4733, 2013. doi: 10.1021/ma4004659.
- [43] A. Bourque, C. R. Locker, and G. C. Rutledge. Molecular dynamics simulation of surface nucleation during growth of an alkane crystal. *Macromolecules*, 49(9):3619–3629, 2016. doi: 10.1021/acs.macromol.5b02757.

- [44] A. J. Bourque and G. C. Rutledge. Heterogeneous nucleation of an n-alkane on graphene-like materials. *European Polymer Journal*, 104(N):64–71, 2018. doi: 10.1016/j.eurpolymj.2018.04.026.
- [45] N. W. Volchko and G. C. Rutledge. Heterogeneous nucleation of high-density polyethylene crystals on graphene within microdomains. *Macromolecules*, 56(11):4123–4134, 2023. doi: 10.1021/acs.macromol.3c00342.
- [46] T. Yamamoto. Molecular dynamics of polymer crystallization revisited: Crystallization from the melt and the glass in longer polyethylene. *The Journal of Chemical Physics*, 139(5):054903, 2013. doi: 10.1063/1.4816707.
- [47] M. A. Hussain, T. Yamamoto, S. F. Adil, and S. Yao. Coarse-grained simulations on polyethylene crystal network formation and microstructure analysis. *Polymers*, 16(7):1007, 2024. doi: 10.3390/polym16071007.
- [48] P. I. Kos, V. A. Ivanov, and A. V. Chertovich. Crystallization of semiflexible polymers in melts and solutions. *Soft Matter*, 17(9):2392–2403, 2021. doi: 10.1039/D0SM01545H.
- [49] J. Morthomas, C. Fusco, Z. Zhai, O. Lame, and M. Perez. Crystallization of finite-extensible nonlinear elastic Lennard-Jones coarse-grained polymers. *Physical Review E*, 96(5):052502, 2017. doi: 10.1103/PhysRevE.96.052502.
- [50] H. Meyer and J. Baschnagel. Structure formation of supercooled polymers in confined geometries - a molecular-dynamics simulation study. *The European Physical Journal E*, 12:147–151, 2003. doi: 10.1140/epje/i2003-10032-8.
- [51] T. Vettorel, H. Meyer, J. Baschnagel, and M. Fuchs. Structural properties of crystallizable polymer melts: Intrachain and interchain correlation functions. *Physical Review E*, 75(4):041801, 2007. doi: 10.1103/PhysRevE.75.041801.
- [52] Z. Zhai, C. Fusco, J. Morthomas, M. Perez, and O. Lame. Disentangling and lamellar thickening of linear polymers during crystallization: Simulation of bimodal and unimodal molecular weight distribution systems. *ACS Nano*, 13(10):11310–11319, 2019. doi: 10.1021/acsnano.9b04459.
- [53] Z. Zhai, J. Morthomas, C. Fusco, M. Perez, and O. Lame. Crystallization and molecular topology of linear semicrystalline polymers: simulation of uni- and bimodal molecular weight distribution systems. *Macromolecules*, 52(11):4196–4208, 2019. doi: 10.1021/acs.macromol.9b00071.
- [54] W. S. Fall, J. Baschnagel, O. Benzerara, O. Lhost, and H. Meyer. Molecular simulations of controlled polymer crystallization in polyethylene. *ACS Macro Letters*, 12(6):808–813, 2023. doi: 10.1021/acsmacrolett.3c00146.

- [55] G. L. Liang, D. W. Noid, B. G. Sumpter, and B. Wunderlich. Molecular dynamics simulations of the hexagonal structure of crystals with long methylene sequences. *Journal of Polymer Science Part B: Polymer Physics*, 31(13):1885–2056, 1993. doi: 10.1002/polb.1993.090311304.
- [56] J. V. Selinger and R. F. Bruinsma. Hexagonal and nematic phases of chains. I. Correlation functions. *Physical Review A*, 43(6):2910–2921, 1991. doi: 10.1103/PhysRevA.43.2910.
- [57] J. V. Selinger and R. F. Bruinsma. Hexagonal and nematic phases of chains. II. Phase transitions. *Physical Review A*, 43(6):2922–2931, 1991. doi: 10.1103/PhysRevA.43.2922.
- [58] G. Reiter and J.-U. Sommer. Crystallization of adsorbed polymer monolayers. *Physical Review Letters*, 80(17):3771, 1998. doi: 10.1103/PhysRevLett.80.3771.
- [59] J.-U. Sommer and G. Reiter. Polymer crystallization in quasi-two dimensions. II. Kinetic models and computer simulations. *The Journal of Chemical Physics*, 112(9):4384–4393, 2000. doi: 10.1063/1.481004.
- [60] G. Dorenbos, J.-U. Sommer, and G. Reiter. Polymer crystallization on pre-patterned substrates. *The Journal of Chemical Physics*, 118(2):784–791, 2003. doi: 10.1063/1.1499957.
- [61] J.-U. Sommer and G. Reiter. Morphogenesis and nonequilibrium pattern formation in two-dimensional polymer crystallization. *Phase Transitions*, 77(8-10):703–745, 2004. doi: 10.1080/01411590410001690873.
- [62] J.-U. Sommer and G. Reiter. Crystallization in ultra-thin polymer films: Morphogenesis and thermodynamical aspects. *Thermochimica Acta*, 432(2):135–147, 2005. doi: 10.1016/j.tca.2005.04.017.
- [63] C. Luo and J.-U. Sommer. Coexistence of melting and growth during heating of a semicrystalline polymer. *Physical Review Letters*, 102(14):147801, 2009. doi: 10.1103/PhysRevLett.102.147801.
- [64] J.-U. Sommer and C. Luo. Molecular dynamics simulations of semicrystalline polymers: Crystallization, melting, and reorganization. *Journal of Polymer Science Part B: Polymer Physics*, 48(21):2222–2232, 2010. doi: 10.1002/polb.22104.
- [65] C. Luo and J.-U. Sommer. Growth pathway and precursor states in single lamellar crystallization: MD simulations. *Macromolecules*, 44(6):1523–1529, 2011. doi: 10.1021/ma102380m.

- [66] A. Statt, P. Virnau, and K. Binder. Finite-size effects on liquid-solid phase coexistence and the estimation of crystal nucleation barriers. *Physical Review Letters*, 114(2):026101, 2015. doi: 10.1103/PhysRevLett.114.026101.
- [67] K. Binder. Theory of the evaporation/condensation transition of equilibrium droplets in finite volumes. *Physica A: Statistical Mechanics and its Applications*, 319(1):99–114, 2003. doi: 10.1016/S0378-4371(02)01581-9.
- [68] L. G. MacDowell, P. Virnau, M. Müller, and K. Binder. The evaporation/condensation transition of liquid droplets. *The Journal of Chemical Physics*, 120(11):5293–5308, 2004. doi: 10.1063/1.1645784.
- [69] M. Schrader, P. Virnau, and K. Binder. Simulation of vapor-liquid coexistence in finite volumes: A method to compute the surface free energy of droplets. *Physical Review E*, 79(6):061104, 2009. doi: 10.1103/PhysRevE.79.061104.
- [70] M. D. Rintoul and S. Torquato. Metastability and crystallization in hard-sphere systems. *Physical Review Letters*, 77(20):4198, 1996. doi: 10.1103/PhysRevLett.77.4198.
- [71] I. Volkov, M. Cieplak, J. Koplik, and J. R. Banavar. Molecular dynamics simulations of crystallization of hard spheres. *Physical Review E*, 66(6):061401, 2002. doi: 10.1103/PhysRevE.66.061401.
- [72] V. Luchnikov, A. Gervois, P. Richard, L. Oger, and J. P. Troadec. Crystallization of dense hard sphere packings: Competition of hcp and fcc close order. *Journal of Molecular Liquids*, 96–97:185–194, 2002. doi: 10.1016/S0167-7322(01)00346-4.
- [73] S. L. Brown, V. D. Shah, M. V. Morrell, M. Zubich, A. Wagner, A. R. Denton, and E. K. Hobbie. Superlattice formation in colloidal nanocrystal suspensions: Hard-sphere freezing and depletion effects. *Physical Review E*, 98(6):062616, 2018. doi: 10.1103/PhysRevE.98.062616.
- [74] F. A. Escobedo and J. J. de Pablo. Monte Carlo simulation of athermal mesogenic chains: Pure systems, mixtures, and constrained environments. *The Journal of Chemical Physics*, 106(23):9858–9868, 1997. doi: 10.1063/1.473874.
- [75] M. Schmidt and H. Löwen. Phase diagram of hard spheres confined between two parallel plates. *Physical Review E*, 55(6):7228, 1997. doi: 10.1103/PhysRevE.55.7228.
- [76] T. Zykova-Timan, J. Horbach, and K. Binder. Monte Carlo simulations of the solid-liquid transition in hard spheres and colloid-polymer mixtures. *The Journal of Chemical Physics*, 133(1):014705, 2010. doi: 10.1063/1.3455504.

- [77] N. Ch. Karayiannis, K. Foteinopoulou, and M. Laso. The characteristic crystallographic element norm: A descriptor of local structure in atomistic and particulate systems. *The Journal of Chemical Physics*, 130(7):074704, 2009. doi: 10.1063/1.3077294.
- [78] N. Ch. Karayiannis, K. Foteinopoulou, and M. Laso. Entropy-driven crystallization in dense systems of athermal chain molecules. *Physical Review Letters*, 103(4):045703, 2009. doi: 10.1103/PhysRevLett.103.045703.
- [79] N. Ch. Karayiannis, K. Foteinopoulou, and M. Laso. Jamming and crystallization in athermal polymer packings. *Philosophical Magazine*, 93(31-33):4108–4131, 2013. doi: 10.1080/14786435.2013.815377.
- [80] P. M. Ramos, M. Herranz, K. Foteinopoulou, N. Ch. Karayiannis, and M. Laso. Identification of local structure in 2-d and 3-d atomic systems through crystallographic analysis. *Crystals*, 10(11):1008, 2020. doi: 10.3390/cryst10111008.
- [81] N. Ch. Karayiannis, K. Foteinopoulou, and M. Laso. The role of bond tangency and bond gap in hard sphere crystallization of chains. *Soft Matter*, 11:1688–1700, 2015. doi: 10.1039/c4sm02707h.
- [82] D. Martínez-Fernández, M. Herranz, K. Foteinopoulou, N. Ch. Karayiannis, and M. Laso. Local and global order in dense packings of semi-flexible polymers of hard spheres. *Polymers*, 15(3):551, 2023. doi: 10.3390/polym15030551.
- [83] J. Benito, N.Ch. Karayiannis, and M. Laso. Confined polymers as self-avoiding random walks on restricted lattices. *Polymers*, 10(12):1394, 2018. doi: 10.3390/polym10121394.
- [84] P. M. Ramos, M. Herranz, K. Foteinopoulou, N. Ch. Karayiannis, and M. Laso. Entropy-driven heterogeneous crystallization of hard-sphere chains under unidimensional confinement. *Polymers*, 13(9):1352, 2021. doi: 10.3390/polym13091352.
- [85] O. Parreño, P. M. Ramos, N. Ch. Karayiannis, and M. Laso. Self-avoiding random walks as a model to study athermal linear polymers under extreme plate confinement. *Polymers*, 12(4):799, 2020. doi: 10.3390/polym12040799.
- [86] C. Pedrosa, D. Martinez-Fernandez, M. Herranz, K. Foteinopoulou, N. Ch. Karayiannis, and M. Laso. Densest packing of flexible polymers in 2D films. *The Journal of Chemical Physics*, 158(16):164502, 2023. doi: 10.1063/5.0137115.
- [87] N. D. Mermin. Crystalline order in two dimensions. *Physical Review*, 176(1):250–254, 1968. doi: 10.1103/PhysRev.176.250.
- [88] N.D. Mermin and H. Wagner. Absence of ferromagnetism or antiferromagnetism in one- or two-dimensional isotropic heisenberg models. *Physical Review Letters*, 17(22):1133, 1966. doi: 10.1103/PhysRevLett.17.1133.

- [89] P. C. Hohenberg. Existence of long-range order in one and two dimensions. *Physical Review*, 158(2):383, 1967. doi: 10.1103/PhysRev.158.383.
- [90] B. I. Halperin. On the hohenberg–mermin–wagner theorem and its limitations. *Journal of Statistical Physics*, 157:521–529, 2019. doi: 10.1007/s10955-018-2202-y.
- [91] B. I. Halperin and D. R. Nelson. Theory of two-dimensional melting. *Physical Review Letters*, 41(2):121, 1978. doi: 10.1103/PhysRevLett.41.121.
- [92] D. R. Nelson and B. I. Halperin. Dislocation-mediated melting in two dimensions. *Physical Review B*, 19(5):2457–2484, 1979. doi: 10.1103/PhysRevB.19.2457.
- [93] A. Jaster. Computer simulations of the two-dimensional melting transition using hard disks. *Physical Review E*, 59(3):2594–2602, 1999. doi: 10.1103/PhysRevE.59.2594.
- [94] K. Binder, S. Sengupta, and P. Nielaba. The liquid–solid transition of hard discs: first-order transition or kosterlitz–thouless–halperin–nelson–young scenario? *Journal of Physics: Condensed Matter*, 14(9):2323–2333, 2002. doi: 10.1088/0953-8984/14/9/321.
- [95] O. Alexiadis, K. Ch. Daoulas, and V. G. Mavrantzas. An efficient Monte Carlo algorithm for the fast equilibration and atomistic simulation of alkanethiol self-assembled monolayers on a Au(111) substrate. *The Journal of Physical Chemistry B*, 112(4):1198–1211, 2008. doi: 10.1021/jp076417+.
- [96] N. Ch. Karayiannis and M. Kröger. Combined molecular algorithms for the generation, equilibration and topological analysis of entangled polymers: Methodology and performance. *International journal of molecular sciences*, 10(11):5054–5089, 2009. doi: 10.3390/ijms10115054.
- [97] T. Shakirov and W. Paul. Crystallization in melts of short, semiflexible hard polymer chains: An interplay of entropies and dimensions. *Physical Review E*, 97(4):042501, 2018. doi: 10.1103/PhysRevE.97.042501.
- [98] P. Kawak, D. S. Banks, and D. R. Tree. Semiflexible oligomers crystallize via a cooperative phase transition. *The Journal of Chemical Physics*, 155(21):214902, 2021. doi: 10.1063/5.0067788.
- [99] T. Shakirov. Flat-histogram algorithms: optimal parameters and extended application. *Arxiv*, 2024. doi: 10.48550/arXiv.2402.05653.
- [100] T. Shakirov. Convergence estimation of flat-histogram algorithms based on simulation results. *Computer Physics Communications*, 228:38–43, 2018. doi: 10.1016/j.cpc.2018.03.009.

- [101] B. Werlich, T. Shakirov, M. P. Taylor, and W. Paul. Stochastic Approximation Monte Carlo and Wang-Landau Monte Carlo applied to a continuum polymer model. *Computer Physics Communications*, 186:65–70, 2015. doi: 10.1016/j.cpc.2014.09.018.
- [102] P. J. Steinhardt, D. R. Nelson, and M. Ronchetti. Bond-orientational order in liquids and glasses. *Physical Review B*, 28(2):784–805, 1983. doi: 10.1103/PhysRevB.28.784.
- [103] H. Eslami, P. Sedaghat, and F. Müller-Plathe. Local bond order parameters for accurate determination of crystal structures in two and three dimensions. *Physical Chemistry Chemical Physics*, 20:27059–27068, 2018. doi: 10.1039/C8CP05248D.
- [104] W. Lechner and C. Dellago. Accurate determination of crystal structures based on averaged local bond order parameters. *The Journal of Chemical Physics*, 128:114707, 2008. doi: 10.1063/1.2977970.
- [105] J. D. Honeycutt and H. C. Andersen. Molecular dynamics study of melting and freezing of small Lennard-Jones clusters. *The Journal of Chemical Physics*, 31(19):4950–4963, 1987. doi: 10.1021/j100303a014.
- [106] D. Faken and H. Jónsson. Systematic analysis of local atomic structure combined with 3D computer graphics. *Computational Materials Science*, 2(2):279–286, 1994. doi: 10.1016/0927-0256(94)90109-0.
- [107] A. Stukowski. Structure identification methods for atomistic simulations of crystalline materials. *Modelling and Simulation in Materials Science and Engineering*, 20(4):045021, 2012. doi: 10.1088/0965-0393/20/4/045021.
- [108] P. M. Larsen. Revisiting the common neighbour analysis and the centrosymmetry parameter. 2020. doi: 10.48550/arXiv.2003.08879.
- [109] Chris H. Rycroft. VORO++: A three-dimensional Voronoi cell library in C++. *Chaos*, 19(4):041111, 2009. doi: 10.1063/1.3215722.
- [110] C. H. Rycroft. Voro++: a three-dimensional Voronoi cell library in C++. <https://math.lbl.gov/voro++/doc>, 2009.
- [111] T. W. Cochran and Y. C. Chiew. Radial distribution function of freely jointed hard-sphere chains in the solid phase. *The Journal of Chemical Physics*, 124(7):074901, 2006. doi: 10.1063/1.2167644.
- [112] W. Mickel, S. C. Kapfer, G. E. Schröder-Turk, and K. Mecke. Shortcomings of the bond orientational order parameters for the analysis of disordered particulate matter. *The Journal of Chemical Physics*, 138(4):044501, 2013. doi: 10.1063/1.4774084.

- [113] J. Haeberle, M. Sperl, and P. Born. Distinguishing noisy crystalline structures using bond orientational order parameters. *The European Physical Journal E*, 42(149):1–7, 2019. doi: 10.1140/epje/i2019-11915-7.
- [114] T. Shakirov. Crystallization in melts of short, semi-flexible hard-sphere polymer chains: The role of the non-bonded interaction range. *Entropy*, 21(9):856, 2019. doi: 10.3390/e21090856.
- [115] D. Frenkel and B. Smit. *Understanding Molecular Simulation: From Algorithms to Applications*. Academic Press, New York, 2001.
- [116] M. E. J. Newman and G. T. Barkema. *Monte Carlo Methods in Statistical Physics*. Clarendon Press, Oxford, 1999.
- [117] D. P. Landau and K. Binder. *Monte Carlo Simulations in Statistical Physics*. Cambridge University Press, Cambridge, 2000.
- [118] B. A. Berg. *Markov Chain Monte Carlo Simulations and Their Statistical Analysis*. World Scientific, Singapore, 2004.
- [119] W. Janke. *Order, Disorder and Criticality: Advanced Problems of Phase Transition Theory Volume 3*. World Scientific, 2012. doi: 10.1142/9789814417891_0003.
- [120] N. Metropolis, A. W. Rosenbluth, M. N. Rosenbluth, A. H. Teller, and E. Teller. Equation of state calculations by fast computing machines. *The Journal of Chemical Physics*, 21(6):1087–1092, 1953. doi: 10.1063/1.1699114.
- [121] W. K. Hastings. Monte Carlo sampling methods using Markov chains and their applications. *Biometrika*, 57(1):97—109, 1970. doi: 10.1093/biomet/57.1.97.
- [122] B. A. Berg. Generalized ensemble simulations for complex systems. *Computer Physics Communications*, 147(1-2):52–57, 2002. doi: 10.1016/S0010-4655(02)00203-5.
- [123] B. A. Berg and T. Neuhaus. Multicanonical algorithms for first order phase transitions. *Physics Letters B*, 267(2):249–253, 1991. doi: 10.1016/0370-2693(91)91256-U.
- [124] B. A. Berg and T. Neuhaus. Multicanonical ensemble: A new approach to simulate first-order phase transitions. *Physical Review Letters*, 68(1):9–12, 1992. doi: 10.1103/PhysRevLett.68.9.
- [125] B. A. Berg. Multicanonical recursions. *Journal of Statistical Physics*, 82:323—342, 1996. doi: 10.1007/BF02189233.
- [126] U. H. E. Hansmann and Y. Okamoto. *Annual Reviews of Computational Physics VI*. World Scientific, Singapore, 1999.

- [127] W. Janke. Multicanonical Monte Carlo simulations. *Physica A: Statistical Mechanics and its Applications*, 254(1-2):164–178, 1998. doi: 10.1016/S0378-4371(98)00014-4.
- [128] P. N. Vorontsov-Velyaminov, N. A. Volkov, A. A. Yurchenko, and A. P. Lyubartsev. Simulation of polymers by the Monte Carlo method using the Wang-Landau algorithm. *Polymer Science Series A*, 52(7):742—760, 2010. doi: 10.1134/S0965545X10070096.
- [129] T. Wüst, Y. W. Li, and D. P. Landau. Unraveling the beautiful complexity of simple lattice model polymers and proteins using Wang-Landau sampling. *Journal of Statistical Physics*, 144:638—651, 2011. doi: 10.1007/s10955-011-0266-z.
- [130] S. Singh, M. Chopra, and J. J. de Pablo. Density of states–based molecular simulations. *Annual Review of Chemical and Biomolecular Engineering*, pages 369—394, 2012. doi: 10.1146/annurev-chembioeng-062011-081032.
- [131] M. P. Taylor, W. Paul, and K. Binder. Applications of the Wang-Landau algorithm to phase transitions of a single polymer chain. *Polymer Science Series C*, 55(1):23—38, 2013. doi: 10.1134/S1811238213060040.
- [132] F. Wang and D. P. Landau. Efficient, multiple-range random walk algorithm to calculate the density of states. *Physical Review Letters*, 86(10):2050–2053, 2001. doi: 10.1103/PhysRevLett.86.2050.
- [133] F. Wang and D. P. Landau. Determining the density of states for classical statistical models: A random walk algorithm to produce a flat histogram. *Physical Review E*, 64(5):056101, 2001. doi: 10.1103/PhysRevE.64.056101.
- [134] D. P. Landau, Shan-Ho Tsai, and M. Exler. A new approach to Monte Carlo simulations in statistical physics: Wang-landau sampling. *American Journal of Physics*, 72(10):1294–1302, 2004. doi: 10.1119/1.1707017.
- [135] C. Zhou and R. N. Bhatt. Understanding and improving the Wang-Landau algorithm. *J*, 72(2):025701(R), 2005. doi: 10.1103/PhysRevE.72.025701.
- [136] Q. Yan and J. J. de Pablo. Fast calculation of the density of states of a fluid by Monte Carlo simulations. *Physical Review Letters*, 90(3):035701, 2003. doi: 10.1103/PhysRevLett.90.035701.
- [137] R. E. Belardinelli and V. D. Pereyra. Fast algorithm to calculate density of states. *Physical Review E*, 75(4):046701, 2007. doi: 10.1103/PhysRevE.75.046701.
- [138] R. E. Belardinelli and V. D. Pereyra. Wang-Landau algorithm: A theoretical analysis of the saturation of the error. *The Journal of Chemical Physics*, 127(18):184105, 2007. doi: 10.1063/1.2803061.

- [139] B. Werlich, M. P. Taylor, and W. Paul. Wang-Landau and Stochastic Approximation Monte Carlo for semi-flexible polymer chains. *Physics Procedia*, 57:82–86, 2014. doi: 10.1016/j.phpro.2014.08.137.
- [140] A. Böker and W. Paul. Wang-Landau simulation of $G\bar{o}$ model molecules. *The European Physical Journal E*, 39(5), 2016. doi: 10.1140/epje/i2016-16005-x.
- [141] F. Liang. On the use of Stochastic Approximation Monte Carlo for Monte Carlo integration. *Statistics and Probability Letters*, 79(5):581–587, 2009. doi: 10.1016/j.spl.2008.10.007.
- [142] F. Liang. An overview of Stochastic Approximation Monte Carlo. *Wiley Interdiscip. Rev. Comput. Stat.*, 6(4):240–254, 2014. doi: 10.1002/wics.1305.
- [143] T. Shakirov, S. Zablotskiy, A. Böker, V. A. Ivanov, and W. Paul. Comparison of Boltzmann and Gibbs entropies for the analysis of single-chain phase transitions. *The European Physical Journal Special Topics*, 226:705–723, 2017. doi: 10.1140/epjst/e2016-60326-1.
- [144] R Core Team. The R project for statistical computing. Technical report, The R Foundation. URL <https://www.r-project.org/>.
- [145] M. Bishop, D. Ceperley, H. L. Frisch, and M. H. Kalos. Investigations of static properties of model bulk polymer fluids. *Journal of Chemical Physics*, 72(5):3228—3235, 1980. doi: 10.1063/1.439559.
- [146] M. Vacatello, G. Avitabile P. Corradini, and A. Tuzi. A computer model of molecular arrangement in a n-paraffinic liquid. *Journal of Chemical Physics*, 73(1):548–552, 1980. doi: 10.1063/1.439853.
- [147] F. T. Wall and F. Mandel. Macromolecular dimensions obtained by an efficient Monte Carlo method without sample attrition. *Journal of Chemical Physics*, 63(11):4592—4595, 1975. doi: 10.1063/1.431268.
- [148] P. V. K. Pant and D. N. Theodorou. Variable connectivity method for the atomistic Monte Carlo simulation of polydisperse polymer melts. *Macromolecules*, 28(21):7224—7234, 1995. doi: 10.1021/ma00125a027.
- [149] V. G. Mavrantzas, T. D. Boone, E. Zervopoulou, and D. N. Theodorou. End-bridging Monte Carlo: A fast algorithm for atomistic simulation of condensed phases of long polymer chains. *Macromolecules*, 32(15):5072—5096, 1999. doi: 10.1021/ma981745g.

- [150] N. Ch. Karayiannis, A. E. Giannousaki, V. G. Mavrantzas, and D. N. Theodorou. Atomistic Monte Carlo simulation of strictly monodisperse long polyethylene melts through a generalized chain bridging algorithm. *Journal of Chemical Physics*, 117(11):PP, 2002. doi: 10.1063/1.1499480.
- [151] N. Ch. Karayiannis, V. G. Mavrantzas, and D. N. Theodorou. A novel Monte Carlo scheme for the rapid equilibration of atomistic model polymer systems of precisely defined molecular architecture. *Physical Review Letters*, 88(10):PP, 2002. doi: 10.1103/PhysRevLett.88.105503.
- [152] V. Luchnikov, A. Gervois, P. Richard, L. Oger, and J. P. Troadec. *Two-Dimensional Crystal*. Academic Press, 1992.
- [153] M. R. Anderberg. *Cluster analysis for applications: probability and mathematical statistics: a series of monographs and textbooks*. Academic Press, New York, 1973.
- [154] M. B. Wilk and R. Gnanadesikan. Probability plotting methods for the analysis for the analysis of data. *Biometrika*, 55(1):1–17, 1968. doi: 10.1093/biomet/55.1.1.
- [155] A. Likas, N. Vlassis, and J.J. Verbeek. The global k-means clustering algorithm. *Pattern Recognition*, 36(2):451–461, 2003. doi: 10.1016/S0031-3203(02)00060-2.
- [156] Xiao-Li Meng and David Van Dyk. The EM algorithm—an old folk-song sung to a fast new tune. *Journal of the Royal Statistical Society: Series B (Methodological)*, 59(3): 511—567, 1997. doi: 10.1111/1467-9868.00082.
- [157] J. Gulden, O. M. Yefanov, A. P. Mancuso, V. V. Abramova, J. Hilhorst, D. Byelov, I. Snigireva, A. Snigirev, A. V. Petukhov, and I. A. Vartanyants. Coherent x-ray imaging of defects in colloidal crystals. *Physical Review B*, 81(22):224105, 2010. doi: 10.1103/PhysRevB.81.224105.
- [158] C. L. Kelchner, S. J. Plimpton, and J. C. Hamilton. Dislocation nucleation and defect structure during surface indentation. *Physical Review B*, 58(17):11085, 1998. doi: 10.1103/PhysRevB.58.11085.
- [159] E. Parzen. On estimation of a probability density function and mode. *The Annals of Mathematical Statistics*, 33(3):1065–1076, 1962. doi: 10.1214/aoms/1177704472.
- [160] B. W. Silverman. *Density estimation for statistics and data analysis*. Chapman Hall/CRC, 1998.
- [161] V. A. Epanechnikov. Non-parametric estimation of a multivariate probability density. *Theory of Probability and Its Applications*, 14(1):153–158, 1969. doi: 10.1137/1114019.

- [162] K. Ch. Daoulas, M. Müller, M. P. Stoykovich, Y. J. Papakonstantopoulos, J. J. de Pablo, P. F. Nealey, S.-M. Park, and H. H. Solak. Directed assembly of copolymer materials on patterned substrates: Balance of simple symmetries in complex structures. *Journal of Polymer Science Part B: Polymer Physics*, 44(18):2589–2604, 2006. doi: 10.1002/polb.20904.
- [163] A. R. Khokhlov and A. N. Semenov. On the theory of liquid-crystalline ordering of polymer chains with limited flexibility. *Journal of Statistical Physics*, 38:161–182, 1985. doi: 10.1007/BF01017855.
- [164] H. Arkin and W. Janke. Gyration tensor based analysis of the shapes of polymer chains in an attractive spherical cage. *The Journal of Chemical Physics*, 138(5):054904, 2013. doi: 10.1063/1.4788616.
- [165] J. L. Colot and M. Baus. The freezing of hard spheres. *Molecular physics*, 56(4):807–824, 1985. doi: 10.1080/00268978500102731.
- [166] D. Frenkel and A. J. C. Ladd. New Monte Carlo method to compute the free energy of arbitrary solids. application to the fcc and hcp phases of hard spheres. *The Journal of Chemical Physics*, 81(7):3188–3193, 1984. doi: 10.1063/1.448024.

Appendix

Local bond order parameters

| | <i>sc</i> | <i>bcc</i> | <i>fcc</i> | <i>hcp</i> |
|-----------|-----------|------------|------------|------------|
| Neighbors | 6 | 14 | 12 | 12 |
| q_2 | 0.0 | 0.0 | 0.0 | 0.0 |
| q_3 | 0.0 | 0.0 | 0.0 | 0.076073 |
| q_4 | 0.763763 | 0.036370 | 0.190941 | 0.097222 |
| q_5 | 0.0 | 0.0 | 0.0 | 0.251586 |
| q_6 | 0.353553 | 0.510688 | 0.574524 | 0.484762 |
| q_7 | 0.0 | 0.0 | 0.0 | 0.310815 |
| q_8 | 0.718070 | 0.429322 | 0.403915 | 0.316992 |
| q_9 | 0.0 | 0.0 | 0.0 | 0.137851 |
| q_{10} | 0.411425 | 0.195191 | 0.012857 | 0.010169 |
| w_2 | 0.0 | 0.0 | 0.0 | 0.0 |
| w_3 | 0.0 | 0.0 | 0.0 | 0.0 |
| w_4 | 0.159317 | 0.159317 | -0.159317 | 0.134097 |
| w_5 | 0.0 | 0.0 | 0.0 | 0.0 |
| w_6 | 0.013161 | 0.013161 | -0.013161 | -0.012442 |
| w_7 | 0.0 | 0.0 | 0.0 | 0.0 |
| w_8 | 0.058455 | 0.058455 | 0.058455 | 0.051259 |
| w_9 | 0.0 | 0.0 | 0.0 | 0.0 |
| w_{10} | 0.090130 | -0.090130 | -0.090130 | -0.079851 |

Table A1: LBO parameters $q_2 - q_{10}$, $w_2 - w_{10}$ for perfect *sc*, *bcc*, *fcc*, *hcp* structures.

LBO parameters

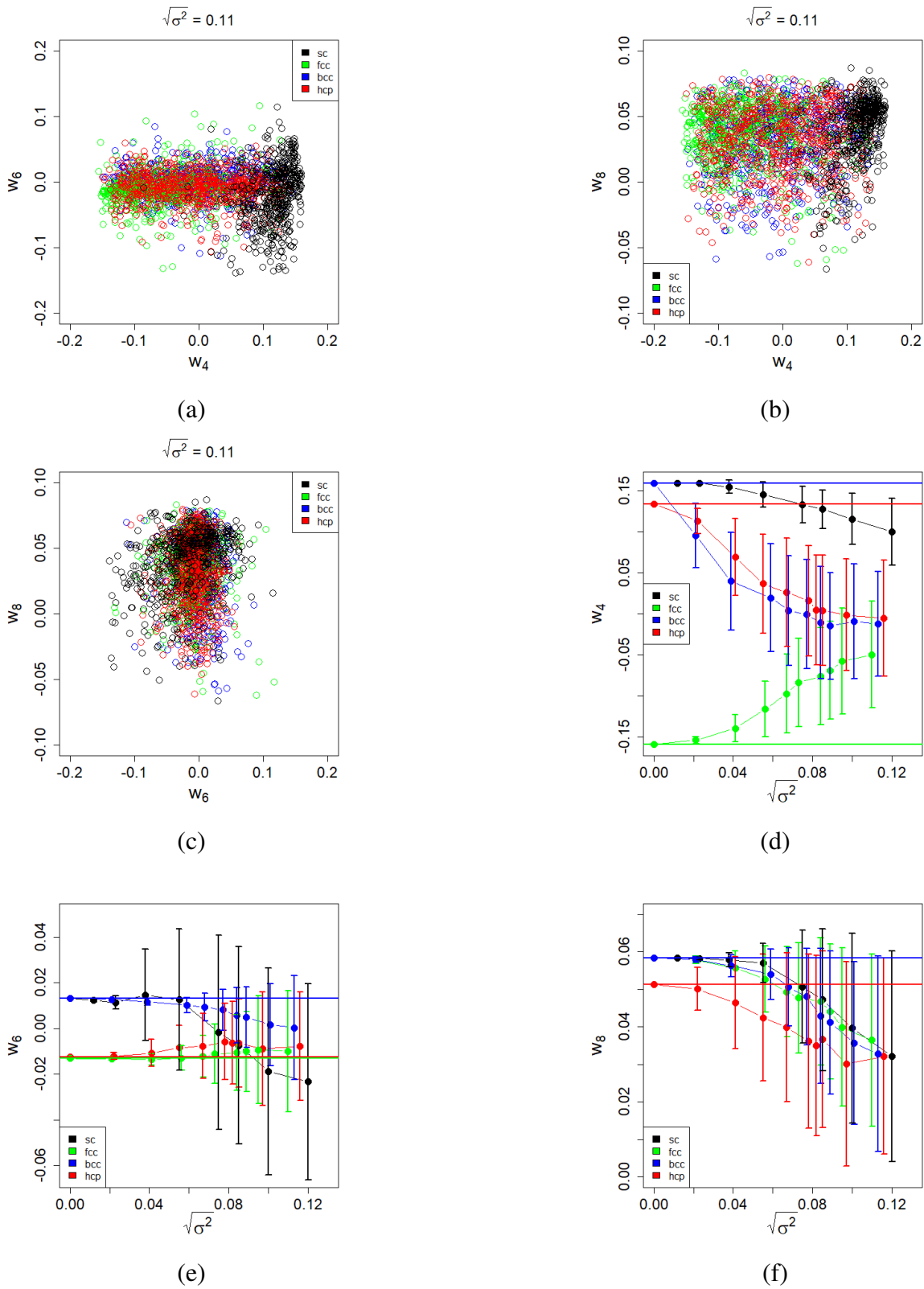


Figure A1: LBO parameters $w_4 - w_6$, $w_4 - w_8$, $w_6 - w_8$ planes (a-c) and mean values of w_4 , w_6 , w_8 (d-f) for noisy test structures.

ALBO parameters

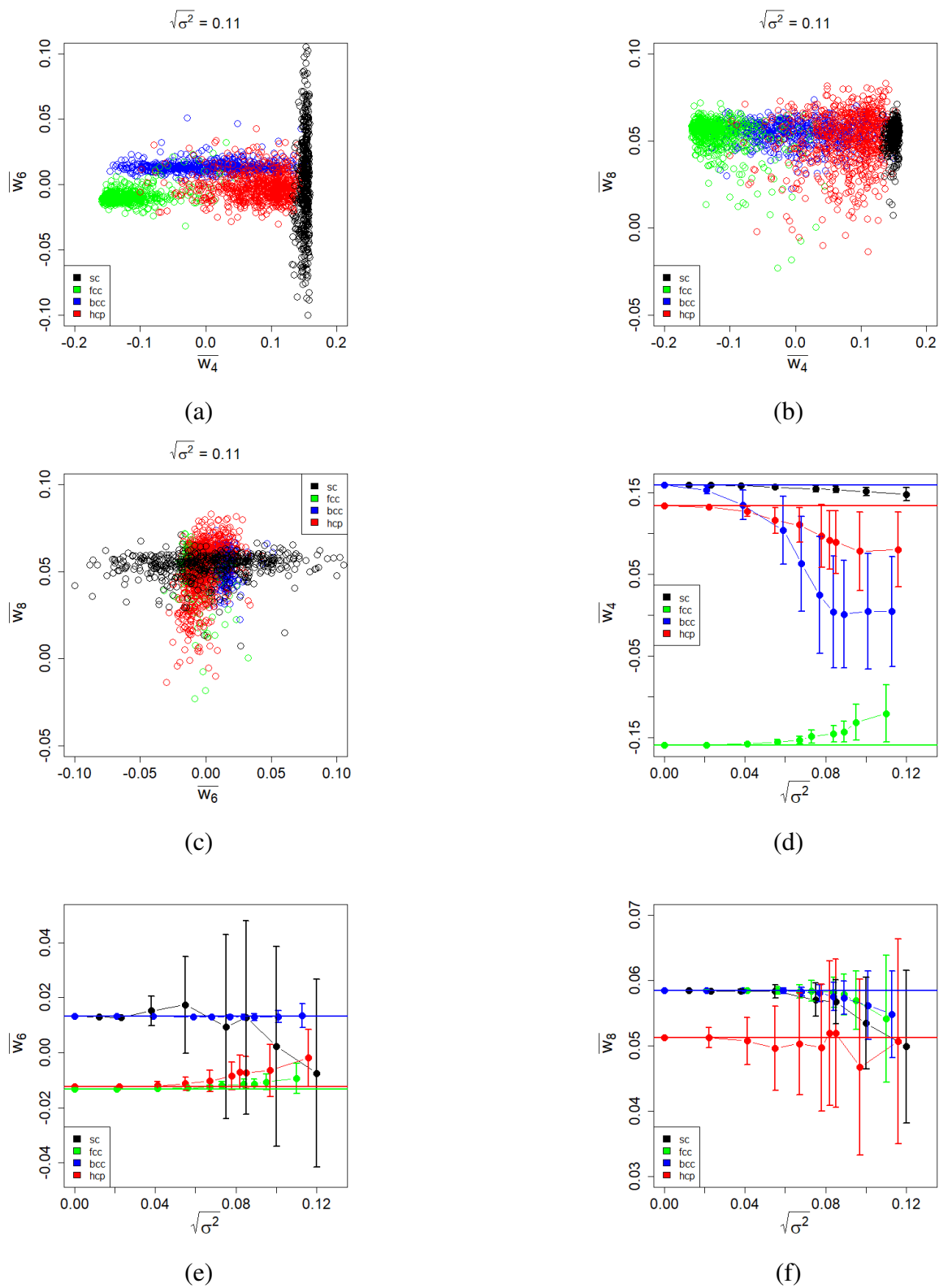


Figure A2: ALBO parameters $\bar{w}_4 - \bar{w}_6$, $\bar{w}_4 - \bar{w}_8$, $\bar{w}_6 - \bar{w}_8$ planes (a-c) and mean values of \bar{w}_4 , \bar{w}_6 , \bar{w}_8 (d-f) for noisy test structures.

ALBO and RLBO parameters

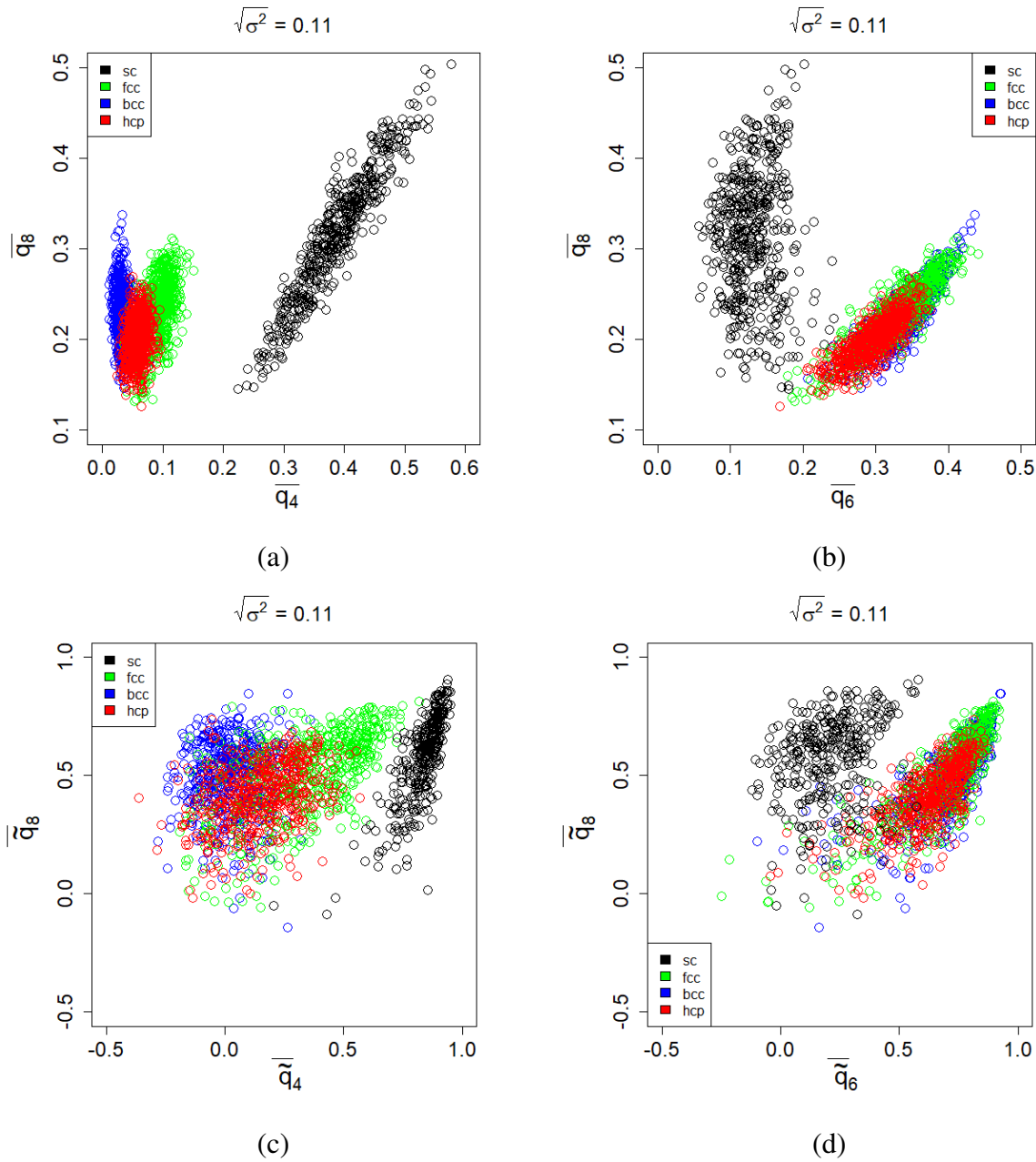


Figure A3: Maps of ALBO parameters: $\bar{q}_4 - \bar{q}_8$ (a), $\bar{q}_6 - \bar{q}_8$ (b); maps of RLBO parameters: $\tilde{q}_4 - \tilde{q}_8$ (c), $\tilde{q}_6 - \tilde{q}_8$ (d) for noisy test structures.

NRLBO parameters

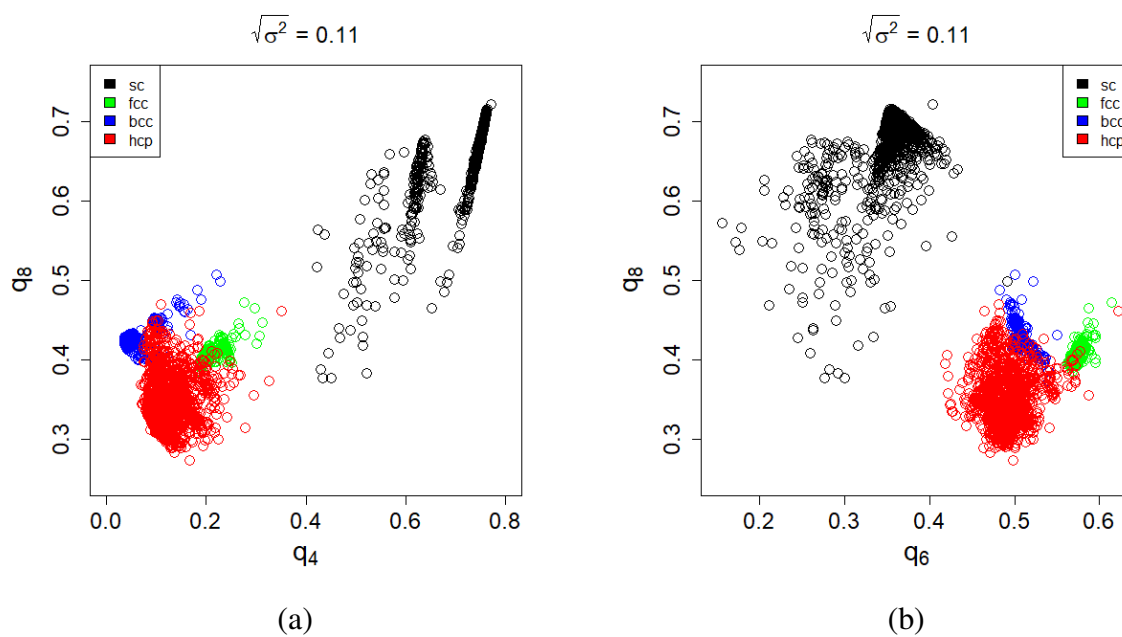


Figure A4: Maps of NRLBO parameters $q_4 - q_8$ (a), $q_6 - q_8$ (b).

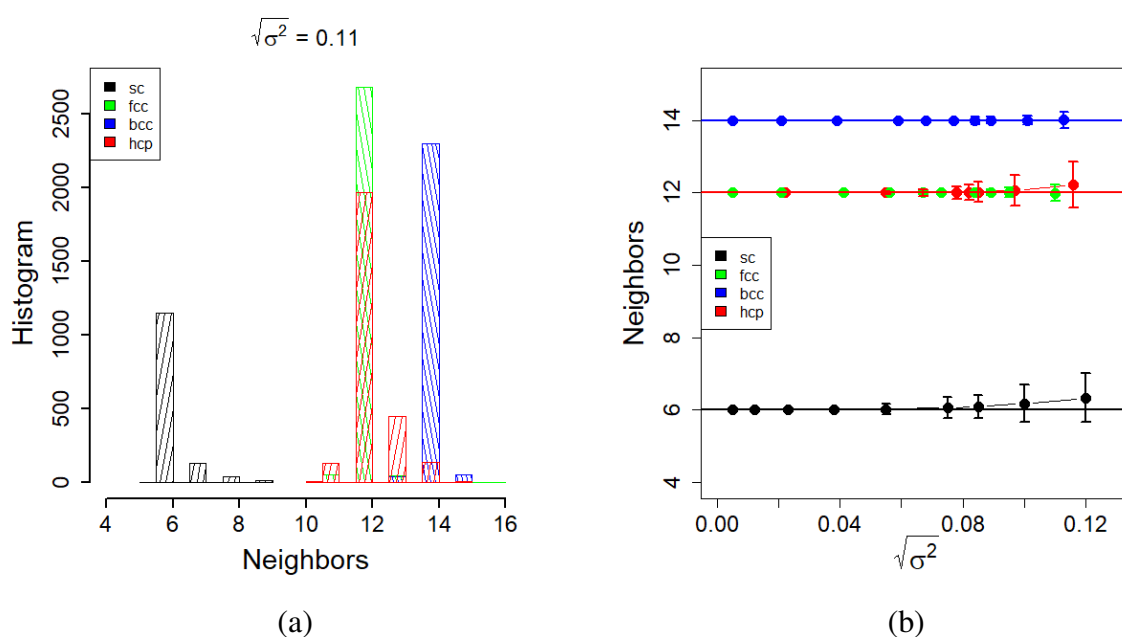


Figure A5: Histogram of neighbors after noise reduction procedure at $\sigma = 0.11$ (a) and mean number of neighbors as function of noise (b) for test structures.

NRLBO parameters

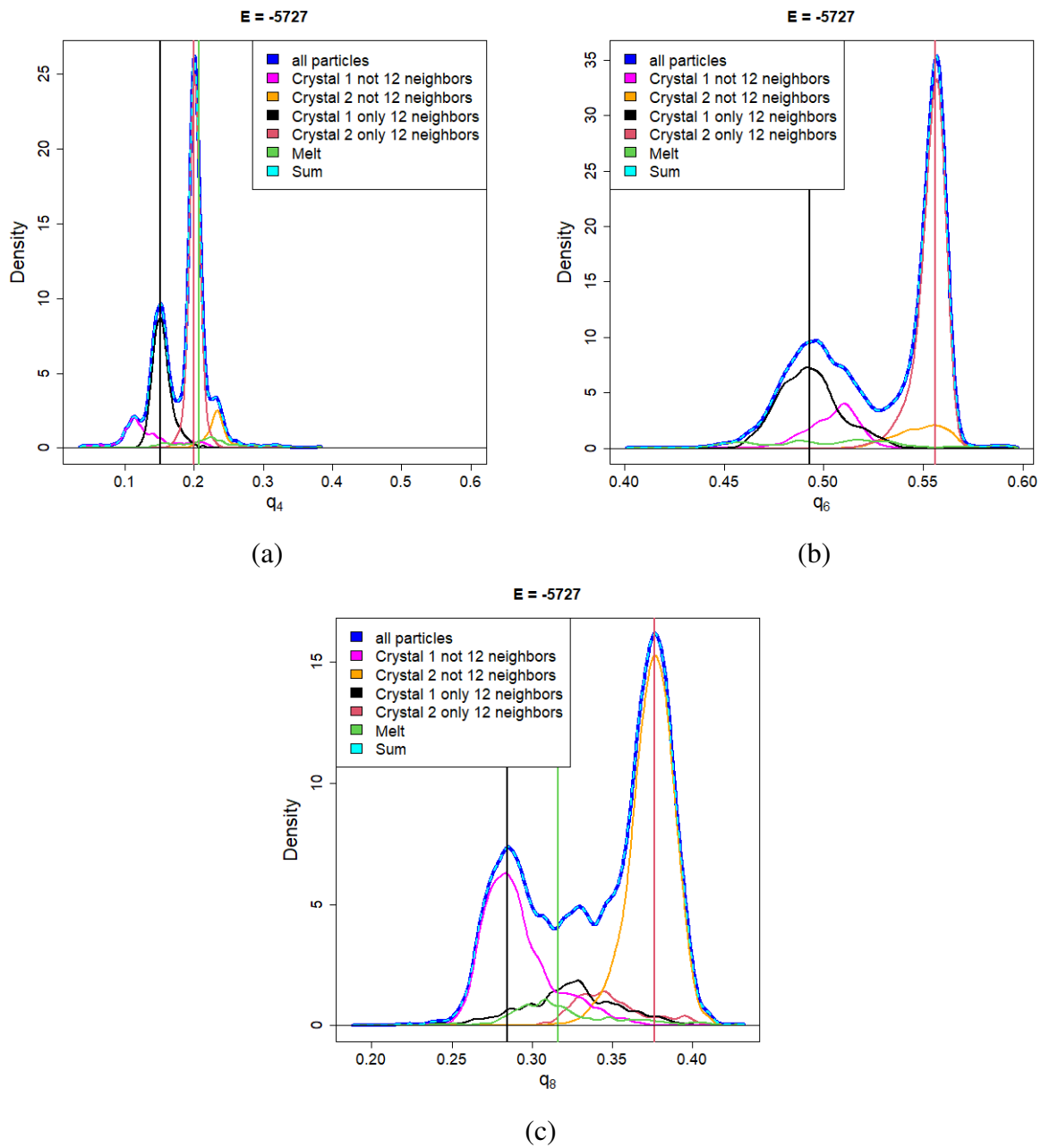


Figure A6: NRLBO parameters distribution for the bulk system $E = -5727$, $L_x = L_y = 20$, $L_z = 19$.

NRLBO parameters

| | color | \bar{q}_4 | \bar{q}_6 | \bar{q}_8 |
|-----------|-------|-------------------|-------------------|-------------------|
| Crystal 1 | black | 0.154 ± 0.036 | 0.495 ± 0.018 | 0.291 ± 0.030 |
| Crystal 2 | red | 0.204 ± 0.027 | 0.553 ± 0.012 | 0.374 ± 0.021 |
| Melt | green | 0.217 ± 0.067 | 0.377 ± 0.067 | 0.321 ± 0.053 |

Table A2: Centers of clusters $\bar{q}_4, \bar{q}_6, \bar{q}_8$ found in the $\{q_4, q_6, q_8\}$ space in the system without walls, $L_x = L_y = 20, L_z = 39$

| | color | \bar{q}_4 | \bar{q}_6 | \bar{q}_8 |
|-----------|-------|-------------------|-------------------|-------------------|
| Crystal 1 | black | 0.154 ± 0.038 | 0.500 ± 0.030 | 0.306 ± 0.037 |
| Crystal 2 | red | 0.213 ± 0.048 | 0.548 ± 0.027 | 0.358 ± 0.032 |
| Melt | green | 0.215 ± 0.072 | 0.352 ± 0.070 | 0.310 ± 0.057 |

Table A3: Centers of clusters $\bar{q}_4, \bar{q}_6, \bar{q}_8$ found in the $\{q_4, q_6, q_8\}$ space in the system with repulsive walls, $L_x = L_y = 20, L_z = 40$

| | color | \bar{q}_4 | \bar{q}_6 | \bar{q}_8 |
|-----------|-------|-------------------|-------------------|-------------------|
| Crystal 1 | black | 0.142 ± 0.036 | 0.509 ± 0.022 | 0.319 ± 0.038 |
| Crystal 2 | red | 0.215 ± 0.050 | 0.551 ± 0.022 | 0.357 ± 0.035 |
| Melt | green | 0.228 ± 0.076 | 0.383 ± 0.072 | 0.325 ± 0.059 |

Table A4: Centers of clusters $\bar{q}_4, \bar{q}_6, \bar{q}_8$ found in the $\{q_4, q_6, q_8\}$ space in the system with potential $U_{at_1}, L_x = L_y = 20, L_z = 20$

| | color | \bar{q}_4 | \bar{q}_6 | \bar{q}_8 |
|-----------|-------|-------------------|-------------------|-------------------|
| Crystal 1 | black | 0.146 ± 0.036 | 0.507 ± 0.021 | 0.309 ± 0.037 |
| Crystal 2 | red | 0.213 ± 0.055 | 0.551 ± 0.025 | 0.356 ± 0.035 |
| Melt | green | 0.225 ± 0.072 | 0.380 ± 0.072 | 0.323 ± 0.058 |

Table A5: Centers of clusters $\bar{q}_4, \bar{q}_6, \bar{q}_8$ found in the $\{q_4, q_6, q_8\}$ space in the system with potential $U_{at_2}, L_x = L_y = 20, L_z = 20$

Searching for translation vectors

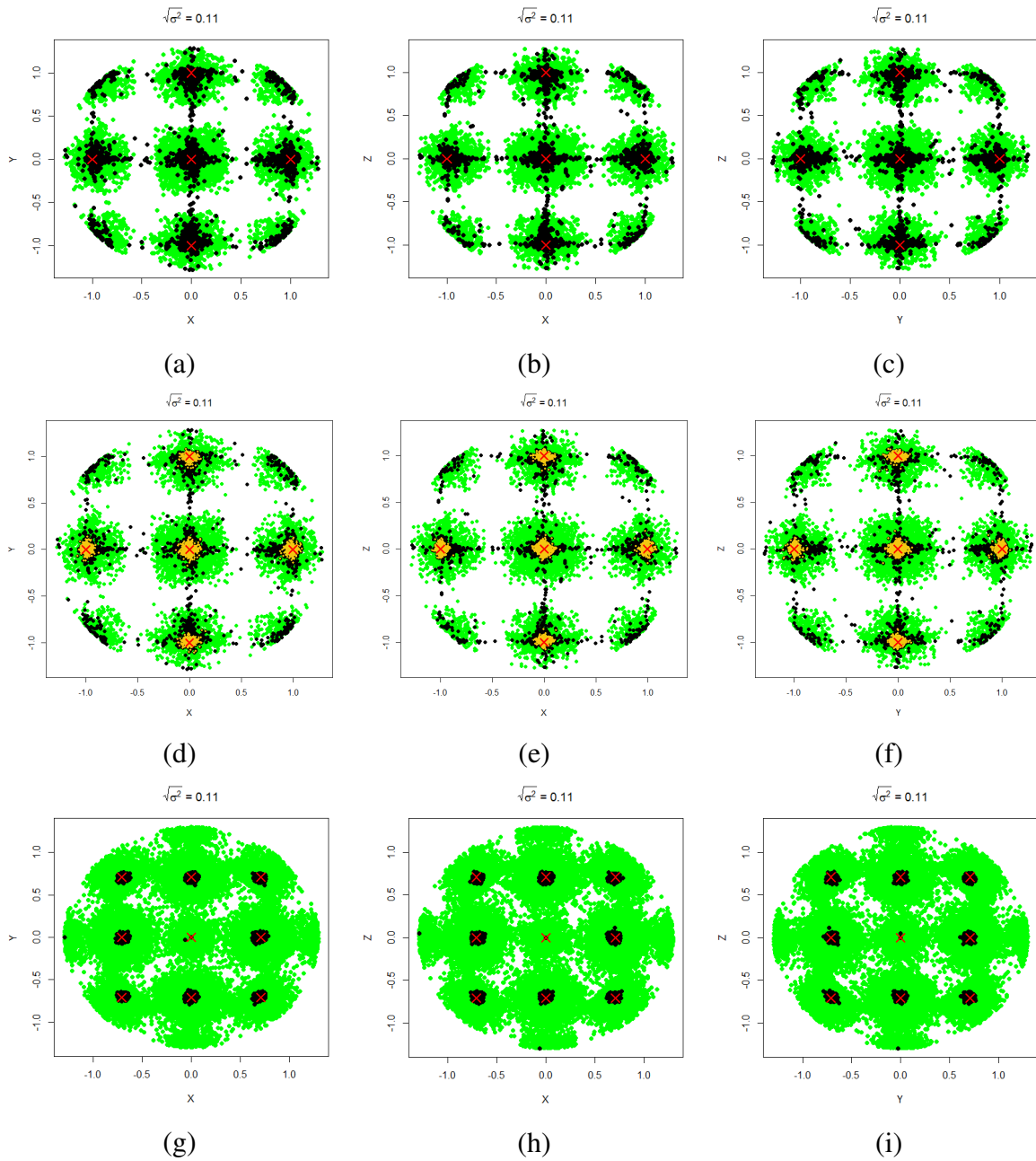


Figure A7: Illustration of reproducing noisy crystal lattice *sc* (a)-(f) and *fcc* (g)-(i) ($\sigma = 0.11$). Green points indicate the particles of the noisy structure *sc* with their nearest neighbors in the cutoff radius $R_c = 1.3$, translated to the origin. Black denotes the points of the crystalline structure reconstructed by found vectors. Red crosses indicate the positions of the particles of the unnoisy structure. The yellow dots correspond to the points of the reconstructed structure, for which the number of neighbors corresponds to the number of neighbors in the undisturbed *sc* structure (6 neighbors).

Searching for translation vectors

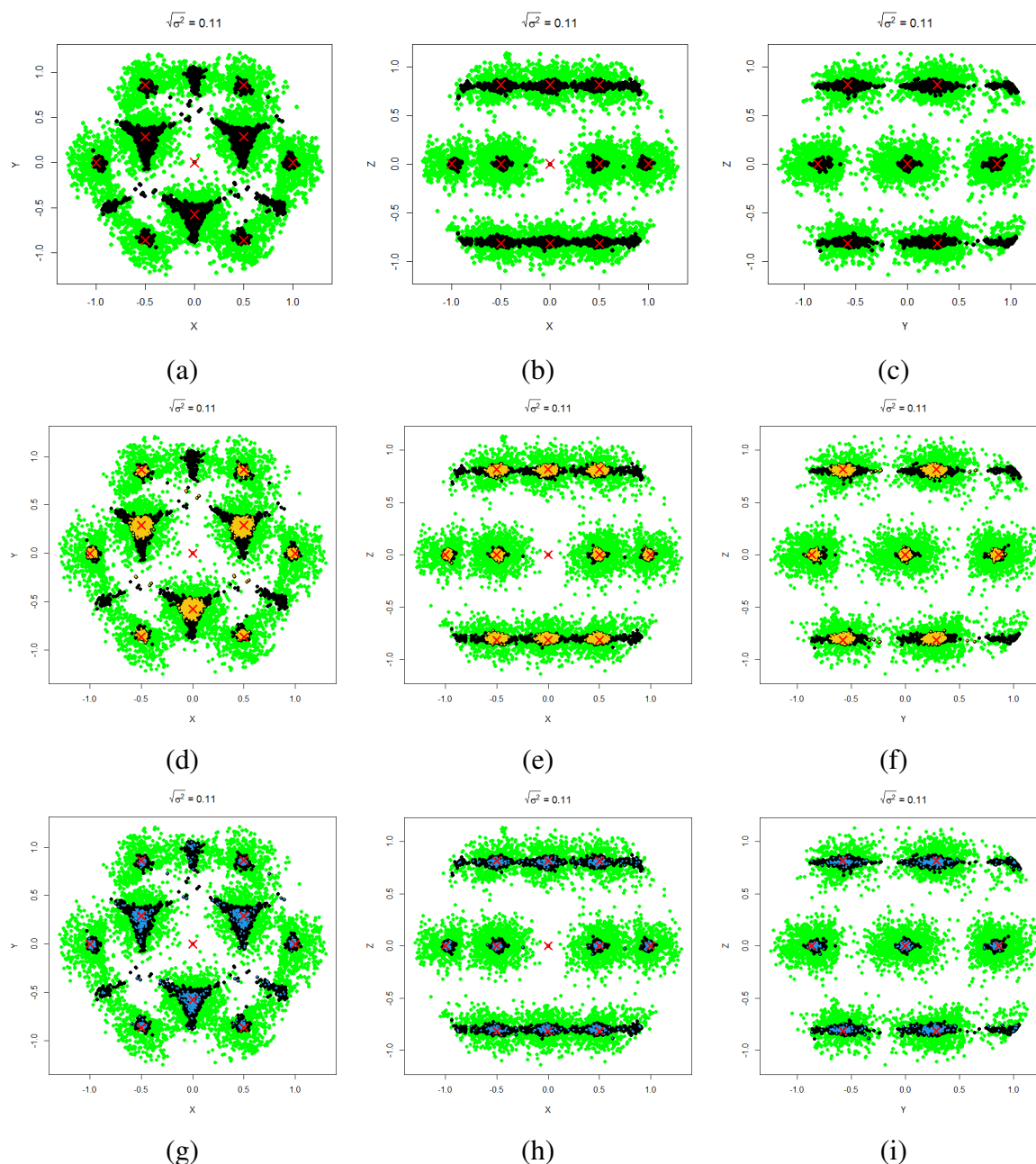


Figure A8: Illustration of reproducing noisy crystal lattice *hcp* ($\sigma = 0.11$). Green points indicate the particles of the noisy structure *hcp* with their nearest neighbors in the cutoff radius $R_c = 1.3$, translated to the origin. Black denotes the points of the crystalline structure reconstructed by found vectors. Red crosses indicate the positions of the particles of the unnoisy structure. The yellow dots correspond to the points of the reconstructed structure, for which the number of neighbors corresponds to the number of neighbors in the undisturbed *hcp* structure (12 neighbors). The blue dots correspond to the points of the reconstructed structure for which the function $F_1 > 0.9 \cdot \max(F_1)$. From the data obtained, it can be seen that the scatter of points in the restored structure (black) is much smaller than in the original noisy structure (green). However, due to the amount of noise, additional clusters of particles (a)-(c) are formed. Figure (c) shows especially clearly that the following coordination sphere is involved in the consideration. Additional filters (restrictions on the number of neighbors or the value of the function F_1) can help improve the result (d)-(i).

Reconstruction procedure for the bulk system $E = -5727, L_x = L_y = 20, L_z = 19$

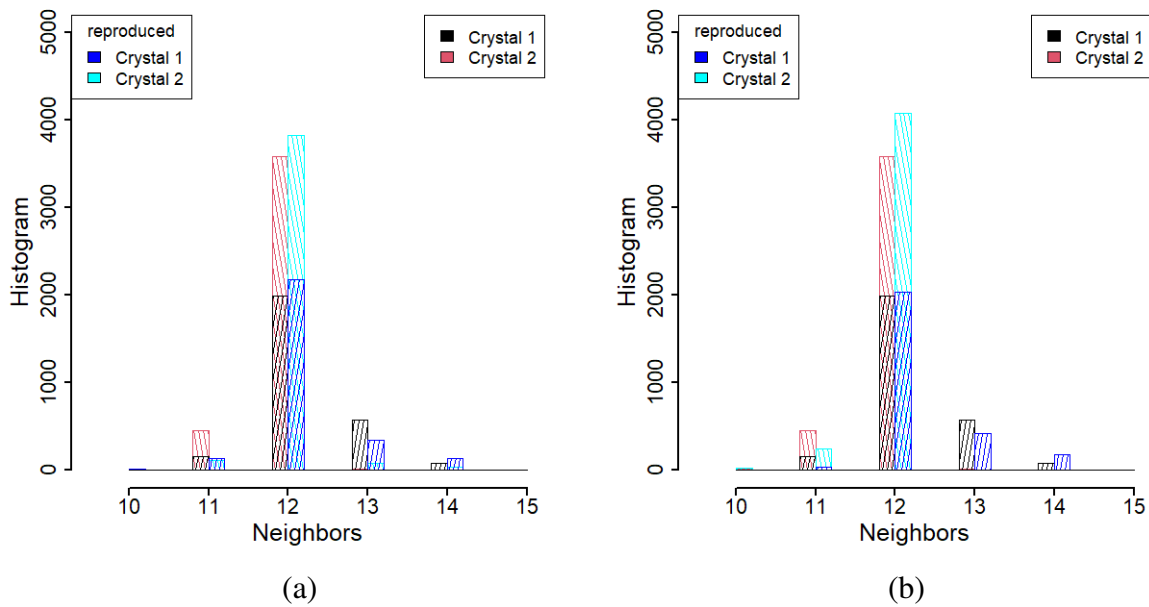


Figure A9: Histogram of neighbors: (a) for reconstructed structures, the assignment to clusters corresponds to clustering at the noise reduction stage; (b) for reconstructed structures, the assignment to clusters is done independently (b).

Reconstruction procedure for the bulk system $E = -5727$, $L_x = L_y = 20$, $L_z = 19$

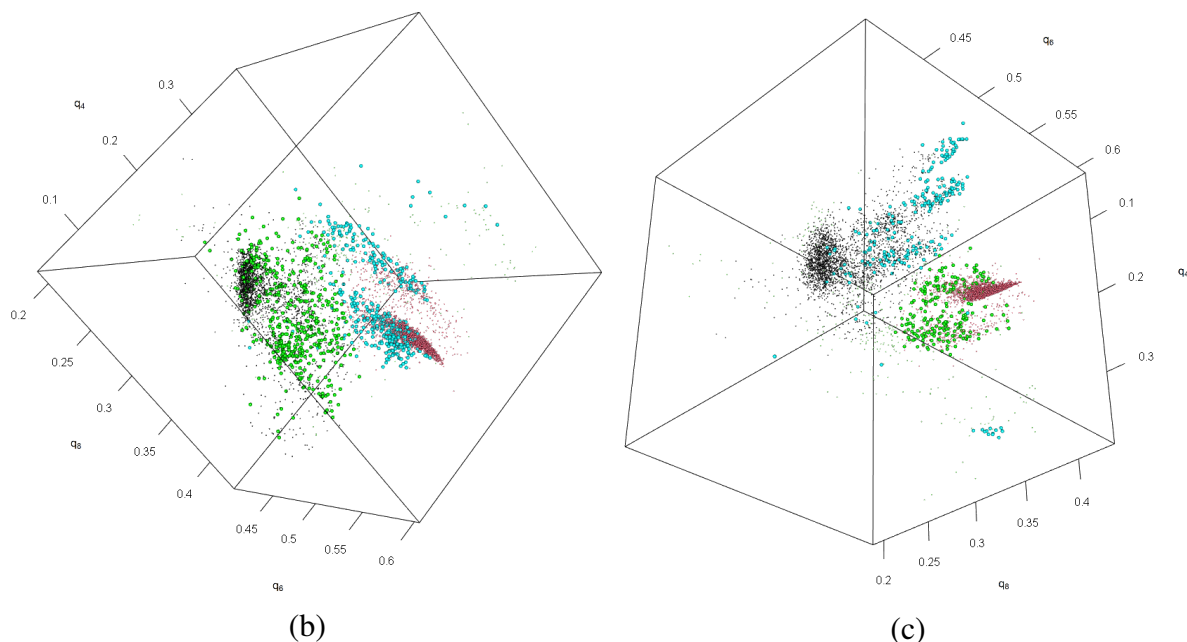


Figure A10: 3d view of LBO parameters for reconstructed system; the NRLBO parameters q_i for the initial particles are plotted in black, red (*Crystal 1*, *Crystal 2*). (a) large green marks those points of the black cluster (*Crystal 1*) for which after reconstructing and independently repainting, the structural type changed from *Crystal 1* to *Crystal 2* or *Melt*. Thus, the black dots in this figure correspond to the "stable" particles of the *Crystal 1* that have not changed their cluster. Additionally, in this figure, the new values of the green "unstable" particles assigned to the new clusters after the reconstructing procedure are applied in cyanide color. (b) similarly, green particles denote "unstable" particles of the *Crystal 2*, and their updated values are indicated by the color cyanide.

Reconstruction procedure for the bulk system $E = -5727, L_x = L_y = 20, L_z = 19$

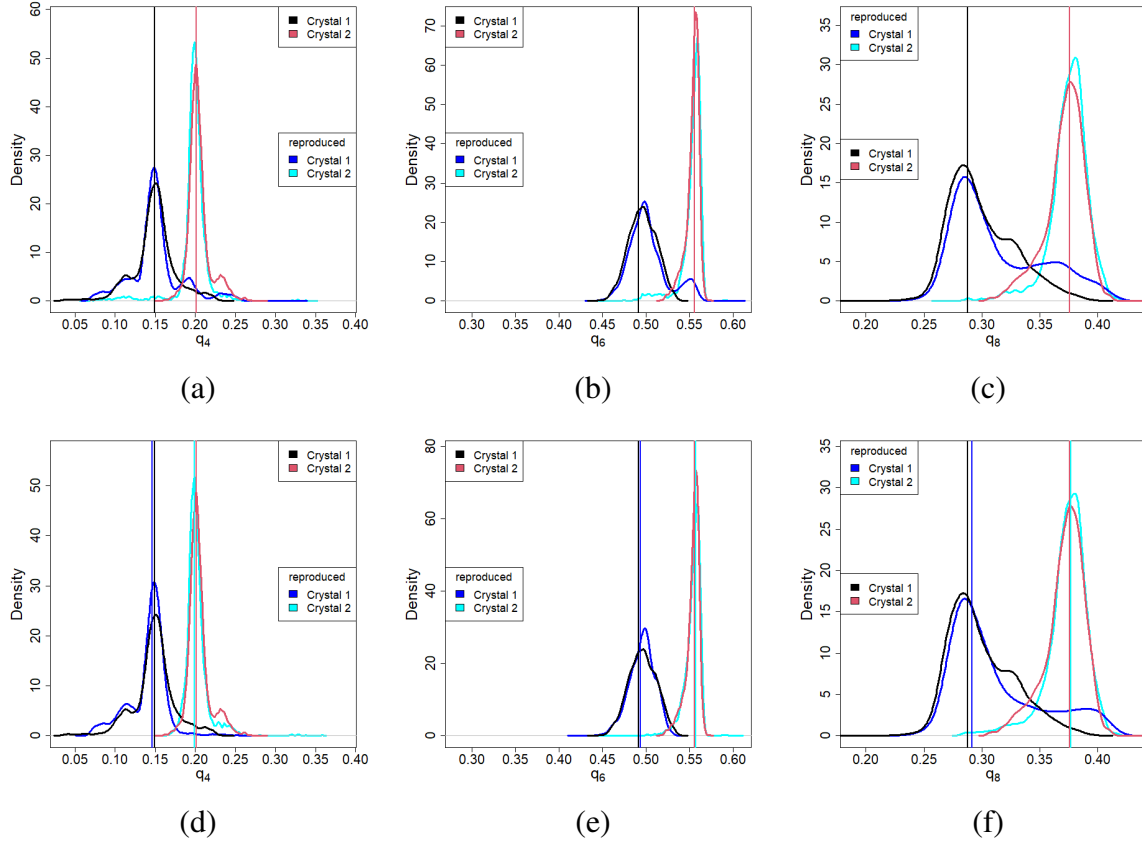


Figure A11: Densities of NRLBO parameters (black and red) for initial structure and LBO for reconstructed system (blue and cyan). For reconstructed structures, the assignment to clusters corresponds to clustering for initial structure (a-c); for reconstructed structures, the assignment to clusters is done independently for initial and reconstructed structure (d-f). The figures show that without repainting of the particles, additional small peaks on reconstructed data (a-c) are observed in the area of the main maxima of the initials clusters: $q_4 \approx 0.18$, $q_6 \approx 0.55$, $q_8 \approx 0.36$ (the blue curves in Fig.(a-c)). After recoloring, the distributions become much more narrow and the "tails" of the side structures in the region of the main peaks are reduced for both blue and cyan curves (d-f). This overlap of distributions suggests that in the boundary region, when the parameters are far from the clusters centers, the separation of particles to a particular cluster is formally possible, but due to the large noise is not reliable.

Reconstruction procedure for the bulk systems, $L_x = L_y = 20$, $L_z = 19$

| E | Crystal 1 (black) | Crystal 2 (red) | Melt (green) | View |
|-------|----------------------|--------------------|-----------------|------|
| -5727 | 2674 (37%) | 4362 (61%) | 163 (2%) | |
| -5104 | 2188 (30%) | 3557 (50%) | 1454 (20%) | |
| -4715 | 1418 (20%) | 3312 (46%) | 2469 (34%) | |
| -3408 | 809 (11%) | 1342 (19%) | 5048 (70%) | |
| -2040 | 89 (1.5%) | 107 (1.5%) | 7003 (97%) | |

Table A6: The number of particles (and percentage) related to a clusters for different energies in the system without walls, $L_x = L_y = 20$, $L_z = 19$ after reconstructing procedure. The colors in the snapshots correspond to the colors used to indicate clusters in the space $\{q_4, q_6, q_8\}$.

Structure factor

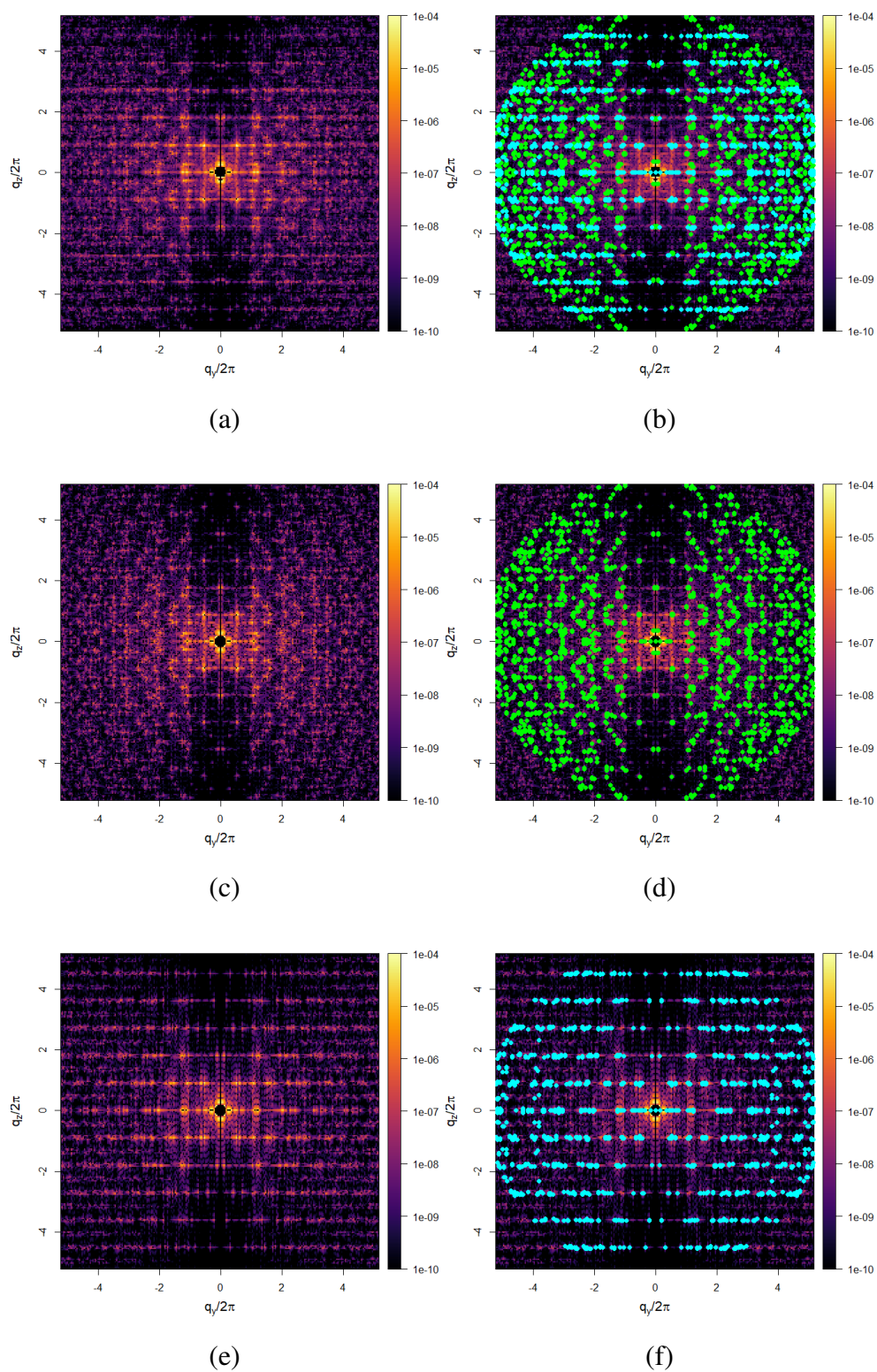


Figure A12: Two-dimensional structure factor for reconstructed systems: for the mixture of *Crystal 1* and *Crystal 2* (a); for the particles from *Crystal 1* (c); for the particles from *Crystal 2* (e); the same structures as (a,c,e) with peaks from reconstructed *Crystal 1* (green) and *Crystal 2* (cyan) (b,d,f). For this set of pictures components q_y , q_z vary from -5.2 to 5.2 with increment of 0.04 .

Thermodynamic properties of big systems:

repulsive walls with $L_x = L_y = 20$, $L_z = 40$ and bulk with $L_x = L_y = 20$, $L_z = 39$

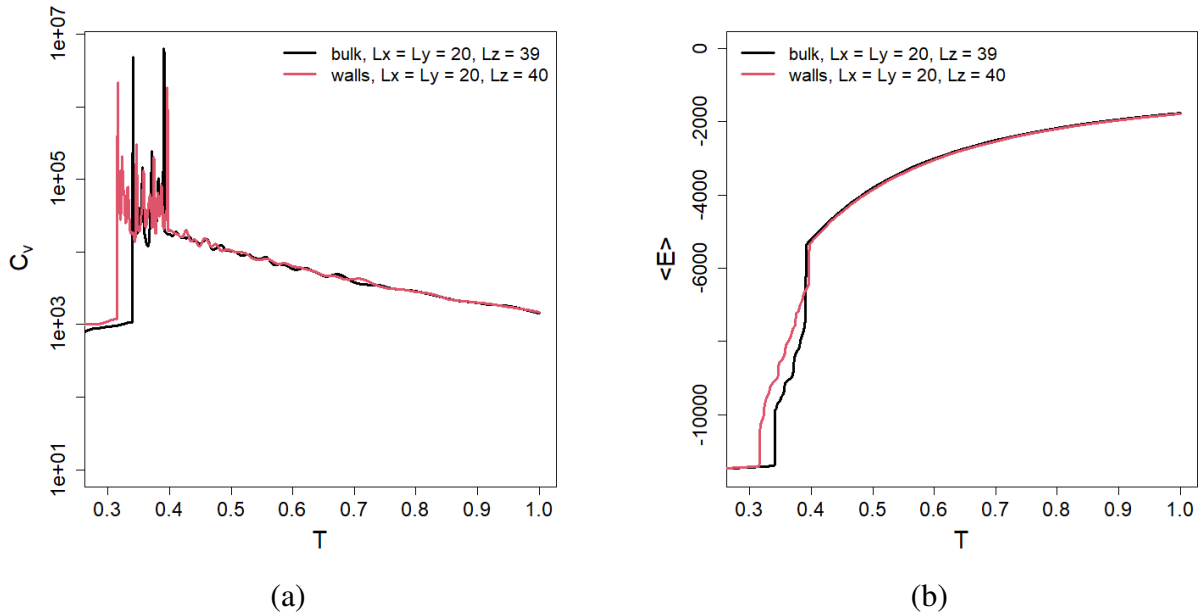


Figure A13: A canonical heat capacity $C_v(T)$ (a) and $\langle E \rangle(T)$ (b) for the system with repulsive walls with $L_x = L_y = 20$, $L_z = 40$, and bulk with $L_x = L_y = 20, L_z = 39$.

Features of systems with attractive walls

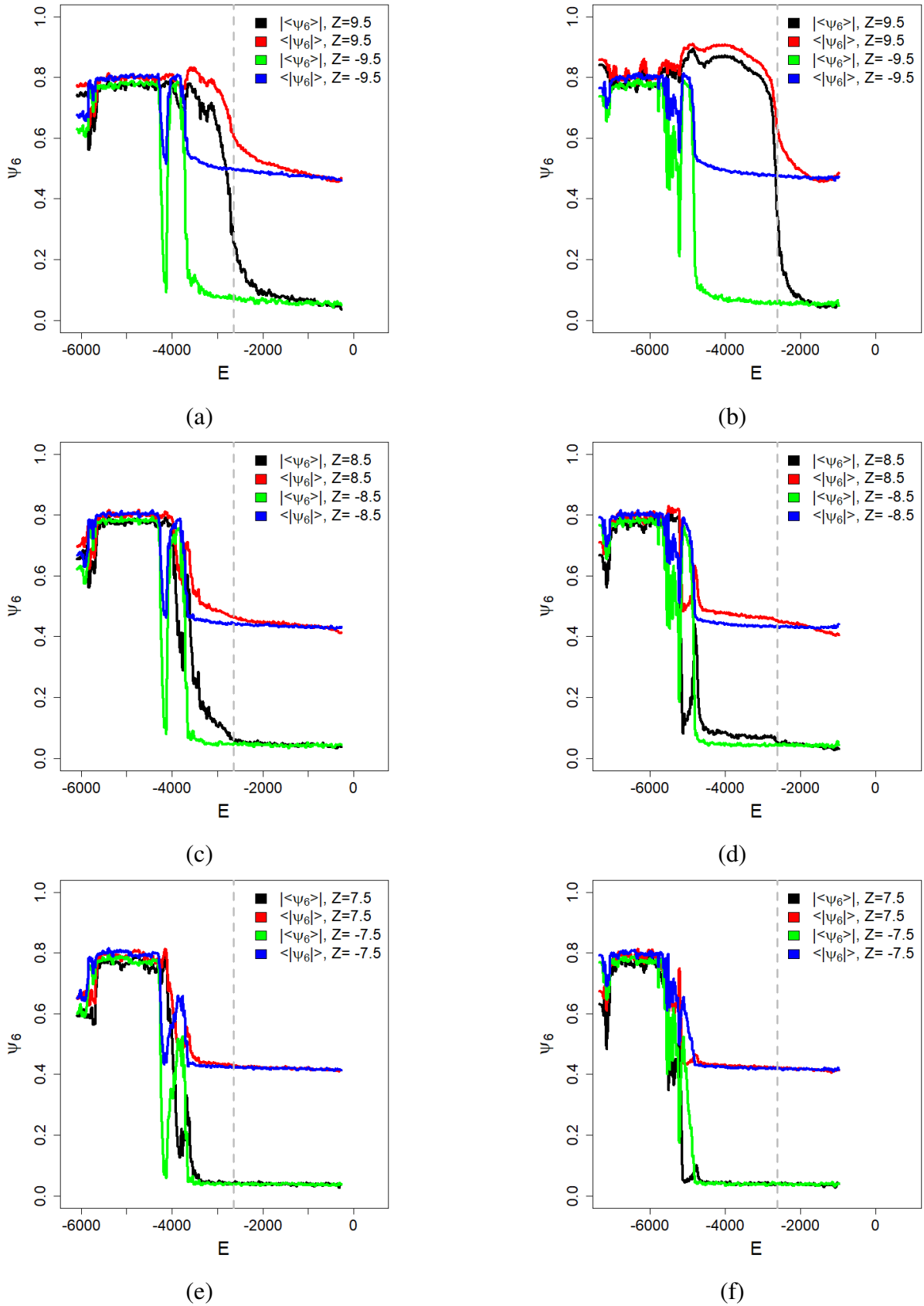


Figure A14: Energy dependencies of parameter ψ_6 for a systems with a potential of U_{at_1} (a,c,e) and U_{at_2} (b,d,f) by layers.

Features of systems with attractive walls

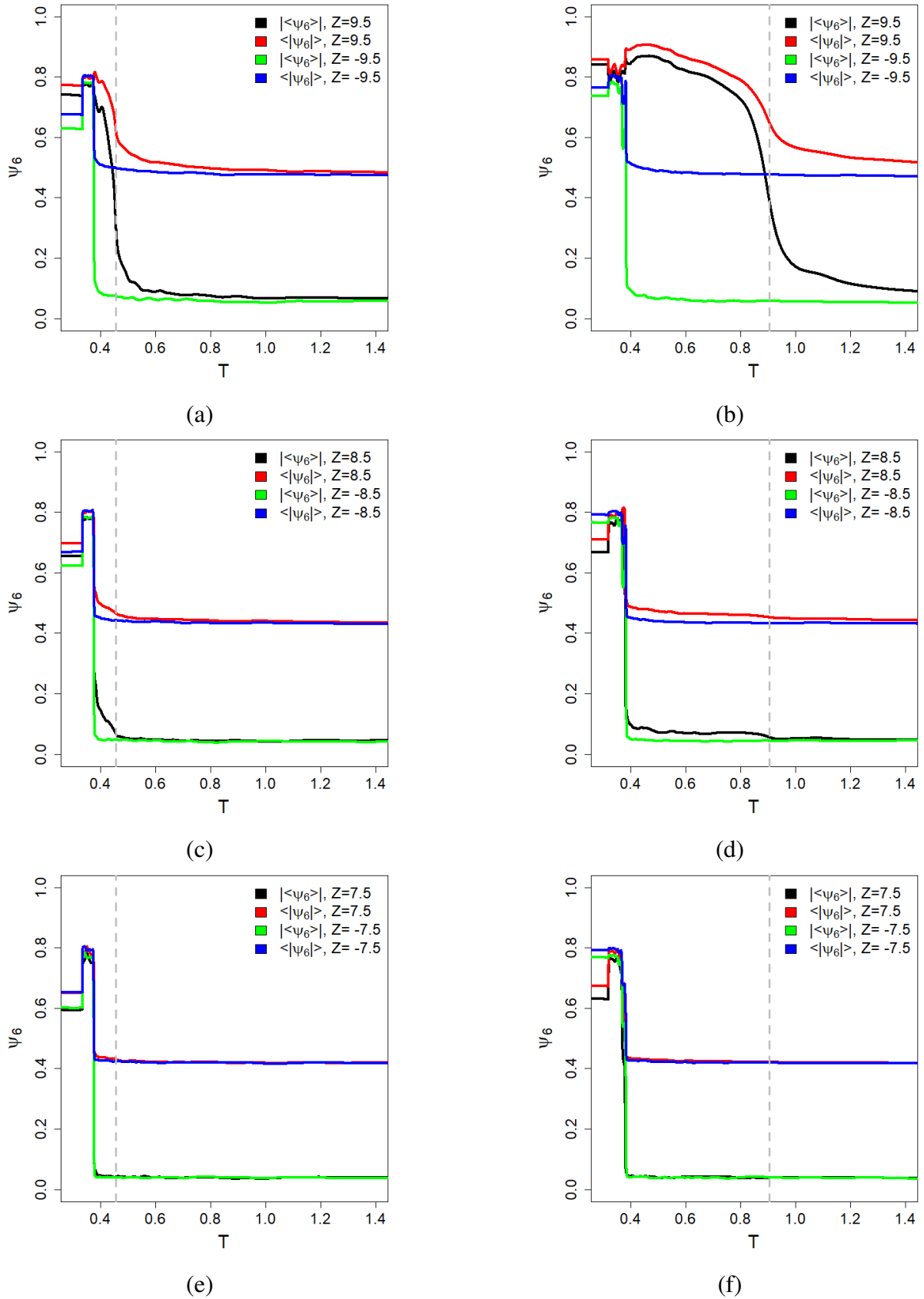


Figure A15: Temperature dependencies of parameter ψ_6 for a systems with a potential of U_{at_1} (a,c,e) and U_{at_2} (b,d,f) by layers.

Results: structure

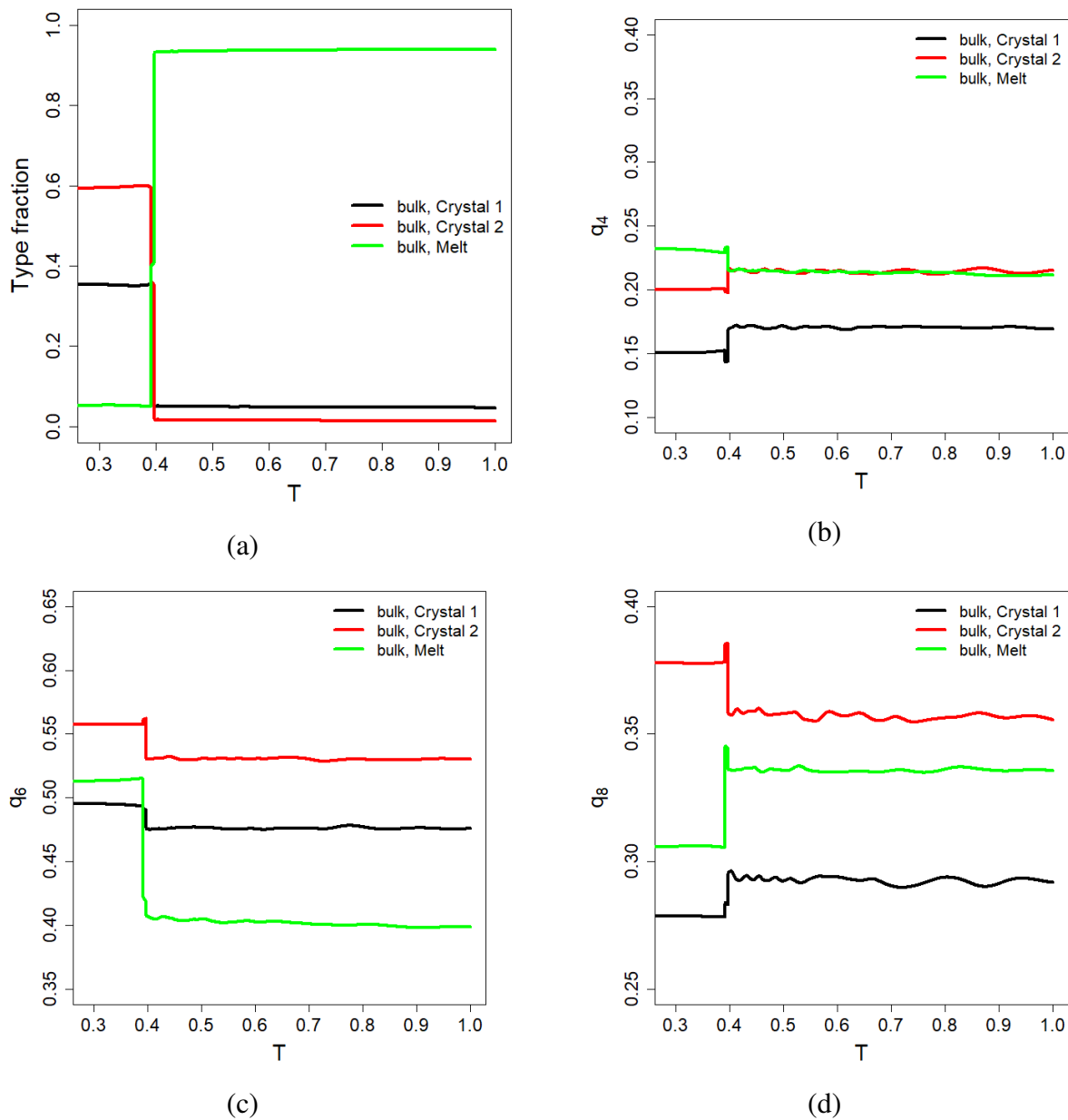


Figure A16: The proportion of particles assigned to different types based on NRLBO parameters (a), q_4 (b), q_6 (c), q_8 (d) for the bulk system $L_x = L_y = 20, L_z = 19$.

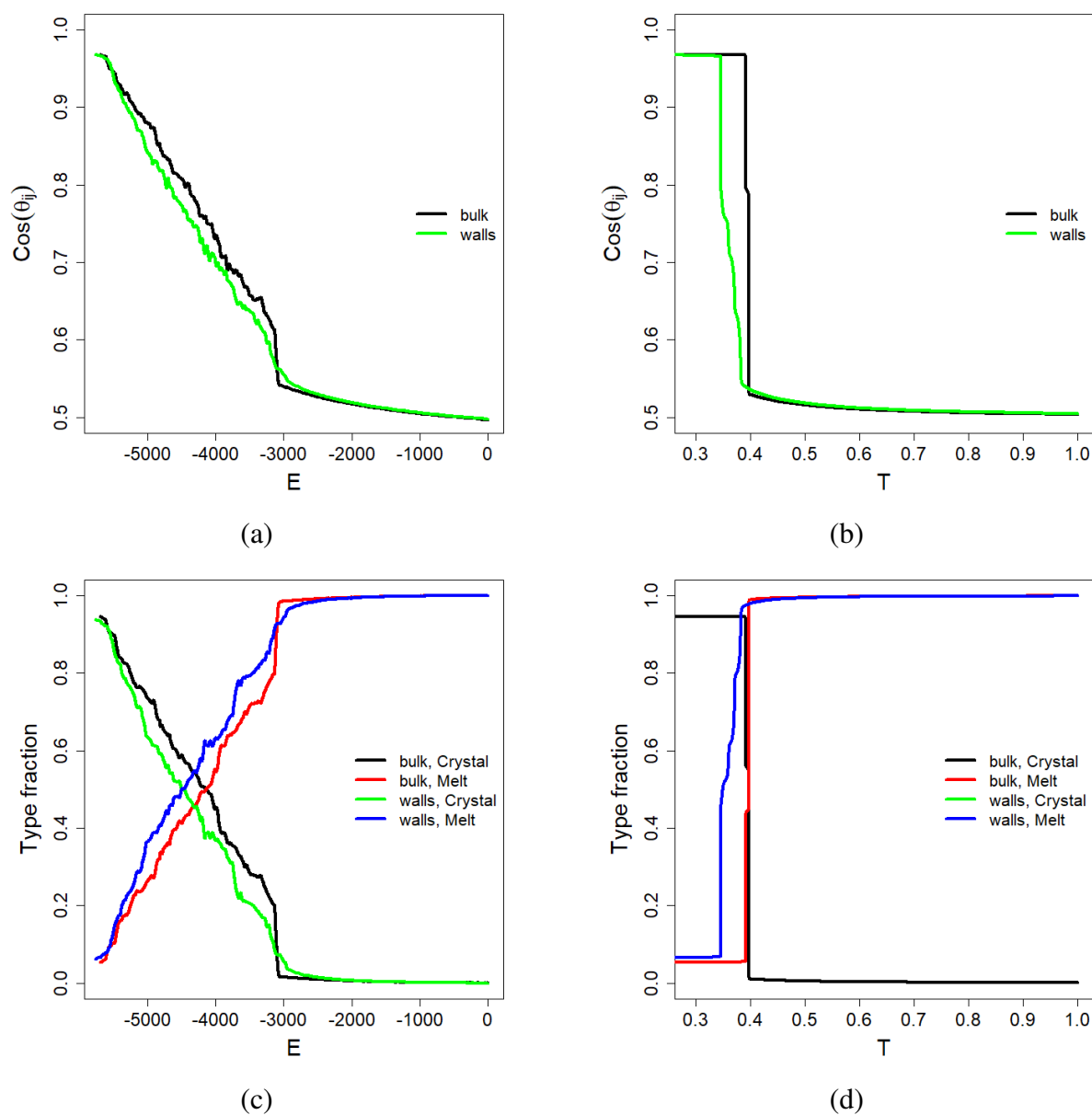


Figure A17: The average cosine angle between the selected bond and their neighboring bonds (a), (b); the proportion of particles assigned to different types based on chain segments alignment analysis (c), (d) for the bulk system $L_x = L_y = 20, L_z = 19$.

Acknowledgement

Since the scientific work is closely connected with a wide range of external circumstances, the thanks listed here apply not only to scientific discussions, but also to all the people who have greatly influenced my philosophy over the past 4.5 years.

The gratitude to my supervisor, PD Dr. Viktor Ivanov, could take several pages, since he provided invaluable support from the relocation stage to the present. I am grateful for giving me the opportunity to work on such an engaging project. I appreciate the balance PD Dr. V. Ivanov established between giving me autonomy and guiding my work. His guidance, willingness to discuss scientific problems, establishing a productive working atmosphere and expanding scientific network were invaluable to me. Additionally, his assistance with everyday issues was particularly important for me as a newcomer to the country. Thanks to his support, I was able to reach my full potential.

I am deeply grateful to Prof. Wolfgang Paul. In Prof. W. Paul's group, you can always share scientific successes, discuss difficulties, and receive valuable feedback in a friendly atmosphere. Despite the wide range of research areas (from quantum mechanics to macromolecular systems) and methods (from machine learning to computer simulation using MC, MD methods) of research in the group, each participant can count on the expert opinion of Prof. W. Paul.

I am thankful to all the members of the scientific group with whom I was lucky to meet. Prof. Stefan Trimper's friendliness, love of science and art, broad outlook and curiosity cannot leave anyone indifferent. PhD students from the Prof. W. Paul's group Kai-Hendrik Henk and Christian Lauer, continue to accompany me in these final stages of my graduate journey, while Dr. Lama Tannoury, Dr. Michael Beyer, Dr. Arne Böker are guiding stars for me, landmarks that showed by their example how to move towards the goal. Our postdoc Dr. Yulia Martemyanova not only participated in scientific discussions, but also showed by example of her family that nothing is impossible in this world.

I am sure that Dr. Timur Shakirov, who recently left the group, played a role in the research of each member of our group, since there are no limits to his outlook, curiosity and desire to share his knowledge. I dare say that he played a key role in my scientific philosophy. I am grateful to him for his patience in very heated discussions and for the endless questions "I wonder, what will happen if..?" I hope I was able to partially quench his scientific appetite and answer some of his questions. I also believe that his enthusiasm will inspire many more people.

My project was funded by the International School for Functional Polymers - AGRIPOLY. Special thanks go to the coordinators who diligently took care of the administrative aspects. I also appreciate the International Office and especially the kind Esther Smykalla for warm welcome upon arrival, assistance with administrative matters and help in settling in for all international students.

Finally, I would like to thank my parents, family and friends from the bottom of my heart, without whom this endeavor would not have been possible. To my lovely mother and considerate father, thank you for everything you have done and continue to do. Your love has been a constant source of calm and I am grateful for the countless sacrifices you have made to ensure my education and well-being.

I want to thank my dear brother, Lesha, who has always served as an example of hard work and perseverance. Thank you for being a reliable support for me and our family.

I am grateful to my friends in my native country for striving to maintain close, trusting relationships despite time and distance. Thanks to dear Viola, Lena, Sveta, Georgy, Yaroslav for inspiring me, finding words of support and comfort, sharing with me all the successes and failures for many years. You help me get to know myself and improve. Among my friends in Halle, Marina Zamsheva, Andrey Zamshev, Irma Schmidt, Maria Samotina, Alina Starostenko have colored my life with bright colors. Thank you for your contribution to my philosophy, soulful time spent together, and invaluable help in my everyday life.

Anton Rymarev has held a special place in my life and heart for the last years. I am grateful to you for patiently sharing with me all the shocks of these years. For not doubting my powers for a moment, and for taking care of me day in and day out. Thank you for making me a better and happier person.

List of Publications

- [F1] A. V. Emelyanenko, E. S. Filimonova, and A. R. Khokhlov, *Molecular origin of the heterogeneity in the nematic and smectic liquid crystals: Elastic constants, gradients of order parameters, and visualization of small objects*, Phys. Rev. E **103** (2021), 022709.
doi: 10.1103/PhysRevE.103.022709
- [F2] A. V. Emelyanenko and E. S. Filimonova, *Molecular-statistical approach to the description of tilted smectic phases*, Phase Transitions, **91** (2018), 984 – 993.
doi: 10.1080/01411594.2018.1506127
- [F3] E. Filimonova, V. Ivanov, and T. Shakirov, *Distinguishing noisy crystal symmetries in coarse-grained computer simulations: New procedures for noise reduction and lattice reconstruction*
In preparation, planned for submission to *The Journal of Chemical Physics*.
Published in Arxiv: <https://arxiv.org/pdf/2404.15539.pdf>
- [F4] E. Filimonova, V. Ivanov, and T. Shakirov, *Crystallization of short semiflexible chains of tangent hard spheres in melts and in thin films: crystal structures and effects of substrates*
In preparation, planned for submission to *The Journal of Chemical Physics*.

Curriculum Vitae

Personal Information:

Name: Evgeniia Filimonova

Education:

since 2019

PhD studies

Martin Luther University Halle-Wittenberg

09/2017- 06/2019 Master of Science in Physics

Moscow State University

Title of the qualifying paper: *Molecular theory of liquid crystals with inhomogeneous distribution of order parameters*

09/2013- 06/2017 Bachelor of Science in Physics

Moscow State University

Title of the qualifying paper: *Polarization in smectic liquid crystals as studied by methods of statistical physics*

Declaration under the Oath

Eidesstattliche Erklärung

I hereby affirm that I have produced this work independently, relying solely on the sources I have cited. Any material taken from external sources, whether quoted or paraphrased, has been appropriately acknowledged.

I declare that all information given is accurate and complete. The thesis has not been used previously at this or any other university in order to achieve an academic degree.

I certify that no criminal or investigative proceedings are pending against me. I affirm that I have no criminal record.

Hiermit bestätige ich, dass ich diese Arbeit unabhängig erstellt und mich ausschließlich auf die von mir zitierten Quellen verlassen habe. Jegliches Material aus externen Quellen, ob zitiert oder paraphrasiert, wurde entsprechend gekennzeichnet.

Ich erkläre hiermit, dass alle gemachten Angaben richtig und vollständig sind. Die Abschlussarbeit wurde bisher weder an dieser noch an einer anderen Universität zur Erlangung eines akademischen Grades verwendet.

Ich bestätige, dass gegen mich kein Straf- oder Ermittlungsverfahren anhängig ist. Ich versichere, dass ich nicht vorbestraft bin.

Place, Date

Ort, Datum

Signature of the applicant

Unterschrift des Antragstellers